UNIVERSITY OF SOUTHAMPTON

Tectonic Evolution of the Corinth Rift

by

Rebecca E. Bell

A thesis submitted in partial fulfillment for the
degree of Doctor of Philosophy

in the
Faculty of Engineering, Science and Mathematics
School of Ocean and Earth Science

June 2008

UNIVERSITY OF SOUTHAMPTON

ABSTRACT

FACULTY OF ENGINEERING, SCIENCE AND MATHEMATICS
SCHOOL OF OCEAN AND EARTH SCIENCE

Doctor of Philosophy

TECTONIC EVOLUTION OF THE CORINTH RIFT

by Rebecca E. Bell

The evolution of extensional processes at continental rift zones provides important constraints on the underlying lithospheric deformation mechanisms, level of seismic hazard and location of likely hydrocarbon traps. The Corinth rift in central Greece is one of the few examples that has experienced a short extensional history (< 5 Myr), has a relatively well–known pre–rift structure, is experiencing pure extension, and is located in a fluctuating marine–lacustrine setting producing characteristic cyclical stratigraphy. Traditionally, the rift has been described as an asymmetric half–graben controlled by N–dipping faults on the southern margin. This view has been challenged by increasing seismic data from the offshore part of the rift which show it is more complex, analogous to more developed rifts like the East African rift and Red Sea. High resolution and deep penetration seismic reflection data across the entire offshore rift zone are combined with onshore geomorphological data to constrain: the architecture of major rift–bounding faults; basin structure; spatial and temporal evolution of depocentres; total extension across the rift; and slip rates of major faults from stratigraphic analysis and dislocation modelling of long term deformation.

Stratigraphy within the offshore Corinth rift is composed of a non reflective older unit (oldest syn–rift sediments are ca. 1–2 Ma) and a well stratified younger unit separated by a ca. 0.4 Ma unconformity. Net basement depth is greatest in the present centre of the rift zone (∼2.7–3 km) and decreases to the east and west (∼1.5–1.6 km). The 0.4 Ma unconformity surface records an important change in rift geometry. Pre. 0.4 Ma, sediment deposition occurred in 20–50 km long isolated basins, controlled by both N and S–dipping faults. Post 0.4 Ma, sediment deposition and basement subsidence has been enhanced in areas between these originally isolated basins creating a single ∼80 km long central depocentre. Since 0.4 Ma activity has became focused on mostly N–dipping faults. However, in the west, N tilting stratigraphy and basement indicate S–dipping faults are locally structurally dominant. Late Quaternary averaged major fault slip rates are ∼3–6 mm/yr on the N-dipping south margin faults, >1.8 mm/yr on S–dipping offshore faults, and ∼1–3 mm/yr on faults in the eastern rift. Total extension over rift history (Late Pliocene to present) has been greatest in the west (∼8 km), with extension distributed over many faults (most now inactive) spaced at 5 km intervals. To the east total extension is reduced (∼5–6 km) and is distributed over fewer faults spaced at 15–35 km intervals. There are large differences in rift character along the rift axis and throughout rift history. The highest geodetic rates over the last 10–100 years are in the western part of the rift and do not correspond to the area of greatest offshore basement depth. This suggests a recent change in the locus of strain focusing, potentially analogous to the change that occurred in rift geometry ca. 0.4 Ma.

DECLARATION OF AUTHORSHIP

I, REBECCA EMMA BELL declare that the thesis entitled "Tectonic evolution of the Corinth Rift" and the work presented in the thesis are both my own, and have been generated by me as the result of my own original research. I confirm that:

- this work was done wholly or mainly while in candidature for a research degree at this University;
- where any part of this thesis has previously been submitted for a degree or any other qualification at this University or any other institution, this has been clearly stated;
- where I have consulted the published work of others, this is always clearly attributed;
- where I have quoted from the work of others, the source is always given. With the exception of such quotations, this thesis is entirely my own work;
- I have acknowledged all main sources of help;
- where the thesis is based on work done by myself jointly with others, I have made clear exactly what was done by others and what I have contributed myself;
- parts of this work have been published as: **Bell, R.E.**, McNeill, L.C., Bull, J. M., Henstock, T. J. Evolution of the offshore western Gulf of Corinth *Geological Society of America, Bulletin*, 120:156-178, 2008.

Signed:

Date:

Contents

Acknowledgements **xiv**

1 Introduction **1**
1.1 The early stages of continental extension 1
1.2 Examples of early continental rifting 2
1.3 Introduction to the Corinth rift 5
1.3.1 Why study the Corinth rift? 5
1.3.2 Corinth rift tectonic controversies 6
1.4 Aims and objectives 6
1.4.1 Objective I: To determine the geometry, style and magnitude of subsidence and extension across the Corinth rift zone 7
1.4.2 Objective II: Determine spatial and temporal rift development 7
1.4.3 Objective III: Link the observations in the Corinth rift to global controls on rift initiation and evolution 8
1.5 Overview of the thesis 8

2 Research Context **11**
2.1 Continental extension 11
2.1.1 Continental deformation theory 11
2.1.2 Mechanisms of Continental Extension 13
2.1.3 Fault mechanics 19
2.2 Tectonic framework of the Aegean region 21
2.2.1 Seismicity and active tectonics 21
2.2.2 Kinematics of Aegean region tectonic movement 22
2.2.3 The GPS velocity field 23
2.2.4 Dynamic deformation models for the Aegean 24
2.3 Geology and tectonics of the Corinth rift 26
2.3.1 Geological history 26
2.3.2 Sedimentary basin architecture 29
2.3.3 Active tectonics 31
2.3.4 Rift structure 35
2.4 Summary of major controversies in Corinth rift tectonics 38

3 Methodology **39**
3.1 The multi–disciplinary approach 39
3.1.1 Onshore geomorphology investigation 39
3.1.2 Multichannel seismic reflection interpretation 39
3.1.3 Dislocation modelling 40

3.2 Datasets . . . 40
3.2.1 Primary seismic reflection and multibeam bathymetry data . . 40
3.2.2 Secondary seismic reflection and multibeam bathymetry data . 42
3.2.3 Published or publicly available datasets . . . 43

4 Tectonic geomorphology of the Corinth rift coastline 44
4.1 Introduction . . . 44
4.1.1 Normal faulting and land movement . . . 44
4.1.2 Movement of the Corinth rift coastline . . . 46
4.2 Deformation Indicators . . . 46
4.2.1 Relative sea level fall: Tectonic uplift or absolute sea level fall indicators . . . 47
4.2.2 Relative sea level rise: Tectonic subsidence or absolute sea level rise indicators . . . 50
4.3 Northern margin field study methodology . . . 50
4.4 Review of tectonic movement along the southern Corinth coastline . . 51
4.4.1 Holocene uplift . . . 51
4.4.2 Late Quaternary uplift . . . 52
4.4.3 Uplift rate trends . . . 53
4.5 Tectonic movement of the northern coastline . . . 53
4.5.1 Alkyonides Gulf: Porto Germeno to Kiriaki . . . 53
4.5.2 The Pangalos peninsula: Kiriaki to Itea . . . 57
4.5.3 Northwest margin: Galaxidi to Nafpaktos . . . 62
4.6 Discussion: Fault control of northern coastline movement . . . 63
4.7 Conclusions . . . 66

5 Evolution of the offshore western Gulf of Corinth 68
5.1 Introduction . . . 68
5.2 Methodology and Data . . . 71
5.2.1 Seismic reflection and swath bathymetry data . . . 71
5.2.2 Depth conversion . . . 71
5.3 Stratigraphic Architecture . . . 71
5.3.1 Shelf and upper slope stratigraphic architecture: The Eratini sub-basin . . . 72
5.3.2 Main basin stratigraphic architecture . . . 76
5.3.3 Correlation between Eratini sub–basin and main Gulf stratigraphic units . . . 78
5.4 Basin Geometry . . . 80
5.4.1 Basement structure . . . 80
5.4.2 Fault Architecture . . . 83
5.4.3 Slip rates . . . 84
5.5 Basin Evolution . . . 90
5.5.1 Eastern study area: Area 1 . . . 90
5.5.2 Central study area: Area 2 . . . 91
5.5.3 Western study area: Area 3 . . . 94
5.6 Discussion . . . 96
5.6.1 Offshore western Gulf fault activity . . . 96

5.6.2 Western Gulf of Corinth rift evolution . . . 98
5.6.3 Total Gulf of Corinth structure and evolution . . . 99
5.6.4 Faulting at depth . . . 99
5.6.5 Comparison with other rifts . . . 101
5.7 Conclusions . . . 102

6 Fault architecture, basin structure and evolution of the Corinth rift, central Greece 103
6.1 Introduction . . . 103
6.2 Tectonic and geological framework of the Corinth rift . . . 104
6.3 Methodology . . . 109
6.3.1 Datasets . . . 109
6.3.2 Depth conversion . . . 109
6.3.3 Onshore data . . . 109
6.4 Fault architecture in the Corinth rift . . . 111
6.4.1 Western Corinth rift fault structure . . . 112
6.4.2 Central Gulf fault structure . . . 112
6.4.3 Eastern Gulf of Corinth fault structure . . . 113
6.4.4 Eastern Corinth rift (Alkyonides Gulf) fault structure . . . 113
6.5 Stratigraphy . . . 114
6.5.1 Stratigraphic architecture of the Western Corinth rift . . . 114
6.5.2 Stratigraphic architecture of the Central Corinth rift . . . 117
6.5.3 Stratigraphic architecture of the Eastern Corinth rift (Alkyonides Gulf) . . . 119
6.6 Basin Geometry . . . 119
6.6.1 Basement structure . . . 119
6.6.2 Sediment thickness . . . 124
6.7 Basin Age . . . 128
6.8 Fault slip rates . . . 129
6.8.1 Slip rate determination method . . . 129
6.8.2 Slip rates within the western rift . . . 131
6.8.3 Slip rates within the central rift . . . 131
6.8.4 Slip rates within the Alkyonides Gulf . . . 133
6.9 3D spatial and temporal rift evolution . . . 134
6.9.1 Zone 1: Western rift . . . 135
6.9.2 Zone 2: Central-western rift . . . 136
6.9.3 Zone 3: Central rift . . . 137
6.9.4 Zone 4: Central–eastern rift . . . 139
6.9.5 Zone 5: Eastern rift- Gulf of Alkyonides . . . 139
6.10 Discussion . . . 141
6.10.1 Corinth rift evolution summary . . . 141
6.10.2 Rift Geometry . . . 145
6.10.3 Rift propagation models . . . 148
6.10.4 Fault interaction and depocentre development . . . 149
6.11 Conclusions . . . 152

7 Total extension and crustal thinning of the Corinth rift 154

7.1 Introduction . . . 154
7.2 Measuring extension across continental rift zones . . . 155
7.3 Method 1: Extension derived from fault displacement . . . 156
7.3.1 Active Corinth rift extension over the last 1 – 2 Ma . . . 158
7.3.2 Total Corinth rift (onshore and offshore) extension over > 2 Ma rift history . . . 162
7.4 Method 2: Crustal thinning stretching factor . . . 165
7.5 Discussion: Implications for the extensional history of the Corinth rift 167
7.5.1 Distribution of extension . . . 167
7.5.2 Upper crustal vs. total crustal extension . . . 171
7.5.3 Detachment faulting in the western rift? . . . 171
7.6 Conclusions . . . 172

8 Long term deformation modelling 173
8.1 Introduction . . . 173
8.1.1 Elastic dislocation models . . . 174
8.1.2 The Earthquake Cycle . . . 176
8.2 Methodology . . . 177
8.2.1 Viscoelastic dislocation models . . . 177
8.2.2 Long term deformation modelling in the Corinth rift . . . 182
8.2.3 Long term deformation in the Alkyonides Gulf . . . 183
8.3 Results . . . 185
8.3.1 Single fault model: East Alkyonides fault and the Skinos/Pisia fault . . . 185
8.3.2 Multiple fault model . . . 189
8.4 Discussion . . . 191
8.4.1 Implications for the Alkyonides Gulf . . . 191
8.4.2 Future of long term Corinth rift deformation models . . . 193
8.5 Conclusions . . . 194

9 Conclusions 196
9.1 How has this study improved our understanding of the Corinth rift? . 196
9.1.1 What is the geometry, style and magnitude of subsidence and extension across the rift? . . . 196
9.1.2 How has the rift evolved spatially and temporally? . . . 199
9.2 How has this study improved our understanding of early continental rifting? . . . 201
9.2.1 How is extension accommodated at the initiation of rifting? . . 201
9.2.2 How do rifts evolve prior to breakup? . . . 202
9.3 Future work . . . 203
9.3.1 Chronostratigraphic record of offshore sediments . . . 203
9.3.2 Dislocation modelling of the western rift region and south coast terraces . . . 204
9.3.3 Basin subsidence and strain analysis . . . 207
9.3.4 Further study into fault activity in the Itea and Antikyra bays 208
9.3.5 Synthesis and new studies in the western Rion graben . . . 208

Bibliography 209

List of Figures

1.1 Some examples of areas of currently active continental lithosphere extension. . . . 3
1.2 Summary of the regions of the Corinth rift discussed in Chapters 4 to 8 of this thesis. . . . 8

2.1 Schematic diagrams showing the **A.** active and **B.** passive modes of rifting. From Corti et al. (2003). . . . 14
2.2 Schematic cartoons of the **A.** McKenzie (1978a) pure shear lithospheric stretching model, and **B.** Wernicke (1981) simple shear extension model. From Ziegler & Cloetingh (2004). . . . 15
2.3 The three fundamental modes of continental extension. **A.** Narrow rift, **B.** Wide rift and **C.** Core complex. From Corti et al. (2003), after Buck (1991). . . . 16
2.4 Principle major basement displacing faults in the Gulf of Suez, with fault width proportional to throw. To the south, structure is dominated by E–dipping faults, whereas W–dipping faults border the Belayim province and E–dipping faults control the northern Darag basin. From Bosworth et al. (2005). . . . 18
2.5 Summary of active faults and earthquake fault plane solutions for earthquakes greater than Mw = 5, in the Aegean region. From Nyst & Thatcher (2004). . . . 21
2.6 **A.** Sketch of the kinematic tectonic movements of the Aegean from McKenzie (1972). **B.** Cartoon of the impact of the Arabian promotory and consequent westward escape of Anatolia (McKenzie 1972) 23
2.7 Compiled GPS velocity field for the Aegean by Nyst & Thatcher (2004). 24
2.8 Principle strain axes across Greece, computed by Clarke et al. (1998). 25
2.9 Tectonic framework of the onshore Corinth rift. . . . 28
2.10 **A.** Location of the Ori (1989) first and second phase Corinth rift basins. **B.** Idealised cross-section across the Corinth rift showing first and second phase deposits (Ori 1989). . . . 29
2.11 Summary of Ms $\geq$5 seismicity. Focal mechanism geometry and sources of data shown in Table 2.1. . . . 34
2.12 **A.** Summary of the Ori (1989) and Le Pichon et al. (1995), Clarke et al. (1998) and Nyst & Thatcher (2004) theories of W to E and E to W rift propagation respectively. **B.** Idealised cross-sections to demonstrate the fundamental aspects of the Jackson (1999), Sorel (2000) and Collier & Jones (2003) theories of across-strike rift propagation. . . . 37

3.1 Summary of the seismic reflection profiles interpreted in this study. . . 41

4.1 Summary of the tectonic vertical motions along the coastline around the Corinth rift. Numbered sites are discussed in text. Onshore vertical movements follow Leeder et al. (submitted). 45
4.2 Sketch diagram of the morphology of wavecut notches and terminology used in this study. 48
4.3 In–situ *L. lithophaga* that has bored into limestone. Photo from www.wooster.edu/geology/Bioerosion. 49
4.4 Holocene and late Quaternary averaged uplift rates along the southern margin, from 21.85° to 23.35°. Locations of numbered points are shown in Figure 4.1 and discussed in text. 52
4.5 Satellite image of the Alkyonides Gulf area (from Google Earth) . . . 54
4.6 **A.** Submerged remains, **B.** well preserved artillery tower and **C.** site map for the 4th century fort of Aegosthena 55
4.7 **A.** Submerged remains in Aliki harbour, **B.** The remains of the sea–gate tower of the fort of Siphai (from Obar 1987), **C.** Site map of the fort of Siphai (from Google Earth) showing the locations of Photos A and B. 56
4.8 **A.** Notched old fan conglomerate on the south side of Porto Germeno bay. **B.** Multiple submerged notches at Paralia Sarandi. Locations shown in Fig. 4.5 57
4.9 Satellite image of the Pangalos peninsula area (from Google Earth) . 58
4.10 **A.** Two notches are observed at low tide at locality 1, Fig. 4.9, **B.** At high tide the roof of the upper notch is only 30 cm above sea level. . . 59
4.11 **A.** Grid of mean sea level notch roof height for the Pangalos peninsula and surrounding area. **B. and C.** Examples of the morphology of notches on the Pangalos peninsula. 60
4.12 **A.** Possible uplifted paleo wavecut notch and wavecut platform on the Milakos peninsula, above the high modern notch level. **B.** Wavecut platforms and paleo notches from the south west Corinth shoreline showing similar geometry (Palyvos et al. 2007). 61
4.13 **A.** View of the N–dipping fault plane above the Milakos peninsula, interpreted on Fig. 4.9. **B.** View of the 75° dipping fault plane. **C.** The bottom of the fault surface appears weathered, vegetated and old. This fault is considered inactive. 62
4.14 **A.** Possible uplifted wavecut platforms eroded into highly deformed limestone in Logos Bay (Fig. 4.9). **B.** Similar levels of platforms are observed further east along the Galaxidi peninsula coastline (Fig. 4.9, location 3). **C.** Proposed uplifted terrace platforms from the south–west Corinth margin, from Palyvos et al. (2007). 64
4.15 Summary figure to show the location of potential uplift and subsidence indicators identified along the northern coastline in this study, and their vertical position relative to mean sea level. 65

5.1 Tectonic framework of the Gulf of Corinth. 69
5.2 Extent of the swath bathymetry (dotted) and seismic reflection profiles (solid lines) collected by the MV Vassilios in 2003 (McNeill et al. 2005a). 72

5.3 **A.** MCS data from the Eratini sub–basin (location identified in Fig. 5.2). **B.** Four clinoform packages (arrowed) are identified within the basin. **C.** Horizons can be correlated with the eustatic sea level curve of Siddall et al. (2003) to estimate horizon age. After McNeill et al. (2005a). 73
5.4 **A.** Close up of the stratigraphy within the Eratini sub-basin (box in Fig. 5.3 B) **B.** Unit III shows a clinoform configuration associated with lacustrine delta progradation during sea level lowstand. The parallel reflections at the base of the unit are probably highstand and transgressive sediments. 74
5.5 **A.** MCS data from the central western Gulf (location shown in Fig. 5.2) **B.** Seismic stratigraphic interpretation showing the two main sediment packages A and B, and horizon correlation with the sea level curve of Siddall et al. (2003) modified for the level of the Rion sill. 77
5.6 **A.** MCS data from the E-W Gulf profile (location shown in Fig. 5.2). **B.** Seismic stratigraphic interpretation showing the two main sediment packages A and B, and horizon correlation with the sea level curve of Siddall et al. (2003) modified for the level of the Rion sill. 78
5.7 Interpreted major faults in the western Gulf of Corinth. Positions of faults are constrained by the seismic profiles and swath bathymetry used in this study and that by McNeill et al. (2005a), and are supplemented by interpretations from Zelt et al. (2004) and Goodliffe et al. (2003). 81
5.8 **A.** TWTT depth to the basement-sediment contact and **B.** TWTT sediment thickness isopach. Produced using the basement interpretations of our MCS study and additional basement interpretations from deep seismic reflection profiles from the R/V Maurice Ewing cruise EW0108/2001 82
5.9 (A.) MCS data from the west of the study area (location in Fig. 5.7). (B.) Structural interpretation of the sub–bottom structure and inset line drawing showing basement depth for this location from Fig. 5.8. . 84
5.10 (A.) MCS data from the center of the study area (location in Fig. 5.7). (B.) Structural interpretation of the sub–bottom structure and inset line drawing showing basement depth for this location from Fig. 5.8. . 85
5.11 (A.) MCS data from the east of the study area (location in Fig. 5.7). (B.) Structural interpretation of the sub–bottom structure and inset line showing basement depth for this location from Fig. 5.8. 86
5.12 **A.** Comparison of the average depth of buried clinoform slope breaks, C1 – C4 (Fig. 5.3) with the eustatic sea level curve of Siddall et al. (2003). **B.** Subsidence rates at the fault plane averaged within each time step between shoreline formation. 87
5.13 **A.** Subsided shoreline, total basement throw and stratigraphic offset measurement methods used in the determination of estimated slip rates for different time periods. **B.** Summary of the estimated slip rates, in mm/yr, for each fault over different time periods, using the three measurement methods described in (A). 88

5.14 **A, B, C, D, E, F, G, H, I, J** Stratigraphic interpretations for the MCS data set in the western Gulf of Corinth. Basement depths are observed directly from the MCS data or derived from the regional grid in Figure 5.8 A (see section 5.4.1 for method). 93
5.15 **A.** Un–interpreted and interpreted MCS data for the boxed region in Figure 5.14 B. Post ca. 0.4 Ma sediments show a southward tilt toward the East Eliki and Akrata faults at the south end of the profile. **B.** Un–interpreted and interpreted MCS data for the boxed region in Figure 5.14 F. Sediments to the south show a preferred southward tilt toward the onshore East Eliki fault, whereas those to the north dip toward the S–dipping West Channel fault. **C.** Un–interpreted and interpreted view of the East Channel fault from the central western gulf (Fig. 5.14 **D.** The East Channel fault is a complex fault zone. 95
5.16 Maps to show major active faults and possible positions of the coastline during the development of the western Gulf of Corinth, together with schematic cross sections. 97
5.17 Summary of evidence concerning the geometry and interaction of western Gulf of Corinth faults at depth. Inset shows the position of the transect and locations of Ms $>$ 5 seismicity in the area from Ambraseys & Jackson (1990) and Bernard et al. (1997). 100

6.1 Tectonic framework of the Corinth rift. 105
6.2 Map to show the coverage of seismic profiles used in this study. Table 6.3 gives further details for each of the surveys. 110
6.3 **A.** Multichannel seismic profile (M.V. Vasilios 2003 survey) from the western Corinth rift. **B.** Interpreted stratigraphy from the western Corinth rift. 115
6.4 **A.** E–W Multichannel seismic profile (M.V. Vasilios 2003 survey) across the western to central rift **B.** Interpreted stratigraphy in the western to central Corinth rift, location shown in Fig. 6.2. 116
6.5 Our interpretation of stratigraphy along the E–W central rift SEIS–GRECE line following Clement (2000) and; Clement et al. (2004). Note y–axis is in time. Location shown in Fig. 6.2. 117
6.6 Our interpretation of stratigraphy along the Hellenic Petroleum line, Profile C after Sachpazi et al. (2003) and Moretti et al. (2003). Note y–axis is in depth. 118
6.7 **A.** Seismic interpretation of profiles from the Alkyonides Gulf from the 1996 M.V. Vasilios cruise, location shown in Fig. 6.2. **B.** Vertically exaggerated view of the seismic stratigraphy on the southern coast of the Alkyonides basin adjacent to the West Alkyonides fault. 120
6.8 TWTT depth to the basement–sediment contact. 123
6.9 Total TWTT sediment thickness within the Corinth rift based on the basement interpretation of Fig. 6.8 and the bathymetry presented in Fig. 6.1. 125
6.10 **A.** Unit B (ca. 1.5 - ca. 0.4 Ma) TWTT sediment thickness within the Corinth rift. **B.** Unit A (ca. 0.4 - 0 Ma) TWTT sediment thickness within the Corinth rift. 126
6.11 Schematic to show the four different methods of slip rate determination that have been used in this study and are described in the text. 130

6.12 Summary of Corinth rift slip rates derived in this study and reviewed from the literature. 132
6.13 Interpretation of the 3D subsurface structure of the western (zone 1) and central–western (zone 2) rift showing variations in the thickness of units A and B. 136
6.14 Interpretation of the 3D subsurface structure of the central–western (zone 2), central (zone 3) and central–eastern (zone 4) rift showing variations in the thickness of units A and B. 138
6.15 Line interpretations from the Alkyonides Gulf showing the changing thickness of pre and post ca. 0.34 – 0.4 Ma sediments in the hanging walls of the West and East Alkyonides faults. Interpreted from the 1996 M.V Vasilios data (after Leeder et al. 1991, Collier et al. 2000, Leeder et al. 2005). Numbered horizons correspond to Oxygen Isotope stages correlation (See Fig. 6.7). 140
6.16 **A.** Major active faults within the Corinth rift interpreted to be responsible for basement subsidence and sediment distribution in the Pliocene to Early Pleistocene (ca. 1.5 to ca. 0.4 Ma). **B.** Schematic cross sections across the western rift, **C.** central rift and **D.** eastern rift. 142
6.17 **A.** Major active faults within the Corinth rift interpreted to be responsible for basement subsidence and sediment distribution from the Middle/Late Pleistocene to recent (ca. 0.4 to 0 Ma). **B.** Schematic cross sections across the western rift, C. central rift and **D.** eastern rift. 144

7.1 Interpreted basement subsidence and fault architecture from the offshore Corinth rift (from Chapters 5, 6). Onshore faults after Collier & Thompson (1991), Roberts (1996), Collier & Jones (2003), McNeill & Collier (2004), Leeder et al. (2005), Rohais et al. (2007). Lines 1 to 4 are the locations of the profiles shown in Fig. 7.2. 157
7.2 Interpretation of basement geometry and fault structure for Transects 1 to 4 (Fig. 7.1). Offshore interpretations after Bell et al. (2008), Chapters 5 and 6. Onshore interpretations after Collier & Jones (2003) and Rohais et al. (2007). Fault throw estimates are shown below fault names, and are discussed further in the text. 159
7.3 **A.** Geodetic extension rates from Clarke et al. (1998) along the red dashed profile shown in Figure 7.1. **B.** Total extension along the Corinth rift. **C.** β stretching factor along the rift. 166
7.4 Depth to Moho beneath Greece from Sachpazi et al. (2007) and Zelt et al. (2005) 168
7.5 Schematically outlined boundaries of the modern active Corinth rift (yellow) and the estimated area of the total Corinth rift (yellow and purple areas). 170

8.1 Effect of changing geometrical fault parameters on the coseismic displacement field created, per metre of slip on a 12 km long normal fault 175
8.2 Schematic diagram of the viscoelastic half–space model. Parameter are explained in text and in Table 8.1 178
8.3 Comparison of postseismic relaxation (**B**) and total postseismic deformation (**C**, coseismic plus postseismic relaxation) 179

8.4 **A.** Effect of viscosity and **B.** Elastic thickness (H) on the total postseismic deformation field over 100 and 100000 years. Other parameters are the same as those used in Figure 8.3. Created using the fortran code V3FASAT (Fukahata & Matsu'ura 2005). 181
8.5 Analysis of the change in vertical displacement for a single footwall point over time, for viscosities of 10^{18} to 10^{21} Pas. Inset figure shows a close up view of the first 5000 years after earthquake slip. Created using the fortran code V3FASAT (Fukahata & Matsu'ura 2005). . . . 182
8.6 **A.** Map of the Alkyonides Gulf area annotated with ca. 130 ka displacement measurements labeled 1 to 3 (referred to in text) **B.** Basement relief across the Alkyonides Gulf. **C.** Comparison of coseismic and postseismic deformation for 1 m slip on the East Alkyonides fault. 186
8.7 Attempts to model the uplift of south margin wavecut platform (point 2, Leeder et al. 1991) and subsidence of south margin delta (point 3, Leeder et al. 2002) and north margin delta (point 1, Chapter 6 Fig. 6.7, Leeder et al. 2005) using a viscoelastic model after 10000τ for various magnitudes of net 130,000 year slip on the East Alkyonides fault and Skinos/Pisia faults independently. Numbers indicate positions of displaced features shown in Fig. 8.6 A. Created using the fortran V3FASAT code (Fukahata & Matsu'ura 2005). 188
8.8 Deformation field for a total of 300 m slip on the East Alkyonides fault, and 200 m slip on the Skinos/Pisia fault. Created using the fortran V3FASAT code (Fukahata & Matsu'ura 2005). 190
8.9 Displacement field created by ca. 130 ka displacement on the Skinos/Pisia, East Alkyonides and Kaparelli faults. Created using the fortran V3FASAT code (Fukahata & Matsu'ura 2005). 191
8.10 Superimposed deformation fields for 300 m slip on the East Alkyonides fault, 200 m slip on the Skinos/Pisia, 39 m slip on the Kaparelli and 50 m slip on the Livadostros fault in the last 130 000 years. Created using the fortran V3FASAT code (Fukahata & Matsu'ura 2005). . . . 192

9.1 Cartoon to show the method of investigating multiple fault activity in the western rift. **A.** Vertical displacement profiles are calculated for estimated slip magnitudes for each of the four faults active along the profile. **B.** These fields are superimposed and slip varied to approximate the elevation at the sites of the uplifted terrace and subsided delta **C.** Cross sections of the structure of the area under investigation, showing high angle planar, and low angle detachment fault geometries. 206

List of Tables

2.1 Summary of seismicity Ms ≥5 for the Corinth rift in recorded history. Focal mechanism solutions shown in Figure 2.11. Sources of data: A = HCMT catalog, B = Bernard et al. (1997), C = Hatzfeld et al. (1996), D = Taymaz et al. (1991), E = Ambraseys & Jackson (1990) 35

5.1 Seismic stratigraphy information summary for the upper shelf/slope: Eratini sub–basin 75
5.2 Seismic stratigraphy information summary for the main deep Gulf . . 79
5.3 Review of sedimentation rates for a variety of locations within the Western Gulf of Corinth (Fig. 5.2) 80
5.4 Slip rates for the North Eratini fault derived from subsidence of paleoshorelines in the Eratini sub–basin 87

6.1 Summary of Holocene coastline vertical movements studies along the Corinth Rift shoreline categorized by the fault probably responsible for the movement. 107
6.2 Summary of late Quaternary vertical movements from studies along the Corinth Rift shoreline categorized by the fault probably responsible for the movement. 108
6.3 Summary of seismic data compiled for use in this study. 111
6.4 Summary of the interpretation scheme used to interpret Alkyonides basin sedimentation (discussed in text and Fig. 6.7) 121
6.5 Vertical subsidence for each of the lowstand shorelines in Fig. 6.7 A, between the age of formation and present day. 135

7.1 Summary of throw values for faults along the transects in Figure 7.1 . 160
7.2 Summary of total extension and β factors across the active part of Corinth rift (black faults only on Fig. 7.2). See Table 7.1 for a summary of fault throws included in the calculation. 162
7.3 Summary of total extension and β factors across the entire Corinth rift, including all fault throws presented in Table 7.1. 165
7.4 Comparison of basement depth, total extension, geodetic extension rates, and β stretching factors across the transects shown in Fig. 7.2 . 167

8.1 Parameters used in viscoelastic dislocation modelling. Source of parameters discussed in text. 187
8.2 Summary of net slip and slip rates for faults in the Alkyonides Gulf that can reproduce the vertical displacement of ca. 130 ka features from viscoelastic dislocation modelling. 192

Acknowledgements

I would first like to express my gratitude toward my primary supervisor Lisa McNeill for her continued support, enthusiasm, hard work and attention to detail that have made working on this PhD such a rewarding experience. I would also like to thank my other supervisors Jon Bull and Tim Henstock for their great scientific insight and encouragement throughout this project.

Thanks must also go to the many other people who have helped me complete this project, including Aaron Micallef and Aris Stefatos for their invaluable help (and knowledge of the Greek language) during the field work in Greece. Thanks also to Carol Cotterill, Mike Leeder and Richard Collier for useful scientific discussion and also Isabelle Ryder for her help in using the dislocation modelling codes. I am also appreciative to Alfred Hirn and George Ferentinos for providing additional seismic reflection profiles for use in this study.

I'd like to finally thank my family, Martin, Elaine and Sarah Bell for their continued support, and my fellow PhD students. In particular, Chris Jeffery, Kirsty Edgar, Mark Vardy, Jo Hopkins and Stuart Boden, among many others who have made my time at the NOC an immensely fun and enjoyable experience throughout, who I shall sincerely miss meeting with in the 'Platform' after work every Friday...

This project has been supported by Natural Environmental Research Council grant NER/S/A/2004/12634.

Chapter 1

Introduction

1.1 The early stages of continental extension

Continental rifts mark the first stage in the breakup of continental crust, which may lead toward the birth of a new ocean basin. The style of extension and strain distribution during the initiation and early stages of intra-continental rifting, is important for understanding the eventual transition to ocean spreading and plate margin development. Continental rifting is associated with normal faulting and the production of subsided basins and uplifted rift flanks. It results in distinctive rift geometries which are recorded by infilling syn–rift sediments and preserved uplifted features. The first models to describe rift initiation assumed they are the result of pure shear uniform stretching leading to necking and isostatic readjustment (McKenzie 1978a). Detailed stratigraphic studies of syn–rift sediments and fault activity now show that rifts are not simple structures, but have highly variable structural geometries along the rift-axis and have often evolved with time. Observations of rift geometry and evolution can provide important controls on large scale lithospheric processes and fault mechanics.

Continental rifts are not only important from a scientific point of view. Unlike the seismically inactive passive margins they will mature into, the initial stages of continental rifting are associated with intense seismic activity. An understanding of faulting and the likely evolution of seismic activity is important in assessing seismic hazard. Economically, continental rift basins from the Carboniferous (e.g., the North Sea) and the Mesozoic-Cenozoic (e.g., eastern China) formed accumulation sites for sediments that have now evolved into large hydrocarbon-bearing basins. The rift's tectonic evolution controls all the essential elements and processes involved in the establishment of a petroleum system including further understanding of maturation histories.

Despite their scientific, social, and economic importance, our understanding of how rifting initiates and evolves to full continental breakup is limited. This is mainly due to the few active examples of continental rifting that have undergone only a few million years of extension. Many rift studies concentrate on the history of individual faults or consider the broad generalised system in a quasi-continuous way. There are few examples of the full assessment of early continental rift systems, in terms of their fault and subsidence geometries, as well as their temporal evolution. The purpose of this thesis is to present, for the first time, a full appraisal of the tectonic evolution of the Corinth rift as an example of a young intra–continental rift.

1.2 Examples of early continental rifting

Continental extension can occur in a wide variety of tectonic settings, and although the tectonic driving force behind each is clearly setting dependent, a number of similarities in rift character suggest they are influenced by generic underlying processes. Observations of continental rifts, together with analytical and numerical modelling, is required to help understand two fundamentally unknown questions in the study of continental rifting:

1. How is extension accommodated at the initiation of rifting?
2. How do rifts evolve prior to breakup?

The best way to understand these processes is to use the observed fault architecture and spatial and temporal variations in structure to constrain models of rift development, and investigate the likely important processes. Figure 1.1 shows examples of active intra-continental pre–breakup rifts (or in some cases rifts that have just initiated to seafloor spreading) from across the world, in a variety of different tectonic settings. The tectonic characteristics of these rifts (from the oldest to the youngest) are described below.

– Lake Baikal

  The Baikal rift is a ∼650 km long intra–continental rift in the suture zone bounding the Siberian craton that began rifting ca. 35 Ma (Mats 1993). The rift is strongly asymmetric controlled by faults on its northwest side (Scholz & Hutchinson 2000). The style of rifting is believed to have varied from strike–slip to pure extension in the Late Miocene–Pliocene related to the general kinematic reorganisation of Asia and the rapid growth of the Tibetan Plateau (Petit & Deverchere 2006).

– Red Sea and Gulf of Aden basins

  Rifting in the Red Sea and Gulf of Aden is associated with the collision of Africa and Eurasia and the emergence of the Afar magmatic plume (Bosworth et al. 2005). Now, the Red Sea and Gulf of Aden both act to separate Africa from

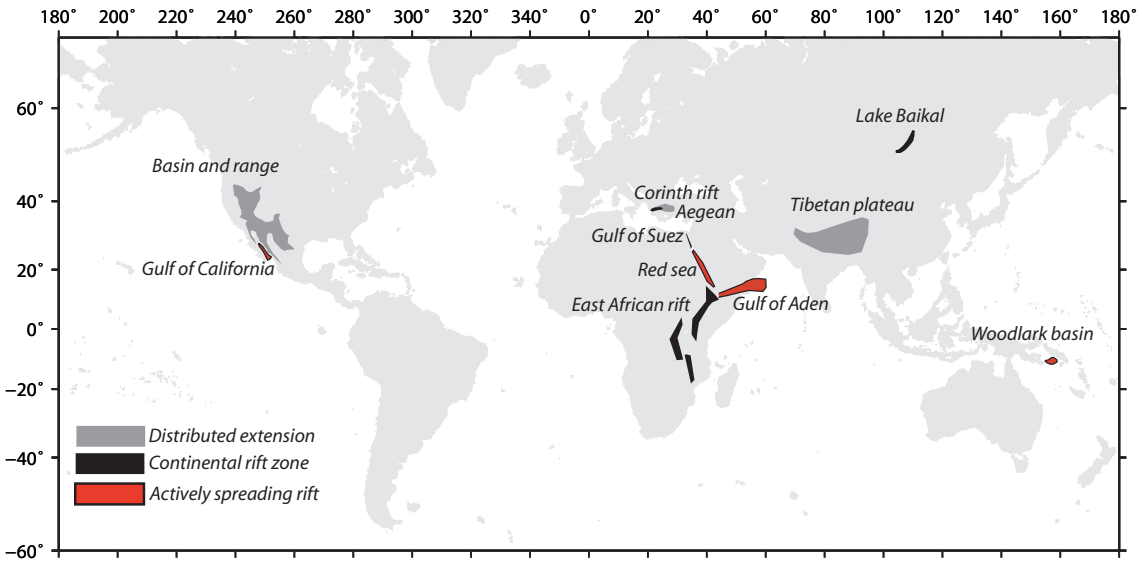

FIGURE 1.1: Some examples of areas of currently active continental lithosphere extension.

Arabia, although both have had very different tectonic histories (Bosworth et al. 2005). The Gulf of Aden experienced oblique continental rifting around 27 Ma, whereas the Red Sea initiated as a pure extension zone and switched to oblique rifting later. Although seafloor spreading now occurs in the Gulf of Aden and the southern central Red Sea area, continental rifting continues in the northern Red Sea and the Gulf of Suez (Gupta et al. 1999, Gawthorpe et al. 2003).

– East African rift

  The East African rift initiated ∼25 Ma and lies to the south of the Red Sea–Gulf of Aden triple junction (Hayward & Ebinger 1996). Unlike the Red Sea and Gulf of Aden it has not progressed to seafloor spreading, and is considered to be a failed arm of the rift zone. It is highly segmented and structurally variable along its ∼2000 km long axis, with areas of high magamatic and amagmatic rifting (Hayward & Ebinger 1996).

– Tibetan Plateau

  The Tibetan Plateau began to form by the collision of Indian and Eurasian plates 50 – 70 Myr. Although the continents have been converging toward each other, and the stress field is predominantly compressive, the Tibetan Plateau is also associated with widespread (∼800 km) extension since at least 14 Ma (Coleman & Hodges 1995). One possible explanation for this extension is gravitational collapse when the Tibetan Plateau reached its maximum elevation (Liu & Yang 2003).

– Basin and Range

  The Basin and Range province formed as a broad region of extension (∼800 km wide) in the back arc area of Farallon plate subduction beneath the North American plate, and extension may now be controlled by the northward movement of

the Pacific plate relative to North America. Extension has been occurring for the last ca. 20 Myr (Hamilton 1987) and is composed of N–S trending faulted footwall mountains (range) and hanging wall valley floors (basin). Both low–angle detachment faulting and high–angle faulting control rift structure (Wernicke 1981, Stein & Barrientos 1985).

– Aegean

The Aegean region has experienced widespread extension from central Greece to western Turkey since ca. 20 - 14 Ma (Seyitoglu & Scott 1996). This region is discussed more thoroughly in Chapter 2. Extension in this area is thought to be due to some combination of: back arc extension due to subduction of the African plate at the Hellenic Trench (McKenzie 1972, 1978b, Angelier 1978); westward propagation of the North Anatolian fault and the westward extrusion of Anatolia (Dewey & Sengor 1979, Taymaz et al. 1991, Armijo et al. 1996); and gravitational collapse of lithosphere thickened in the Hellenide orogeny (Jolivet 2001, Le Pourhiet et al. 2003). The Gulf of Corinth is a high strain band within the wide Aegean deformation field. The most recent and main phase of extension in this basin is thought to be less than ∼3 Ma, making it an extremely young rift basin.

– Gulf of California

The Gulf of California is an example of complex rifting dominated by oblique extension, with sea floor spreading to the south and continental extension to the north (Lizarralde et al. 2007). Rifting began 12 – 15 million years ago when subduction ceased west of the Baja California peninsula. Within the rift there is evidence that extension has shifted from East to West (Aragon-Arreola et al. 2005a, Aragon-Arreola & Martin-Barajas 2005b).

– Woodlark Basin

Extension within the Woodlark Basin, Papua New Guinea, is young (∼6 Ma) (Taylor et al. 1999, Goodliffe & Taylor 2007, Little et al. 2007) and has just began to initiate seafloor spreading. It is an example of an oblique transpressional system caused by the irregular boundary between the Pacific and Indo–Australian plates. Strain localisation and seafloor spreading have occurred in a time transgressive fashion, with spreading propagating from East to West. The system is associated with rifting along low angle faults with high asymmetry (Goodliffe & Taylor 2007).

These examples highlight the full variety of tectonic settings that rifts can form in, from compressional, transpressional, transtensional to fully tensional. They also show that the structure of rifts is not simple, and variations exist in the width of the extensional zone, degree of rift basin segmentation, the angle of faults, degree of magmatic activity, and style of rift propagation. Continental rifts show a much higher level of

structural complexity than is observed at oceanic rift zones (Sobolev & Rundquist 1999).

1.3 Introduction to the Corinth rift

The Corinth rift is a 100 km x 30 km high strain band between northern Greece and the Peloponesse, within the Aegean active tectonic zone (Figs. 1.1 and 1.2). It includes the marine Gulf of Corinth and Alkyonides Gulf basins and an area of now inactive faulting on the southern margin. The rift is believed to have an extensional history of 2 – 5 Ma, making it a very young, if not the youngest, example of continental rifting. The rift is extending continental crust in a north–south direction at a rate of up to 15 – 20 mm/yr (Clarke et al. 1998). The rift cuts across the older north–south structural grain of the Pindos mountain chain that forms the pre–rift basement.

1.3.1 Why study the Corinth rift?

For a number of reasons, the Corinth rift is a good choice of rift to investigate the problem of how continental rifts initiate and evolve. Justification for its selection over the examples given above is outlined below.

1. Although the rift is located within the complex Aegean tectonic system, it experiences almost pure N–S extension and so is generally less complicated than other rifts where oblique extension and strike–slip faulting is common (e.g., Gulf of California) or where there are magmatic influences (e.g., East African rift).
2. The rift has a short, less than 2 – 5 Ma extension history. Therefore, early syn–rift sediments offshore are not deeply buried and are still fairly easily seismically imaged. Seafloor spreading has not yet initiated and faulting relations between the two conjugate margins are not obscured. Additionally, there has not been enough time for any complex tectonic overprinting.
3. The current N–S extension phase is cross–cutting relatively simple and well–known pre–rift basement structure, making the distinction between the old and new tectonic phases clear.
4. The rift is seismically active and is extending at a high rate. This has resulted in a wealth of long term deformation indicators along the coastline, and short term deformation is resolvable by geodetic methods.
5. The fortuitous position of the Corinth rift in a fluctuating land–locked setting has allowed the deposition of characteristic cyclical stratigraphy influenced by tectonics and sea level variation. This provides the potential for the high resolution study of rift stratigraphy.
6. The relatively small size of the rift means it is feasible to attempt a study of the offshore and onshore area at a fairly high resolution.

7. There has been no magmatic component to obscure earlier rift stratigraphy.

1.3.2 Corinth rift tectonic controversies

Not only is the rift important as an example of young continental rifting, but throughout the last few decades of study a number of controversies have arisen in regard to its structural style which must be addressed. The solutions to these controversies will be influential for large scale models of continental rifting, and also understanding regional Aegean tectonics and appreciating seismic hazard.

1. There is a debate in the literature regarding the importance of low angle or detachment faulting versus high angle ($40 - 60^\circ$ dip) faulting in the rift (Chapter 2, section 2.3.3). This ongoing debate has strong implications for the fundamental mode of extension of rifts, dominated by either pure or simple shear mechanisms.
2. Short term geodetic extension rates cannot be reconciled with long term estimates of extension from known faulting. The overall morphology of the currently active rift also does not match the pattern of short term activity (Chapter 2, section 2.3.3). Possible reasons for the discrepancy could include: strain redistribution through time, significant unknown fault activity, or aseismic extension.
3. Historically, the rift has been described as a 'simple asymmetric half graben', mostly based on coastal geomorphology. From the previous comparison of rifting worldwide, if this were true, the Corinth rift would be an exception as the other rifts show significant segmentation and spatial and temporal variability. Seismic profiles suggest the Corinth rift has experienced a more complex history and have challenged this simple hypothesis (e.g., Stefatos et al. 2002, Sachpazi et al. 2003, Moretti et al. 2003, McNeill et al. 2005a). A systematic study of fault geometry is required to examine the true complexity of the Corinth rift and investigate how it compares with other rift zones worldwide.

1.4 Aims and objectives

The aim of this thesis is to understand the complete tectonic evolution of the Corinth rift in order to: answer scientific controversies regarding extensional style in the rift; learn more about generic early continental extension processes, which are still poorly understood; and contribute toward understanding of local seismic hazard. This will be achieved through: field investigations; detailed interpretation of offshore seismic reflection data; numerical assessment of extension and fault slip rates; and compilation of this new information with published literature, focused toward fulfilling the objectives defined below.

The key difference between this work and previous Corinth studies is that this is the first to integrate information from onshore and offshore parts of the entire Corinth system to synthesise rift evolution history.

1.4.1 Objective I: To determine the geometry, style and magnitude of subsidence and extension across the Corinth rift zone

1. Determine the geometry and number of major active faults responsible for Corinth rift deformation:
   (a) Is extension distributed over a number of faults or concentrated on single border faults?
   (b) Is basin structure controlled by faults with the same dip direction or does dominant fault polarity vary along the rift axis?
   (c) Do high angle or low angle faults dominate structure?
2. Document the dominant structural style:
   (a) Does a half graben or full graben morphology dominate?
   (b) Are there structural changes along the rift?
   (c) What is the magnitude of total basement subsidence?
3. Quantify slip rates on individual faults:
   (a) Do fault slip rates vary along the rift?
   (b) Have fault slip rates varied over time?
   (c) Can dislocation modelling of the observed vertical displacement field determine long term fault slip rates and constrain fault geometry?
4. Quantify short term and long term extension rates across the rift:
   (a) Is there spatial variation in extension rate along the rift?
   (b) Are geodetic short term extension rates, long term extension on faults and degree of crustal thinning in agreement?

1.4.2 Objective II: Determine spatial and temporal rift development

1. Determine how fault activity has affected sediment deposition:
   (a) Can seismic facies of offshore sediments be linked to tectonic and climatic processes?
   (b) Are there variations in offshore seismic stratigraphy that indicate changing tectonic regime?
2. Deduce the pattern of strain distribution as the rift has evolved:
   (a) Does faulting migrate across the rift zone with time, causing basin widening or narrowing?

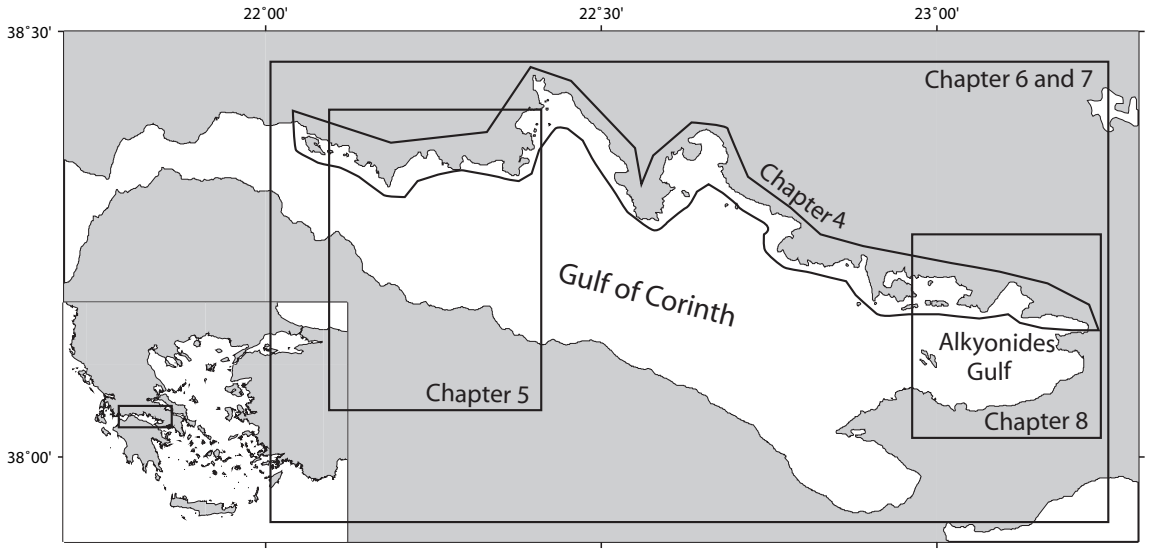

FIGURE 1.2: Summary of the regions of the Corinth rift discussed in Chapters 4 to 8 of this thesis.

(b) Does the locus of rifting change position and cause rift propagation along axis?

3. Determine an estimated rift chronology from offshore stratigraphy and compare with onshore stratigraphic sequences:
   (a) When did the currently active rift bordering faults initiate?
   (b) How does this rift initiation age compare with estimates from the onshore rift component?
   (c) How has fault initiation propagated along the rift?
4. Predict the likely future geometry of the Corinth basin, based on modern extension rates and patterns of faulting throughout its history:
   (a) Where is strain focused now, and where may it likely be focused in the future?

1.4.3 Objective III: Link the observations in the Corinth rift to global controls on rift initiation and evolution

1. How is extension accommodated at the initiation of rifting?
2. How do rifts evolve prior to continental breakup?

1.5 Overview of the thesis

The following section briefly describes the content of each of the chapters presented in this thesis. Figure 1.2 summaries the regions of the Corinth rift which are the focus of Chapters 4 to 8.

Chapter 2 is a broad review of the literature to put this study in context. This chapter highlights the current understanding of continental extension kinematics and dynamics, focusing on early rift processes. This is followed by a detailed account of Aegean tectonics and a review of the geology and tectonics of the Corinth rift.

Chapter 3 presents a brief summary of the main approach and methodology used in this thesis as well as the datasets involved. More in–depth descriptions of data and methods can be found in the introductions of each of the following chapters.

Chapter 4 focuses on the influence of active tectonics on the coastal morphology of the Corinth rift and the record of vertical movement preserved. The chapter reviews typical methods used to qualitatively and quantitatively assess the tectonic and sea level controlled movement of base level. This follows with a brief review of measurements of movement from the southern shoreline over the last three decades. The results of new field work from the northern margin of the Corinth rift are presented that aim to investigate the influence of neotectonics in this infrequently examined part of the rift (Fig. 1.2).

Chapter 5 discusses the results of analysis of high resolution multichannel seismic reflection data in the western part of the Corinth rift (Fig. 1.2). This chapter presents details of the stratigraphic framework used throughout this study and discusses the tectonic complexities observed from basin analysis in the western rift. Fault slip rates are quantified and a scenario of western rift evolution is presented. This chapter appears in its published form in Bell et al. (2008), published by the **Geological Society of America, Bulletin**.

Chapter 6 extends the stratigraphic interpretation presented in Chapter 5, to the rest of the Corinth rift, in order to investigate basin–wide tectonic evolution. Deeper penetrating seismic reflection profiles are integrated to produce, for the first time, an estimate of the 3D basement–sediment contact surface in the offshore Corinth rift. Offshore hanging wall stratigraphic interpretations are combined with onshore uplift measurements to deduce total throw on faults, and hence slip rates averaged over a range of time periods. This chapter presents a scenario for fault initiation and temporal tectonic changes in the complete Corinth rift system. This chapter will be submitted to **Basin Research** in May 2008.

In **Chapter 7** the total extension across the Corinth rift is determined from fault offset along four N–S profiles along the rift. This is compared with the β stretching factor derived from crustal thinning. This analysis is used to test if upper crustal faults can explain the level of total crustal extension, or if detachment faulting or depth–dependent stretching mechanisms need to be employed.

Chapter 8 uses the technique of viscoelastic dislocation modelling to reproduce the long term deformation field associated with a particular system of faults. This method is applied in the relatively tectonically simple Alkyonides Gulf (Fig. 1.2) to constrain

how much activity is required on the four faults in the area over the last ca. 130 ka to reproduce observed deformation.

Chapter 9 reviews the key conclusions and outcomes of this study, and the new contribution it makes to science, in terms of the objectives outlined in section 1.4. The thesis is completed with a review of potential future work, in order to develop or constrain the ideas presented in this study.

All attempts have been taken to avoid repetition in this thesis, however due to the inclusion of published and submitted peer–reviewed articles there will, inevitably, be some reiteration within introductory sections.

Chapter 2

Research Context

The understanding of continental extension has progressed from simple instantaneous pure shear stretching models toward incorporating the crustal and lithospheric processes behind specific rift features and spatial and temporal evolutionary trends. Much of the advancement in knowledge is derived from the detailed observation of worldwide rift characteristics. The purpose of the following review is to provide the reader with a broad understanding of continental extension theory and the details of regional Aegean tectonics. This is essential to place the new Corinth rift research presented in this thesis into a regional and global context. The history of previous Corinth rift tectonic studies will be critically reviewed, highlighting the need for the work presented in this thesis. More detailed reviews of the literature, specific to the topics discussed in Chapters 4 to 8, are provided in the introductory sections of each chapter.

2.1 Continental extension

2.1.1 Continental deformation theory

The theory of plate tectonics, devised in the 1960's (e.g., Vine & Matthews 1963), has revolustionised Earth Sciences and has created a powerful prediction tool in the investigation of the movement of the Earths surface. Movements of the oceanic plates, which deform generally only at their edges with essentially flat rigid interiors, can be accounted for using plate tectonic theory. Deformation within continents, however, which often happens thousands of miles away from plate boundaries and involves deformations of the crust in the production of mountains and sedimentary basins, cannot be simply explained using the plate tectonic kinematic model (Molnar et al. 1973).

The difference in deformation style between the oceans and continents reflects fundamental differences in their chemical, mechanical, thermal and rheological properties

(Molnar 1988). Olivine-rich oceanic lithosphere is strong down to depths of around 80 km, whereas quartz–rich continental lithosphere maintains brittle strength only in the upper 5 – 10 km. Below this, the lithosphere is aseismic, until stronger olivine–rich lithosphere is reached at depth (Brace & Kohlstedt 1980, Chen & Molnar 1983). This 'jam–sandwich' view of continental rheology is, however, contested by some authors (e.g. Maggi et al. 2000, Jackson 2002) based on earthquake focal depths apparently 40 – 50 km deep in North India. The strong rigid, dense character of oceanic lithosphere leads to its coherent and sustained subduction at convergent margins, whereas in continental lithosphere stresses may be transmitted, resulting in wide deformation zones (Molnar et al. 1973).

The mechanisms controlling continental rifting and sedimentary basin production remained poorly understood, until McKenzie (1978a) proposed the 'stretching theory' to account for the formation of rifted basins. McKenzie (1978a) proposed that rifting is a two stage subsidence process, involving an initial short active rifting stage, followed by a post–rifting later thermal contraction and subsidence. Initially, subsidence occurs due to the mechanical stretching of the continental lithosphere. Later, the upwelled asthenosphere, which isostatically balances the decrease in crustal mass, cools and thermally contracts, producing a second phase of post–rift subsidence.

The exact nature of the processes involved in the early stages of rifting, prior to ocean crust emplacement and seafloor spreading, is not accounted for in this purely kinematic model. Although not explicitly specified or required by the numerical 'stretching model', normal faulting is believed to be the process responsible for controlling the mechanical subsidence stage (McKenzie 1978a). The post–rift subsidence follows an exponential cooling law rather like the deepening of ocean basin floor with age (Parsons & Sclater 1977, Stein & Stein 1992), and is relatively well constrained and can explain the subsidence history of older basins (Bond & Kominz 1984, Stewart et al. 2000). The initial mechanical stage of rifting is much more variable between basins and complex. In most large scale modelling, subsidence during this stage is either assumed to be instantaneous (McKenzie 1978a), or given a finite short time interval over which to occur (Jarvis & McKenzie 1980) with no further details applied. The large scale morphology of conjugate passive margins, however, depends on these processes. For example, the distinctive geometry of the North American and Labrador Sea margins, are thought to be the result of the distribution of initial extension and propagation of faulting along the margin during the very early stages of continental rifting (Dunbar & Sawyer 1987, 1989a,b).

The simple McKenzie (1978a) model cannot explain many features of currently active rift zones. For example: the occurrence of magmatic as opposed to amagmatic rifts in some areas; low angle and detachment faulting predominating over high angle average dip faulting in cases; the formation of metamorphic core complexes; why rifts are often segmented; why rifts are often asymmetric; and why they have uplifted rift flanks.

2.1.2 Mechanisms of Continental Extension

In order to study in more detail the processes involved at the initiation of continental rifting, presently active rifts should be studied in preference to older basins. Active rifts are more useful as they presently experience seismicity and active fault scarps are often visible. Older basins have gone through the second thermal stage of subsidence (McKenzie 1978a) and have often accumulated many kilometres of sediment, with their conjugate margins now thousands of kilometres apart and have undergone significant tectonic overprinting. This makes the younger active stage difficult to view in detail within older basins, such as the Gulf of Mexico and North Sea.

Figure 1.1 presents examples of currently active continental rifts worldwide. Active rift systems can be narrow, independent rifts (e.g., the East African rift, Woodlark basin, and Lake Baikal, Fig. 1.1) or be composed of many widely distributed basins over a region of hundreds of kilometres (e.g., the Basin and Range, Aegean, and Tibetan plateau, Fig. 1.1). The driving forces causing lithospheric rifting are broadly divided into two categories; active and passive (Sengor & Burke 1978). Active mechanisms involve upwelling asthenospheric plumes causing the lithosphere to thin and fracture in response to volcanic doming, then initiating mechanical rifting (e.g. Sengor & Burke 1978, Ruppel 1995, Corti et al. 2003, Fig. 2.1 A). In this process volcanism pre–dates mechanical rifting. Passive processes instead result from regional stress fields that induce extension in the lithosphere and initiate rifting (Fig. 2.1 B). Volcanism in this case post–dates initial rifting. In some cases, it is difficult to determine if a rift formed by passive or active processes and it is possible for a rift to show evolution between these two end member controls (Huismans et al. 2001).

Although the dynamic driving forces behind the deformation of each rift is dependent on regional tectonic setting, some features are common to rifts in different settings. Below, features that typify rift zones are reviewed together with possible mechanisms for their formation.

Magmatism

The intensity of magmatism is highly variable at rifts in terms of its volume and timing, and some rifts do not experience any magmatic activity at all. Although active rifting is associated with asthenospheric plumes and volcanism, even passive rifts, after the initiation of rifting would experience some magmatism (Ziegler & Cloetingh 2004). Passive rift extension results in adiabatic decompression of the lower lithosphere and upper asthenosphere, resulting in partial melting and diapiric rise along fractures in the lithosphere. The volume and composition of melts is related to the degree of extension, thermal state of the asthenosphere, presence of volatiles, and the thickness of the lithosphere (McKenzie & White 1989, Ziegler & Cloetingh 2004). Plate motion may also play a role in the presence or absence of magmatism. If plate divergence

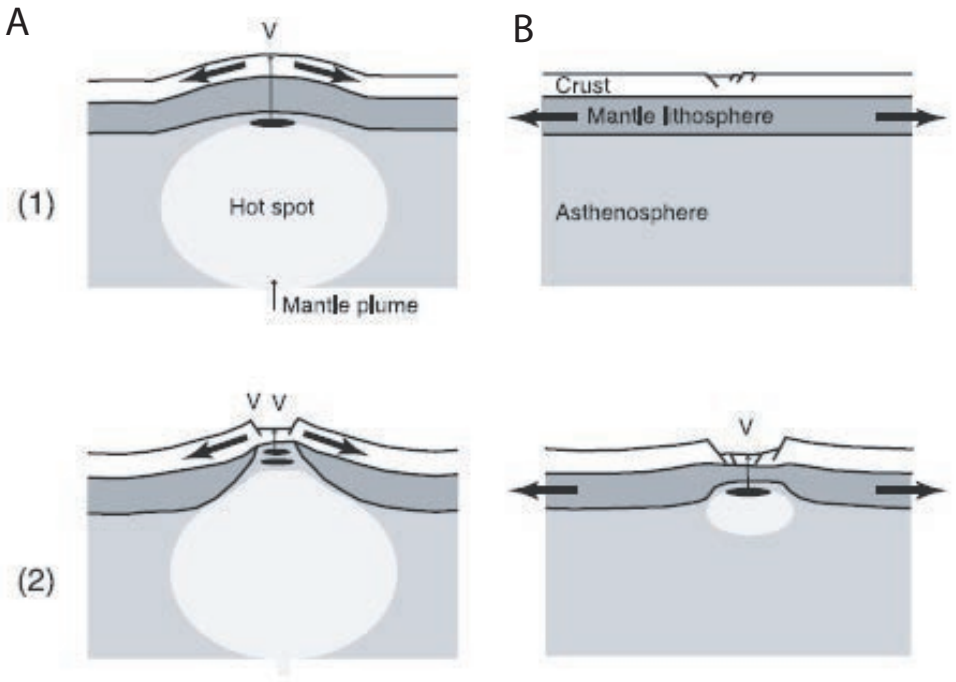

FIGURE 2.1: Schematic diagrams showing the **A.** active and **B.** passive modes of rifting. From Corti et al. (2003).

can continue unimpeded, asthenospheric melt will accrete as oceanic lithosphere. If however, the plate divergence becomes impeded by far–field compressional stress (e.g., as in the Red Sea) then thermal thinning of the mantle lithosphere occurs with the wide emplacement of basalts (Ziegler & Cloetingh 2004).

Low angle faulting and rift asymmetry vs. high angle faulting and rift symmetry

The McKenzie (1978a) model is a one layer model with pure shear stretching of the entire lithosphere (Fig. 2.2 A). This results in the formation of a symmetrical graben structure bounded by equally important normal faults on both sides of the basin (Fig. 2.2 A). However, pure shear models and depth-dependent stretching models do not explain the gross structural asymmetry of some extended continental areas, such as: the East African rift (Rosendahl 1987, Hayward & Ebinger 1996); Gulf of Suez (Gupta et al. 1999, Gawthorpe et al. 2003); and Lake Baikal (Mats 1993). Wernicke (1981) has attributed asymmetric 'half graben' structures to simple shear on a single normal fault cutting the entire lithosphere (Fig. 2.2 B). These two models are end–members and mixed pure shear/simple shear mechanisms have been proposed (e.g. Kusznir et al. 1991).

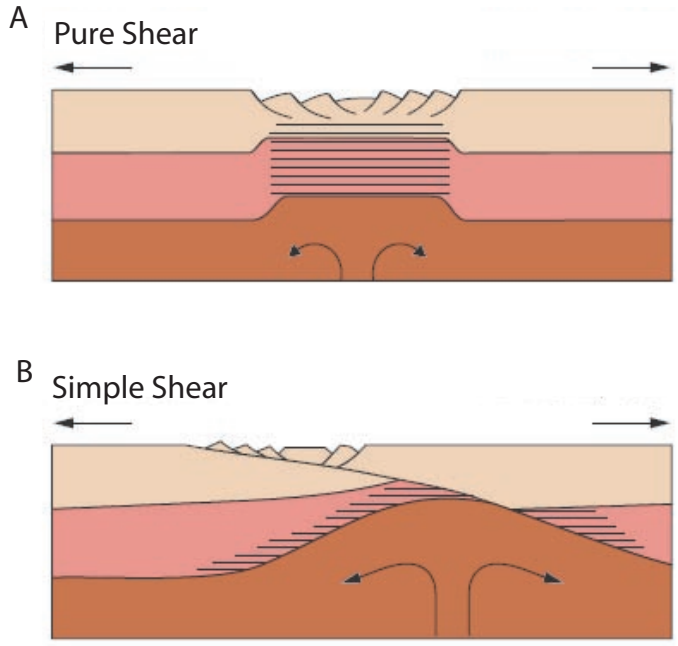

FIGURE 2.2: Schematic cartoons of the **A.** McKenzie (1978a) pure shear lithospheric stretching model, and **B.** Wernicke (1981) simple shear extension model. From Ziegler & Cloetingh (2004).

Magmatic intrusion has been suggested as a possible explanation for the initiation of low angle faulting (Parsons & Thompson 1991). Half graben, rather than symmetrical graben structures could instead be the result of structural heterogeneity (single weak fracture zone), only sufficient strain for activation of one fault (Rosendahl 1987), or mantle geometry (asymmetry due to shear zones in lower crust, Le Pourhiet et al. 2003). The development of asymmetric versus symmetric rifting has been suggested by Dunbar & Sawyer (1989a) to be controlled by pre–existing structural heterogeneities in either the crust (resulting in focused asymmetric rifting) or in the mantle (causing localised extension in the mantle but distributed symmetric rifting in the crust).

Broad versus narrow rifts

Three different fundamental modes of continental rifting are recognised; narrow rifts, wide rifts and core complexes (Fig. 2.3, Buck 1991). Narrow rifts are areas of concentrated lithospheric extension, less than 100 – 150 km wide. Examples include: the East African rift system; Baikal rift; Red Sea; Gulf of Corinth; and Woodlark basin (Fig. 1.1). Narrow rifts are associated with large changes in crustal thickness and topography in the faulted graben area (Fig. 2.3 A). Wide rifts are areas of highly extended terrain that show relatively uniform lithospheric thinning over a distance

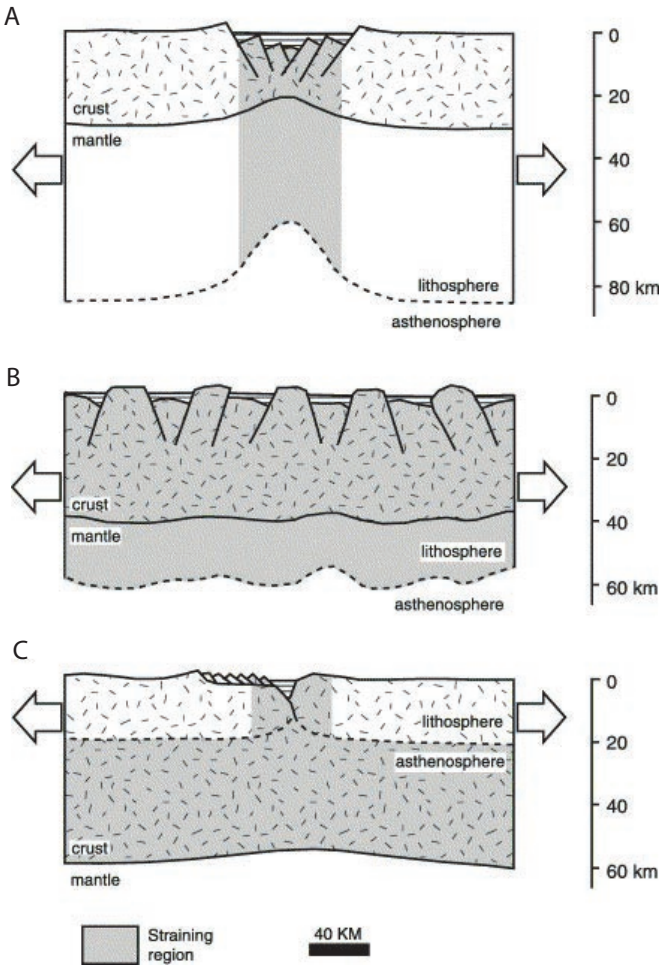

FIGURE 2.3: The three fundamental modes of continental extension. **A.** Narrow rift, **B.** Wide rift and **C.** Core complex. From Corti et al. (2003), after Buck (1991).

wider than the lithospheric thickness (i.e. > 100 km, Fig. 2.3 B). Examples include: the Aegean; Basin and Range Province, and Tibetan Plateau (Fig. 1.1). Extensional strain is not distributed uniformly over these regions, but is concentrated in many individual basins spanning a region up to 1000 km wide. The Corinth rift is an example of one of these high–strain regions within the wider Aegean deformation zone.

Three major characteristics have been suggested to control the mode of extension: 1) Strain rate; 2) initial thermal conditions and crustal thickness; and 3) mechanical instability caused by layered rheology (e.g. Buck 1991, Buck et al. 1999, Corti et al. 2003). Continental thinning results in the cooling of lithosphere brought closer to the surface (England 1983) and this will become stronger as a result of cooling. Because extension occurs preferentially in weak layers, continued extension will cause cooling and make these layers stronger (Kusznir & Park 1987). If strain rates are low, cooling dominates and weak layers become strong, leading to the redistribution of strain elsewhere and the generation of a wide rift. If strain rates are high, extension

occurs faster than cooling and narrow rifts are formed (Kusznir & Park 1987). Buck (1991) suggest the reason for narrow and wide rifts is instead due to buoyancy forces controlled by lithospheric thickness and temperature profile, with narrow rifts forming with lower temperature lithosphere and broader zones of rifting forming if the lithosphere is warmer. Syn–rift cooling causes lithospheric strengthening, as deduced by Kusznir & Park (1987), however it also leads to the development of plastic behavior. If plastic layers exist, independent of extension rate, extension will be focused and produce a narrow rift without migration (Bassi 1995). As well as these processes, magmatic intrusion and loss of cohesion on faults may lead to a preference for narrow rift zones (Buck et al. 1999) and, in contrast, viscous flow and regional compensation of extension related relief could cause broad zones of rifting (Buck et al. 1999).

Rift Segmentation

Rift zones are generally not continuous structures controlled by a single through–going fault, but are instead segmented and controlled by multiple, often en–echelon shorter fault segments. Similar scales of rift segmentation in a variety of tectonic settings suggest segmentation is a fundamental feature controlled by the thermal and mechanical properties of the crust and lithosphere, rather than by regional tectonic forces. Figure 2.4 is an example of fault geometry from the Gulf of Suez. It demonstrates the degree of segmentation and changes in fault dip direction common along the rift axis (Bosworth et al. 2005). Segmentation and changes in fault polarity are also observed in the Basin and Range (Stewart 1980); East African rift (Rosendahl 1987); and the now inactive North Sea (Cowie et al. 2000).

Mid–ocean ridge seafloor spreading centres have a regular, along axis segmentation, thought to be the result of segmented magma supply from the upwelling mantle (Whitehead et al. 1984). A similar explanation may be appropriate for segmentation of magmatic continental rift zones (Behn & Lin 2000). Alternatively, rift segmentation may be controlled by pre-existing structures and lines of weakness. This, however, is thought to be unlikely at some rift zones due to the regular repeating nature of basin geometries along axis, and the poor correlation between rift segments and pre-existing structures (Ebinger 1989). Instead, the segmentation may be a fundamental length scale inherent to rifting itself. Observations at the East African rift suggest that segmentation length may increase with rift evolution, due to fault propagation and the coalescence of older smaller segments into a single larger depocentre (Ebinger 1989).

Strain redistribution, extension focusing and rift propagation

Differences in the magnitude of total extension and migration of extensional activity, both along and across the rift axis, are commonly observed at presently active continental rifts and spreading centres, for example: the East African rift, (Rosendahl

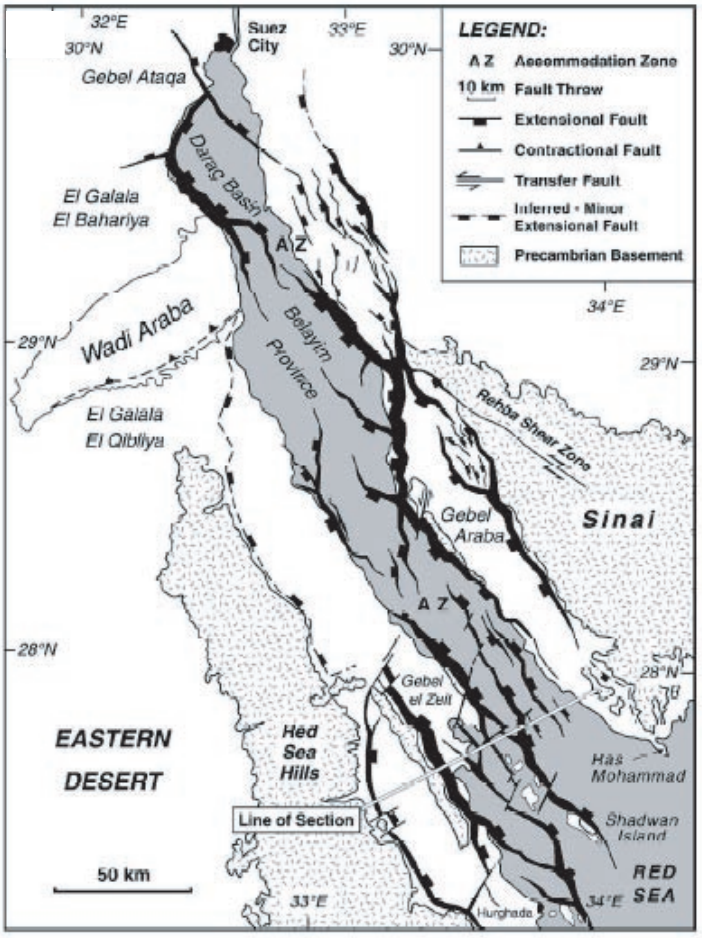

FIGURE 2.4: Principle major basement displacing faults in the Gulf of Suez, with fault width proportional to throw. To the south, structure is dominated by E–dipping faults, whereas W–dipping faults border the Belayim province and E–dipping faults control the northern Darag basin. From Bosworth et al. (2005).

1987, Hayward & Ebinger 1996); Gulf of Suez, (Gupta et al. 1999, Gawthorpe et al. 2003); the Woodlark basin, (Taylor et al. 1999); Red Sea, (Steckler & ten Brink 1986); Gulf of California, (Aragon-Arreola et al. 2005a) and some passive margins (e.g., Dunbar & Sawyer 1989b).

Dunbar & Sawyer (1989a) have suggested pre–existing lithospheric weaknesses in the crust and upper lithosphere are responsible for the focusing of extension and locus of later continental breakup. Where rifts are parallel to the pre–existing structural grain, necking occurs and spreading is promoted, whereas where rifting crosses the structural grain, greater extension usually occurs before spreading. This has been used to explain differences in the magnitude of continental extension along the central Atlantic and northern Atlantic basins (Dunbar & Sawyer 1989b).

Migration of sedimentary depocentres both along and across rift axis, may result from slow extension rates within a sedimentary basin (Kusznir & Park 1987, van Wijk & Cloetingh 2002, Mauduit et al. 2007). In this case lithospheric cooling (rather than

heating) occurs until eventually the lithosphere at the location of the first basin becomes stronger than the surrounding lithosphere. Extension and basin formation will migrate elsewhere where the lithosphere is weaker. Similarly, shifts in the location of maximum deformation with time in the Red Sea could be the result of lithospheric strength variations (caused by thickness, composition and geothermal gradient) controlling the position of rifting (Steckler & ten Brink 1986). Migration of deformation in the Gulf of California, is suggested to be the result of changes in the locus of strain toward zones of lower yield stress, produced by higher thermal conditions caused by discrete volcanism (Aragon-Arreola et al. 2005a, Aragon-Arreola & Martin-Barajas 2005b).

Goldsworthy & Jackson (2001) suggest that the interplay between crustal stresses generated by fault related relief and the strength of major faults is responsible for the migration of fault activity. Continued offset on major faults results in stress changes that eventually may inhibit further slip on that fault (Forsyth 1992). It may be energetically favorable instead for new faults to initiate and activity to migrate elsewhere.

Ebinger (1989) propose that the western branch of the East African rift propagated by the connection of originally isolated rift basins. Thus, the age of subsidence along a rift zone is diachronous. Fault propagation between two initial basins may be the result of stress concentration and crack propagation between two en–echelon crack tips (Ebinger 1989).

The suggested rift propagation mechanisms described above fall into two categories. Those which involve whole lithospheric processes (i.e. thermal lithospheric cooling, thermally induced stress changes), and others that involve stress changes due to fault interactions.

2.1.3 Fault mechanics

To fully understand the mechanisms of rifting, an appreciation of how faults act in isolation and also how they interact with one another must be established. The geometry and evolution of large normal faults in extensional areas are topical issues in Earth Sciences.

Normal faulting and earthquakes

Normal faulting is not only associated with subsidence and the production of accommodation space, but also uplift of the footwall into highlands (Vening Meinesz 1950, Jackson & McKenzie 1983). Footwalls of normal faults uplift due to elastic rebound caused by stress reduction across the faults during slip. Although the stress changes across footwall and hanging wall are the same; due to the generally 45 to 60° dip of normal faults, subsidence of the hanging wall is significantly greater than uplift of

the footwall during an earthquake. Normal faulting also perturbs isostatic conditions and the unloaded footwall block rises with the hanging wall correspondingly sinking (Vening Meinesz 1950). The ratio between uplift and subsidence depends, not only on the mass of unloaded material (i.e. the slip), but also on the elastic thickness of the lithosphere and fault dip (summarised by Watts 2001).

Uplift to subsidence ratios of displacement, during an earthquake (coseismic), may be deduced from: the surface displacement field derived from leveling; vertical GPS measurements; or Interferometric Synthetic Aperture Radar (InSAR) images (e.g. Wright et al. 2006, Funning et al. 2007). Although, depending on the timescales of measurement, these methods may include a component of postseismic relaxation. The uplift to subsidence ratio (U:S) is typically found to be in the range of 1:8 – 9 for 45 – 50° dipping faults (King et al. 1988). Some time after an earthquake, however, this uplift to subsidence ratio reduces significantly, with the uplift component increasing. This is due to postseismic viscous relaxation, which is effective after the Maxwell time has been reached (Rundle 1982). After complete viscous relaxation (around 100–1000 maxwell times) a ratio of ∼1:2 – 3 is estimated (Armijo et al. 1996).

Fault interaction

Fault interactions are important in influencing the structure of rift zones and their propagation. A major constraint on the geometry of fault zones is the fact that coexisting faults must not cross at depth. Crossing faults will be displaced and slip vectors are likely to no longer lie in the plane of the fault, rendering the faults inactive (Jackson & McKenzie 1983). This simplifies the possible geometry of active extensional zones and may explain why normal faults often dip in the same direction over large areas. Rotation of faults with time can mean they become unfavorably orientated for frictional slip and new faults may be initiated instead. These second generation faults may truncate older first generation faults as well as uplifting hanging wall sediments.

The tips of en–echelon fault segments may overlap in map view. Depending on the level of interaction and linkage between the overlapping segments, Peacock & Sanderson (1994) define a four stage evolutionary process to explain the interaction. Relay ramps are transfer zones between two overlapping fault segments that have the same dip direction. Bedding within the relay ramp is reorientated to remain in continuity with the hanging wall and footwall. These relay ramps are often warped and fractured to transfer extension between the normal fault segments. With time the two segments may become ‘hard–linked’ by a through going fracture (Gibbs 1984).

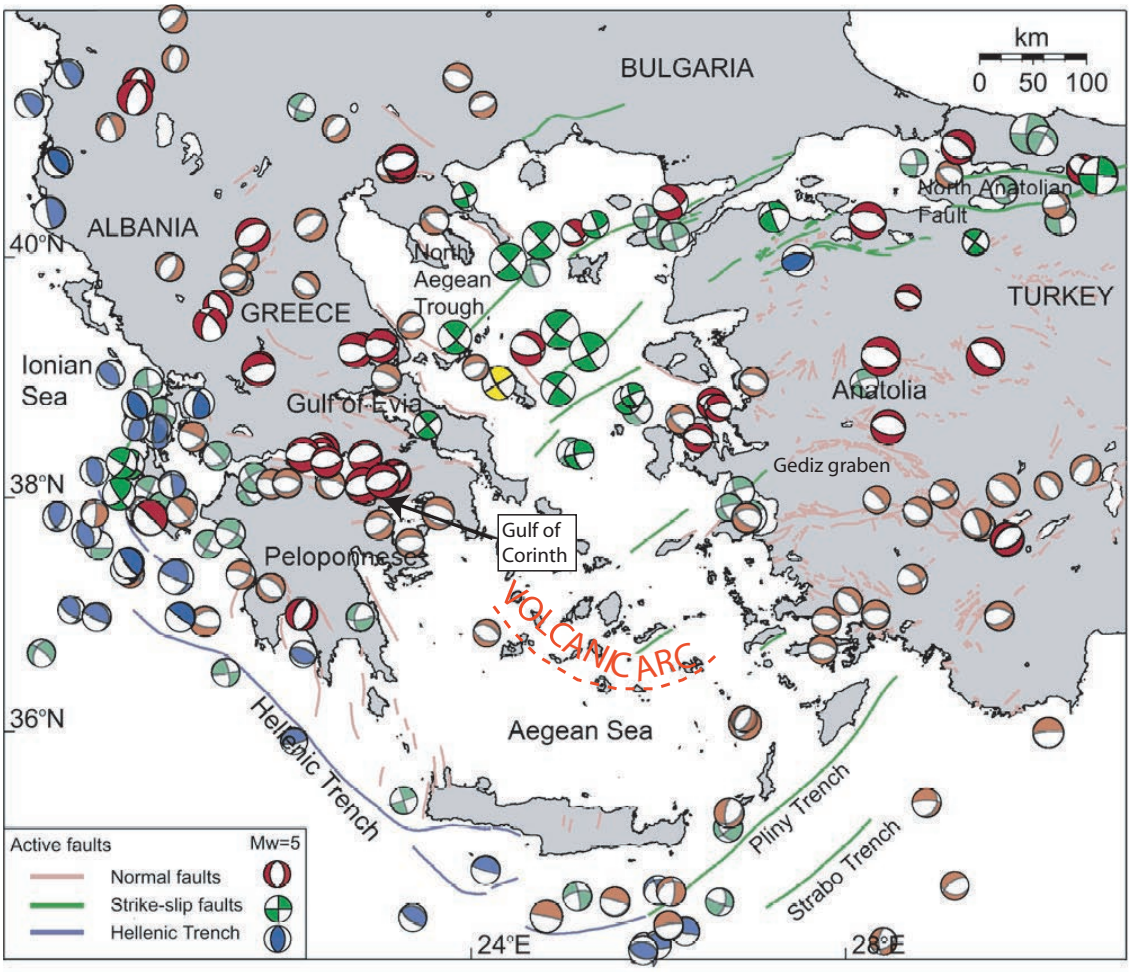

FIGURE 2.5: Summary of active faults and earthquake fault plane solutions for earthquakes greater than Mw = 5, in the Aegean region. From Nyst & Thatcher (2004).

2.2 Tectonic framework of the Aegean region

The Aegean region of the Alpine–Himalayan chain, including Greece, Turkey, Albania, Yugoslavia, and Bulgaria, is currently experiencing a wide range of tectonic phenomena including subduction, strike slip faulting and extensional deformation (e.g. McKenzie 1972, 1978b, Dewey & Sengor 1979, Fig. 2.5).

2.2.1 Seismicity and active tectonics

Seismicity is not homogeneous across the Aegean region, but is concentrated in high strain bands with relatively aseismic areas between them (McKenzie 1972, 1978b, Fig. 2.5). Focused seismicity occurs in an arcuate band between SW Greece (Peloponnese) and SW Turkey, along the North and East Anatolian faults in Turkey, and in several E–W trending bands in central Greece and western Anatolia (Fig. 2.5). Other areas show more diffuse deformation. Such a distribution of deformation has led to a debate

in the literature: should the kinematics of the area be described in terms of a number of rigid blocks or 'microplates', analogous to plate tectonics; or is it more correct to consider the deformation as quasi-continuous**?**

Compressional faulting (blue in Fig. 2.5) is restricted to an arcuate band which follows the trace of the Hellenic and Pliny trenches to the south of Crete and trends NW in the Ionian sea to the west of Greece and Albania. This deformation is associated with the subduction of the African plate beneath the Eurasian plate, with a convergence rate of up to 4 cm/yr (Casten & Snopek 2006). The plate boundary is defined by a Wadati–Benioff zone that dips north with an amphitheatric–like shape with earthquake hypocenters to a depth of 200 km (Taymaz et al. 1990). The deep water trenches do not trace the plate subduction, but are basins in the transitional zone between the Mediterranean Ridge and the forearc rise (Crete-Scarpanto and Rhodes). The true deformation front is south of the Mediterranean Ridge.

Northern Turkey experiences strike–slip faulting and seismicity (green in Fig. 2.5) along the North Anatolian fault, which is responsible for the movement of Anatolia away from the Black Sea block and northward moving Africa/Arabia. To the west, the North Anatolian fault splits into two strands that become more SW orientated relative to the E–W trend of the fault to the east (Fig. 2.5). Field work has shown that these strands do not cross Greece, but instead are suggested to enter a 'locking' orientation that obstructs the further westward movement of Anatolia (Dewey & Sengor 1979). In the southern part of the Aegean sea, there is comparatively little seismicity.

Western Turkey is associated with a distributed zone of extensional seismicity, between the subduction zone and the North Anatolian fault (Fig. 2.5). The extensional regime has created major WNW–ESE trending extensional graben (e.g. the Gulf of Gediz, Kocyidit et al. 1999). Similarly, throughout central Greece extensional seismicity dominates, with the formation of a number of E–W striking rifts, the largest including the Gulf of Corinth and Gulf of Evvia (Fig. 2.5).

2.2.2 Kinematics of Aegean region tectonic movement

The first simple kinematic model of Aegean deformation was presented by McKenzie (1972) (Fig. 2.6 A). This model suggests that active deformation in the Aegean is dominated by the southward movement of the southern Aegean relative to Eurasia and the subduction of the African plate at the Hellenic trench, and the westward motion of Anatolia toward Greece accommodated by the North Anatolian fault. The reason for the lateral westward escape of Turkey is thought to be related to the shape of the African plate indentor, having a protrusion in the area of Arabia, which causes continent–continent collision here, whilst ocean is still consumed to the east and west (Fig. 2.6 B). The shortening in the Bitlis suture is taken up by the westward extrusion of Turkey (McKenzie 1972). This simple model, however, does not explain the nature

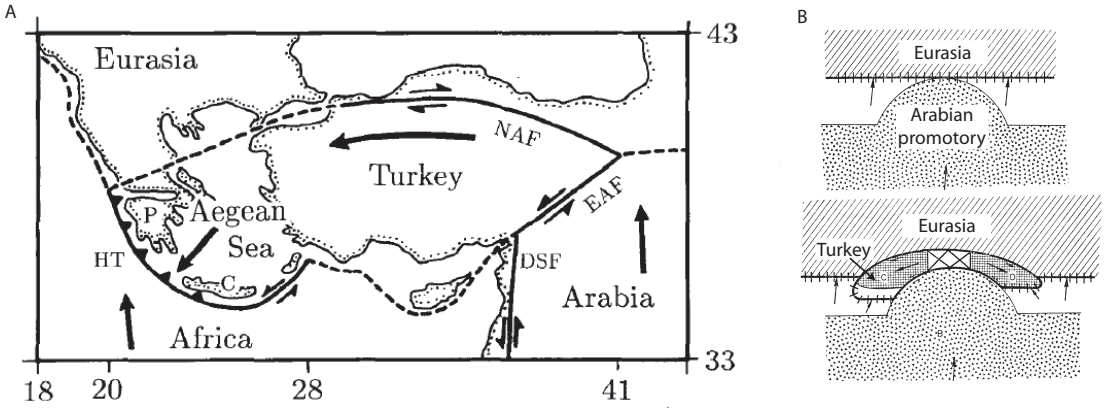

FIGURE 2.6: **A.** Sketch of the kinematic tectonic movements of the Aegean from McKenzie (1972). NAF is the North Anatolian fault, EAF is the East Anatolian fault, DSF is the Dead sea transform, C is Crete and P is the Peloponnese. **B.** Cartoon of the impact of the Arabian promotory and consequent westward escape of Anatolia (McKenzie 1972)

of deformation in Greece and SW Turkey, or whether the North Anatolian fault extends west of the Aegean sea (McKenzie 1972, extended the North Anatolian fault across Greece, although no strike slip seismicity or field evidence has been recorded there, Fig. 2.6 A). These areas have been studied in terms of seismicity, velocity field and fault architecture from field work and satellite imagery to establish a more realistic kinematic scenario.

2.2.3 The GPS velocity field

GPS (global positioning systems) methods are used in the Aegean to quantify and describe patterns of modern Aegean deformation providing clues to the large scale kinematics. Davies et al. (1997) reoccupied military triangulation points from the 1890's, to investigate the changing shape of Greece over the last ca. 100 years. Studies by Clarke et al. (1998), Briole et al. (2000), McClusky et al. (2000), Nyst & Thatcher (2004) and Avallone et al. (2004) have recorded the velocity field over a ca. 10 – 20 year interval. In general, the velocity field of the Aegean may be used to define microplates which are responsible for the tectonic movement of the Aegean (Nyst & Thatcher 2004). The velocity field in Figure 2.7 has been compiled from geodetic studies over the last 20 years by Nyst & Thatcher (2004). This figure shows Anatolia moving westward at 15 – 25 mm/yr relative to Eurasia. The south Aegean (and Peloponesse) is moving SSW at ∼30 mm/yr and central Greece is moving clockwise, with a speed of 5 mm/yr in NW Greece, increasing to 30 mm/yr at the Gulf of Evvia.

The movements of these microplates describe kinematically why extension is occurring in the Corinth rift. The clockwise rotation of central Greece and the SW translation of the Peloponesse result in the N–S opening of the Corinth rift. GPS velocity measurements indicate that the rift is opening at a rate of ∼5 mm/yr or less at its eastern

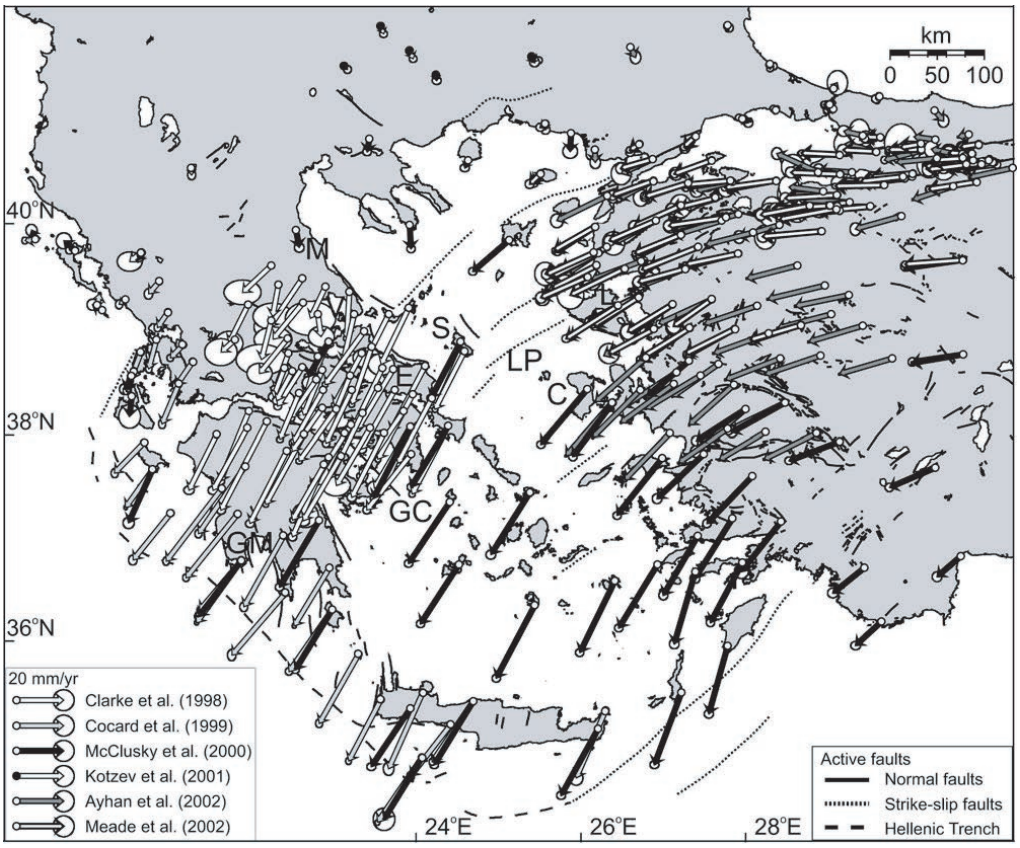

FIGURE 2.7: Compiled GPS velocity field for the Aegean by Nyst & Thatcher (2004).

end (in the Alkyonides Gulf), increasing to ∼15 mm/yr in the central rift, and is as high as ∼20 mm/yr in the west (Clarke et al. 1998, Briole et al. 2000, McClusky et al. 2000, Nyst & Thatcher 2004). This velocity field equates to an increase in strain from east to west along the Corinth rift (Fig. 2.8). A comparison of geodetic strain with calculated seismic estimates of strain using the Kostrov (1974) method from faults, shows that especially in the western rift, a great deal more geodetic strain has been occurring than has been released in seismic events (Clarke et al. 1998). This may point to increased seismic hazard in these areas, strain release on faults that were not identified in 1998, or aseismic strain release (Clarke et al. 1998).

2.2.4 Dynamic deformation models for the Aegean

From the analysis of the seismicity and kinematics of the Aegean region, three possible end–member models have been presented to explain the dynamics behind the existence of distributed extension in central Greece and SW Turkey: 1) Tectonic escape (Dewey & Sengor 1979), 2) Back–arc Spreading (Le Pichon & Angelier 1981) and 3) Orogenic collapse.

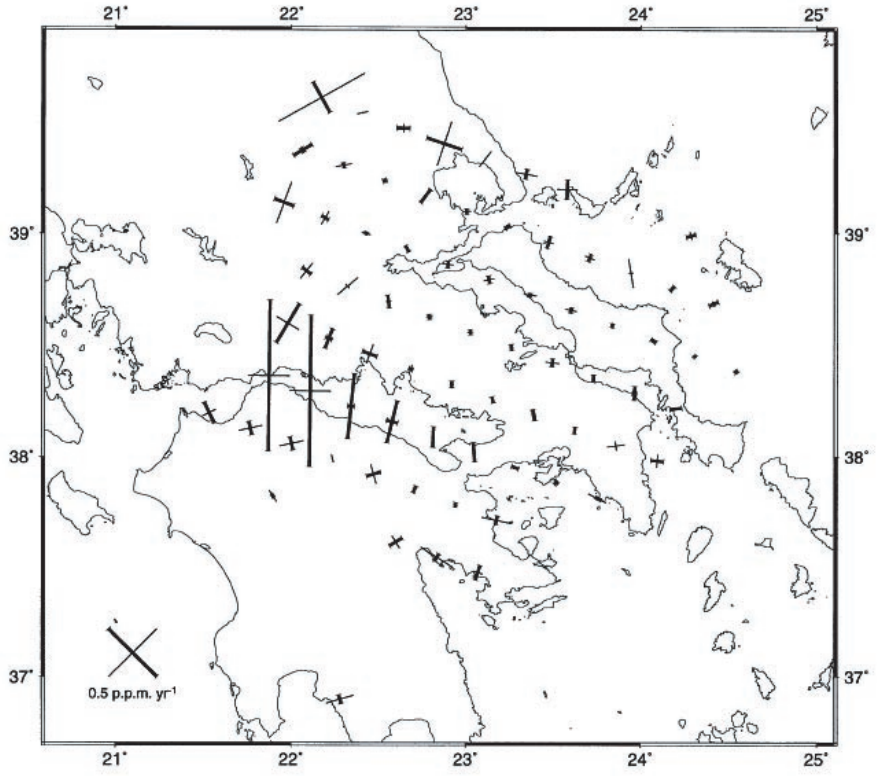

FIGURE 2.8: Principle strain axes across Greece, computed by Clarke et al. (1998).

Westward tectonic escape

Extension within central Greece and SW Turkey may be the result of the westward escape of the Anatolian microplate in the late Miocene (Dewey & Sengor 1979). Dewey & Sengor (1979) propose that the 'locking' of the North Anatolian fault in the Aegean sea, to the NE of the Corinth rift, results in an element of compression, which is relieved by extension of the West Anatolian graben system. Taymaz et al. (1991) suggest that westward movement of Anatolia causes greater rotation in the eastern Aegean than can occur in the west, due to the presence of a buoyant continental collision barrier (fixed margin) in Albania. Because right–lateral motion can not be transferred completely across Greece, it results in N–S orthogonal extension to compensate (the 'broken slat model'). However, such tectonic escape models have been challenged based on chronology. Seyitoglu & Scott (1996) suggest that palynological age estimates for the initiation of the E–W trending Buyuk Menderes basin in SW Turkey are of the order 20 – 14 Ma; which is significantly earlier than the collision of Eurasia and Arabia, thought to be responsible for the initiation of the North Anatolian fault, ∼15 Ma.

Alternatively, Armijo et al. (1996) suggest that faulting within the Corinth rift in the last ca. 5 Ma may be the result of the inhomogeneous stress field of the south–westward propagating tip of the southern branch of the North Anatolian fault.

Backarc spreading

The inception of Hellenic subduction is thought to have occurred ca. 13 Ma, with potential back–arc spreading initiating in the Miocene (Le Pichon & Angelier 1979). Although this is older than the initiation of Corinth rift tectonics, it is too young compared to the initiation of extension in the SW Turkey basins (Seyitoglu & Scott 1996). In addition, the Corinth rift does not actually lie in a back–arc environment. Instead, it has formed in the forearc region between the subduction front and the projection of the line of active volcanoes (Fig. 2.5). This mechanism alone, is therefore unlikely to fully explain the rift's origin.

Orogenic collapse

Extensional provinces often occur in regions that have previously undergone compression (Dewey 1988). This may be because crustal thickening and related magmatic activity add a thermal anomaly to the lithosphere which promotes rifting. Thickened crust is also gravitationally unstable and could collapse under its own weight. This is commonly thought to be the cause of rifting in the Tibetan Plateau. The region undergoing current extensional deformation in the Aegean was previously an area of compression in the formation of the Alpine-Hellenide mountain chain (e.g. Robertson & Dixon 1984, Piper 2006). Seyitoglu & Scott (1996) suggest that if gravitational spreading occurred immediately after the end of the Paleogene shortening, it could account for the onset of Aegean extension in the grabens of SW Turkey.

These are end–member mechanisms, and in reality Aegean extension may be some combination of all/both gravitational spreading and tectonic escape (Bozkurt & Sozbilir 2004). Constraints on rifting mechanisms are likely to result from a more detailed chronology of the oldest extensional grabens.

2.3 Geology and tectonics of the Corinth rift

The Corinth rift plays a key role in accommodating strain in the Aegean region. Its syn–rift sediment architecture, active tectonics and overall rift structure provide clues to its tectonic evolution. In the following section, literature concerning tectonics of the rift is reviewed, with the aim of presenting current deformation models that attempt to explain its initiation and propagation.

2.3.1 Geological history

Pre–rift basement

Current active extensional deformation (within the last 5 Ma) truncates older basement geology of the Pindos mountain chain that was shortened by a series of collisions

in the late Mesozoic–early Tertiary Alpine orogeny (Robertson & Dixon 1984, Pe-piper & Piper 2002, van Hinsbergen et al. 2005, Piper 2006). The basement rocks of today's Aegean are the east and west passive margins of the ancient Tethys ocean, consumed as a line of ophiolites orientated NNW-SSE in mainland Greece and ENE-WNW in the western Turkey. Basement rocks are Mesozoic pelagic cherts and carbonates overlain by Tertiary flysch (Robertson & Dixon 1984).

Neogene to modern syn–rift geology

The NNW-SSE Mesozoic thrust sequences have been truncated by rifting of the ESE-WNW Corinth basin. The age of the initiation of this rifting remains controversial. Ori (1989) suggests the extensional history of the Corinth rift is concurrent with the formation of the Aegean sea, which began rifting 6 – 18 Ma (Angelier 1978). However, the oldest syn–rift sediments that have been dated from the Corinth area have an age of only ∼3.6 – 4 Ma (Collier & Dart 1991), and the oldest syn-rift sediments from the western rift are thought to be of a similar age (Rohais et al. 2007).

Geological mapping of the distribution of older syn–rift sediments shows that the southern rift margin, at the initiation of rifting (e.g. defined by the Kalavrita fault in the west), was much further south than the currently active south margin (e.g. the Eliki and Aigion faults) (Ori 1989, Dart et al. 1994, Collier & Jones 2003, Rohais et al. 2007, Ford et al. 2007, Fig. 2.9). Ori (1989) interpret that the geology of the south coast of the Gulf of Corinth can be split into two phases, which represent two distinct episodes with different tectonic character. The first stage lower group sediments are deposited over a wide area, in a probable shallow–marine or lacustrine setting; indicating gradual slow subsidence during the initial stages of rifting. First stage deposits are now observed up to 20 km south of the shoreline with elevations of almost 2 km, having been uplifted in the footwalls of younger fault systems (e.g. Ori 1989, Sorel 2000, Collier & Jones 2003, Rohais et al. 2007, Ford et al. 2007, Fig. 2.9). The distribution of these sediments outlines the original 'Proto–Corinth rift' morphology, and an idealised cross–section of this system is shown in Figure 2.10. More recently, field studies have mapped in detail the stratigraphy of this lower–stage deposit, which is controlled by a number of now inactive faults, in an attempt to produce a chronology of faulting and syn–rift deposition during this stage (e.g. Sorel 2000, Collier & Jones 2003, Malartre et al. 2004, Rohais et al. 2007, Ford et al. 2007). Rohais et al. (2007) and Ford et al. (2007) consider that rifting has occurred in three stages, with the current phase focused predominantly offshore.

The second sedimentation phase (defined the middle group by Rohais et al. 2007) is marked by a dramatic increase in subsidence and the formation of thick Gilbert fan deltas in a deeper water setting (Ori 1989, Dart et al. 1994, Fig. 2.10). The timing of this change in tectonic regime, from distributed extension to more focused fault acuity is also controversial. Recent dating of sanidines from a Megara basin tuff and

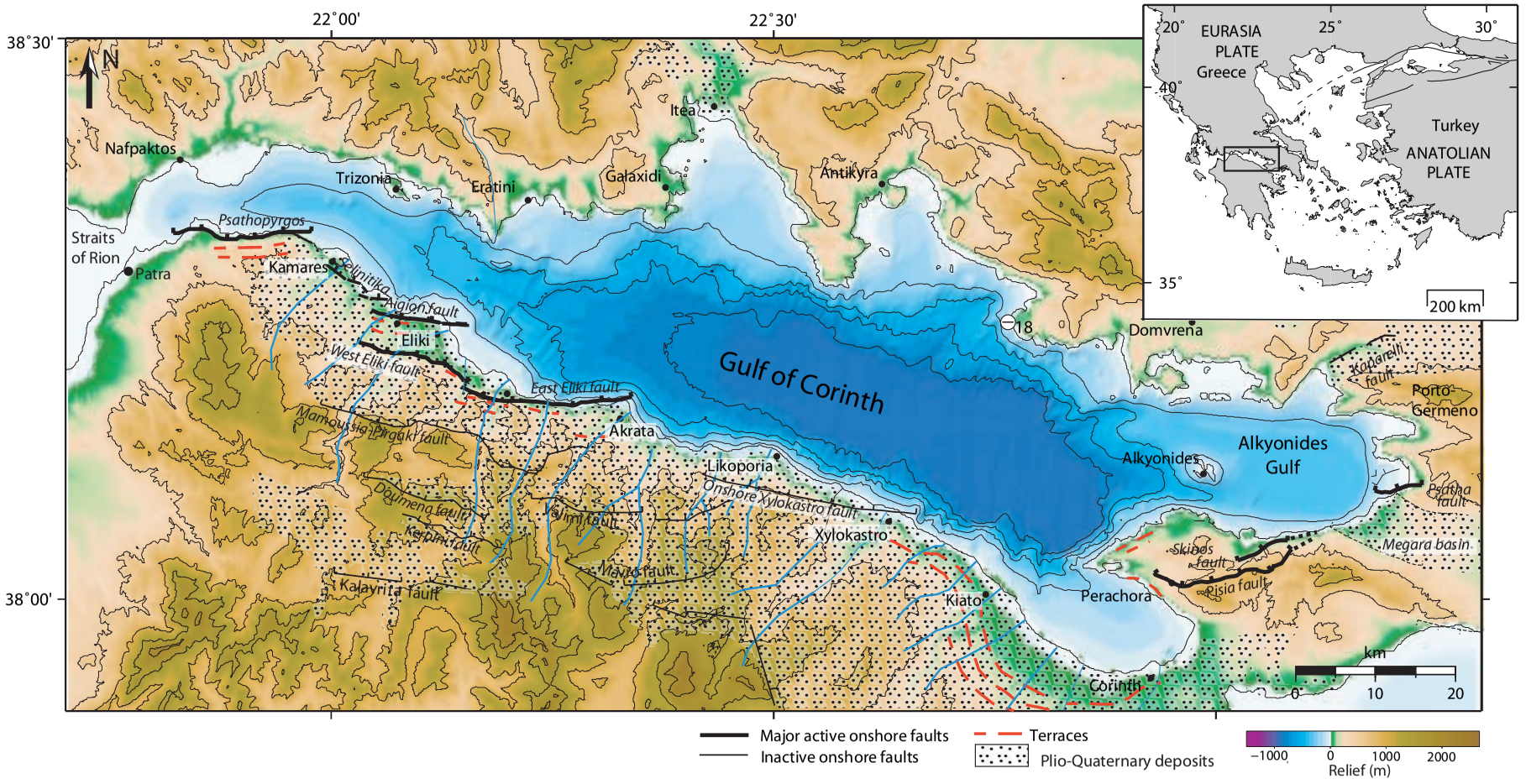

FIGURE 2.9: Tectonic framework of the onshore Corinth rift. The locations of major onshore fault locations after Armijo et al. (1996), Stefatos et al. (2002), Leeder et al. (2005), McNeill et al. (2005b), Palyvos et al. (2005), Rohais et al. (2007). Topography is from the Shuttle Radar Topography Mission (http://srtm.usgs.gov), bathymetry is derived from the swath bathymetry M.V. Vasilios 2003 cruise (McNeill et al. 2005a) and R/V Maurice Ewing 2001 (Zelt et al. 2004). South coast drainage from Zelilidis (2000). Areas of Plio–Quaternary sediment deposition from Armijo et al. (1996), Stefatos et al. (2002). Un-ornamented areas are basement rock.

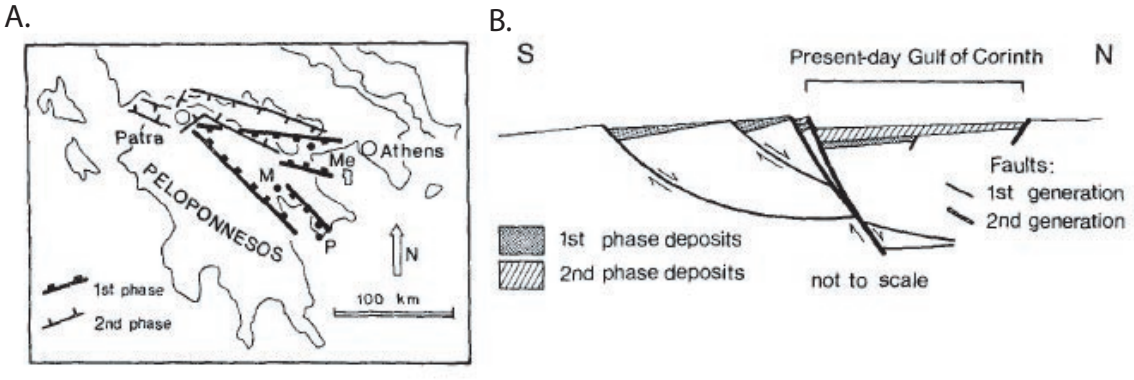

FIGURE 2.10: **A.** Location of the Ori (1989) first and second phase Corinth rift basins. **B.** Idealised cross-section across the Corinth rift showing first and second phase deposits (Ori 1989).

magnetostratigraphy suggest that the currently active faults in the Alkyonides Gulf initiated in the Late Pliocene post ca. 2.2 Ma (Leeder et al. submitted). Initiation of the modern phase of active faulting in the western rift however, is believed to have occurred ca. 0.7 – 1.0 Ma (McNeill & Collier 2004, McNeill et al. 2005b) with the more recent Aigion fault initiating ca. 0.2 – 0.3 Ma further north (De Martini et al. 2004, McNeill et al. 2007). The currently active Corinth rift faults initiated between ca. 1 to 2 Ma, from the sparse chronology available.

The Corinth rift is composed of not only the current offshore basin and coastal faults, but also the onshore, now inactive faults particularly on the southern margin (Fig. 2.9). The **'entire'** Corinth rift as described in this thesis is composed of all the faults that have ever acted in the vicinity of the current rift and the **'currently active'** Corinth rift is defined as the region bordered by the currently active faults.

Ori (1989) proposed the first deformation model to account for the two stage tectonic history. This idea has now evolved into a three stage model by Rohais et al. (2007) who also consider the current modern phase of offshore sedimentation. Ori (1989) suggested that the original rift formed in response to opening of the Aegean sea, by west to east propagation of faulting, about a hinge south of Patra (Fig. 2.10 A). Since the inception of this original tectonic model, more detailed onshore field studies, geodetic data and an understanding of the offshore realm have led to modifications. These new models are summarised in section 2.3.4, after the following review of rift sedimentology, active tectonics and crustal structure.

2.3.2 Sedimentary basin architecture

The sedimentary architecture of syn–rift deposits, infilling space created by tectonic activity, can be very important in deciphering the tectonic evolution of an area (e.g. Watts 1989, Gawthorpe et al. 1994). Unconformities, growth structures and onlap and offlap features within sediment packages can be used to assess the activity of faults.

The stratigraphic architecture of the offshore and onshore parts of the Corinth rift is described below, in terms of its use in defining the tectonic character of the system.

Onshore sedimentation and geomorphology

The northern shore is almost completely devoid of recent sediments (Stefatos et al. 2002), in contrast to the thick syn–rift sediment basins on the southern margin (Fig. 2.9). Gilbert type fan deltas form offshore where rivers enter the basin; for example the Alepochori fan on the south coast of the Alkyonides Gulf (Leeder et al. 2002) and the Eratini fan on the north coast (Hasiotis et al. 2006). The northward migration of fault activity, described above, has uplifted older deltas and provided a very detailed record of the balance between tectonics and eustatic sea level (Dart et al. 1994, Malartre et al. 2004, Rohais et al. 2007, Ford et al. 2007).

Fan deltas in tectonically active areas can derive their clastics from the footwalls of active faults, and the position of rivers can also be controlled by tectonics (Dart et al. 1994, Zelilidis 2000). Fan deltas exhibit characteristic facies associations of coarse grained topset beds, sloping foreset beds and fine-grained bottomsets (Eliott 1978). Deltas grow by progradation of sediment wedges into water–filled basins. The architecture of delta depositional sequences and their stacking pattern record the interaction of variations in base level movement (i.e. either sea level or tectonic ground level changes), climate and sediment supply. Delta morphology can be numerically modelled to investigate the details of subsidence history (Watts 2001, Gawthorpe & Hardy 2002).

Offshore sedimentation and sediment transport

The deepest bathymetry in the Corinth rift occurs between Derveni and the Perachora peninsula (Heezen et al. 1966, Taylor et al. 2003, McNeill et al. 2005a, Sakellariou et al. 2007, Fig. 2.9). Bathymetry of the south margin is fault controlled and steep, whereas the seafloor shallows more gently on the north margin, forming shallow platforms in the Antikyra and Itea bays. Rift bathymetry has an overall asymmetric profile with the deepest seafloor closer to the southern margin with a maximum depth of ∼900 m. Submarine canyons are observed predominantly on the southern margin (Charalampakis et al. 2007) and an E–W axial drainage channel flows from the western rift into the central basin (McNeill et al. 2005a). The Corinth rift is connected to the Saronic Gulf at its eastern end by the man–made Corinth canal, and to the Ionian ocean across the Rion sill to the west. The Rion sill is a submerged terrace that lies 60 – 70 m below current sealevel, and formed in response to erosion during sea level lowstands (Perissoratis et al. 2000).

The predominate depositional mechanisms offshore are hemipelagic sedimentation, turbidite and debris flows; interpreted from seismic reflection character, gravity coring

(Heezen et al. 1966) and the frequency of submarine cable breaks, suspected to be the result of high density underwater currents (Ferentinos et al. 1988). Seismic reflection surveys show that the shallow sediments of the main offshore basin are composed of alternating high and low frequency reflection bands, which are parallel and continuous (e.g. Brooks & Ferentinos 1984, Higgs 1988, Sachpazi et al. 2003, McNeill et al. 2005a). Perissoratis et al. (2000) suggest that the origin of the alternating seismic character is related to eustatic sea level change. This has been confirmed by piston coring in the central Gulf of Corinth (Moretti et al. 2004) and Alkyonides Gulf (Collier et al. 2000). Sachpazi et al. (2003) interpret five ∼100 ka sediment cycles from seismic stratigraphy within the Gulf of Corinth main basin. Below these well–stratified cyclic sediments a thick non–reflective package exists of unknown origin (Sachpazi et al. 2003).

2.3.3 Active tectonics

Faulting

Dramatic fault–related topography is observed along the southern margin of the Corinth rift. Active fault surfaces in basement limestone are smooth, polished planes with corrugations parallel to the slip vector, with dips typically between 40 – 70° (Roberts & Jackson 1991). Continuing efforts are being made to map in detail all of the now active and inactive faults onshore and offshore and understand their relative chronology.

a) Inactive south coast faults

In the Megara basin (south of the Alkyonides basin, eastern Corinth rift, Fig. 2.9), inactive faults trend SE–NW and were responsible for the creation of the basin now being uplifted by active faults (e.g. Collier et al. 1992, Leeder et al. submitted). Many E–W trending, now inactive faults exist on the south–west margin of the Corinth rift, including the Kalavrita, Kerpeni, Doumena and Mamoussia-Pirgaki faults (Fig. 2.9). These faults were active during the first stage of rift development, discussed previously (Ori 1989). The relative timing of activity of each of these faults and how they interact at depth is subject to debate and contributes to one of the greatest Corinth rift controversies: is there a low-angle detachment underlying the western rift**?** (Rigo et al. 1996, Bernard et al. 1997, Sorel 2000, Westaway 2002, Collier & Jones 2003, Gautier et al. 2006, Rohais et al. 2007, Ford et al. 2007).

Sorel (2000) interpret the most southern of the inactive onshore faults in the western part of the rift as a listric, low–angle fault, based on the 25°N dip angle of the fault plane. This fault borders the Khelmos summit and marks the southern boundary of the rift. The interpretation of this fault by Sorel (2000), follows claims by Doutsos & Poulimenos (1992) that this fault becomes a sub–horizontal detachment at depth continuing to the north, and higher angle surface faults sole onto it. In this model,

the total throw on any of the high angle faults is limited by the depth to the detachment and the detachment itself forms the major extensional control on rift geometry. The Sorel (2000) deformation model suggests that faulting on the southern margin began initially at the Khelmos detachment, and later high angle faulting initiated in its hanging wall, gradually migrating in a northward direction and widening the basin. This model has been tested numerically by Chery (2001), who suggest, if it is correct, in the future the Corinth rift may become a fully developed metamorphic core–complex, like the Snake Range in Nevada.

However, this deformation model has been fiercely challenged. Collier & Jones (2003) suggest instead that the entire system could be formed by comparatively high angle normal faults bounding narrow half grabens, which were back-tilted by progressive footwall uplift. This is supported by Westaway (2002), who propose that the low angle of the Khelmos fault (named the Kalavrita fault here) is likely the result of tilting from an initial $\sim 45^{\circ}$ dip angle. From detailed stratigraphic mapping, Collier & Jones (2003) interpret that the timing of faulting is more complex than the simple northward progression proposed by Sorel (2000). Many of the south west faults (including Kalavrita, Kerpini and Doumena) were active at the same time, and deformation was distributed over a wide area. Subsequently, activity focused on individual faults, like the Mamoussia-Pirgaki fault, causing enhanced subsidence and allowing the Gilbert fan deltas of the second phase to deposit (Ori 1989). This evolutionary scenario is not compatible with gradual propagation above a low angle detachment. Instead it is similar to the 'rift climax' theory, applied to other basins (e.g. North Sea, Gulf of Suez), where initial slow subsidence is followed by an abrupt increase in subsidence rate (e.g., Gupta et al. 1998) or strain localisation models caused by second generation faulting (e.g., Jackson 1999).

b) Active south coast faults

The southern shoreline of the Corinth rift is bordered by en–echelon fault segments including from west to east: the Psathopyrgos, Selinitika, Aigion, East and West Eliki, Xylokastro, Pisia, Skinos and Psatha faults (Fig. 2.9). Between the tip of the East Eliki and Xylokstro faults, the uplift of the coastline suggests major faults, just offshore, are likely to be present (e.g. Armijo et al. 1996, Stefatos et al. 2002). Equally, in the Alkyonides basin offshore fault segments are believed to be influential on coastline movement (Leeder et al. 1991). No significant active S–dipping faults are observed along the northern margin except at Delphi. The Kaparelli fault, to the north of the Alkyonides Gulf, slipped in the 1981 earthquake sequence, however its low cumulative scarp suggests it experiences much less earthquake activity than south coast faults (Jackson et al. 1982, Benedetti et al. 2003, Kokkalas et al. 2007). South margin border faults dip north, and uplift older Gilbert fan deltas in their footwall, and downthrow the Corinth basin in their hanging wall. These fault segments measure

between 15 – 20 km in length and strike 90° – 105°. The length of these segments probably limits the maximum size of earthquakes in this area to Ms 6.7 (Ambraseys & Jackson 1990). Although the possibility of rupture of multiple segments, in the same event, has been entertained (Andrews & Schwerer 2000, McNeill & Collier 2004).

Slip rates of these coastal faults have been estimated from: uplift rates of wavecut notches, remains of marine organisms and marine terraces (by assuming a probable uplift to subsidence ratio, e.g., McNeill & Collier 2004); elastic modelling (Armijo et al. 1996, De Martini et al. 2004); paleoseismology from fault trenching (Collier et al. 1998); and ^{36}Cl cosmogenic exposure dating (McNeill et al. in prep). Late Quaternary slip rates of faults bordering the Gulf of Corinth have been estimated between ∼3 – 11 mm/yr using these methods. Within the Alkyonides Gulf slip rates are generally lower, ∼1 – 3 mm/yr. Holocene slip rates are greater than those averaged over the Late Quaternary throughout the south margin of the Corinth rate. Slip rates of south coast faults are discussed in more detail in Chapter 4, section 4.4.

c) Offshore faults

Previously, the northern margin of the Corinth rift has been described as passively down–flexing in the hanging wall of the major en–echelon N–dipping fault systems on the southern shoreline (Heezen et al. 1966, Brooks & Ferentinos 1984, Stefatos et al. 2002). However, recently S–dipping faults in the offshore region of the Corinth rift have been identified as potentially important in controlling rift structure (Moretti et al. 2003, McNeill et al. 2005a).

Although a number of offshore seismic surveys have now been conducted in the Corinth rift, none so far, provide a well-constrained coverage in which to produce a reliable fault map and systematically investigate changes in rift geometry. One of the challenges of this thesis is to compile all existing and available data–sets to compile an up–dated, well constrained picture of faulting within the rift.

Seismicity

a) Large Earthquakes Ms ≥ 5

The distribution of modern Corinth rift seismicity, with surface wave amplitude magnitude (Ms) greater than 5, is shown in Figure 2.11 (sources of CMT solutions shown in Table 2.1). The most recent and well studied earthquakes are the sequence of earthquakes that occurred in the Alkyonides Gulf in 1981 (Jackson et al. 1982, Taymaz et al. 1991). Three earthquakes with magnitudes Ms ≥6 occurred within two weeks. The first two shocks are thought to have been caused by ruptures on the Skinos and Pisia faults and possibly the offshore Perachora fault (Jackson et al. 1982). The third shock took place on the minor S–dipping Kaparelli fault on the north margin. The

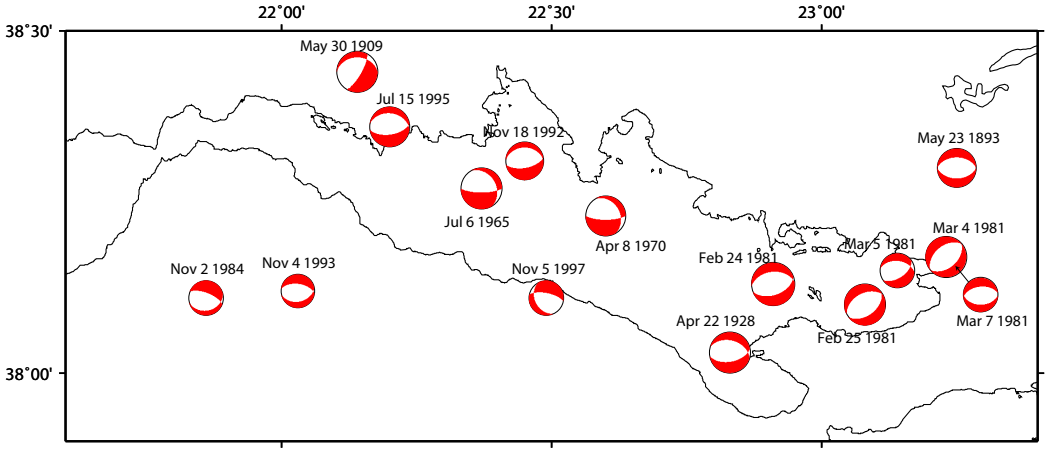

FIGURE 2.11: Summary of Ms ≥5 seismicity. Focal mechanism geometry and sources of data shown in Table 2.1.

aftershocks of the 1981 events constrain the depth to the seismogenic zone in the Alkyonides Gulf at ∼12 km (King et al. 1985).

Earthquakes in the western rift have been examined by Bernard et al. (1997) and Hatzfeld et al. (1996). They determine that the likely fault plane for the 1995 Aigion earthquake and 1992 Galaxidi earthquake were the result of slip on either a N–dipping 30 – 40° fault, or a high angle S–dipping fault. Bernard et al. (1997) prefer the low angle N–dipping plane from geodetic data. No obvious fault has been interpreted in this area to explain the geometry of the rupture plane. These possible low angle nodal planes are sometimes used to support the detachment hypothesis, although an angle of 30 – 40° is much steeper than expected for such sub–horizontal detachment surfaces.

b) Microseismicity

A number of microseismicity and aftershock studies in the western rift have been conducted in an attempt to determine the geometry of active faulting. Rigo et al. (1996) suggest how high angle planar normal faults rupture the lithosphere and root into deeper semi–brittle lithosphere. They find that seismicity clusters on a 10 – 20° N–dipping zone in the western rift, which they propose is an extension of the Psathopyrgos fault as a low angle detachment at a depth of 9 – 11 km. This view is supported by the work of Gautier et al. (2006). In contrast Hatzfeld et al. (2000) infer that microseismicity defines a sub–horizontal plane (base of the seismogenic zone) in the western rift equivalent to the brittle–ductile transition.

The presence or absence of a detachment or low angle faulting is still one of the hottest debates in Corinth rift extension studies. Confusion is beginning to enter the literature in terms of the level of evidence for and against the existence of a detachment.

Date	Ms	Lat.(°)	Long.(°)	Strike(°)	Dip(°)	Rake(°)	Depth(km)	Source
Nov 5 1997	5.4	38.11	22.49	281	67	-117		A
July 15 1995	6.2	38.36	22.2	277	33	-77	10	B
Nov 4 1993	5.2	38.12	22.03	79	37	-105	15	A
Nov 18 1992	5.9	38.31	22.45	270	30	-81	7.4	C
Nov 2 1984	5.4	38.11	21.86	77	28	-121	15	A
Mar 7 1981	5.4	38.16	23.24	91	41	-84	15	D
Mar 5 1981	5.3	38.15	23.14	276	43	-59	15	D
Mar 4 1981	6.3	38.17	23.23	50	45	-90	7	D
Feb 25 1981	6.4	38.10	23.08	241	44	-85	8	D
Feb 24 1981	6.7	38.13	22.91	264	42	-80	12	D
Apr 8 1970	6.18	38.23	22.6	90	74	-115	6	E
Jul 6 1965	6.38	38.27	22.37	90	74	-115		E
Apr 22 1928	6.3	38.03	22.83	285	40	-70	9	E
Oct 17 1914	6.2	38.34	23.46	100	45	-90	10	E
May 30 1909	6.3	38.44	22.14	30	74	-115	10	E
May 23 1893	6.0	38.30	23.25	270	45	-90	10	E

TABLE 2.1: Summary of seismicity Ms ≥5 for the Corinth rift in recorded history. Focal mechanism solutions shown in Figure 2.11. Sources of data: A = HCMT catalog, B = Bernard et al. (1997), C = Hatzfeld et al. (1996), D = Taymaz et al. (1991), E = Ambraseys & Jackson (1990)

The observations of: the low–angle Khalmos/Kalavrita onshore fault and proposed detachment at a shallow crustal level of ∼3 km (Sorel 2000); the ∼30° dipping possible fault plane solution for the Aigion and Galaxidi earthquakes (Bernard et al. 1997, Hatzfeld et al. 1996); the ∼15° N-dipping zone of microseismicity at a depth of 9 – 11 km; and a possible sediment–basement detachment surface interpreted within seismic reflection data (Taylor et al. 2003, Sachpazi et al. 2003) have all been used as evidence for a detachment surface. In truth, the interpreted low angle detachment onshore is much too shallow to correlate with the microseismicity zone. The 30 – 40° fault plane solutions are also not consistent with a ∼15° detachment.

2.3.4 Rift structure

Upper crustal fault geometry

The geometry of inactive onshore faults at depth and their relation with currently active faults, remains unknown. The presence of either high angle planar faults extending to the brittle–ductile transition or high angle faults becoming listric at depth and soleing out onto a sub–horizontal detachment, have strong implications for models of rift evolution.

Previous concepts of the across rift fault geometry assumed that the rift is a simple asymmetric half graben, with uplift of the southern margin and maximum basement subsidence adjacent to south coast faults, with an overall subsiding northern margin.

Offshore seismic reflection data has revealed that this rift geometry is over simplistic. In reality the rift shows strong evidence of varying geometry along axis, with S–dipping offshore faults being important in the west (Stefatos et al. 2002, Sachpazi et al. 2003, McNeill et al. 2005a). In the previous review of global rifts it was found that rifts are often segmented, experience changing dominant fault polarity and may have complex geometries. The Corinth rift seems to exhibit similar geometrical complexity. A systematic study of the changing geometry in space and time is required to determine rift evolution models.

Crustal thickness

The pre–rift basement beneath the offshore Corinth rift has been imaged by deep seismic reflection profiles presented by Sachpazi et al. (2003), Clement et al. (2004) and Zelt et al. (2004). These profiles show that basement reaches a maximum depth of ∼3 km. A complete spatial view of basement depth has not yet been produced. Moho topography beneath the Corinth rift has been interpreted by Zelt et al. (2005) based on a tomographic inversion of PmP reflection times and the Moho topography beneath the rest of Greece has been determined by Sachpazi et al. (2007). Moho topography within the Corinth rift shows a gradual decrease from 42 km in the west to < 30 km in the east. Crustal thickness of the Corinth rift is described in more detail in Chapter 7, section 7.4.

Deformation models for Corinth rift evolution

A number of simple evolutionary models for the Corinth rift's initiation and propagation have been proposed, in light of the sedimentological, fault geometry and crustal studies outlined above. The evolutionary models fall into two categories: those which account for how the rift may have propagated in an along axis direction, and those that describe the across axis changes.

a) Along axis rift propagation

Ori (1989) proposed west to east propagation, about a rotational pole to the south of Patra. Such a mechanism would account for the relatively narrow width of the Alkyonides Gulf at the eastern end (Fig. 2.12 A). Le Pichon et al. (1995), Armijo et al. (1996) and Clarke et al. (1998) instead suggest east to west propagation, with the western rift being younger, less extended and shallower than the central rift and with higher geodetic extension rates. At the Corinth rift, northern Greece shows an overall clockwise rotation, whereas the Peloponnese is rotating anti-clockwise (Fig. 2.12 A). In the Le Pichon et al. (1995) and Nyst & Thatcher (2004) model of rift propagation, this rotation causes an increase in velocity vector from east to west in the Corinth rift, resulting in an E–W opening of the region with a pole of rotation

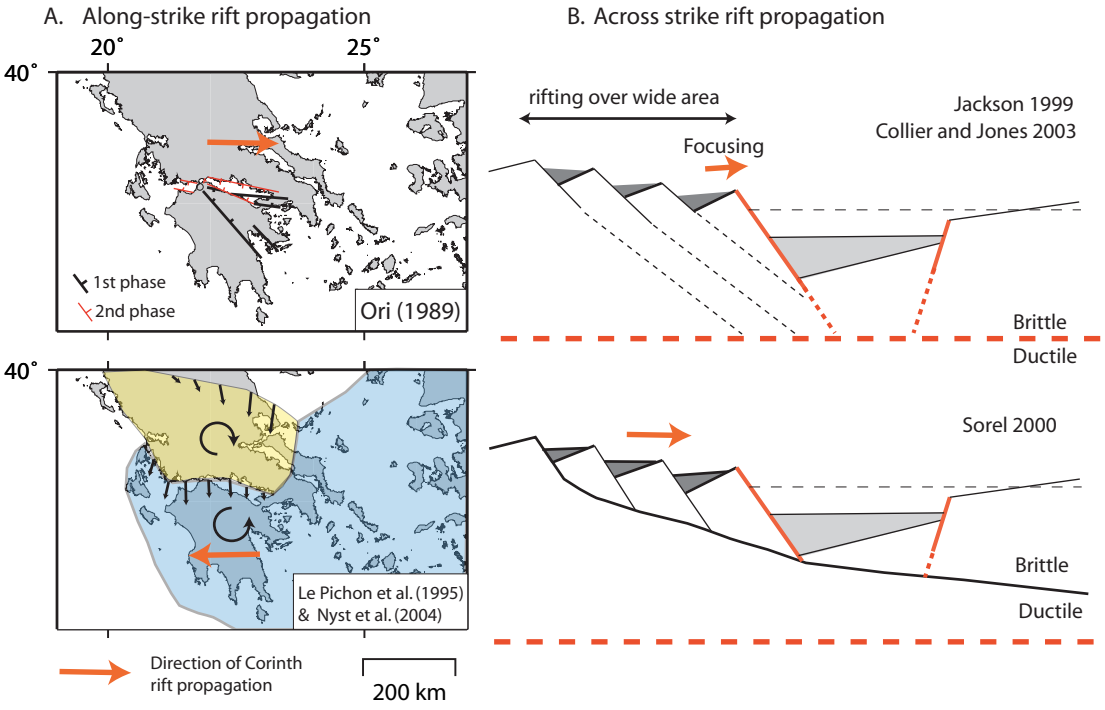

FIGURE 2.12: **A.** Summary of the Ori (1989) and Le Pichon et al. (1995), Clarke et al. (1998) and Nyst & Thatcher (2004) theories of W to E and E to W rift propagation respectively. **B.** Idealised cross-sections to demonstrate the fundamental aspects of the Jackson (1999), Sorel (2000) and Collier & Jones (2003) theories of across-strike rift propagation.

centered in the Athens area. Propagation models can only be tested by a more precise chronology of the age of syn–rift sediments from east to west. The detailed analysis of the 3D geometry of basin stratigraphy may also provide clues to the character of along axis evolution. Has it progressed in a unidirectional manner or is it more spatially variable and complex?

b) Across axis rift propagation

The southern margin has experienced a history of northward migration of faulting, into the hanging wall of older faults. This propagation has been described as the result of faulting above a low angle detachment (e.g., Sorel 2000) and that it results from initially distributed planar high angle faulting, later becoming focused on second generation individual faults (e.g., Jackson 1999, Collier & Jones 2003, Fig. 2.12 B).

Detachment faulting influences basement geometry and therefore stratigraphy in distinctive geometrical ways (Gibbs 1984). A detailed investigation of the offshore western rift stratigraphy could constrain if it is compatible with a low angle detachment surface and provide, in the absence of high quality basement imaging, the best evidence to prove or disprove the existence of a detachment.

2.4 Summary of major controversies in Corinth rift tectonics

1. Are the tectonics of the western rift controlled by a sub–horizontal detachment surface? If so, is that detachment the 3 – 4 km sub sediment–basement contact suggested by Sorel (2000), Taylor et al. (2003) and Sachpazi et al. (2003), or the deep microseismicity defined 10 – 15 km N–dipping detachment? Is there evidence for detachment tectonics less than 50 km to the east, in the central and eastern parts of the rift?
2. How important are S–dipping faults in controlling rift structure? Do they play a potentially important role in rift extension and/or have they been influential in rift development in the past?
3. Has the rift experienced unidirectional E–W or W–E propagation, a synchronous initiation or a complex opening history?
4. How do offshore syn–rift stratigraphic patterns evolve with time? Can the same patterns also be observed in the onshore record and what does it mean for evolutionary scenarios?
5. How does the long term total extension across the rift compare with short term geodetic rates? Do they suggest changes in strain localisation over time?

In order to answer these questions a full appraisal of the geometry of rifting along and across the entire Corinth rift is required. Although many individual studies have been attempted, none so far have developed a stratigraphic framework for the rift to investigate changes in syn–rift sediment architecture, basement geometry or the history of major faults.

Chapter 3

Methodology

3.1 The multi–disciplinary approach

The thesis objectives (Chapter 1, section 1.4) are achieved using a highly multi–disciplinary approach, combining: onshore geomorphology studies; offshore seismic interpretation; and dislocation modelling methods to study the entire Corinth rift as a complete tectonic system. In this chapter these methods are introduced.

3.1.1 Onshore geomorphology investigation

Onshore, a thorough field investigation of the tectonics of the poorly explored northern margin of the Corinth rift from Antirrio in the west to Porto–Germeno in the East, has been conducted (Chapter 4). Coastline movements in this area are studied through the identification of indicators of recent relative base level change (described in detail in Chapter 4, section 4.2). This work follows extensive similar investigations along the southern margin where uplifted notches, benches, terraces and marine organisms have been identified, and in some cases dated. Along the northern coastline these same methods are applied in this study including the investigation of more subtle subsided features.

3.1.2 Multichannel seismic reflection interpretation

In order to investigate variations in fault–controlled sediment deposition the stratigraphic framework of the Corinth rift has been established using seismic facies parameters and seismic interpretation principles described by Vail et al. (1977) and Brown & Fisher (1980). Seismic interpretation of digital SEGY data has been performed using the Seismic Micro–Technologies **KINGDOM Softwear 2d/3dPAK**. Paper–copy only seismic profiles have been interpreted by hand on paper and interpretations digitised to be combined with digital data in a **Fledermaus** 3D visualisation

environment. 3D horizon surfaces and sediment isopachs have been interpolated from 2D seismic data through a combination of **Generic Mapping Tools (GMT)** (Wessel & Smith 1995) gridding algorithms and hand contouring. Sediment surfaces and multibeam bathymetry have been visualised using **ArcGIS** and **Fledermaus**.

3.1.3 Dislocation modelling

Elastic and viscoelastic dislocation modelling are used to determine slip rates from long term deformation patterns. These methods are described in detail in Chapter 8. Elastic codes follow the Okada (1985) formulation and have been provided as the MATLAB program **disloc3d** by the COMET group, University of Oxford (P. England pers. comm. 2005). Viscoelastic modelling uses the Fortran **V3FASAT** code written and supplied by Y. Fukahata, University of Tokyo.

3.2 Datasets

In this study newly acquired seismic reflection profiles and swath bathymetry from the western Corinth rift (*primary data*) have been combined with higher resolution versions of partially published datasets (*secondary data*). These have also been integrated with all known published Corinth rift seismic profiles to achieve better coverage over the entire offshore rift (Fig. 3.1 and Plate 1, in the sleeve at the back of the thesis).

3.2.1 Primary seismic reflection and multibeam bathymetry data

The primary, new data, examined in this thesis are a suite of high resolution multichannel seismic (MCS) reflection profiles and multibeam swath bathymetry, from the western Corinth rift collected by MV Vasilios in July 2003 under the direction of the Universities of Southampton, Patras, and Leeds (McNeill et al. 2005a). Seismic reflection data were collected using a 150 – 2000 Hz sparker source and a 60 channel, 1 m group spacing streamer. Ten N – S profiles were acquired across the rift, with an average length of 12 km with a 3 km spacing; together with a 40 km E – W tie line (Fig. 3.1, Plate 1). Penetration down to 1 to 1.5 s two way travel time (TWTT) allowed basement imaging, except in the deepest parts of the basin. Swath bathymetry coverage in the western rift was collected using a Reson Seabat 8160 50 kHz multibeam echo sounder. Further details of the processing of seismic and bathymetry data can be found in Cotterill (2006) and the entire dataset is shown on Plates 2.1 to 2.2.

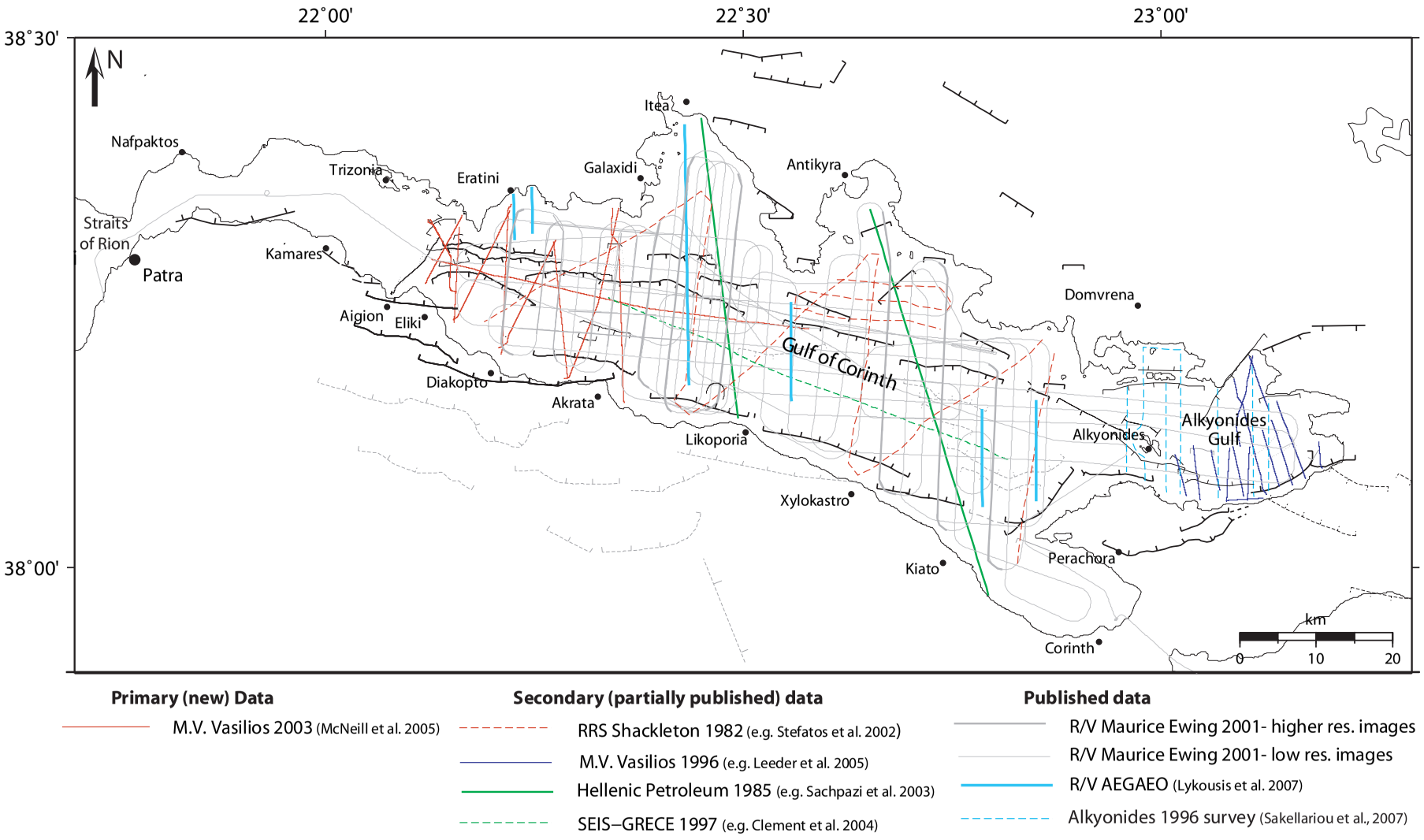

FIGURE 3.1: Summary of the seismic reflection profiles interpreted in this study.

3.2.2 Secondary seismic reflection and multibeam bathymetry data

Other seismic reflection and swath bathymetry datasets have been compiled together with the high resolution western Gulf data to obtain better coverage of tectonic structures across the whole rift. These data are summarised in Figure 3.1. A larger version of this figure, together with bathymetry and interpreted offshore faults, can be found on Plate 1. Below, other datasets are described that have been available for use in this project (partially or fully published), supplied by colleagues also working in the Corinth rift.

RRS. Shackleton 1982

Seismic data and line interpretations from the 1982 RRS. Shackleton cruise which cover the central rift in SW–NE and N–S transects, have been published by Brooks & Ferentinos (1984), Higgs (1988) and Stefatos et al. (2002). Profiles have been acquired using a single–channel air–gun, with imaging to a maximum two–way travel time (TWTT) of 2 s. Collaboration with A. Stefatos and G. Ferentinos of the University of Patras have allowed access to six of these central rift profiles, and also an E–W survey to the south of Antikyra Bay for use in this project. These data provide coverage of the detailed shallow stratigraphy in the central rift and allow interpretations from the western rift to be extended eastward.

M.V. Vasilios 1996

The M.V. Vasillios cruise of 1996 focused on the acquisition of single–channel sparker and pinger seismic profiles from the Alkyonides Gulf, with a maximum penetration depth of 0.85 s two way travel time. Results from these data have been presented by Collier et al. (2000), Leeder et al. (2002) and Leeder et al. (2005). Access to this dataset for use in this project (in the form of A0 paper copies of profiles), has been provided by M. Leeder, University of East Anglia. Track lines are shown in Fig. 3.1 and Plate 1.

Hellenic Petroleum lines 1985

Two maxipulse explosive source multichannel seismic profiles, shot by Hellenic Petroleum in 1985, crossing the central Gulf of Corinth have been reprocessed by Clement (2000) and are also presented in Sachpazi et al. (2003), Moretti et al. (2003) and Clement et al. (2004). These lines are much deeper than any of the other academically published data, imaging to a depth of 6 s, clearly imaging basement even in the deepest parts of the rift. Larger time–scale paper copies of these data have been provided for use in this study by A. Hirn, Institut de Physique du Globe de Paris.

SEIS–GRECE 1997

The SEIS–GRECE 1997 study was primarily a wide–angle refraction study, however, some multichannel seismic data were shot. Due to the long streamer, only one line crossing the Gulf of Corinth east to west was successful, imaging to a depth of 4 s. This profile is presented in Clement (2000) and Sachpazi et al. (2003), and provides a unique image of the along axis changes in basement depth and sediment architecture. A larger scale paper copy of this profile has been provided by A. Hirn, Institut de Physique du Globe de Paris.

3.2.3 Published or publicly available datasets

In addition to the partially or fully published datasets described above, the interpretation of all published seismic profiles have been added to the compilation in order to further increase coverage (Fig. 3.1 and Plate 1).

The RV Maurice Ewing conducted an extensive multichannel air–gun survey of the Corinth rift in 2001. Seismic imaging down to 6 s was possible across the entire rift, providing depth to basement everywhere. Unfortunately, very little of these data have yet been published. Some profiles have been presented by Goodliffe et al. (2003) and Zelt et al. (2004) and these provide important constraints on basement depth used in this study (Fig. 3.1 and Plate 1). In addition, low resolution images of the entire survey may be found at the University of Texas, Marine Science Data Center (http://www.ig.utexas.edu/sdc/). These images provide additional control on basement depth and sediment thickness at a broad scale.

Lykousis et al. (2007) present a number of N–S seismic reflection profiles, with a maximum imaging depth of 1.8 s, from across the rift. These lines provide additional control on shallow stratigraphic interpretation. Additionally, Sakellariou et al. (2007) publish a number of profiles in the Alkyonides Gulf, with maximum depth of 0.9 s (Fig. 3.1 and Plate 1).

Chapter 4

Tectonic geomorphology of the Corinth rift coastline

4.1 Introduction

4.1.1 Normal faulting and land movement

The competition between tectonic and surface processes is responsible for the geomorphology of the Earth's surface. Normal faulting results in a component of uplift and a component of subsidence, and land will rise up or down depending on where in the deformation field it lies. The coastline is a very good indicator of uplift or subsidence, as sea level is a linear base level marker. Many techniques exist for assessing the rates of vertical crustal movements on near–coastal faults, including the identification and dating of: the displacement of shoreline markers; disturbance of in–situ marine organisms from their usual habitation depth and the vertical shifting of man–made structures.

Studies of coastline movements in tectonically active areas are important in order to assess the current activity of faults that are often offshore and not directly visible. Coastal movements may also be used as constraints in dislocation modelling to assess the total slip that has occurred on an individual fault or on a multi–fault system (e.g. Hubert et al. 1996, Stiros et al. 2007).

The purpose of the following review of Corinth south coast vertical movements and the collection of new observations from the northern margin is primarily to determine which parts of the Corinth coastline are tectonically influenced and the locations of active faults. The observations presented in this chapter will be used in the dislocation modelling in Chapter 8 in order to test multi-fault scenarios that can reproduce the observed coastal movements.

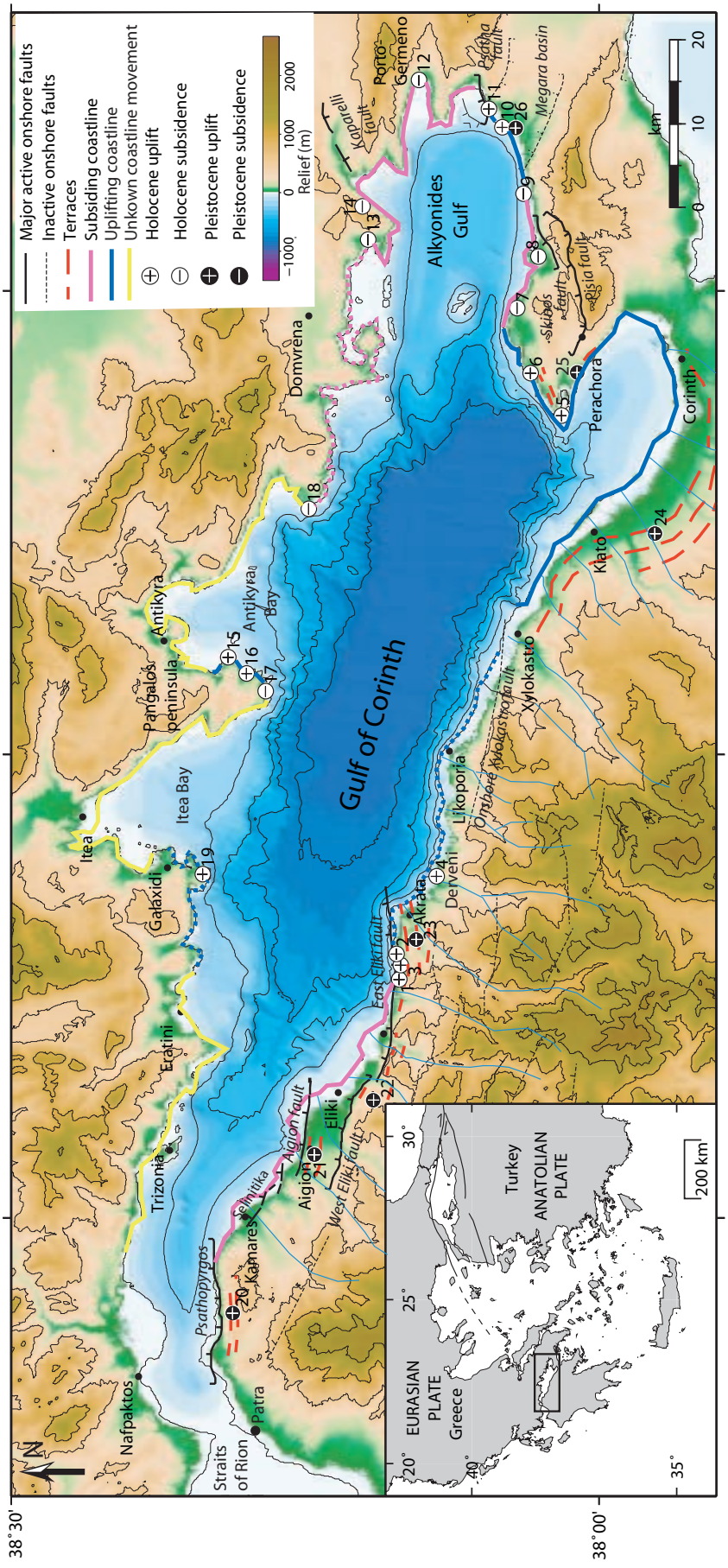

FIGURE 4.1: Summary of the tectonic vertical motions along the coastline around the Corinth rift. Numbered sites are discussed in text. Onshore vertical movements follow Leeder et al. (submitted).

4.1.2 Movement of the Corinth rift coastline

The southern coastline mostly lies in the immediate footwall (or in some cases hanging wall) of en–echelon N–dipping faults, and shows evidence of recent tectonic movement and a history of older uplift on now inactive faults (Fig. 4.1). The proximal location of the coastline relative to fault traces, the hard limestone lithology, and the richness of datable marine fauna has resulted in a vast number of publications and a detailed knowledge of coastline movements. These studies are reviewed in section 4.4, and in Figure 4.1.

The northern margin, by contrast, has traditionally been assumed to be subsiding along its entire length (e.g., Stefatos et al. 2002). This is supported by the sinuous trace of the coastline, lack of young marine sediments, and more subdued topography when compared to the Peloponnese, thought to be caused by landscape drowning under the influence of N–dipping faults on the southern margin (Fig. 4.1). However, there are areas on the north coast that are locally very linear and could be fault controlled (e.g., sections of the coastline south of Domvrena and Galaxidi, Fig. 4.1). Although the dramatic morphology of the southern margin points toward its relative dominance in terms of uplift, the northern margin may show local uplift. Assessments of the current fault activity affecting the north coast in general, are limited in comparison with the south coast. This inequality in the study of the two regions may be due to the lower accessibility of the northern margin (the area is much less populated with few concrete roads) and the fact that a large part of the north-western margin is composed of easily erodible flysch (Piper 2006). Also, offshore faults may be further from the coastline and any uplift component will be small compared to that on the south coast.

Field studies have been conducted in October 2004 and March 2005 by R. Bell, L. McNeill, and A. Micallef, to investigate the character of the northern margin. The objective was to confirm if subsidence is occurring along the entire length of the northern margin, from Porto-Germeno in the east to Nafpaktos in the west (Fig. 4.1) or if there are localised areas of stability or uplift.

4.2 Deformation Indicators

In order to investigate the tectonic processes that have occurred along a stretch of coastline, features must be identified that have been displaced upwards (uplifted) or downwards (subsided). Such features have been named *Geomorphic Markers* by Burbank & Anderson (2001), and provide a reference frame from which deformation can be determined.

Geomorphic markers are often sea level indicators and are used to identify movement away from the height of the mean paleo sea surface. The measure, however, is a relative one as the apparent movement of geomorphic markers may be caused by

both eustatic or regional sea level change and tectonic movement. Tectonic uplift and sea level fall result in upward relative movements of the marker from the paleo sea surface (negative base level movement), and both tectonic subsidence and sea level rise create a downward relative displacement (positive base level movement). Only with a detailed knowledge of absolute sea level change can the true tectonic signature be revealed.

4.2.1 Relative sea level fall: Tectonic uplift or absolute sea level fall indicators

Tectonic uplift and/or sea level fall often create very obvious geomorphic markers which can be preserved for a long time. There are two major classes of negative base level movement proxy;

- 1) Erosional features such as wavecut notches and marine terraces
- 2) Depositional features such as marine organisms, beach rock and constructional marine terraces

Wavecut notches, benches and terraces

Wavecut notches are the most precise indicators of rates of uplift, if datable material is available (Burbank & Anderson 2001). Physical and biological processes are strongly focused at the air–sea–land interface. Bioerosion, chemical erosion, and wave impact result in loosening and plucking away of bedrock fragments, resulting in a 'nick' in the cliff which develops into the feature known as a wavecut notch (Fig. 4.2).

Wavecut notches form very close to sea level in quiet conditions. In more turbulent areas with a large tidal range, the level of deepest cut may be up to 2 m above sea level (Kershaw & Guo 2001). The width of marine notches increases gradually above the notch floor to the most convex part of the notch known as a 'vertex', which is the level that best approximates mean sea level (Fig 4.2, Pirazzoli 1986). From this point, the width of the notch decreases upwards to the top of the notch, forming the notch roof at high tide level (Fig. 4.2). Wavecut notches are produced at times of relative sea level stillstand when the same level is maintained for a long period of time. If, subsequently, the uplift of land (e.g., due to fault movement) exceeds sea level rise, notches may be preserved above sea level and a new notch forms at sea level. Multiple notches are therefore convincing evidence of sustained coastal uplift with fluctuating sea level. Bioerosion and wave action deepen wavecut notches and may lead to instability of the above cliff followed by mass movement. The failure of this material leads to the formation of a wavecut platform as the sea cliff retreats (Fig. 4.2). If uplift rates exceed sea level variation, these wavecut platforms can emerge and appear as sub–horizontal flat–topped benches in the landscape.

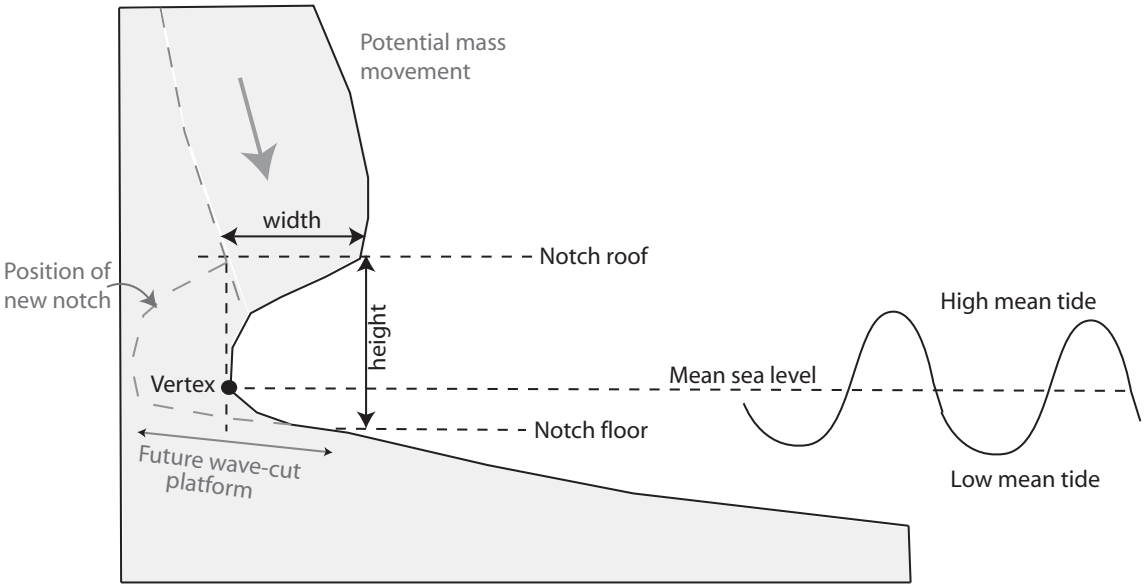

FIGURE 4.2: Sketch diagram of the morphology of wavecut notches and terminology used in this study.

Along many tectonically uplifting coasts, flights of marine terraces provide evidence for negative movements of base level: relative sea level fall. Coastal terraces are broad flat areas, which form when sea level remains constant with respect to land for periods of 1000 years or more. There are two main classes of marine terrace, erosional and constructional. Erosional terraces are formed by wave erosion driving a sea–cliff landward. The inner edge represents the base of the former sea cliff and can be used as a proxy for sea level (Burbank & Anderson 2001, McNeill & Collier 2004). Constructional marine terraces can occur if relative sea level is stable, and waters are warm and clear, so coral and algae deposits build up. Depositional terraces may also occur by progradation of deltas resulting in a gently seaward dipping surface and topography across the paleo delta parallel to the paleo coastline. In these constructional cases the outer terrace edge is a more realistic indication of paleo mean sea level (McNeill & Collier 2004).

If uplift rates exceed sea level rise, marine terraces can emerge, but the record of terrace uplift is often fragmentary due to poor terrace preservation (McNeill & Collier 2004). Younger terraces can reoccupy or erode older ones so large parts of the record may be lost (Anderson et al. 1999). A staircase of rising marine terraces records uplift in the geological record. Ideally, each terrace level would be dated in order to determine variability of uplift rates. Where datable material is scarce the sequence of terraces can be correlated with sea level fluctuations for a range of probable uplift rates (constrained by available chronology) and used to estimate the age of each terrace.

FIGURE 4.3: In–situ *L. lithophaga* that has bored into limestone. Photo from www.wooster.edu/ geology/Bioerosion.

Depositional indicators

The presence of in–situ marine material, for example intertidal organisms in life position or beach rock above sea level, is a clear indication of relative sea level fall. Beach rock deposits are simply rocks formed of cemented beach sediments, such as well-rounded pebbles and shells. Their presence above the normal tidal range is an indicator of negative base level change.

Two species of intertidal marine organism in particular are very useful in the Corinth rift region. *Lithophaga lithophaga* is a species of bivalve that occurs along the Mediterranean, Red Sea, and the Atlantic Ocean coasts (El-Menif et al. 2007). These bivalves can live in depths of up to 30 m but the densest populations lie within 1 m of the sea surface. They are a species of bivalve that use acid (agglutinant substances) to bore into limestone (lithophaga means 'which eats stone', Fig. 4.3). *L. lithophaga* is a shade–loving organism, and can burrow up to 20 cm into rock (www.mnhn.fr/mnhn/bimm/Protection/fr/Especes). The cone shaped bore holes produced by these bivalves, and sometimes the bivalve itself, can become uplifted and preserved far above mean sea level by relative base level fall. Approximate mean sea level is marked by the shallowest occurrence of *L. lithophaga*.

The coral *Cladocora caespitosa* occurs throughout the Mediterranean, and has been used to date terraces along the south coast of the Corinth rift. It lives in water depths of 1 – 20 m (McNeill & Collier 2004). It has been suggested that *C. caespitosa* fossils are more abundant in middle–late Pleistocene deposits than they are today, possibly related to climate change (Peirano et al. 2004).

4.2.2 Relative sea level rise: Tectonic subsidence or absolute sea level rise indicators

Indicators of tectonic subsidence or sea level rise are much harder to identify as they will be submerged features. In some areas of Greece and other localities around the Mediterranean apparent subsidence of archaeological structures has been interpreted to imply tectonic subsidence. One such example is the submergence of the harbour of Kenchreai, which was once the port of ancient Corinth on the Saronic Gulf and the site of a major Roman cemetery (Stiros 2001). Submerged wavecut notches, platforms and beach rock are other evidence for relative sea level rise. As well as being water covered, encrusting organisms and sedimentation make these features, which are obvious to see above water, difficult to detect when submerged.

4.3 Northern margin field study methodology

Coastal localities along the northern margin were accessed by road and on foot in order to identify any of the geomorphic indicators described above to provide evidence for the nature of coastline movement. This is challenging given the poor accessibility of certain areas of the coastline, for example, the eastern side of Antikyra bay and western side of the Pangalos peninsula (Fig. 4.1). In order to explore some of the more inaccessible areas and obtain a continuous view of portions of the coastline, small fishing vessels were hired locally from Antikyra and Galaxidi to supplement road access (east of Pangalos peninsula, south of Galaxidi, and to the east of Antikyra Bay (Section 4.5.2)). Unfortunately, some areas (notably the western side of the Panaglos peninsula) remain unexplored to date.

The key observations made in the northern margin study were the changing character of wavecut notches observed along the coastline and evidence of uplifted wavecut platforms. Measurements of the notch vertex and roof above sea level were recorded, together with the 'height' between notch roof and notch floor. The time of day that measurements were made was also recorded. The tidal range in the Mediterranean is low, generally not more than ∼40 cm (Tsimplis et al. 1995). However, given potential notch heights of generally less than 2 m it is still important to consider the tidal state at the time of notch measurement, in order to assess if notches have been uplifted or if they just appear high above sea level because they were measured at low tide. Tidal correction estimates have been applied to measurements using tidal data from the Galaxidi and Corinth tidal stations, accessed through Easy Tide, www.easytide.ukho.gov.uk.

4.4 Review of tectonic movement along the southern Corinth coastline

4.4.1 Holocene uplift

Holocene uplift in the Corinth rift is recorded by uplifted wavecut notches and uplifted marine organisms. The marine bivalve *L. lithophaga* occurs along the southern margin of the Corinth rift, providing material for radiocarbon dating in order to quantify uplift. Uplift evidence near Diakofto and Paralia Platanou in the footwall of the East Eliki fault is well studied, due to the richness of marine organisms 10 – 15 m above sea level and multiple notched levels (e.g. Stewart & Vita-Finzi 1996, Stewart 1996, Pirazzoli et al. 2004, points 1 and 2 respectively on Figs. 4.1 and 4.4). Uplift rates show a relatively linear trend up to a present–day elevation of 6 m. At Diakofto, uplift rates of 0.9 – 1.5 mm/yr are estimated and 0.8 – 2.1 mm/yr at Paralia Platanou (Fig. 4.4, Stewart & Vita-Finzi 1996, Stewart 1996). These two sites provide an average uplift rate for the East Eliki footwall of ∼1.5 mm/yr over the last ∼3 ka. The elevation of radiocarbon dated shell material from a beach pebble conglomerate in the Ladopotamas fan, close to the East Eliki fault plane, suggest a similar uplift rate of 1.4 – 2.0 mm/yr averaged over the last ∼4 ka (McNeill & Collier 2004, point 3, Figs. 4.1 and 4.4).

At Aegira (also known as Mavra Litharia), notch levels and dated marine organisms suggest slightly higher rates of 1.3 – 2.2 mm/yr in the footwall of the offshore Derveni fault (Stewart & Vita-Finzi 1996, Stewart 1996, Pirazzoli et al. 2004, point 4 on Figs. 4.1 and 4.4).

Along the Perachora peninsula e.g., at Heraion and Mylokopi (Points 5 and 6 respectively on Figs. 4.1 and 4.4), notched levels and dated *L. lithophaga* suggest consistent uplift rates of ∼0.5 – 0.7 mm/yr over the last 6.4 ka (Pirazzoli et al. 1994, Kershaw & Guo 2001). At locations 7, 8, and 9 (Fig. 4.1), submergence of the shoreline followed the 1981 sequence of earthquakes (Jackson et al. 1982, Vita-Finzi & King 1985). Further east along the coastline at locations 10 and 11 (Fig. 4.1), uplift caused by the 1981 earthquakes occurred in the footwall of the Psatha fault (Jackson et al. 1982, Vita-Finzi & King 1985). At Psatha, notched levels record a Holocene uplift rate of 0.3 mm/yr (Leeder et al. 1991).

Figure 4.4 shows the Holocene uplift rates along the Corinth rift axis. However, care must be taken in directly comparing these measurements as they have been estimated using a number of different eustatic or regional sea level curves (e.g., Flemming 1978, Imbrie et al. 1984). The choice of sea level curve will affect the amount of vertical displacement that is attributed to tectonics.

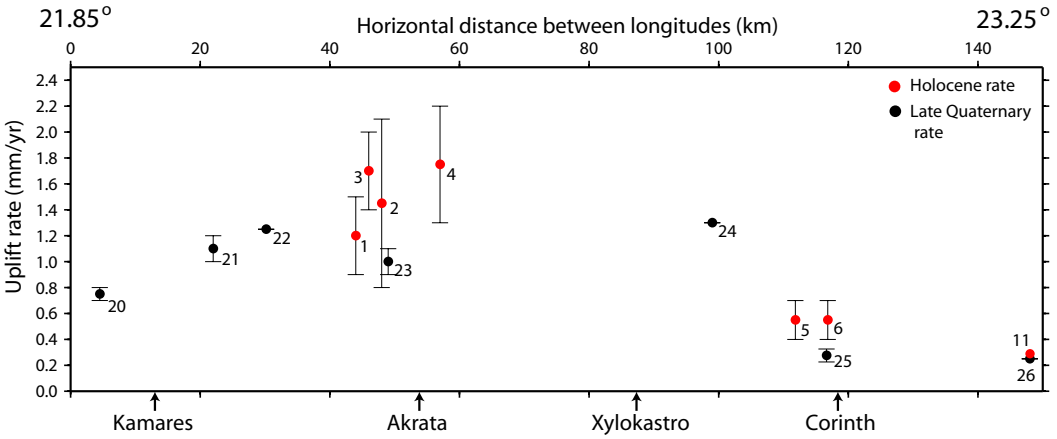

FIGURE 4.4: Holocene and late Quaternary averaged uplift rates along the southern margin, from 21.85° to 23.35°. Locations of numbered points are shown in Figure 4.1 and discussed in text.

4.4.2 Late Quaternary uplift

Continued late Quaternary uplift is demonstrated by high south coast topography, flights of marine terraces, and uplifted Gilbert fan deltas. Uplifted marine terraces are well preserved in the eastern part of the Gulf (east of Derveni, Fig. 4.1), and are less well preserved in the west. They record a history of at least 400,000 years of Late Quaternary uplift in the area (Kerauden & Sorel 1987, Armijo et al. 1996, McNeill & Collier 2004). Kerauden & Sorel (1987) identify marine terraces between Corinth and Xylokastro (Fig. 4.1). Correlation of the altitude of terraces with the age of marine highstands (Imbrie et al. 1984), suggests that the oldest terrace is ∼450 ka (Kerauden & Sorel 1987). Armijo et al. (1996) map terrace levels from 10 to 400 m, 2 – 20 km from the Xylokastro fault plane, in the same area. They deduce uplift rates of ∼1.3 mm/yr at the Xylokastro fault plane from dated material and sea level correlation (point 24 on Figs. 4.1 and 4.4).

McNeill & Collier (2004) identify nine discontinuous terrace levels in the footwall of the East and West Eliki faults (Fig. 4.1). From dated Pleistocene corals and correlation to eustatic sea level highstands, an uplift rate of ∼1 mm/yr is estimated for the East Eliki fault. Uplift rates from terraces in the footwall of the West Eliki fault are slightly higher at ∼1.25 mm/yr (De Martini et al. 2004, Figs. 4.1 and 4.4, point 22). De Martini et al. (2004) also identify seven terraces in the footwall of the Aigion fault, recording uplift rates of ∼1.05 – 1.2 mm/yr (point 21 on Figs. 4.1 and 4.4). In the westernmost Gulf of Corinth, Houghton et al. (2003) have suggested an uplift rate on the Psathopyrgos fault of ∼0.7 – 0.8 mm/yr (point 20 on Figs. 4.1 and 4.4), although this may be an underestimate (P. De Martini, pers. comm. 2007).

From Perachora to Alepochori, late Quaternary averaged uplift rates are consistently ∼0.2 – 0.3 mm/yr (points 25 and 26 Leeder et al. 1991, Dia et al. 1997, Leeder et al. 2003, 2005).

4.4.3 Uplift rate trends

Comparison of Holocene and late Quaternary averaged uplift rates along the southern Corinth margin (Fig. 4.4) highlight two clear trends (also see Fig. 13 in McNeill & Collier 2004). Firstly, the uplift rate is not consistent along the southern margin. The Alkyonides Gulf is associated with much lower uplift rates than are observed in the Gulf of Corinth, where the rates are up to 4 times greater. Although there is a lack of uplift information between Xylokastro and Derveni, it appears that uplift rates in the central part of the rift are relatively consistent, around ∼1.0 – 1.3 mm/yr, when averaged over the late Quaternary. Toward the western rift, uplift rates decrease to ∼0.7 – 0.8 mm/yr (Fig. 4.4), although much higher estimates up to ∼1.5 mm/yr have been suggested in the same area (P. De Martini 2007 pers. comm.). Holocene uplift rates are greater than rates averaged over the late Quaternary along the south coast (Fig. 4.4), suggesting a recent increase in tectonic activity (McNeill & Collier 2004).

4.5 Tectonic movement of the northern coastline

In this section observations from new field studies investigating neotectonic activity along the northern coastline are presented. For clarity, the observations have been geographically grouped into areas that show similar vertical coastline movement trends.

4.5.1 Alkyonides Gulf: Porto Germeno to Kiriaki

The northern coastline of the Alkyonides Gulf (Fig. 4.5) shows many features characteristic of drowned topography, including: shallowly submerged archaeological ruins; multiple submerged notches; and submerged beach rock.

Submerged archaeological remains

Porto Germeno (Fig. 4.5) at the eastern extremity of the Alkyonides Gulf, lies to the south of the Kaparelli fault which ruptured in 1981 (Jackson et al. 1982). The town is famous for being the site of the ancient city of Aegosthena (also Egosthena) that consisted of a fortified citadel connected to the sea by two fortification walls, thought to date back to 343 BC (Obar 1987). The citadel was defended by eight artillery towers incorporated into the perimeter wall and the northern wall is the most well preserved. At the modern coastline, the remains of this wall consist of four stacked blocks of conglomerate (Fig. 4.6 A). The lowest block is submerged by 40 cm at low tide and current marine influence is observed up to a height of 60 cm above low tide level from the presence of live limpets. Some clearly in–situ foundation blocks form rectangular units measuring 4 m x 2 m and can be recognised onshore and offshore

FIGURE 4.5: Satellite image of the Alkyonides Gulf area and localities discussed in this study (from Google Earth). Archaeological sites: 1=Fort of Aegosthena, 2=Fort of Siphai, 3= Aghious Vasilios. Notches discussed in text: 4, 5=Paralia Sarandi, 6=Ag. Ionnis.

with their interiors filled by rubble. The wall section of the ruin and the rectangular units can be observed for a distance of at least 5 m away from the coastline below sea level.

The blocks seen at the coastline are believed to be the remains of the final tower of the northern wall, where now only the foundations are observed underwater (Obar 1987, Fig. 4.6 B and C). The submergence of the remains has two possible explanations: 1) The tower structure, and western end of the wall, were intentionally built partly below sea level as a jetty type structure; or 2) the structures were originally built above sea level and have since been submerged by tectonic subsidence. The similarity in morphology of these ruins to the submerged Kerchreai harbour (Mourtzas & Marinos 2004) is good evidence for the Aegosthena offshore ruins also being submerged harbour structures. The Aegosthena submerged blocks have previously been used as evidence for subsidence by Vita-Finzi & King (1985), who report that there has been a ∼1.5 m relative sea level rise since the fourth century BC. This leads to an estimated subsidence rate of ∼0.7 mm/yr (Westaway 1996). However, Vita-Finzi & King (1985) do not mention the original elevation of the harbour structures used in their measurement of relative sea level rise. Therefore their estimate cannot be confirmed or supported by the measurements made in this study.

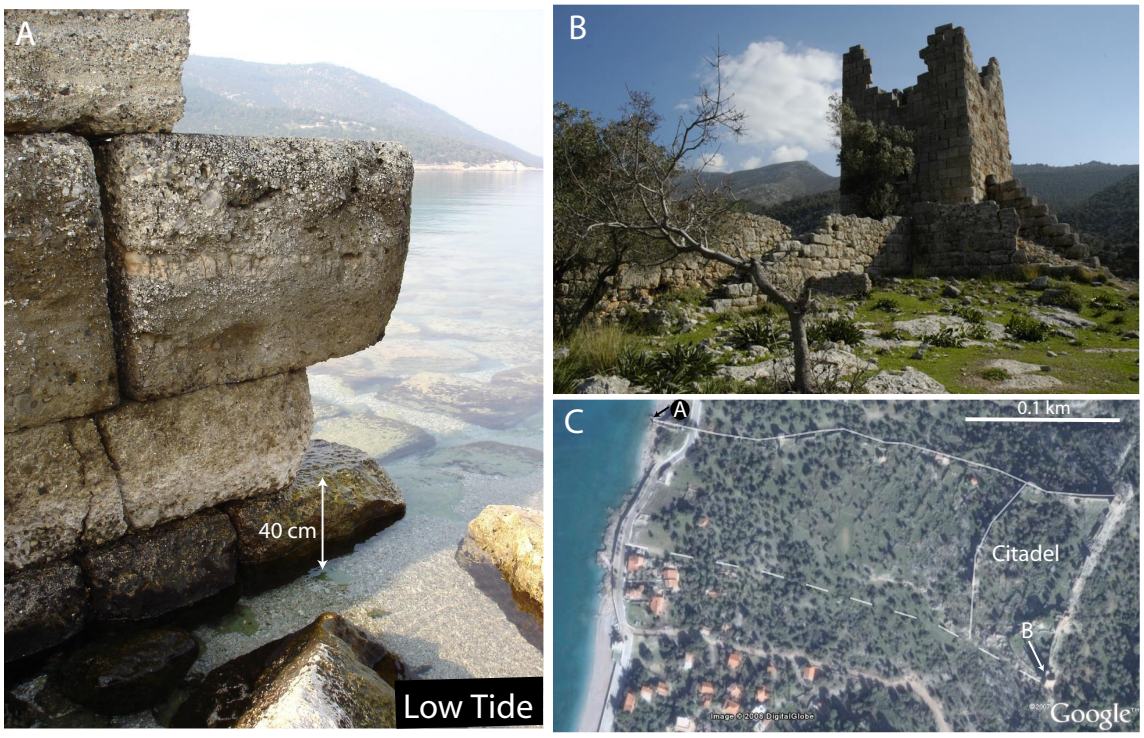

FIGURE 4.6: **A.** Blocks forming part of the submerged remains of the northern wall of the Aegosthena 4th century fortress. **B.** Well preserved SE artillery tower of the Aegosthena fortification. **C.** Site map of the fort of Aegosthena over the image of the site today (from Google Earth). White lines show the interpreted position of the perimeter walls of the fortress. Positions of photos A and B are indicated. (site map and photo B from J.M. Harrington http://en.wikipedia.org/wiki/Image:Aigosthena-plan.jpg)

Very similar ruins are also observed at Aliki, further to the west in Domvrena bay (Figs. 4.5 and 4.7). A coherent wall–like structure extends into the sea, and appears to be the continuation of an inland wall now bisected by a road (Fig. 4.7 A, B and C). To the south of this wall, submerged foundation blocks outline 5 m x 5 m rectangular units, for a distance of 50 m along the beach. The tops of these foundation blocks are 20 – 25 cm below low tide sea level. Toward the eastern end of the submerged ruins, a beach platform lies 25 cm below mean sea level also suggesting subsidence.

These ruins belong to the ancient fortification of Siphai (Obar 1987), thought to date from 371–362 BC. They consist of the remains of two catapult towers and a sea–gate tower, probably once connected to the offshore wall (Fig. 4.7 B). However, no mention of the original purpose of the rectangular submerged foundation blocks can be found in the literature. Vita-Finzi & King (1985) suggest that the coastal remains of Siphai have subsided by ∼2.0 m beneath the sea since the 4th century BC, leading to a subsidence rate estimate of ∼0.8 mm/yr (Westaway 1996). Again, without a knowledge of the assumed initial elevation of the structures this estimation can not be confirmed by this study.

Similar, partly submerged archaeological remains have been reported by Stiros et al.

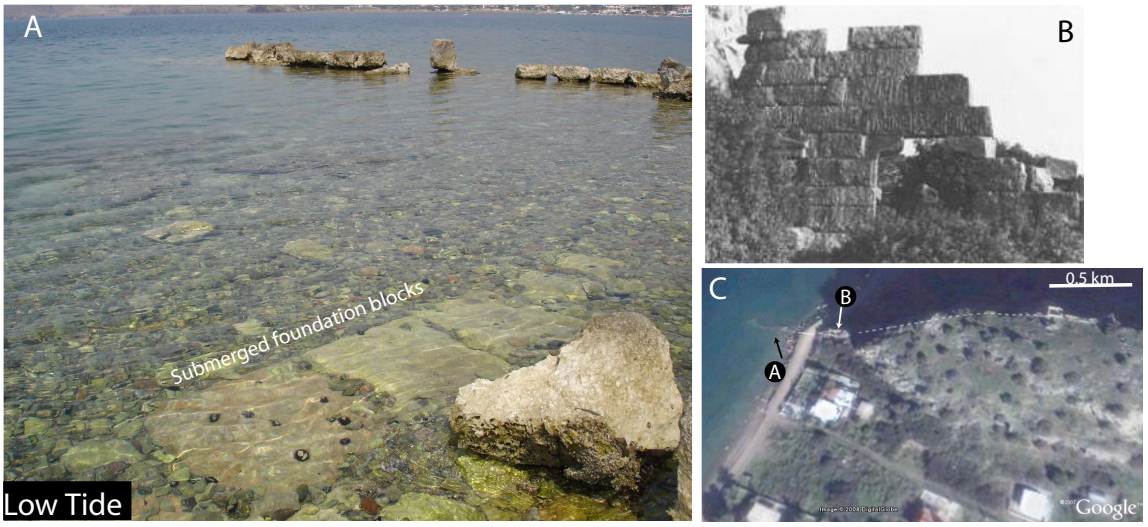

FIGURE 4.7: **A.** Submerged remains in Aliki harbour, **B.** The remains of the sea–gate tower of the fort of Siphai (from Obar 1987), **C.** Site map of the fort of Siphai (from Google Earth) showing the locations of Photos A and B.

(2007) in the Aghious Vasilios Bay area (between Aliki and Porto Germeno in the hanging wall of the Kaparelli fault), which they suggest are ca. 2000 years old (Fig. 4.5). These authors propose that during and following the 1981 earthquakes, about 1 m of this beach was lost and the archaeological remains were submerged further.

Submerged multiple notches

Most of the coastline of the north Alkyonides Gulf is composed of either basement limestone or old fan conglomerate which have effectively preserved modern marine notches. On the southern side of the bay of Porto Germeno, wide asymmetric notches are observed in cemented conglomerate. These notches are deep, and cut up to 1 m into the rock with very flat, horizontal notch roofs that lie at high tide sea level with the vertex of the notch occurring ∼18 cm below high tide level (Fig. 4.8 A). The notch floor is highly eroded and has become colonised by sea urchins. The total notch height from roof to notch floor is ∼2 m, and the notch floor shows no evidence of multiple notching. Because the tidal range in the Mediterranean is low, generally not more than ∼40 cm, if the coastline was stable, modern notches measuring significantly greater than 40 cm from floor to base would not be expected in a relatively sheltered bay. This may suggest severe erosion of the notch floor by bioeroders at a constant base level or may mean a gradual relative base level rise (caused by tectonic subsidence or sea level rise) (Pirazzoli 1986).

At Paralia Sarandi and Ag.Ionnis (Figs. 4.5 and 4.8 B), the presence of at least two submerged notches is evidence for tectonic subsidence or sea level rise. The upper notch has a height of 50 cm, with its vertex 30 cm below mean sea level. The lower

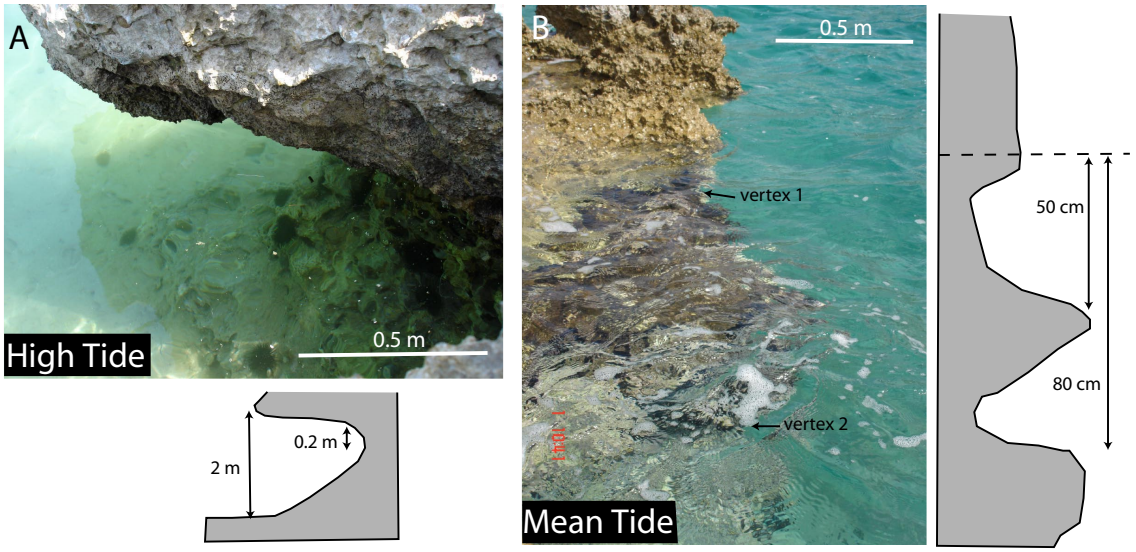

FIGURE 4.8: **A.** Notched old fan conglomerate on the south side of Porto Germeno bay. **B.** Multiple submerged notches at Paralia Sarandi. Locations shown in Fig. 4.5

.

notch floor lies approximately 80 – 120 cm below sea level. These two submerged notches are also accompanied by the presence of meteoric rillenkarren weathering markings in the limestone (Glew & Ford 1980) very close to sea level. This erosion type is significantly different to the usual pitted marine erosion patterns, and suggests these rocks have been above sea level for sufficient time to acquire this sub-aerial erosion pattern.

4.5.2 The Pangalos peninsula: Kiriaki to Itea

Between Kiriaki and Itea, prominent notches are cut into the coastal bedrock limestone (Figs. 4.1 and 4.9), however no evidence of *L. lithophaga* borings or any other uplifted organism is found. The heights of notches differ significantly along the coastline. The aim of the following study of notches in the Pangalos peninsula area is to determine if the heights of notches are indicative of relative base level change, or if they are simply modern notches controlled by the combined effects of tides and storms.

Differentiating between modern and uplifted notches

The limestone basement of the Antikyra and Pangalos peninsula coast is notched, with evidence of multiple notches in some areas. At location 1 (Fig. 4.9) two notches with vertices are observed at 10 cm and 50 cm above low tide level (Fig. 4.10 A). However, on return to this area at high tide, the 10 cm vertex notch was completely

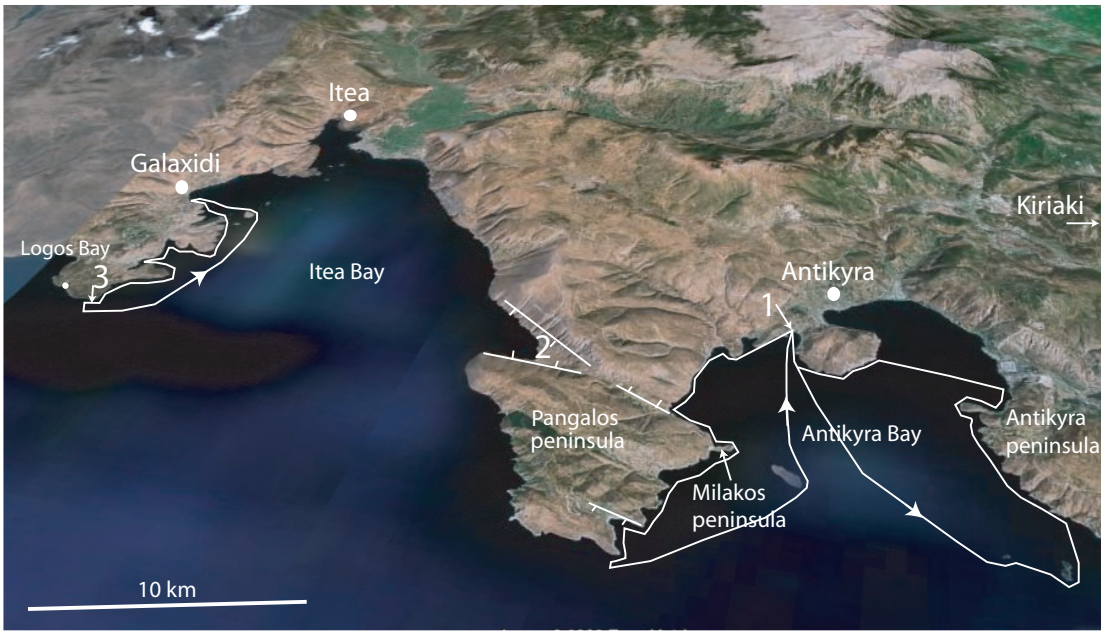

FIGURE 4.9: Satellite image of the Pangalos peninsula area (from Google Earth). White arrowed lines indicate areas covered by small fishing boat. Location 1: Position of photo 4.10; 2: the only studied area of the inaccessible western side of the Pangalos peninsula; 3: position of photo 4.14 B. Panaglos peninsula faults after Stefatos et al. (2002), Moretti et al. (2003) and this study.

submerged and the upper notch looks like a typical modern notch with its vertex only slightly above mean sea level. The two notch levels are therefore probably related to high and low tide levels and not relative sea level change. Double notches are observed elsewhere on the Pangalos peninsula, however the upper notch is always the most prominent.

In order to investigate if there is a true variation in notch height, or evidence of multiple notches related to relative sea level change along the Pangalos peninsula, notches at the coastline were examined by road access, and observed by small fishing boat along the tracks shown in Figure 4.9. Access to only one location was possible along the remote western side of the Pangalos peninsula (location 2 on Fig. 4.9). Notch vertices, notch roofs and depths were measured (from the shore) or estimated (when observed by boat) relative to sea level at the time of recording. These measurements have later been roughly corrected for tidal variation. The height of notch roofs above mean sea level are displayed as a grid in Figure 4.11. Where double notches are present the more developed upper notch is included in this grid. Notch height is believed to be a more consistent measure of notch geometry in this case, as it is more difficult to estimate the height of the vertex from the boat than the more obvious notch roof level.

Notch heights, when corrected to mean sea level, still show variation in magnitude (Fig. 4.11). This suggests a real increase in notch height around the Milakos peninsula, which extends eastward from the mid-point of the Pangalos peninsula (Fig. 4.9).

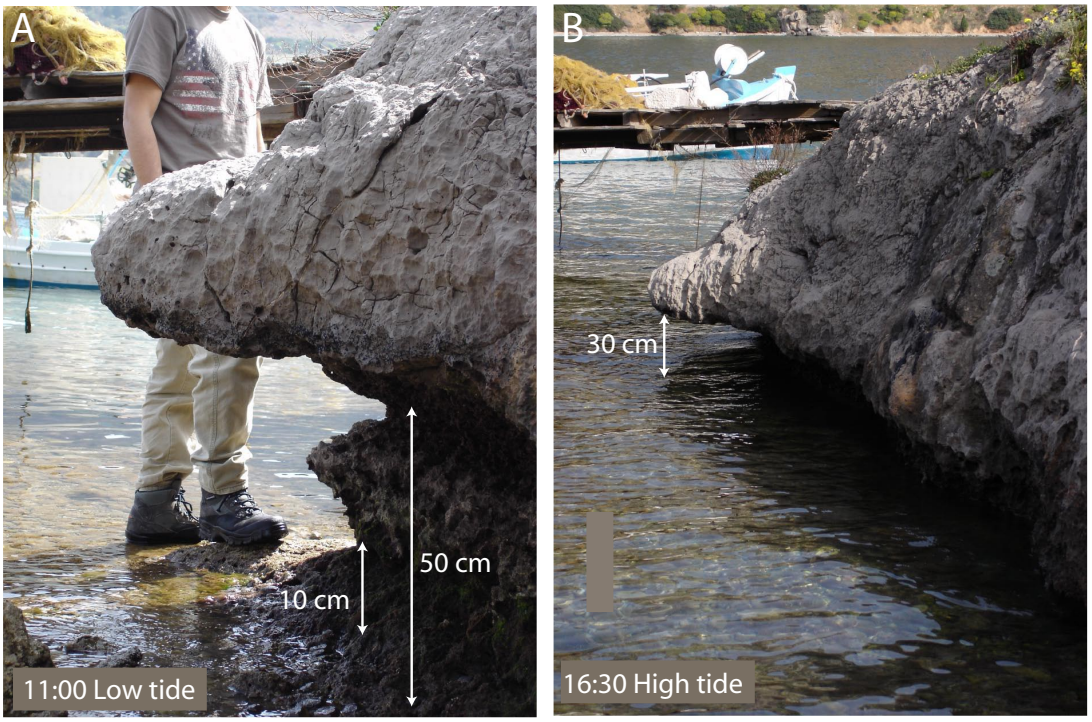

FIGURE 4.10: **A.** Two notches are observed at low tide at locality 1, Fig. 4.9, **B.** At high tide the roof of the upper notch is only 30 cm above sea level.

Notch heights less than ∼40 cm above mean sea level are common, and may be considered to be the modern notch level. Notch levels reach up to ∼150 cm above mean sea level on the Milakos peninsula, and their height is unlikely to be the result of tidal range in the Mediterranean. It is noted, however, that the prevailing wind direction makes strong waves common on the north side of the Milakos peninsula (Fig. 4.11). The location of this peninsula, in the footwalls of an onshore and offshore fault (interpreted by Moretti et al. 2003), support the possibility of tectonic uplift. If at least one of these faults was active, it would result in uplift of the peninsula (Fig. 4.11). Likely activity of these faults is discussed further in section 4.6. If this area is uplifting, the complete absence of *L. lithophaga* or evidence of any other uplifted marine organisms (except for two small barnacles on a 1.5 m high platform discussed in next section) is unusual. This absence may be due to high inputs of fresh water along some portions of the northern shoreline making conditions unfavorable for *L. lithophaga* (as suggested by J. Laborel in Stiros et al. 2007).

Possible uplifted wavecut platforms (Milakos peninsula)

The hypothesis that the Milakos peninsula is uplifting is further supported by the morphology of the coastline (Fig. 4.12). On the northern side of the Milakos peninsula, two levels of possible marine notches and abraded wavecut platforms are observed, providing strong evidence for uplift in this area (Fig. 4.12 A). Above the

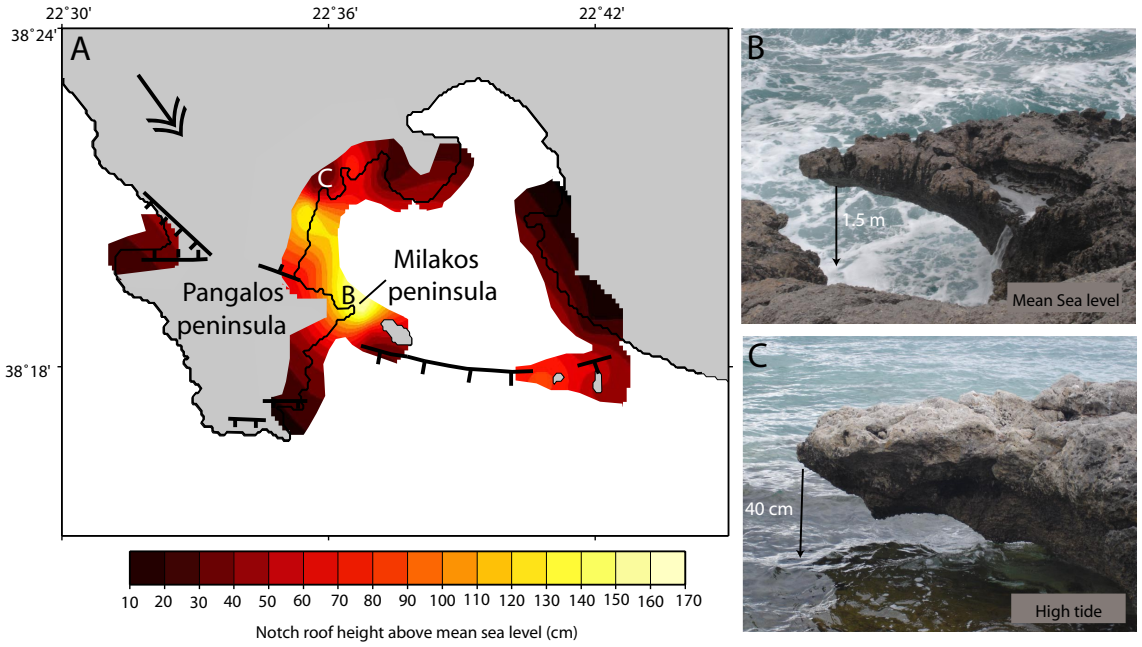

FIGURE 4.11: **A.** Grid of mean sea level notch roof height for the Pangalos peninsula and surrounding area. **B. and C.** Examples of the morphology of notches on the Pangalos peninsula. The roof of notch B is 1.5 m above mean sea level. A notch of this height suggests either tectonic uplift or high wave impact. Arrow indicates the direction of the prevailing wind direction. Onshore faults after Stefatos et al. (2002) and offshore faults from Moretti et al. (2003).

∼1.5 m interpreted modern notch discussed previously (Fig. 4.11 B) lies a planar sub–horizontal platform ∼1.5 – 2 m above sea level (Fig. 4.12 A). The smoothness of this platform may be the result of wave abrasion suggesting it has since been uplifted. Unfortunately, the only possibly datable evidence of uplift atop this platform are two small cemented barnacles which could not be prised from the rock. Their presence 1.5 – 2 m above sea level, however, is in itself strong evidence in support of uplift. The ∼1.5 m wide platform is backed by a small cliff (∼ 1 – 1.5 m high) with a notch at the cliff base, 20 cm deep and 30 cm wide. This concave depression could be a paleo wavecut notch. The highly pitted marine erosion of the limestone here, unlike the characteristic rillenkarren meteoric erosion elsewhere on the Pangalos peninsula in rocks of the same altitude, provides more evidence for an original marine setting for these features and subsequent relative sea level fall. Above the paleo cliff, a second platform exists (top right of Fig. 4.12 A). The whole Milakos peninsula is no more than 5 m above sea level and it is possible that the peninsula has been entirely uplifted due to fault activity. The similarity in morphology of the platforms and notched cliff to examples from other parts of the Corinth rift (Palyvos et al. 2007, Fig. 4.12 B,), and elsewhere (Pirazzoli 1986) provide a strong case for uplift.

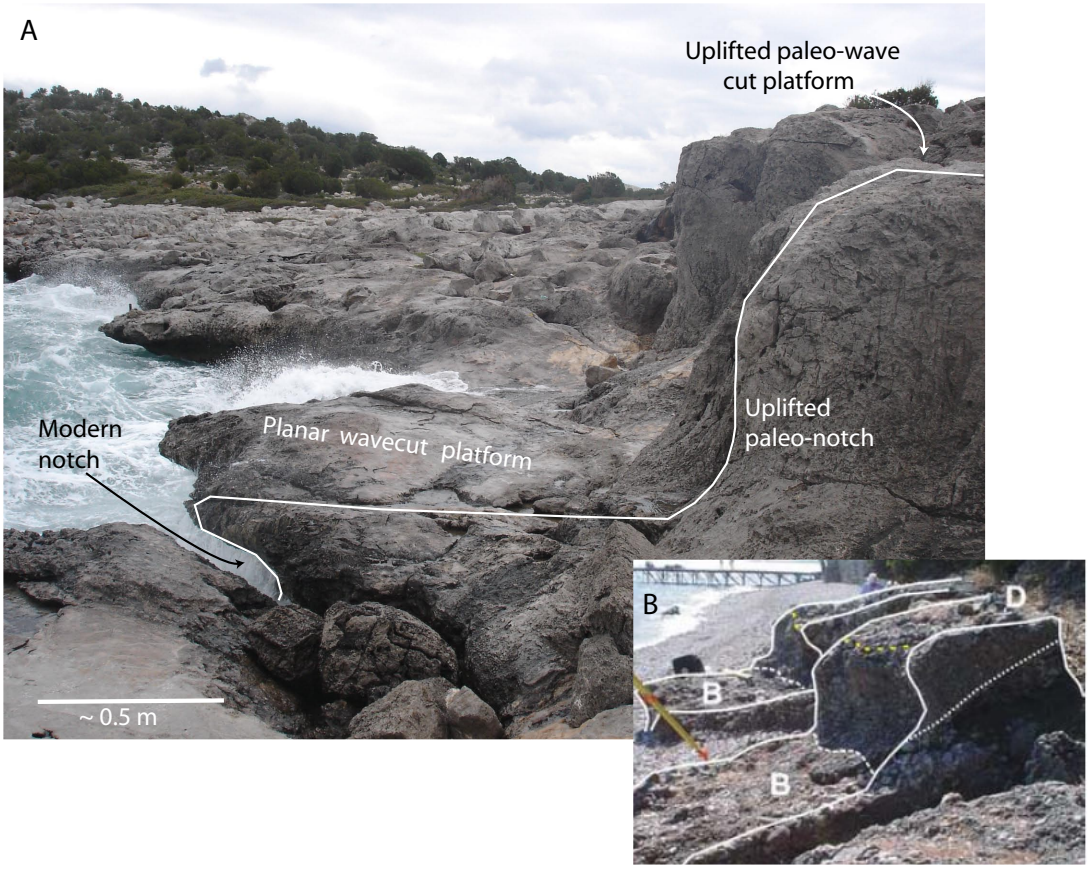

FIGURE 4.12: **A.** Possible uplifted paleo wavecut notch and wavecut platform on the Milakos peninsula, above the high modern notch level. **B.** Wavecut platforms and paleo notches from the south west Corinth shoreline showing similar geometry (Palyvos et al. 2007).

Pangalos peninsula fault activity

Several onshore faults are known to cross the Pangalos peninsula, and these have been visited during field work and have been previously discussed by Moretti et al. (2003). A N–dipping fault extending E–W along the Pangalos peninsula north of the Milakos peninsula has a strike of 100° and dip of 75° (Figs. 4.9 and 4.13). This fault surface is pitted, well vegetated, and appears old and inactive (Fig. 4.13 C). No difference in notch height was noted across the fault at the coastline, supporting inactivity.

A S–dipping fault is observed toward the south of the Pangalos peninsula, with friable sandy bedded deposits in its hanging wall (also discussed by Moretti et al. 2003, Fig. 4.9). It is unclear if these deposits are aeolian, or marine and the result of relative base level fall. From the weathered and vegetated nature of this fault plane it is unlikely to have been active recently. Although no evidence for current activity on onshore faults was interpreted in this study, Causse et al. (2004) suggest that a S–dipping fault on the southern tip of the Pangalos peninsula has been active in the last 300 – 400 ka, based on dating of calcite veins along the fault plane.

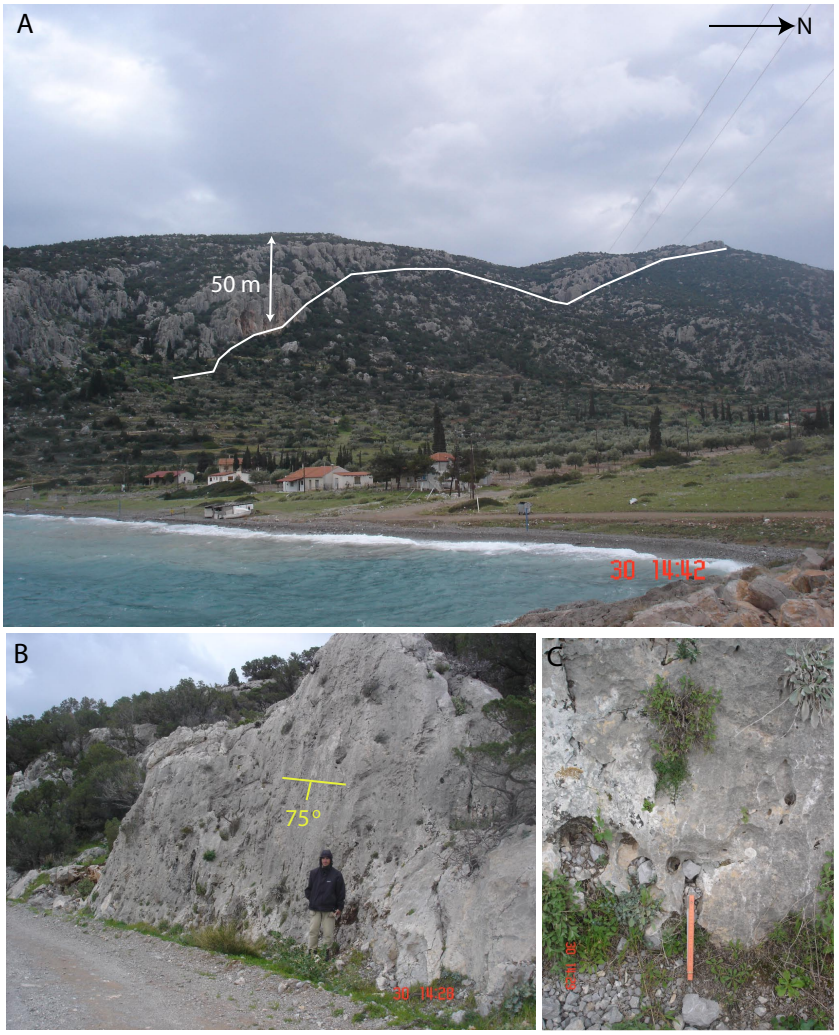

FIGURE 4.13: **A.** View of the N–dipping fault plane above the Milakos peninsula, interpreted on Fig. 4.9. **B.** View of the 75° dipping fault plane. **C.** The bottom of the fault surface appears weathered, vegetated and old. This fault is considered inactive.

The timing and rate of the potential uplift described here cannot be constrained due to the absence of datable material. It is unclear if these features record Holocene uplift, or if they could be related to much older possibly pre–Quaternary relative sea level fall.

4.5.3 Northwest margin: Galaxidi to Nafpaktos

Although the area between Galaxidi and Nafpaktos is large, it has very low neotectonic indicator preservation potential. A large portion of the coastline here is composed of Eratini fan deposits (modern fluvial and beach sediments) and Tertiary flysch deposits, which are easily eroded and do not preserve notches. Only between Itea and Galaxidi have modern notches been preserved (Fig. 4.9).

Possible uplifted wavecut platforms

Four planar platforms are observed in highly brecciated limestone in Logos bay (Figs. 4.9 and 4.14 A). These benches, at ∼0.5, 1.5, 3.5, and 6 m above sea level, have been cut across the deformed bedding, suggesting they are not related to bedding surfaces. However, they cannot be traced continuously across Logos bay, due to the highly erodable nature of the deformed rock. Similar looking bench levels were observed ∼ 2 km further east along the coastline during the boat survey (Figs. 4.9, location 3 and 4.14 B). The consistent occurrence of these bench elevations along at least ∼2 km of the southern Galaxidi peninsula suggest they could be the result of tectonic uplift. The linear nature of the coastline here also suggests the possibility of tectonic control (i.e. a controlling offshore E–W striking fault). The form of these terraces (in terms of approximate height and width) matches closely that observed on the south–western margin of the Corinth rift by Palyvos et al. (2007). These authors find sub–horizontal erosional benches in conglomerate with inner edge elevations of 0.5 m and 1.5 m and a 2 m high bench with no visible inner edge (Fig. 4.14 C). The similarity of the north margin Galaxidi benches with those on the south coast, where uplift is confirmed by exposed marine organisms, is strong evidence to suggest a tectonic origin for the features in Figs. 4.14 A and B.

4.6 Discussion: Fault control of northern coastline movement

In summary, the results of the field studies described here show that relative sea level rise (interpreted as tectonic subsidence) does not occur along the entire length of the northern margin. The northern shore of the Alkyonides Gulf is subsiding, as shown by multiple submerged ca. 350 BC fortifications, submerged beach rock, and wavecut notches. The extent of subsidence interpreted along the northern shore is outlined in Fig. 4.1 and the depth of subsided features below mean sea level is summarised in Fig. 4.15. However, in the Pangalos peninsula and Galaxidi regions, potentially uplifted wavecut notches and convincing wavecut platforms suggest that these areas have experienced tectonic uplift (extent of uplift along the northern coastline is outlined in Fig. 4.1 and potential uplift indicators are summarised in Fig. 4.15). There are still some areas of the northern margin that have not been adequately studied due to access problems (the western Pangalos peninsula and coastline to the east of Domvrena to Antikyra Bay) and others where coastline movement cannot be resolved due to preservation problems (Eratini to Nafpaktos). In the following section the northern coastline movements described above are linked to activity on both onshore and offshore faults. Figure 6.1 from Chapter 6 is referred to, and any offshore faults mentioned here are described in more detail in this later chapter.

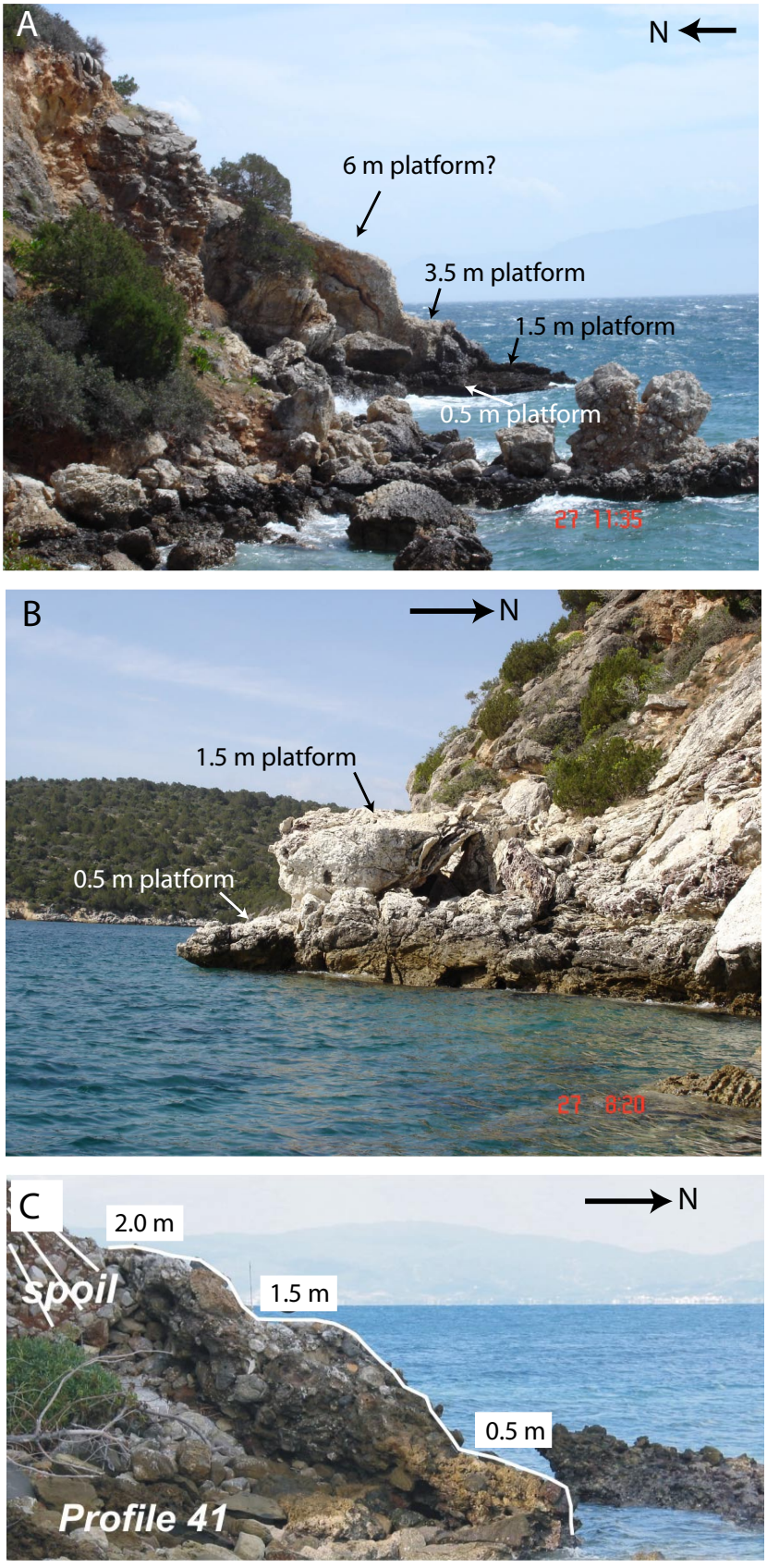

FIGURE 4.14: **A.** Possible uplifted wavecut platforms eroded into highly deformed limestone in Logos Bay (Fig. 4.9). **B.** Similar levels of platforms are observed further east along the Galaxidi peninsula coastline (Fig. 4.9, location 3). **C.** Proposed uplifted terrace platforms from the south–west Corinth margin, from Palyvos et al. (2007).

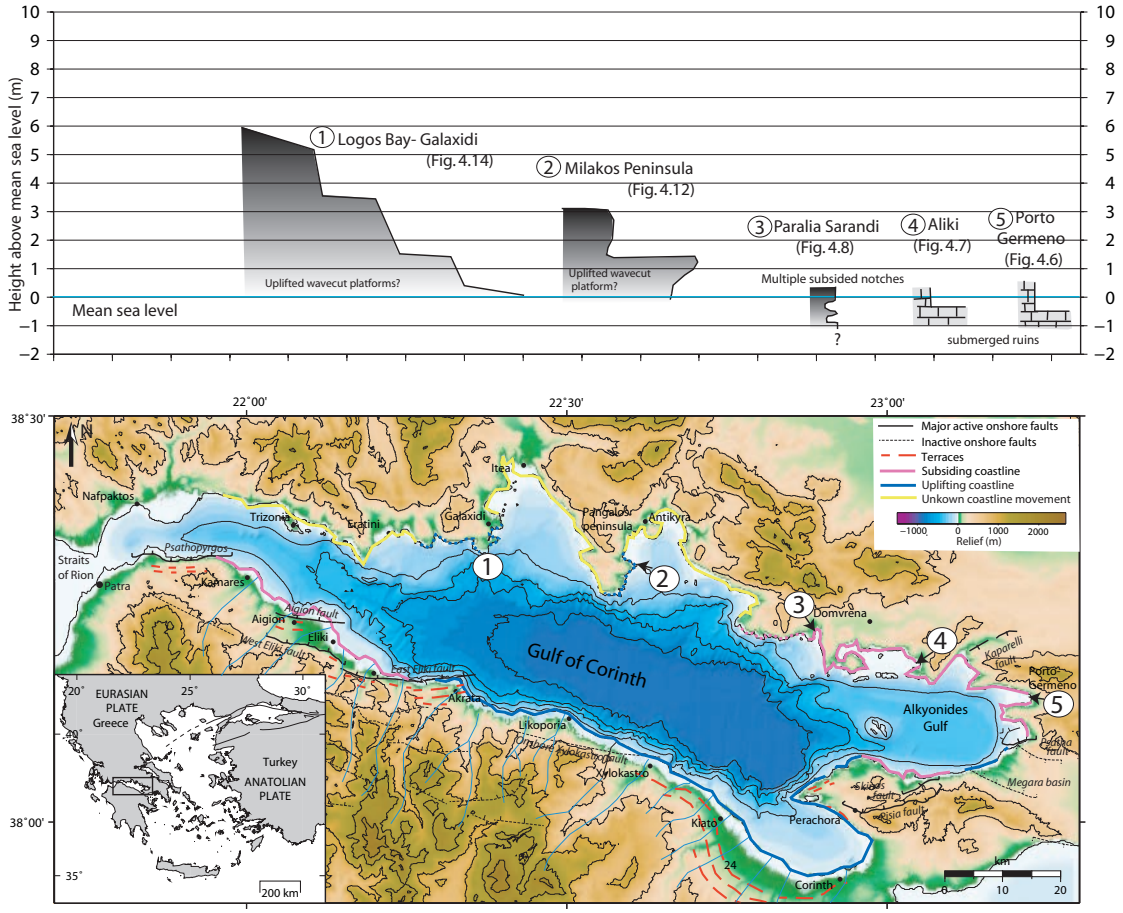

FIGURE 4.15: Summary figure to show the location of potential uplift and subsidence indicators identified along the northern coastline in this study, and their vertical position relative to mean sea level.

In the Alkyonides Gulf the observed subsidence of Porto Germeno is likely related to activity on the S–dipping Kaparelli fault, and potentially is also influenced by the subsidence field of the East Alkyonides and Psatha faults further south (Figs. 4.1 and 6.1, Chapter 6). The coastline bordering both the north and south margins of the small Porto Germeno Bay are linear and Sakellariou et al. (2007) suggest that they are fault controlled. If this is the case these offshore Porto Germeno Bay faults may also be responsible for the subsidence of the fort of Aegosthena. No data from this offshore area has been available in this study to confirm the interpretation of these faults. The subsided fort of Siphai at Aliki lies in the footwall of the Likoporia fault, and in the hanging wall of interpreted faults bordering Domvrena Bay (Sakellariou et al. 2007). These offshore faults are likely responsible for the subsidence of Aliki. Multiple submerged wavecut notches at Ag. Ionnis on the Livadostros fault footwall (Fig. 4.5) suggests that this footwall is currently subsiding and the fault is inactive. However, offshore seismic data from Sakellariou et al. (2007) indicate that this fault has produced a recent seafloor scarp. Also, dislocation modelling discussed in Chapter 8 concludes that the Livadostros fault must have been active over the last 130 ka, in

order to allow subsidence of lowstand deltas by ∼70 m offshore the Alkyonides north margin. These results and observations indicate that the Livadostros fault is probably active, but its location in the subsidence field of more frequently active faults on the south margin results in the observed current subsidence of the footwall.

Observations of probable uplifted wavecut notches and platforms suggest that fault activity is focused in the area of the Milakos peninsula, on the eastern side of the Pangalos peninsula (Figs. 4.11 and 4.12). This area is within the footwall of a N–dipping onshore fault (Fig. 4.13) and a S–dipping offshore fault interpreted by Moretti et al. (2003) (Fig. 4.11). The onshore fault is argued to be inactive (section 4.5.2) based on the weathered and vegetated appearance of the fault plane. It is also unlikely that this fault is wholly responsible for the uplift, as similarly high notch heights are also recored further north along the coastline, in the hanging wall of this onshore fault (Fig. 4.11). Alternatively, the offshore fault interpreted by Moretti et al. (2003) would predict maximum uplift of the Milakos peninsula with uplift decaying to the north, as is generally observed in the pattern of notch height. However, this scenario would require maximum uplift in the area of the Milakos island but notch heights around this island are less than those on the Milakos peninsula. Potentially other offshore faults in the area may be responsible for the uplift. Unpublished high resolution pinger seismic data collected by the University of Patras show that offshore faults do exist in this area (A. Stefatos pers. comm. 2006). Unfortunately, these data were not available for use in this study, and the examination of the sub surface in this area is highlighted in Chapter 9 as an important area for future study. Offshore of the Galaxidi peninsula two high resolution N–S sparker seismic profiles, described in Chapter 5, show a number of S–dipping parallel faults that disrupt sediments (Fig. 5.7). It is possible that the eastward extension of these faults may cause uplift of the linear south Galaxidi peninsula as suggested by wavecut platforms above sea level.

4.7 Conclusions

1. Vertical movement of the south Corinth rift coastline is caused by activity on major E–W trending onshore and offshore faults. Uplift is generally seen along the southern margin, except where parts of the coastline are located in the hanging wall of N-dipping faults. Late Quaternary averaged uplift rates range from ∼0.7 – 1.4 mm/yr in the Gulf of Corinth, and are much lower (∼0.2 – 0.3 mm/yr) in the Alkyonides Gulf. Holocene rates are also generally greater than Late Quaternary averaged rates along the south margin.

2. The entire northern coastline is not subsiding as previously suggested. However, the timing and rate of uplift is unconstrained and is likely much smaller than the south margin. Quantitative estimates of uplift have not been obtained from the north margin due to the general absence of *L. lithophaga* and other subaerial

marine organisms, potentially due to environmental controls (e.g. high fresh water input).

3. The Alkyonides Gulf: The northern shore of the Alkyonides Gulf is subsiding, confirmed by the; submergence of the remains of three ca. 350 BC fortifications, multiple submerged notches, and submerged beach rock. Subsidence rates from the submerged archaeology have been suggested to be ∼0.7 – 0.8 mm/yr. This subsidence is likely related to the presence of active offshore faults in the Porto Germeno Bay and Domvrena Bay areas interpreted by Sakellariou et al. (2007). The more distant Kaparelli and south coast faults may also exert some influence.

4. Pangalos peninsula: High notch roofs up to ∼1.5 m and preserved subaerial wavecut platforms are evidence for uplift of the Milakos peninsula region of the Pangalos peninsula. Although little evidence of subaerial marine material exists (except for the presence of two barnacles ∼1.5 m above sea level) the comparison of the morphology of these terraces with confirmed uplifted platforms from the south margin of the Corinth rift and elsewhere provide strong evidence for a marine origin. Uplift of the Milakos peninsula is potentially related to offshore faults in the Antikyra bay, rather than the apparently inactive looking onshore faults. However, the systematic study of faulting in Antikyra Bay is yet to be published.

5. Galaxidi: At least three erosional wavecut platforms are discontinuously observed along a ∼2 km stretch of the linear south Galaxidi peninsula coastline at heights of 0.5, 1.5 and 3.5 m above mean sea level. Potential faults responsible for this uplift have been interpreted within seismic data from Chapter 5, which show a number of S–dipping faults disrupting sediments and basement topography to a small degree just south of the Galaxidi peninsula.

Chapter 5

Evolution of the offshore western Gulf of Corinth

Bell, R.E., McNeill, L.C., Bull, J.M., and Henstock, T.J.

Geological Society of America, Bulletin; v. 120 no. 1/2 p. 156-178; doi:10.1130/B26212.1

Manuscript Received 1 March 2007, Revised Manuscript Received 22 May 2007, Manuscript Accepted 5 July 2007

5.1 Introduction

The style of extension and strain distribution during the initiation and early stages of intra–continental rifting is important for understanding the eventual transition to ocean spreading and plate margin development. Few active extensional systems record less than a few million years of fault history, allowing for the study of early rifting processes. The Gulf of Corinth, a high strain band in the active Aegean region, measures 100 km by 20 km and records a Pliocene–Recent history of N–S extension, against the structural grain of the Pindos mountain chain (McKenzie 1972, Roberts & Jackson 1991). It is significantly smaller and younger than other examples of continental extension, like the more diffuse ∼800 km wide Basin and Range province (ca. 20 million years old, Hamilton 1987), the extensive East African rift system (extension began ca. 32 Ma, Omar & Steckler 1996) and the Baikal rift (extension began ca. 35 Ma, Mats 1993). Extensional deformation within central Greece is thought to be related to some combination of: back arc extension due to subduction at the Hellenic Trench (McKenzie 1972, Doutsos et al. 1988); westward propagation of the North Anatolian fault (Taymaz et al. 1991, Armijo et al. 1996); and gravitational collapse of lithosphere thickened in the Hellenide orogeny (Jolivet 2001).

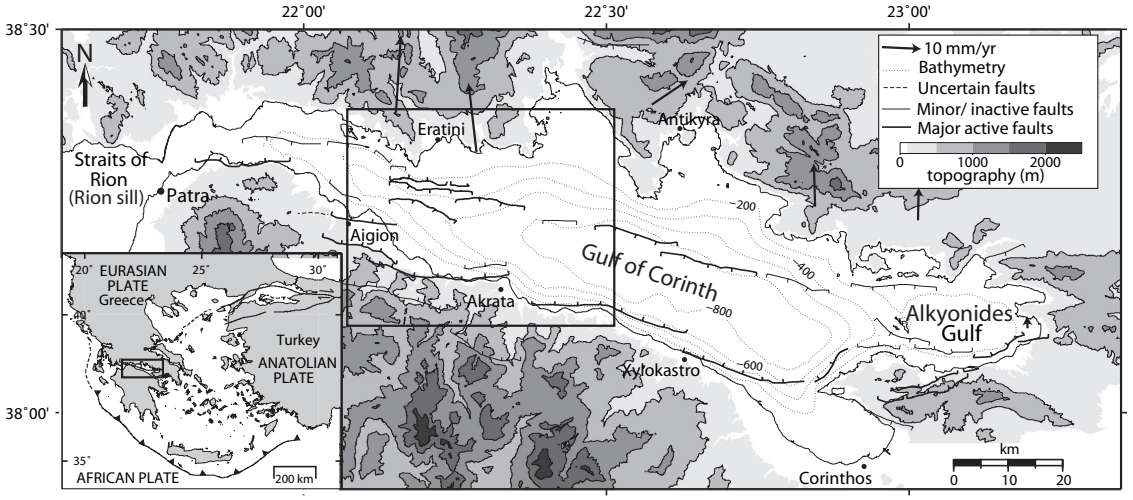

FIGURE 5.1: Framework of the Gulf of Corinth. The locations of major on– and offshore faults are taken after Stefatos et al. (2002), Leeder et al. (2005), McNeill et al. (2005a), and this study. Topography is from the Shuttle Radar Topography Mission (http://srtm.usgs.gov) and bathymetry is reproduced from the GEBCO Digital Atlas published by the British Oceanographic Data Centre on behalf of IOC and IHO, 2003. Inset: Summary of Aegean regional tectonics. Arrows are north coast GPS velocity vectors for a stationary southern coastline, from Clarke et al. (1998) Fig. 16.

The Gulf of Corinth rift structure has often been generalized as an E–W striking asymmetric half graben, with N–S extension controlled by a series of N-dipping normal faults along the southern margin together with minor S–dipping antithetic faults (e.g. Roberts & Jackson 1991, Armijo et al. 1996, Fig. 5.1). The geology of the steep south coast footwall mountains results from the exhumation of Gilbert type fan deltas due to northward propagation of fault activity (Ori 1989, Dart et al. 1994, Gawthorpe et al. 1994) and, marine terraces superimposed on the current master fault footwall (McNeill & Collier 2004). Deformation and fault activity within the Gulf of Corinth area, over varying timescales, has been assessed through the analysis of instrumentally recorded recent seismicity (e.g. Jackson et al. 1982), historical seismicity (e.g. Ambraseys & Jackson 1990), paleoseismology (e.g. McNeill et al. 2005b) and geomorphology. Footwall uplift and fault slip rates have been estimated by the identification and dating of uplifted marine sediments (Pirazzoli et al. 1994, Armijo et al. 1996, Stewart & Vita-Finzi 1996, McNeill & Collier 2004).

Pleistocene south coast uplift rates correlate to possible fault slip rates of the order 4 – 11 mm/yr (e.g. Armijo et al. 1996, McNeill et al. 2005b). Slightly higher uplift rates are obtained from Holocene base level markers (e.g. wave cut notches Pirazzoli et al. 1994) suggesting a recent increase in deformation rate (e.g. Leeder et al. 2003, McNeill & Collier 2004, Pirazzoli et al. 2004). Current regional extension rates have been assessed from GPS data (e.g. Davies et al. 1997, Clarke et al. 1998, Briole et al. 2000) and are found to increase from < 5 mm/yr in the east, to $> \sim 10 - 15$ mm/yr in the west (Fig. 5.1). In the western Gulf in particular, there is a discrepancy between the extension rates predicted based on onshore fault activity and that observed across

the rift. An explanation proposed for this discrepancy is that offshore faults could contribute significantly to the extension (Brooks & Ferentinos 1984, Stefatos et al. 2002, Moretti et al. 2003, Sachpazi et al. 2003, McNeill et al. 2005a). It has been suggested that the master fault currently controlling rift geometry changes from being a south coast N–dipping fault in the east of the rift, to a S–dipping offshore fault in the west (Stefatos et al., 2002; Sachpazi et al., 2003; McNeill, 2005). Such changes in the polarity of basin segments along strike in a rift system are also common in the East African Rift (Rosendahl 1987). Alternatively, slip could be occurring on a deep low angle fault, allowing for reconciliation with geodetic extension rates. Sorel (2000) suggest a low angle N–dipping detachment can be mapped on the south coast, a view which may or may not be supported by the location of microseismicity (Rigo et al. 1996, Gautier et al. 2006). The importance of high and low angle fault activity in producing the geometry of rift systems has been debated at other rift zones, such as the Basin and Range Province and Papua New Guinea (Wernicke & Burchfiel 1982, Taylor et al. 1999).

In this paper we interpret the geometry of major offshore faults in the western Gulf and assess their contribution to syn–rift deformation, building on the work of Stefatos et al. (2002), Sachpazi et al. (2003) and McNeill et al. (2005a) and incorporate current knowledge of onshore structures as described above. We will analyze western Gulf basin structure, estimate fault slip rates, and investigate the evolution of the western rift in space and time. In this way we hope to contribute toward a general understanding of the relationship between individual faults and their impact on stratigraphy and help to address how common half graben vs. graben structures and high vs. low angle faulting is in this and other young continental rifts. This will be achieved through the stratigraphic analysis of high resolution seismic reflection profiles.

The Gulf is connected to the Mediterranean by the Rion sill at its western end which lies 60 – 70 m below present day sea level (Perissoratis et al. 2000) (Fig. 5.1). This 2 km wide erosional terrace is probably composed of Early Pleistocene or Pliocene strata (Chronis et al. 1991). Holocene deltaic sequences up to 15 – 20 m thick bank against the sides of the terrace (Perissoratis et al. 2000). The lack of recent fault offset on the terrace suggests that there has been very little change in its absolute depth at least throughout the Late Pleistocene (Perissoratis et al. 2000). Stratigraphic evidence presented by McNeill et al. (2005a), which has been developed by our study supports a lack of vertical movement on the Rion sill. Based on sedimentology at the eastern end of the Gulf (Collier & Dart 1991) and the projection of Late Quaternary uplift rates, there has not been a marine connection during episodes of sea level lowstand at the Corinth isthmus since at least 450 – 800 ka (uplift rates of 0.2 – 0.3 mm/yr from Collier et al. 1992, Leeder et al. 2005). As such, during recent sea level lowstands the Gulf has become an isolated lake, predominantly controlled by the level of the Rion sill. This oscillation between lake and open–ocean environment produces sedimentary cycles sensitive to sea level fluctuation. This leads to a rich and

detailed stratigraphic record of tectonism and climate variation. Coring in the central Gulf (Moretti et al. 2004) and Alkyonides Gulf (Collier et al. 2000) shows sediments were deposited in both marine and lacustrine environments supporting a hypothesis of changing environment. The seismic stratigraphy of sub–surface sediments within the central Gulf suggests a cyclicity in sediment properties controlled by 100 ka sea level cycles (Perissoratis et al. 2000, Sachpazi et al. 2003, Leeder et al. 2005, Lykousis et al. 2007).

5.2 Methodology and Data

5.2.1 Seismic reflection and swath bathymetry data

High resolution multichannel seismic (MCS) reflection profiles and multibeam swath bathymetry were collected in the western Gulf by MV Vassilios in July 2003 under the direction of the Universities of Southampton, Patras, and Leeds. Seismic reflection data were collected using a 150-2000 Hz sparker source and a 60 channel, 1m group spacing, streamer. Ten N–S profiles were collected across the rift together with a 40 km E–W tie line (Fig. 5.2). Penetration down to 1 to 1.5 s two way travel time (TWTT) allowed basement imaging except in the deepest parts of the basin. This dataset has been supplemented by published and publicly available data to investigate basement depth in the deep basin (e.g. Goodliffe et al. 2003, Sachpazi et al. 2003, Zelt et al. 2004). Swath bathymetry coverage is outlined in Figure 5.2 and was collected using a Reson Seabat 8160 50 kHz multibeam echo sounder.

5.2.2 Depth conversion

To make quantitative assessments of fault activity we have depth–converted some parts of the MCS data. Depth conversion was conducted based on a velocity profile compiled from typical interval velocities used during data stacking, velocity estimates for the Alkyonides Gulf (Collier et al. 2000), direct measurements from shallow sediments (Moretti et al. 2004) and generalized sediment curves from Hamilton (1979, 1980). Using our velocity curve, sediments with a TWTT of between 0 – 0.5 s and 0.5 – 1 s below the seafloor have estimated average velocities of 1.5 – 2.0 km/s and 2.0 – 2.5 km/s, respectively.

5.3 Stratigraphic Architecture

To extract quantitative tectonic information it is important to establish the stratigraphic framework and, where possible, estimate ages of horizons. The offshore stratigraphy exhibits a distinct character in the shelf and upper slope regions when compared to the deeper Gulf due to the more direct impact of sea level fluctuations.

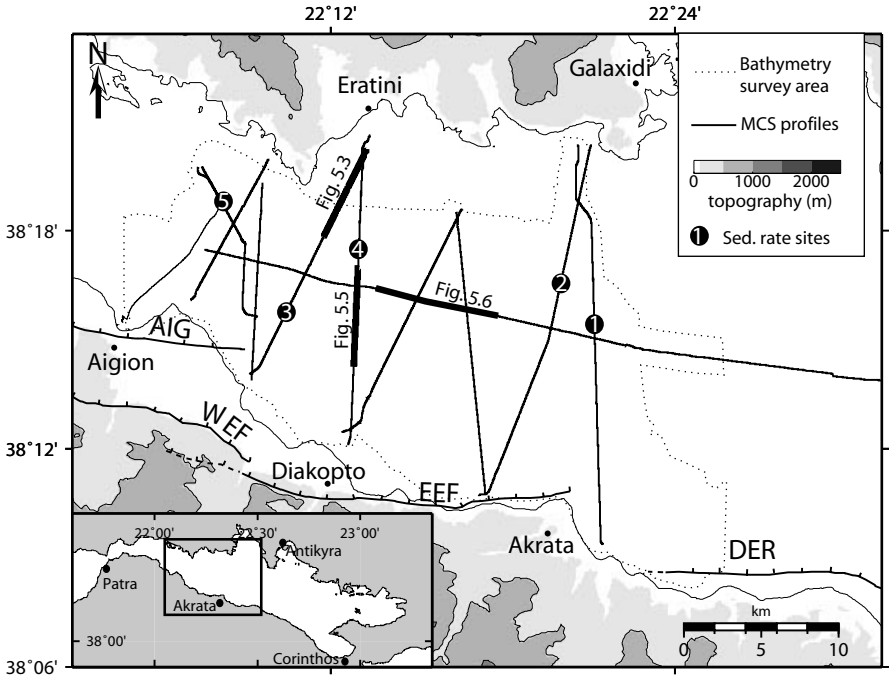

FIGURE 5.2: Extent of the swath bathymetry (dotted) and seismic reflection profiles (solid lines) collected by the MV Vassilios in 2003 (McNeill et al. 2005a). Sedimentation rate calculations at the labeled sites are given in Table 5.3. AIG: Aigion fault; WEF: West Eliki fault; EEF: East Eliki fault; DER: Derveni fault.

5.3.1 Shelf and upper slope stratigraphic architecture: The Eratini sub-basin

A local fault–controlled depocentre, known as the Eratini sub–basin, was previously identified offshore Eratini (McNeill et al. 2005a, Lykousis et al. 2007, Fig. 5.3). The basement–sediment contact dips south at ∼15 – 18° and the sediment wedge thickens toward the N–dipping North Eratini fault (after McNeill et al. 2005a). The sediments can be divided into two major packages separated by an unconformity (horizon U, Fig. 5.3 B). We have identified five units within the well–stratified basin sediments above horizon U, based on reflection geometry and termination and likely sea level control (units I to V, Fig. 5.3 B and Table 5.1). Near the northern shallow margin of the sub-basin we interpret four distinct clinoform (sloping depositional surface) packages, each located progressively northward (arrowed on Fig. 5.3 B). The steeply–dipping clinoforms within each package flatten basinward to become parallel to shallow–dipping continuous reflections.

Similar sedimentary architecture was interpreted in this area by McNeill et al. (2005a) and Lykousis et al. (2007) and from other parts of the Gulf (Collier et al. 2000, Leeder et al. 2002, 2005) and elsewhere in the world, e.g. Lake Edward (McGlue et al. 2006) and Lake Malawi (Scholz & Finney 1994). Clinoform units are indicative of

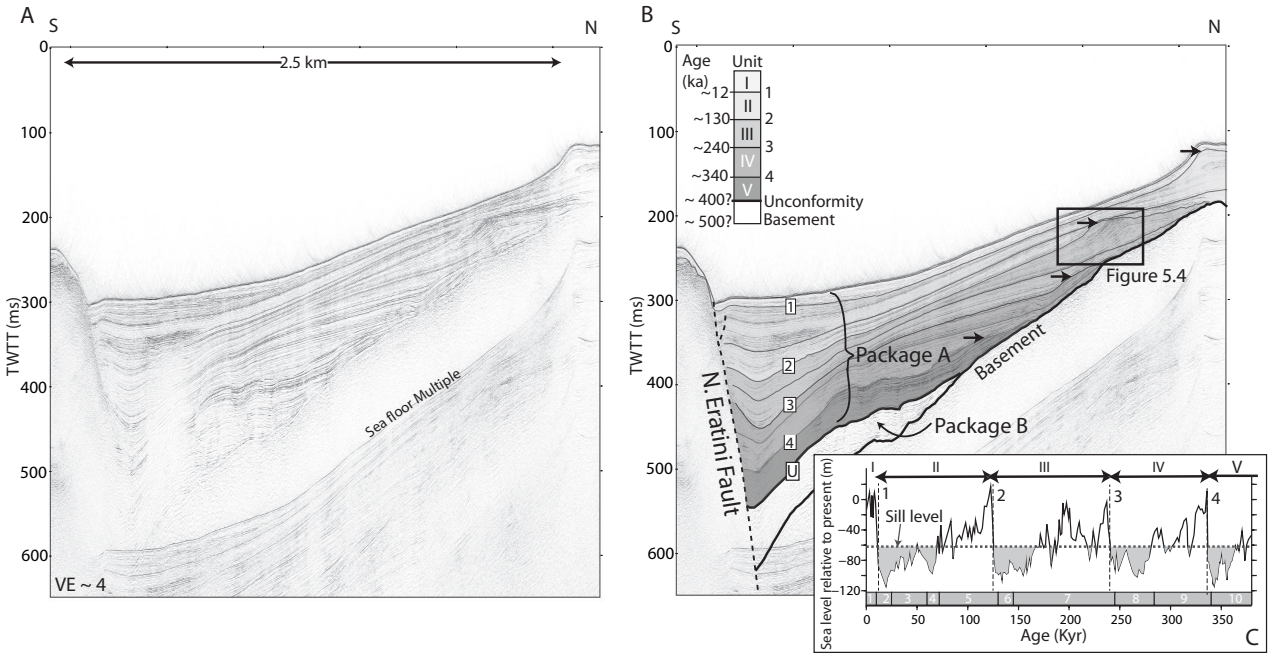

FIGURE 5.3: **A.** MCS data from the Eratini sub–basin (location identified in Fig. 5.2). **B.** Four clinoform packages (arrowed) are identified within the basin. The shallowest clinoform within each package marks the end lowstand shoreline, formed before the Rion sill flooded during marine transgression. Un–numbered lines represent interpreted marine to lacustrine transitions. **C.** Horizons can be correlated with the eustatic sea level curve of Siddall et al. (2003) to estimate horizon age. After McNeill et al. (2005a).

progradational shoreline deltas formed in response to a falling or static lowstand sea level, forcing the shoreline basinward (e.g. Vail et al. 1977, Gawthorpe et al. 1994, Leeder et al. 2002, 2005). We interpret the clinoform units in this study as deltaic deposits formed when eustatic sea level dropped below the level of the Rion sill and the Gulf became an isolated lake (Perissoratis et al. 2000, Leeder et al. 2005, McNeill et al. 2005a, Lykousis et al. 2007). The youngest slope break of each clinoform package formed at the depth of the Rion sill.

The slope breaks of each of the preserved youngest delta surfaces (labeled horizons 1 to 4 in Fig. 5.3 B) lie at average depths of ∼95, 160, 210 and 260 m below sea level. If the Rion sill has remained at a depth of ∼60 – 70 m below sea level (Perissoratis et al. 2000) and the Gulf has remained closed at the Corinth Isthmus during at least the last four lowstands (Collier & Dart 1991, Collier et al. 1992), the sill–flooding events may be correlated with a eustatic sea level curve (e.g. Siddall et al. 2003, Fig. 5.3 C), assuming that there has been no significant erosion. We estimate the ages of end lowstand shorelines, represented by horizons 1, 2, 3 and 4, at ca. 12, 130, 240, 340 ka respectively (Fig. 5.3 C and Table 5.1). If our assumption that the sill has remained static is not correct, this will not greatly affect the age estimates because the eustatic sea level curve is very steep during transgressions (Fig. 5.3 C). Currently there are no core data in this area to verify our age assignment.

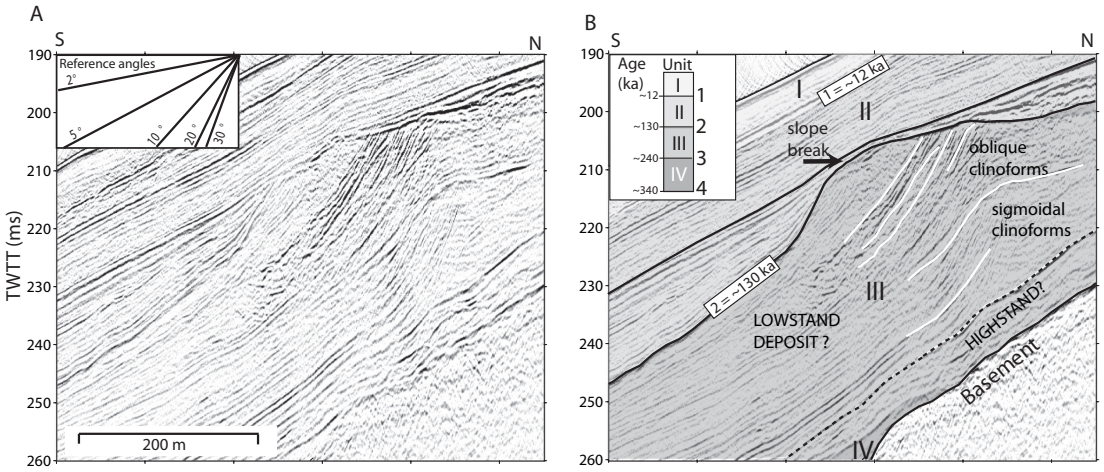

FIGURE 5.4: **A.** Close up of the stratigraphy within the Eratini sub-basin (box in Fig. 5.3 B) **B.** Unit III shows a clinoform configuration associated with lacustrine delta progradation during sea level lowstand. The parallel reflections at the base of the unit are probably highstand and transgressive sediments.

Unit I, between the sea bed and horizon 1, is composed of parallel and continuous reflections that have the same character throughout the sub–basin. The unit has a relatively constant thickness (∼7 m) and drapes pre-existing topography (Table 5.1). Based on our correlation and that of McNeill et al. (2005a) and Lykousis et al. (2007), this unit is interpreted as Holocene marine sediments. The seismic character of the sediments seen here is similar to the Holocene veneer seen elsewhere in the Gulf.

Based on our correlation units II, III and IV record sedimentation during both marine and lacustrine conditions as sea level fluctuated through 100 ka cycles. As an example, Figure 5.4 shows a close up of stratigraphy within unit III. Below horizon 2 (ca. 130 ka) reflections have a low-medium amplitude and a well developed clinoformal character. The oldest clinoforms in the unit downlap onto a high amplitude horizon (dashed in Fig. 5.4 B). Below this horizon reflections show no evidence of clinoformal character and have generally a higher amplitude than the clinoformal reflections above (Fig. 5.4 B). We suggest that these parallel sediments, extending to horizon 3 (ca. 240 ka), formed by marine aggradation during a sea level highstand, analogous to the modern deposition of unit I (Fig. 5.3 B).

Maximum sedimentation rates can be estimated for units I to IV at the slope break position and average values deduced for the distal basin, based on the interpreted stratigraphy (Table 5.1). Sedimentation rates for marine unit I are ∼0.5 – 0.6 mm/yr across the sub-basin. Units II to IV show similar sedimentation rates, with a maximum of ∼0.45 mm/yr and average values of ∼0.25 mm/yr away from clinoform packages.

Sequence		Seismic character		Unit thickness (m)		Geological significance	Horizon age (ka)	Sedimentation rate (mm/yr)	
Boundary	Unit	Illustration	Description	North margin	Distal			North margin	Distal
Sea bed							0		
	I		High-amplitude, low-frequency, parallel and continuous reflectors mantle topography	~7	~7	Highstand marine deposit		0.6	0.6
1						Stage 1–2 boundary	ca. 12		
	II		Low-amplitude, high-frequency, oblique clinoforms at north margin; basinward and basal reflections are conformable	~50	~22	Lake deltas and transgressive deposits		0.45	0.2
2						Stage 5e–6 boundary	ca. 130		
	III		Low-amplitude, high-frequency, sigmoidal clinoforms. Distal and basal reflections parallel	~35	~25	Lake deltas and transgressive deposits		0.35	0.25
3						Stage 7c–8 boundary	ca. 240		
	IV		Low-amplitude, high-frequency, low-angle clinoforms. Distal and basal reflections parallel	~35	~18	Possible lake deltas and transgressive deposits		0.35	0.2
4						Stage 9–10 boundary	ca. 340		
	V		Low-amplitude, gently dipping clinoforms			Possible lake deltas		0.4	0.25
U						Unconformity	ca. 400		
			Poorly stratified with no clinoforms					0.4	0.25
Basement						Basement limestone	ca. 500		

TABLE 5.1: Seismic stratigraphy information summary for the upper shelf/slope: Eratini sub–basin

Below units I to V, there is a change in seismic character at the horizon designated U (Fig. 5.3 B). This horizon separates well–stratified clinoform packages from a unit with few traceable reflections that extends down to basement (horizon U to basement in Fig. 5.3 B). If we assume that average sedimentation rates have remained constant, we predict an age of ca. 0.4 Ma for horizon U and ca. 0.5 Ma for the oldest sediments in the basin.

5.3.2 Main basin stratigraphic architecture

Stratigraphy in the main Gulf can be divided into two distinct seismic packages (A and B) (see Figs. 5.5 and 5.6). The upper package (A) is well–stratified with parallel continuous reflection horizons which show cyclical seismic properties. The deeper package (B) contains few reflections that can be traced for any significant distance (Figs. 5.5 B and 5.6 B). The two packages are separated by an unconformity (horizon U) which is identified throughout the study area as a strongly reflective surface with some degree of angular truncation (Fig. 5.6 B). The same surface was identified in the Eratini sub–basin (Fig. 5.3), and Sachpazi et al. (2003) have suggested a similar division of stratigraphy further east within the central Gulf, but an exact correlation between the units in the different areas is unconfirmed.

Package A contains four cyclical units (I to IV) which we propose can be related to 100 ka climate/sea level cycles (Figs. 5.5 B and 5.6 B). Unit I, between the sea bed and horizon 1 is well stratified with high amplitude, low frequency, continuous parallel reflections which diverge at topographic depressions and near growth faults (Figs 5.5 B, 5.6 B and Table 5.2). Our E–W tie line crosses the Marion Du Fresne long piston core site and horizon 1 can be correlated with the location of a lacustrine–marine boundary dated at ca. 12 ka (Moretti et al. 2004). Unit I has been deposited in post ca. 12 ka marine conditions.

Reflections in the upper part of unit II have lower amplitudes and higher frequencies than those in unit I (Figs. 5.5 B, 5.6 B and Table 5.2). The shallowest sediments of unit II have been sampled (Moretti et al. 2004) and correspond to lacustrine sedimentation prior to Rion sill flooding ca. 12 ka. From the limited core data available it appears that a change in seismic character from high amplitude/low frequency in unit I, to low amplitude/high frequency in unit II, reflects a change in Gulf conditions from marine (highstand) to lacustrine (lowstand). This seismic character variation has also been identified by Perissoratis et al. (2000) who postulate that during glacial lowstands the frequency of turbidite deposition may increase in the main Gulf due to the emergence of unstable margin slopes.

These two seismic facies types can be distinguished in older, underlying units. We interpret horizons 2 and 3 as transitions between lacustrine and marine conditions (Figs. 5.5 B and 5.6 B). These horizons have been correlated with the eustatic sea

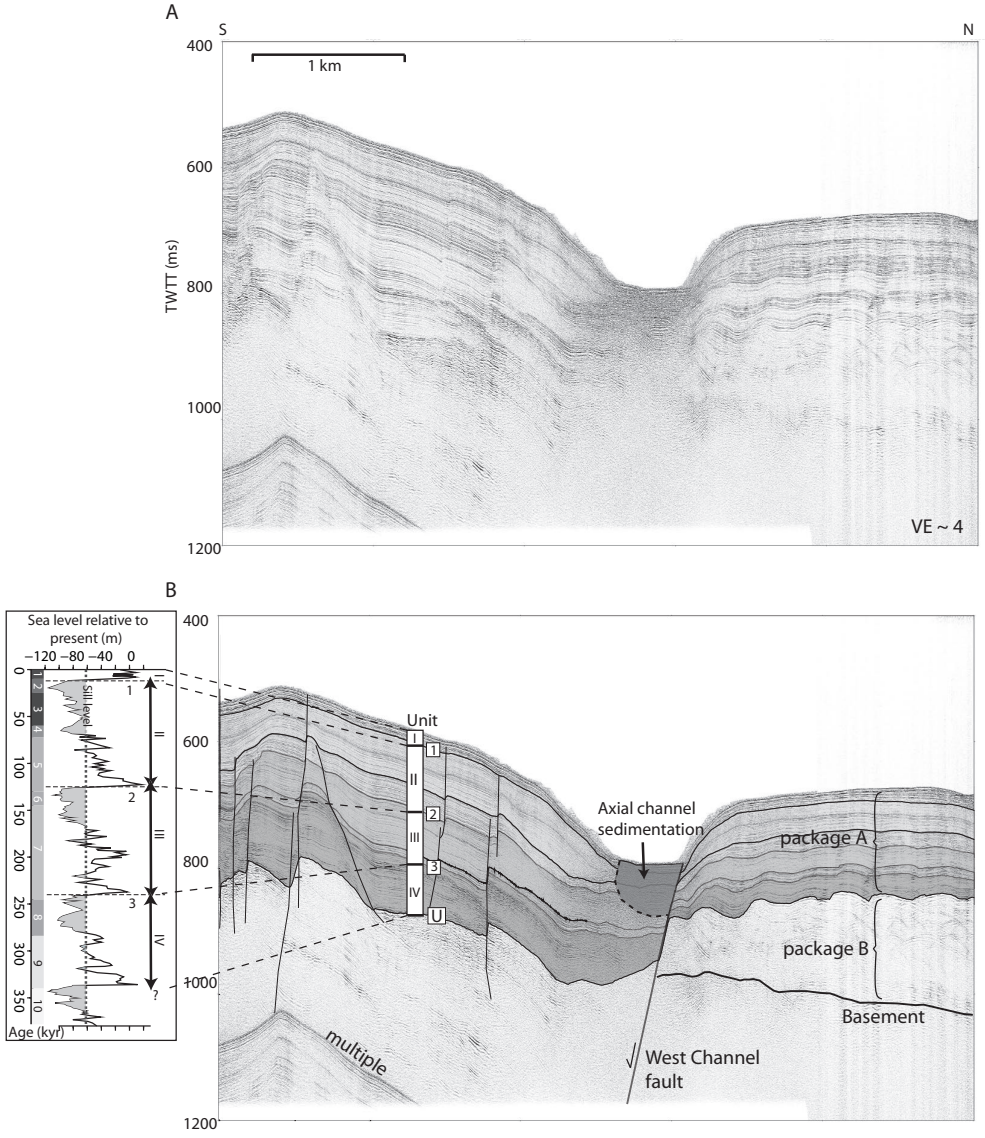

FIGURE 5.5: **A.** MCS data from the central western Gulf (location shown in Fig. 5.2) **B.** Seismic stratigraphic interpretation showing the two main sediment packages A and B, and horizon correlation with the sea level curve of Siddall et al. (2003) modified for the level of the Rion sill.

level curve of Siddall et al. (2003) yielding age estimates of ca. 130 and 240 ka for horizons 2 and 3 respectively (Table 5.2).

We estimated sedimentation rates within the main Gulf, for undisturbed sediments away from major faults, over different time periods, based on our age estimates (Table 5.3). Weighted average sedimentation rates of ∼1.0 – 1.2 mm/yr are obtained in the eastern part of the western Gulf, decreasing to ∼0.5 – 0.55 mm/yr in the center of the study area. For the former, values are within the range of rates suggested elsewhere in the central Gulf over the last ca. 20 ka (Moretti et al. 2004, 1.2 mm/yr,). The sedimentation rates estimated in this study are therefore realistic (giving increased confidence in age assignment to horizons). Extending these sedimentation rates gives

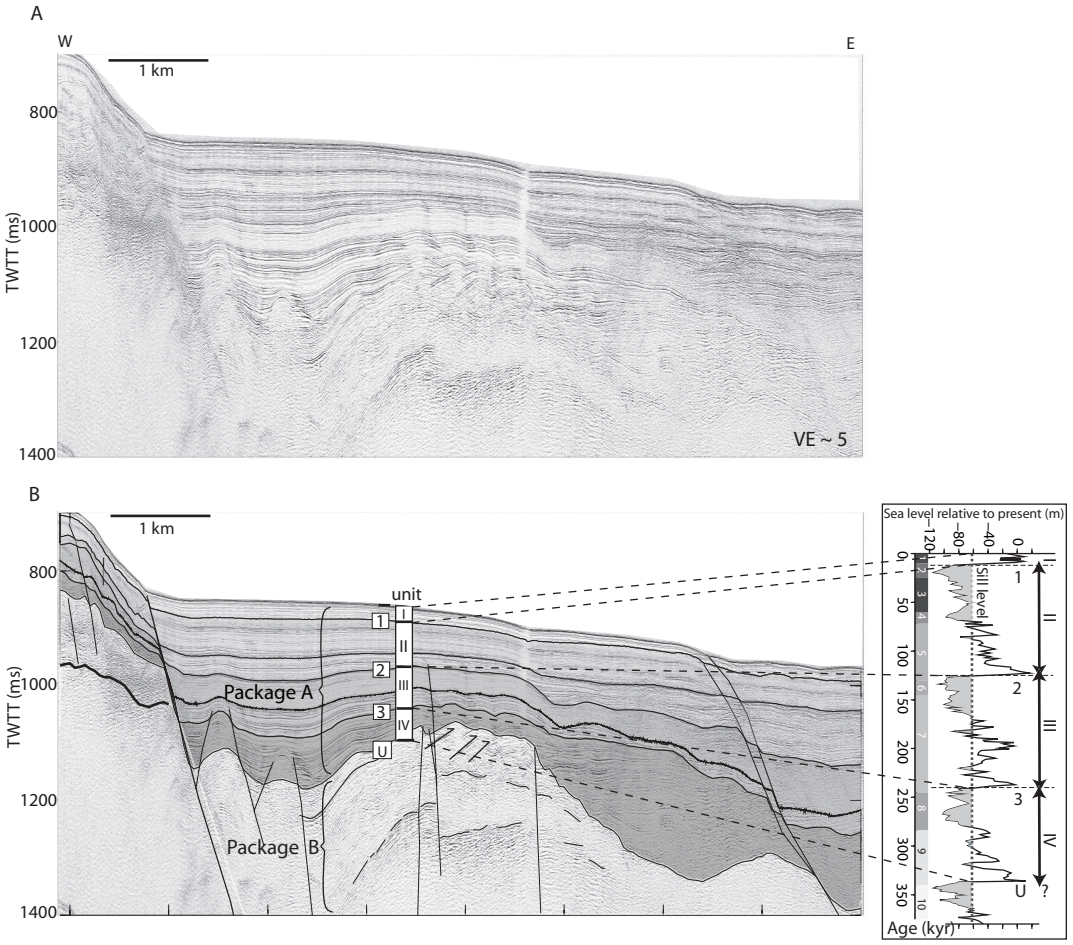

FIGURE 5.6: **A.** MCS data from the E-W Gulf profile (location shown in Fig. 5.2). **B.** Seismic stratigraphic interpretation showing the two main sediment packages A and B, and horizon correlation with the sea level curve of Siddall et al. (2003) modified for the level of the Rion sill.

age estimates of ca. 0.3 - 0.42 Ma for the unconformity surface, horizon U (Figs. 5.5 B, 5.6 B and Table 5.3).

Very few traceable reflectors are observed in package B and all have low amplitudes when compared to package A. Especially in the eastern study area, the unit is partly below the depth of seismic recording, but published data has been integrated into this study allowing further interpretation (e.g. Goodliffe et al. 2003, Sachpazi et al. 2003, Clement et al. 2004, Zelt et al. 2004). Analysis of published data and extrapolation of our average sedimentation rates yields an age for the oldest sediments within the deepest western basin of ca. 1.5 Ma.

5.3.3 Correlation between Eratini sub–basin and main Gulf stratigraphic units

Sedimentation and seismic stratigraphy in the marginal Eratini sub–basin and in the main Gulf are both controlled by Quaternary sea level (climatic) variations (Tables

Sequence		Seismic character		Unit thickness (m)		Geological significance	Horizon age (ka)	Sedimentation rate (mm/yr)	
Boundary	Unit	Illustration	Description	North margin	Distal			North margin	Distal
Sea bed							0		
	I		High-amplitude, low-frequency, continuous parallel reflectors diverge into depressions	~12	~15	Marine, hemipelagic and turbidites		0.9–1.2	1–1.5
1						Stage 1–2 boundary	ca. 12		
	II		Low-amplitude, high-frequency, parallel reflectors. Higher amplitude, lower frequency reflections at base	~110	~55	Lacustrine (frequent turbidites) to marine		0.9–1.0	0.45–0.5
2						Stage 5e–6 boundary	ca. 130		
	III		Low-amplitude, high-frequency, semi-continuous reflections. Higher amplitude and lower frequency at base	~125	~50	Lacustrine (frequent turbidites) to marine		1.0–1.4	0.35–0.45
3						Stage 7c–8 boundary	ca. 240		
	IV		Low-amplitude, high-frequency reflections	~120	~50	Lacustrine		1.0–1.2	0.4–0.5
U						Unconformity	ca. 300–400		
			Poorly stratified with the occasional traceable horizon					1.0–1.2	0.4–0.5
Basement						Basement limestone	ca. 1500 (E) ca. 500 (W)		

TABLE 5.2: Seismic stratigraphy information summary for the main deep Gulf

Location	0–12 ka sedimentation rate (mm/yr)	12–130 ka sedimentation rate (mm/yr)	130–250 ka sedimentation rate (mm/yr)	Weighted average sedimentation rate (mm/yr)	Age of unconformity (Ma)	Age of basement-sediment contact (Ma)
1	0.88	0.9	1.4	1.2	ca. 0.31	1.2–1 .5
2	1.17	1.0	0.96	1.0	ca. 0.36	1.2–1.45
3	1.05	0.52	0.45	0.54	ca. 0.38	1.4–1.6
4	1.1	0.49	0.36	0.51	ca. 0.31	0.49–0.55
5	1.52	0.44	0.35	0.4*	ca. 0.33	0.47–0.51

Note: Sedimentation rates have been calculated over the time periods 0–12 ka, 12–130 ka, and 130–250 ka. A weighted average has then been calculated from these values.
*Not including Holocene debris flow

TABLE 5.3: Review of sedimentation rates for a variety of locations within the Western Gulf of Corinth (Fig. 5.2)

5.1 and 5.2). The unconformity between well stratified and poorly stratified sediments is seen in both the stratigraphy of the northern Eratini sub–basin and in the main Gulf. Extrapolating estimated sedimentation rates in both environments yields a similar age of the unconformity, horizon U, of ca. 0.4 Ma. The age of the basement–sediment contact in the deepest parts of the Gulf is estimated at ca. 1.5 Ma, which contrasts with the younger age (ca. 0.5 Ma) we determined for the Eratini sub–basin and elsewhere on the northern margin in general (Table 5.3).

5.4 Basin Geometry

5.4.1 Basement structure

Interpretation of the MCS and swath bathymetry data has led us to identify five dominant active offshore faults; the South Eratini, North Eratini, East Channel, West Channel and Akrata faults (Fig. 5.7, see also Stefatos et al. 2002, McNeill et al. 2005a, Lykousis et al. 2007). These faults, with throws of > 0.5 s TWTT ($>$ $\sim$450 m), and are seen to dissect basement, are responsible for the observed basin geometry, together with the East and West Eliki, Derveni and Aigion faults along the southern coastline. Figure 5.7 also shows other major faults that are either buried and no longer active, or have throws < 0.5 s TWTT. Minor faults that do not displace basement, have limited or no surface expression, cannot be traced between profiles due to lengths < 5 km or have unfavorable trends, are not shown on Figure 5.7.

Basement is clearly imaged in the seismic data of this study down to 1.5 s TWTT. Other published and publicly available datasets (Zelt et al. 2004, seismic images from

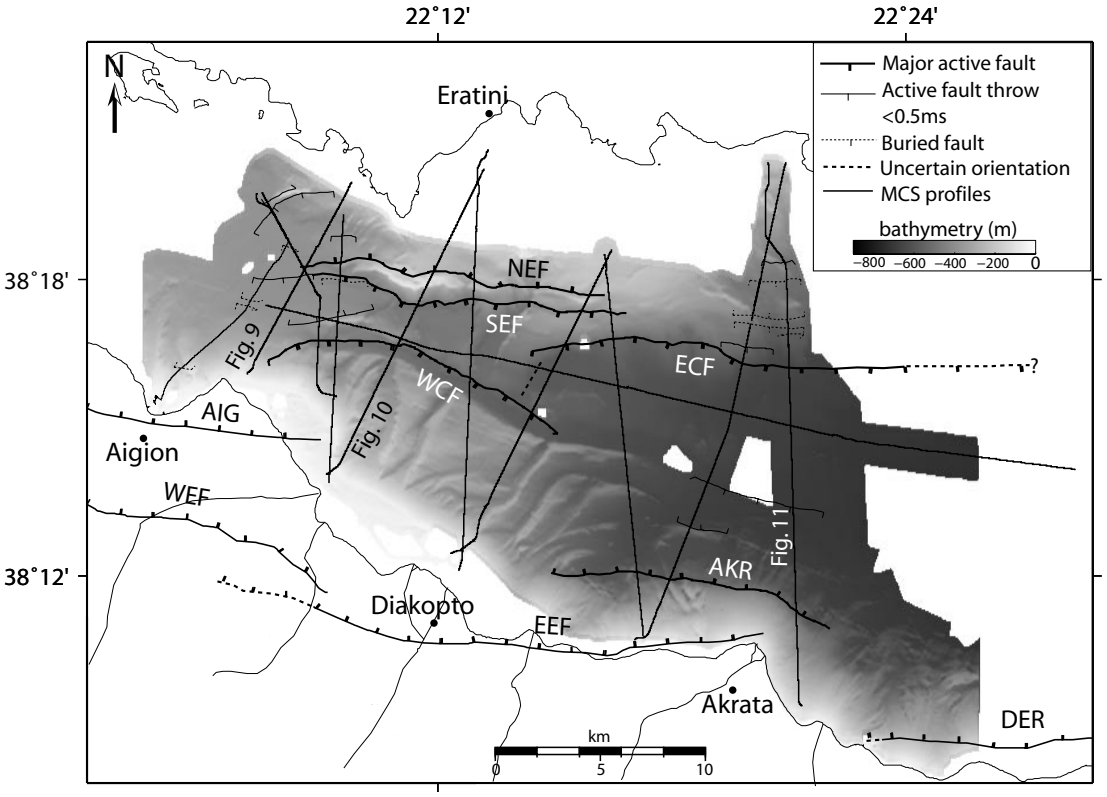

FIGURE 5.7: Interpreted major faults in the western Gulf of Corinth. Positions of faults are constrained by the seismic profiles and swath bathymetry used in this study and that by McNeill et al. (2005a), and are supplemented by interpretations from Zelt et al. (2004) and Goodliffe et al. (2003). AIG: Aigion fault; WEF: West Eliki fault; EEF: East Eliki fault; DER: Derveni fault; WCF: West Channel fault; ECF: East channel fault; SEF: South Eratini fault; NEF: North Eratini fault; AKR: Akrata fault.

the R/V Maurice Ewing cruise EW0108/2001 accessed through the Marine Seismic Data Center at http://www.ig.utexas.edu/sdc/) were incorporated to produce a time–structure contour map of the sediment–basement contact and an isopach of the total sediment thickness (Fig. 5.8 A and B respectively). The basement structure of the western Gulf can be broadly separated into a major depocentre to the south (> 0.8 s below the seafloor, containing up to ∼2 km of sediments, Fig. 5.8) and a shallower region to the north, controlled by the traces of the East and West Channel faults. The basement–sediment contact in the hanging wall of the S–dipping West Channel and East Channel faults gradually increases in depth to the east, reaching ∼2.8 km, with the surface dipping 12 – 18° N toward the fault planes (Fig. 5.8 A). The basement surface between the East Channel fault and Akrata fault deepens adjacent to both fault structures with a central structural high (Fig. 5.8 A and B).

North of the East and West Channel fault trace, basement depth is typically shallower than ∼0.4 s TWTT (∼0.45 km) below the seafloor (Fig. 5.8 B), with localized fault–controlled highs and lows. The region between the eastern tip of the West Channel fault and western tip of the East Channel fault has been warped into a relay ramp

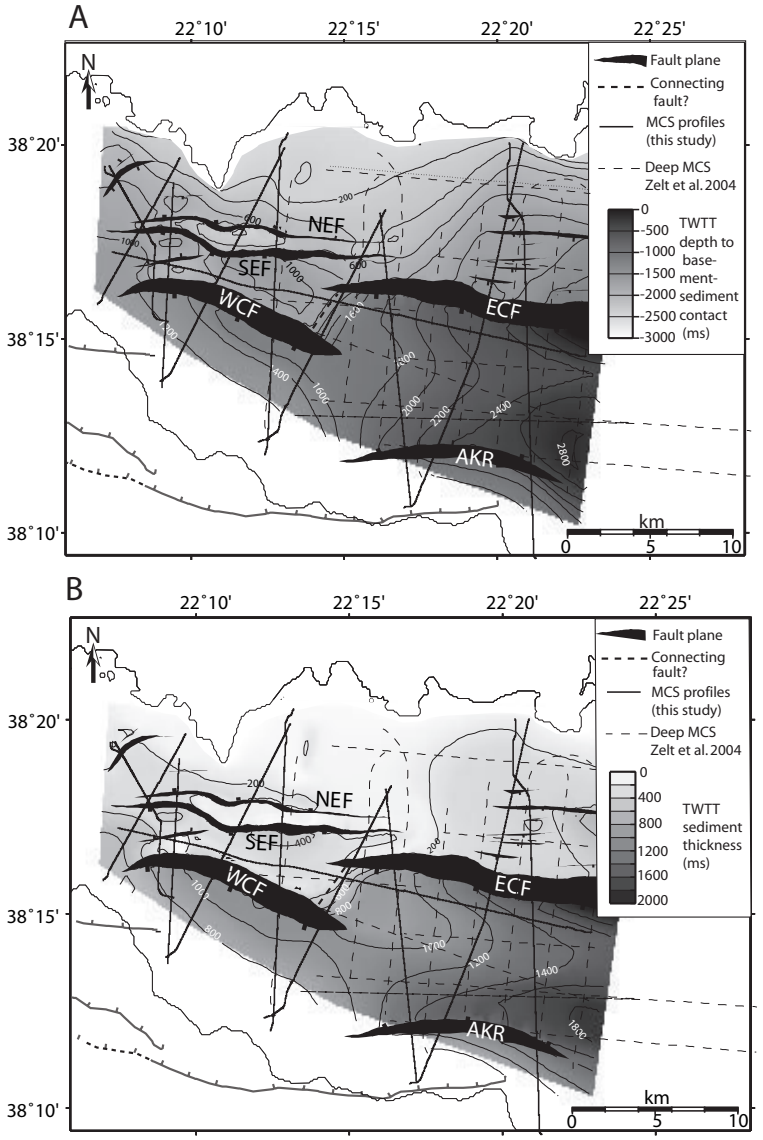

FIGURE 5.8: **A.** TWTT depth to the basement-sediment contact and **B.** TWTT sediment thickness isopach. Produced using the basement interpretations of our MCS study and additional basement interpretations from deep seismic reflection profiles from the R/V Maurice Ewing cruise EW0108/2001 (Zelt et al. 2004, ; seismic images accessed through the Marine Seismic Data Center at http://www.ig.utexas.edu/sdc/)

structure. Tie lines crossing this region suggest that the relay ramp has been breached by a connecting fault which now links the West and east Channel faults (Fig. 5.8 and seen in Fig. 5.6), but the precise orientation of this fault cannot be resolved.

The North Eratini fault has caused subsidence and ∼8° tilting of the basement toward the south and production of the Eratini sub–basin against the uplifted horst footwall block (Fig. 5.8 and shown in Fig. 5.3). North of the Eratini sub–basin, on the shelf, the basement platform is sub-horizontal at a depth of ∼100 m. Activity in the hanging wall of the South Eratini fault has resulted in tilting and deepening of the basement

surface northwards. Thus the western Gulf of Corinth basement topography is highly variable and is clearly controlled by major active normal faults.

5.4.2 Fault Architecture

The North and South Eratini faults have a similar length of ∼15 km and overlap completely, producing a prominent topographic basement horst between the fault traces (Figs. 5.7, 5.8, 5.9 and 5.10). The North Eratini fault dips N at ∼60° (producing the Eratini sub–basin in its hanging wall) and the South Eratini fault dips S at 50 – 60° exposing steep basement fault scarps that are visible in the bathymetric data (Fig. 5.7). Toward the western fault tips the basement horst is buried (Fig. 5.9) and it reaches a minimum depth below sea level of 150 m in the fault center (Fig. 5.10).

To the east, the East Channel fault is observed in the seismic profiles as a basement–displacing fault that creates a sediment sea bed scarp (Figs. 5.8 and 5.11). The fault dips ∼60 – 70° S in shallow sediments decreasing to ∼45 – 55° in basement (data from Goodliffe et al. 2003, Zelt et al. 2004). The East Channel fault overlaps the eastern tip of the South Eratini fault by ∼5 km (Figs. 5.7 and 5.8).

The West Channel fault (equivalent to the Sub-channel fault of McNeill et al. 2005a) overlaps the North and South Eratini faults, lies ∼3 km south of the South Eratini fault, and dips S at ∼45 – 60° within shallow sediments (Fig. 5.10). This fault controls the position of the central axial channel for at least 15 km and overlaps the tip of the East Channel fault by ∼2 km (Fig. 5.7). This fault has also been interpreted by Stefatos et al. (2002) and is clearly visible with significant basement offset in deeper seismic profiles (e.g., Goodliffe et al. 2003, Zelt et al. 2004, : Fig. 5.8).

The Akrata fault (also interpreted by Stefatos et al. 2002) produces steep sediment slopes along the southern margin of the Gulf and causes significant basement offset for ∼15 km (Figs. 5.8 and 5.11, supplemented by data from Goodliffe et al. 2003, Zelt et al. 2004). The Akrata fault dips N at ∼60° and lies ∼4 km north of, and may be a splay of the major East Eliki fault.

In addition to these major active normal faults, a number of more minor basement and seafloor–displacing faults also exist. West of Eratini, short (∼4 – 5 km) fault segments dissect the basement into three horst blocks and graben, trending roughly NE–SW (Figs. 5.7 and 5.9). The Trizonia sub-aerial horst block (Fig. 5.1) is probably one of these local horst–graben systems. Just south of the Galaxidi peninsula, a series of ∼3 – 10 km long faults offset the basement surface (Fig. 5.7 and N end of Fig. 5.11).

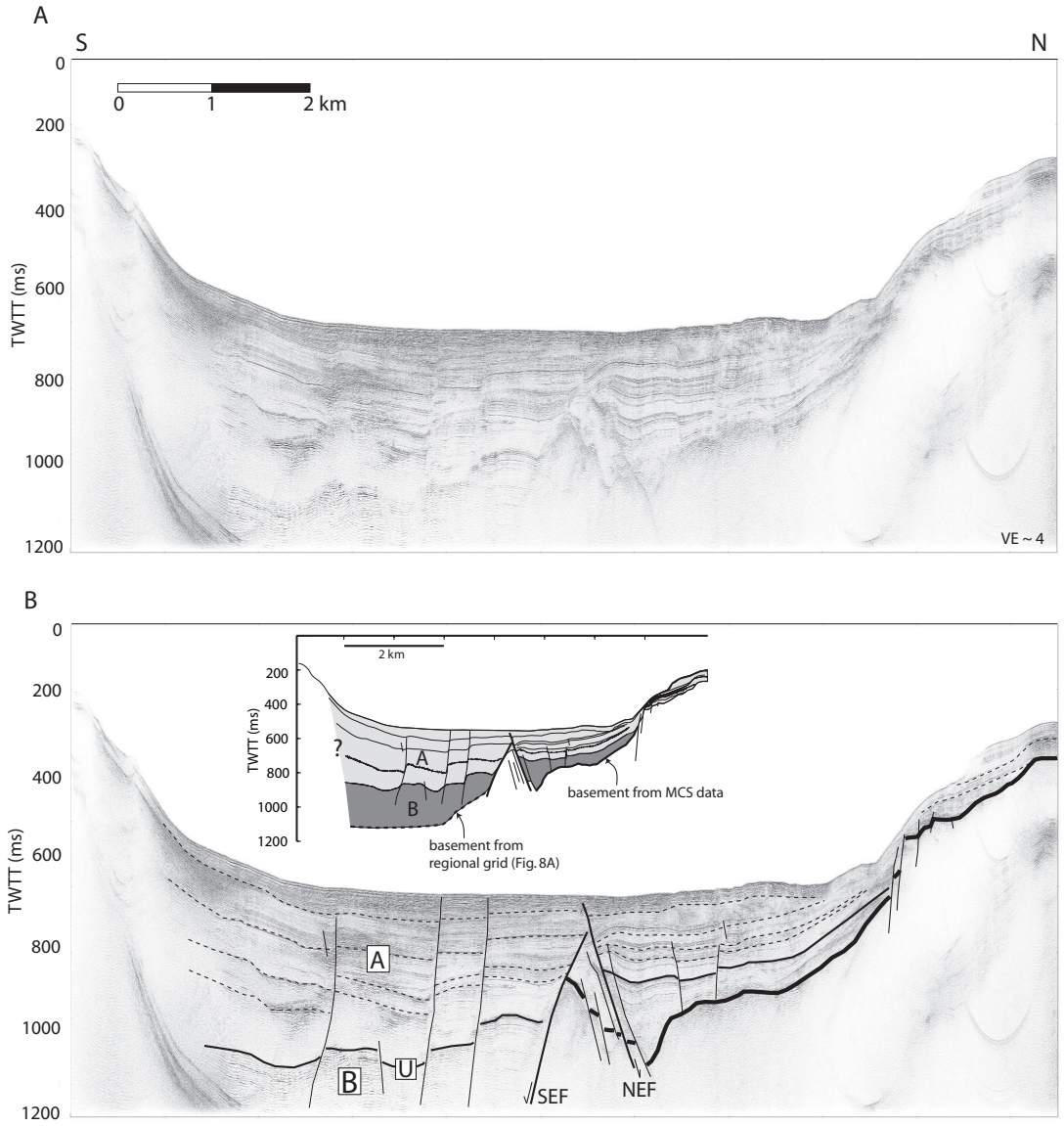

FIGURE 5.9: (A.) MCS data from the west of the study area (location in Fig. 5.7). (B.) Structural interpretation of the sub–bottom structure and inset line drawing showing basement depth for this location from Fig. 5.8.

5.4.3 Slip rates

5.4.3.1 North Eratini fault

The stratigraphy and preservation of four lowstand clinoformal deltas within the Eratini sub-basin (Figs. 5.3 and 5.4) is a function of the balance between sediment influx, eustatic and local sea level fluctuation and tectonic activity (namely fault–controlled subsidence). The slope break positions of the clinoformal units (e.g. Fig. 5.3) are useful as they are believed to form in ∼0 – 10 m of water (M. Leeder, pers. comm., 2006) and are thus good paleo sea level indicators. Fig. 5.12 A shows the average depths to each of the four lowstand delta slope breaks in Package A (Figs.

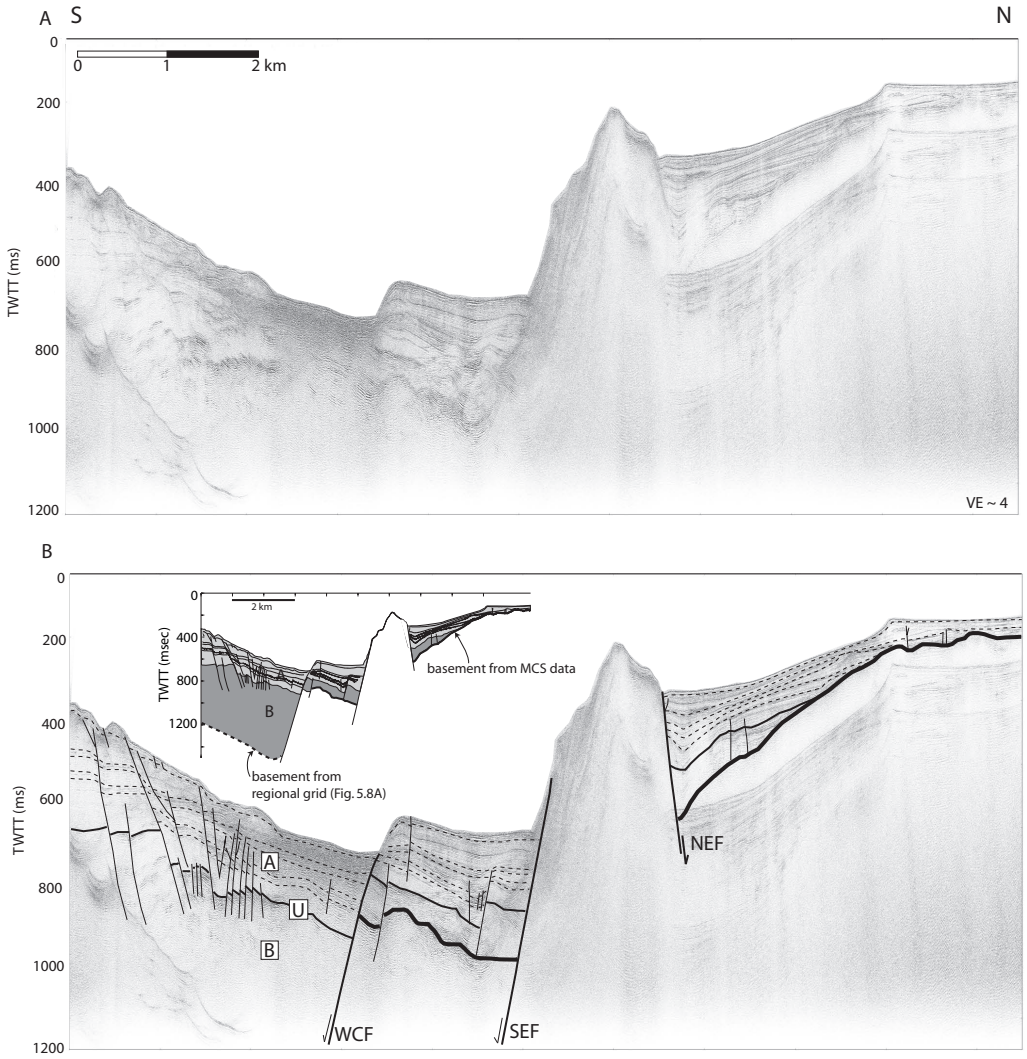

FIGURE 5.10: (A.) MCS data from the center of the study area (location in Fig. 5.7). (B.) Structural interpretation of the sub–bottom structure and inset line drawing showing basement depth for this location from Fig. 5.8.

5.3 and 5.13 A), and the vertical subsidence for each of the horizons is given in Table 5.4 (assuming lowstand level was controlled by a relatively static Rion sill). The subsidence at the fault plane itself, rather than at the slope break positions (∼2.5 km from the fault), is thought to be ∼10% higher, given the best fit displacement decay curves of Armijo et al. (1996), and we have used this value in our calculations. In order to estimate the throw on the fault from the subsidence component we can apply an uplift: subsidence ratio in order to determine total slip rate. Applying the methodology of McNeill et al. (2005a), and based on a review of the available literature and long term uplift: subsidence estimates in the Gulf and measured fault dip, we have used a ratio of 1:1.2–2.2. This yields a late Quaternary to Holocene slip rate on the North Eratini fault of 0.9 – 1.8 mm/yr and 2 – 6.7 mm/yr for the

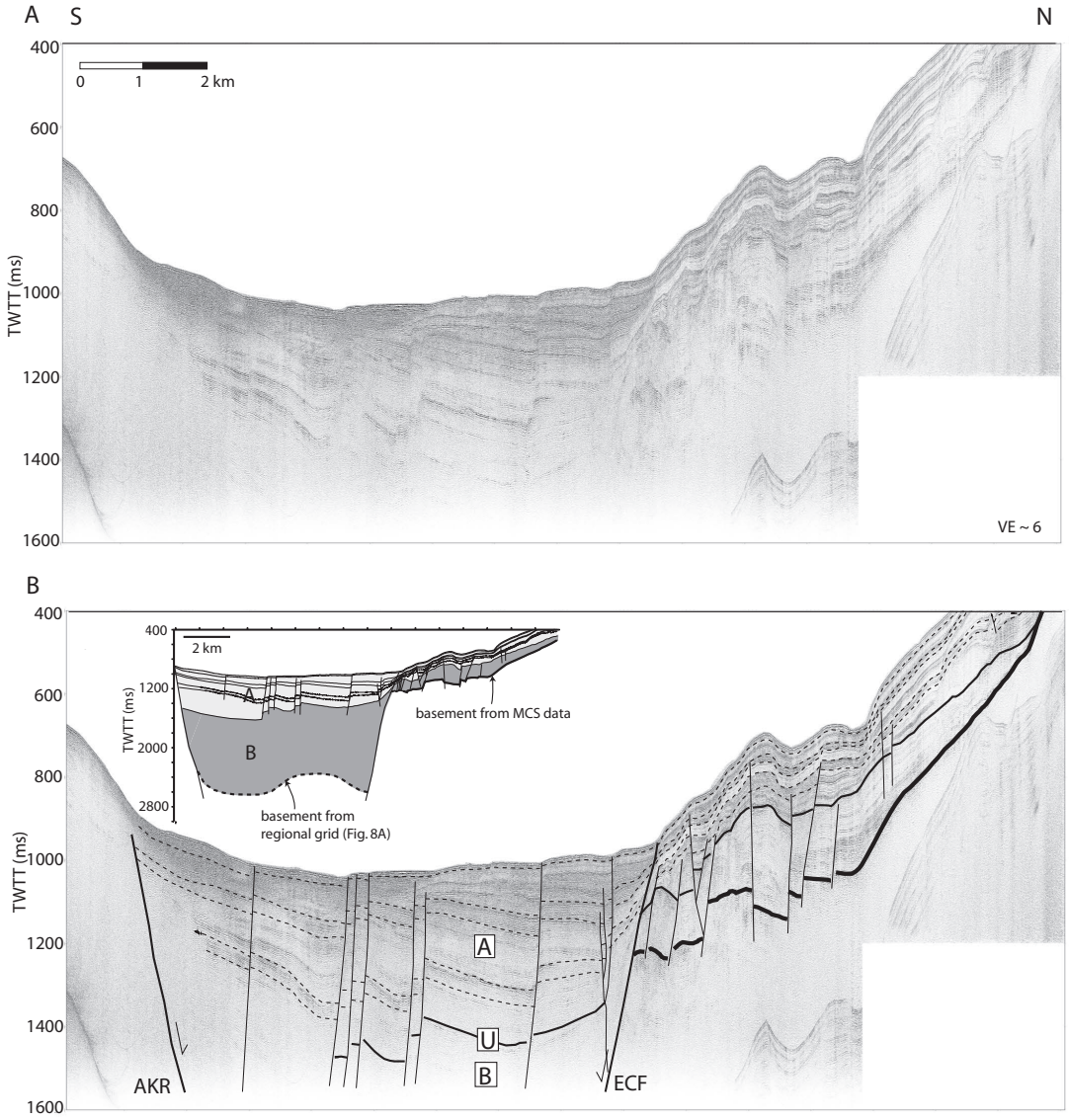

FIGURE 5.11: (A.) MCS data from the east of the study area (location in Fig. 5.7). (B.) Structural interpretation of the sub–bottom structure and inset line showing basement depth for this location from Fig. 5.8.

Holocene (Table 5.4 and Fig. 5.13 B). Due to the young age (ca. 12 ka) and shallow depth of C1 the uncertainty in the slip rate calculation is higher than for the other shorelines, yet we are confident that subsidence has significantly accelerated in the Holocene.

The apparent basement throw of the North Eratini fault provides an additional slip–rate estimation (averaged over ∼0.5 myr), which is a minimum value due to the possibility of erosion of the top of the horst block (Figs. 5.10 and 5.13 A). Total basement offset of ∼400 m yields a minimum Quaternary averaged slip of ∼0.9 mm/yr for the center of the North Eratini fault, similar to the rate derived from clinoform subsidence (Fig. 5.13 B).

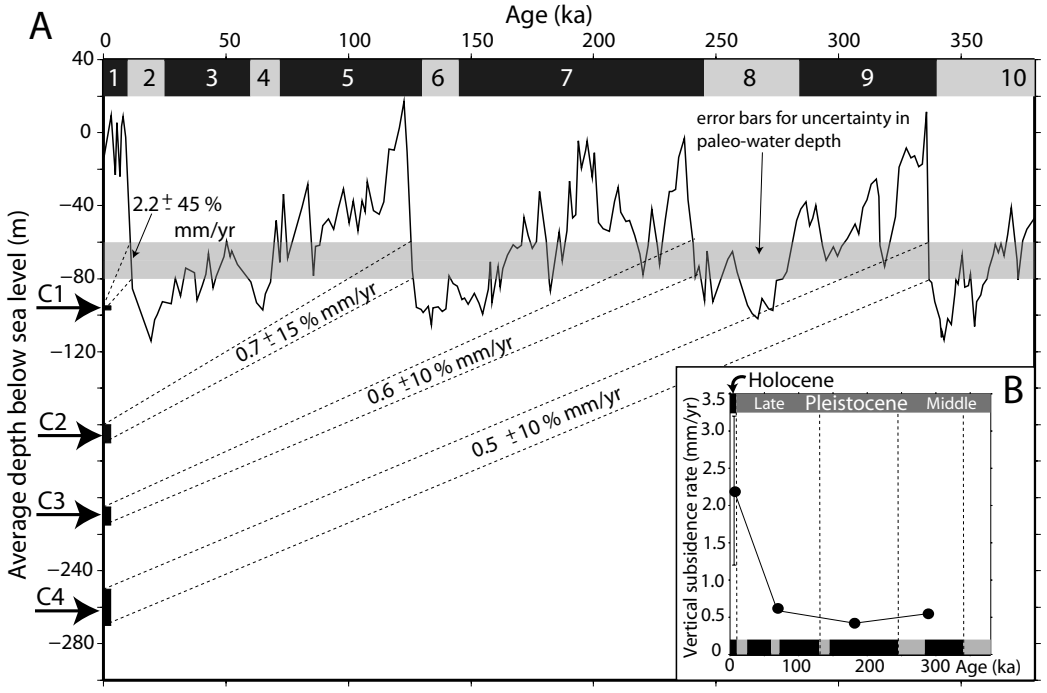

FIGURE 5.12: **A.** Comparison of the average depth of buried clinoform slope breaks, C1 – C4 (Fig. 5.3) with the eustatic sea level curve of Siddall et al. (2003). **B.** Subsidence rates at the fault plane averaged within each time step between shoreline formation. Results suggest that subsidence was relatively constant within the Late Pleistocene but has increased within the Holocene, assuming sill depth, lowstand level and water depth of formation are approximately constant and accurate.

Paleoshoreline	Age (ka)	Depth (m)	Vertical subsidence (m)	Fault slip rate* (mm/yr)
C1	ca. 12	~95	~25 ± 10	2–6.7
C2	ca. 130	~160	~90 ± 10	1–1.9
C3	ca. 240	~210	~140 ± 10	0.9–1.5
C4	ca. 340	~260	~190 ± 10	0.9–1.4

Note: Fault-slip rates in this table are averages between the time of formation of the clinoform surface and present day.

*Assuming a 10% decay in subsidence at ~2.5 km from fault plane and an Uplift:Subsidence ratio of 1:1.2–2.2

TABLE 5.4: Slip rates for the North Eratini fault derived from subsidence of paleoshorelines in the Eratini sub–basin

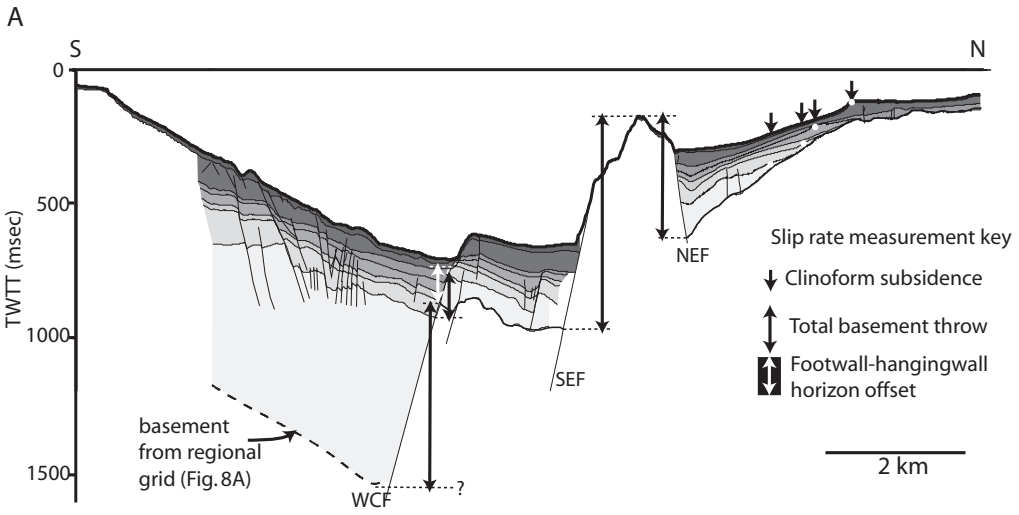

B

Fault	Age range (ka) 0 12 125 240 340 400 500 1500	Slip rate measurement
NEF	2 -6.7; 1 - 1.8; 0.9 - 1.5; 0.9 - 1.4; 0.5 - 0.7; 0.3 - 0.6; 0.4 - 0.6; slip rates in mm/yr	Clinoform subsidence
WCF	~0.4; ~0.5; ~0.15; ~0.6; ~0.7	Horizon offset; Horizon offset; Horizon offset; Interpolated basement throw
ECF	~1.2	Interpolated basement throw

FIGURE 5.13: **A.** Subsided shoreline, total basement throw and stratigraphic offset measurement methods used in the determination of estimated slip rates for different time periods. **B.** Summary of the estimated slip rates, in mm/yr, for each fault over different time periods, using the three measurement methods described in (A). Slip rates in white boxes have the highest confidence level; those in light gray boxes are associated with uncertainty in unknown paleo–topography and those in black have been determined using the interpolated basement structure of Fig. 5.8.

5.4.3.2 South Eratini fault

No horizons can be correlated between the South Eratini fault hanging and footwall (Fig. 5.10 and 5.13 A). We can only obtain a minimum estimate of average Quaternary fault slip based on the basement throw (Fig. 5.13 A). At the center of the fault, total basement offset is ∼630 m (Fig. 5.10) which gives a minimum slip rate of ∼1.4 mm/yr.

5.4.3.3 West Channel fault

The seismic data show that footwall and hanging wall stratigraphy can be traced across the West Channel fault, however paleo–topography at the time of sediment deposition is uncertain (Fig. 5.10). A significant seafloor scarp related mostly to the axial channel exists today and it is unlikely that post ca. 0.4 Ma horizons were continuous across the fault during their initial deposition. Slip rates calculated based on the offset of these horizons (Fig. 5.13 A) are therefore probably a maximum as some contribution may be due to paleo–topography. Average maximum slip rates derived from offset of the ca. 0.4 Ma unconformity and ca. 0.25 Ma horizon are ∼0.4 mm/yr and ∼0.5 mm/yr respectively (Fig. 5.13 B). Slip rates, however, between ca. 0.4 Ma and ca. 0.25 Ma are significantly reduced at ∼0.15 mm/yr. Little sediment thickening of post ca. 0.4 Ma stratigraphy occurs across the West Channel fault, suggesting low fault activity since then. Paleo–topography created pre ca. 0.4 Ma results in larger than expected horizon offsets and misleadingly high slip rates when total offset on the ca. 0.4 and ca. 0.25 Ma horizons is considered. Total basement offset for the West Channel fault yields an average slip rate since ca. 1.5 Ma of ∼0.6 mm/yr, however we recognise this value is subject to large uncertainties in basement throw (Fig. 5.13 B). Given the measured slip rates we can calculate an estimate of the ca. 1.5 – 0.4 Ma slip rate of ∼0.7 mm/yr (Fig. 5.13 B).

5.4.3.4 East Channel fault

Although footwall and hanging wall stratigraphy is preserved across the East Channel fault, a scarp of up to ∼300 m exists at the modern sea floor (Fig. 5.11). This paleo–topography probably existed throughout post ca. 0.4 Ma deposition, and as such meaningful slip rates can not be derived. In a qualitative sense, the thickening of package A is much smaller than that of package B across the East Channel fault (Fig. 5.11), indicating a decrease in slip rate for the period 0 – ca. 0.4 Ma compared to ca. 1.5 – ca. 0.4 Ma.

Estimates of total basement throw yield average slip rates in the last ca. 1.5 Ma up to ∼1.2 mm/yr (Fig. 5.13 B). The greater total basement subsidence and higher overall slip rate indicate the East Channel fault is more significant than the West Channel fault.

5.5 Basin Evolution

The structure of the western offshore Gulf of Corinth basin appears to be distinct in the east, west and center and we will discuss rift evolution in the context of these three regions (Fig. 5.14). Area 1, to the east, is dominated by two depocentres, one in the hanging wall of the East Channel fault and the other adjacent to the Akrata fault (Fig. 5.8 B). The second region (central, area 2), is more structurally complex with highly variable sea floor and basement topography. In area 3 to the west, the subsurface is broken into a series of NE–SW trending horst and graben. Figure 5.14 shows the locations of these areas and gives interpretations of the full MCS dataset (also see Plates 2.1 and 2.2 at the back of the thesis for the original seismic reflection data from which these interpretations were made).

5.5.1 Eastern study area: Area 1

Basin deformation: ca. 1.5 – ca. 0.4 Ma (Package B)

There is considerable variation in pre ca. 0.4 Ma sediment thickness (package B) within area 1 (Figs. 5.14 A, B, C). The thickness of ca. 1.5 – ca. 0.4 Ma sediments increases five fold between the footwall and hanging wall of the East Channel fault with the greatest thickness occurring at the east end of area 1 reaching $>$ $\sim$1250 m (1 s TWTT) (Figs. 5.14 A, B). Sediment thickness suggests this fault continues further east beyond the study area. The onshore East Eliki fault and offshore Akrata fault have together amassed a package B thickness of $\sim$900 m (0.75 s TWTT) in their hanging walls (Fig. 5.14 B) and the Akrata fault may be a splay of the East Eliki fault. Package B contains a limited number of traceable, coherent reflectors, but the general northward dip of observable horizons and sediment thickening toward the north (Figs. 5.14 A, B), supports the offshore S–dipping East Channel fault being significant at this time and location.

Basin deformation: ca. 0.4 – 0 Ma (Package A)

Package A in this area shows less thickness variation than package B. North of Akrata (Fig. 5.14 B, C and 5.15 A) thickening and tilting of post ca. 0.4 Ma sediments is consistently toward the south. At this location, the N–dipping East Eliki fault on the south margin of the Gulf, and the Akrata fault control overall southward tilting and sedimentation post ca. 0.4 Ma.

Sediment thickness change across the East Channel fault is much less exaggerated than in the period ca. 1.5 – ca. 0.4 Ma. Although thickening occurs across the East Channel fault, into its hanging wall (Figs. 5.14 A, B, C) and Holocene deformation proves the structure still active, south coast faults (East Eliki and Derveni fault?) dominate post ca. 0.4 Ma, and activity on the East Channel fault has decreased.

5.5.2 Central study area: Area 2

Basin deformation: ca. 1.5 – ca. 0.4 Ma (Package B)

The greatest thickness of pre ca. 0.4 Ma sediments within area 2 is seen in the hanging wall of the West Channel fault with a maximum thickness of ∼850 m (∼0.7 s TWTT),

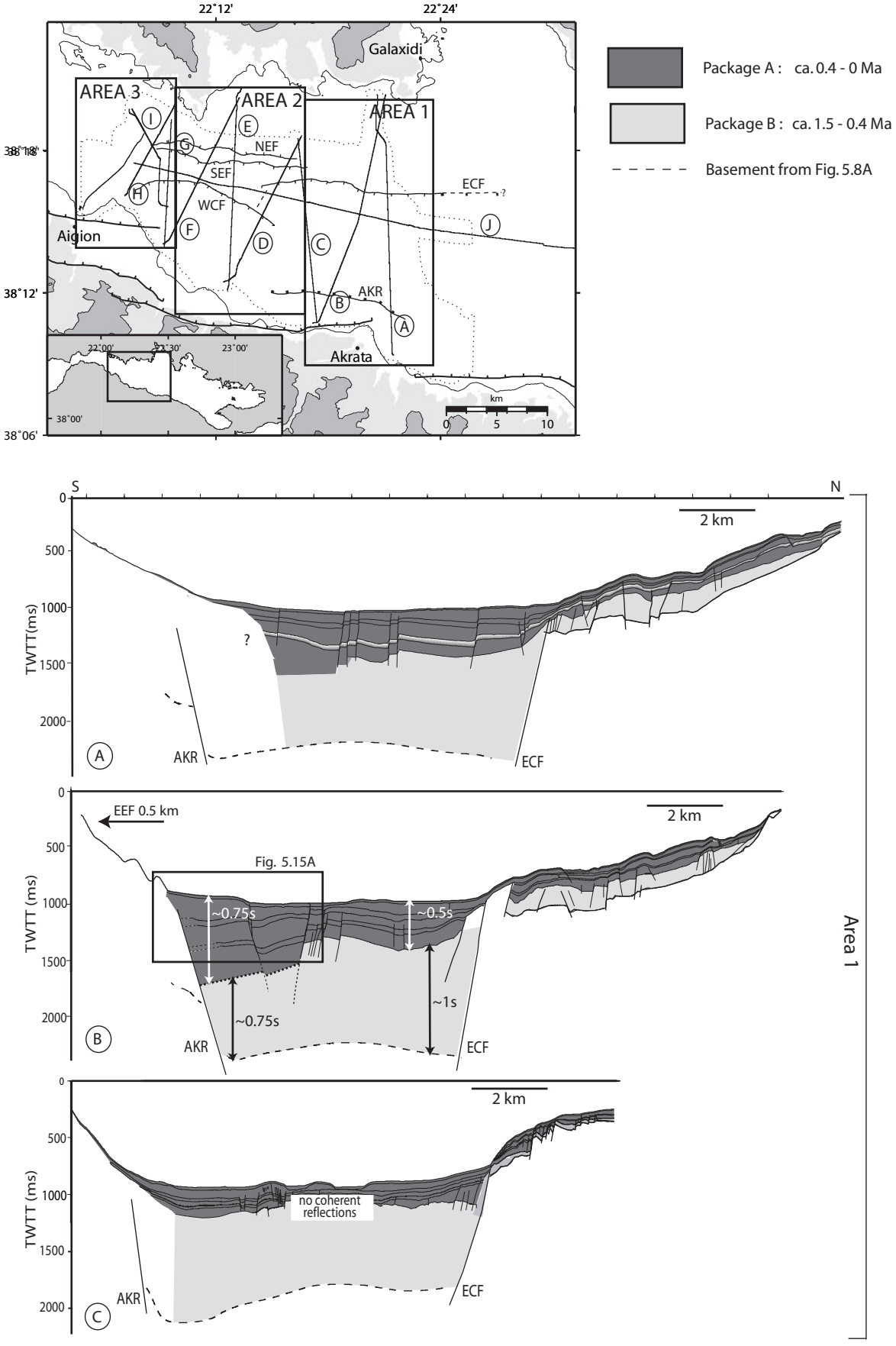
22°12'
22°24'
Galaxidi
AREA 3
AREA 2
AREA 1
I
E
G
NEF
SEF
H
WCF
ECF
F
D
C
J
Aigion
AKR
B
A
38°12'
22°00'
22°30'
23°00'
Akrata
38°00'
38°06'
km
0
5
10
Package A : ca. 0.4 - 0 Ma
Package B : ca. 1.5 - 0.4 Ma
Basement from Fig. 5.8A
S
N
2 km
TWTT(ms)
?
AKR
ECF
EEF 0.5 km
Fig. 5.15A
~0.75s
~0.5s
~1s
~0.75s
no coherent reflections
Area 1

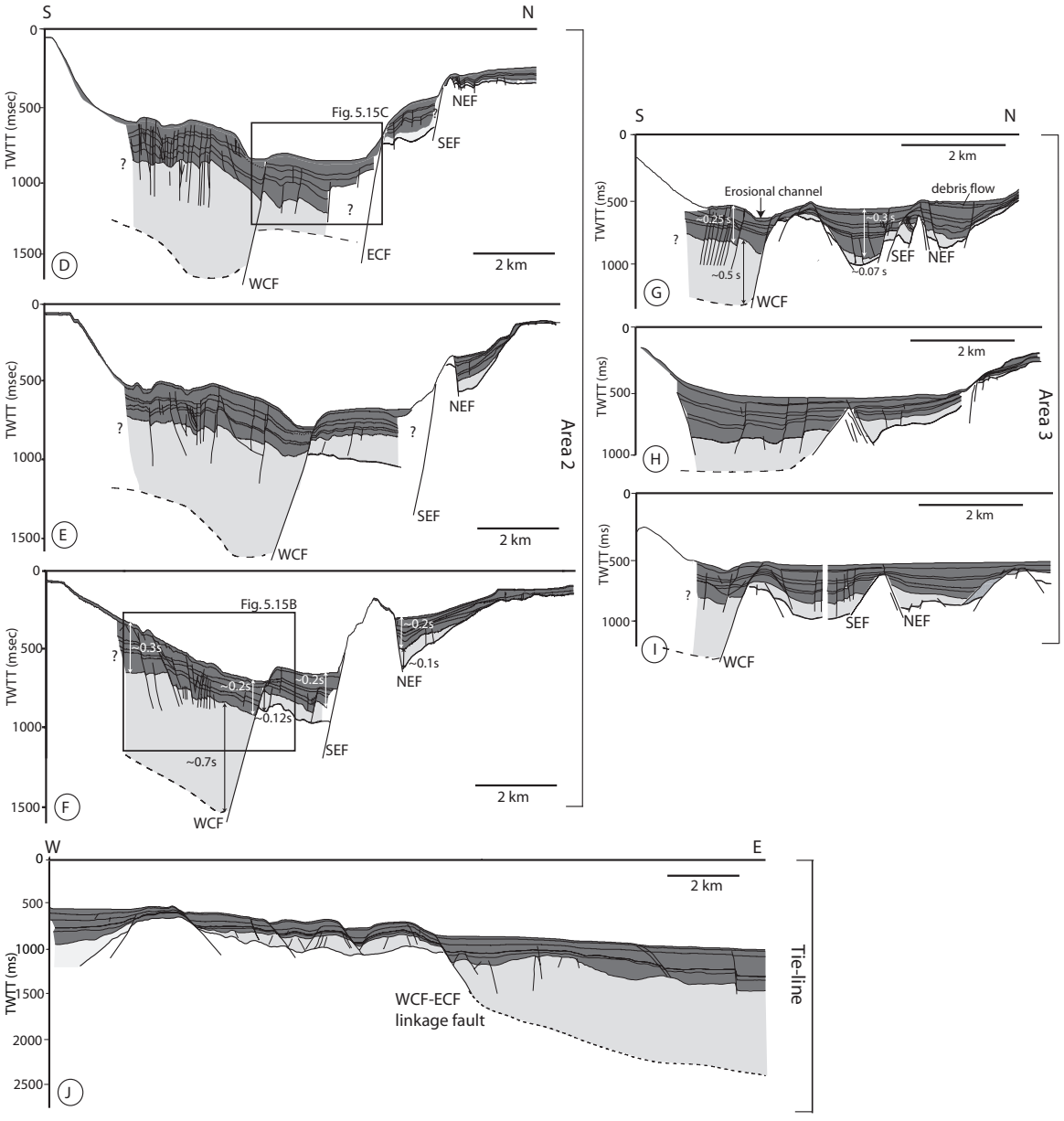

FIGURE 5.14: **A, B, C, D, E, F, G, H, I, J** Stratigraphic interpretations for the MCS data set in the western Gulf of Corinth. Basement depths are observed directly from the MCS data or derived from the regional grid in Figure 5.8 A (see section 5.4.1 for method).

significantly thinner than was observed further east (area 1) (Figs. 5.14 D, E, F). The basement–sediment contact in the hanging wall of the West Channel fault, and reflections within package B show a dominant tilt north. Package B sediments in the footwall of the West Channel fault and within the hanging wall region of the North and South Eratini faults are much thinner, at ∼180 m (0.15 s TWTT). This suggests that in the time period between the initiation of offshore syn–rift sedimentation and ca. 0.4 Ma, the dominant structure was the West Channel fault. Its dominance over N–dipping south coast faults, during at least some part of the deposition of package B, as we do not image package B in its entirety, is clear from the N–tilted sediments and half graben geometry (Fig. 5.14 D, E, F).

Basin deformation: ca. 0.4 – 0 Ma (Package A)

Stratigraphy at the southern end of profiles in area 2 thickens and tilts south, probably due to the activity of the onshore N–dipping East Eliki fault; this is most obvious in profile Figure 5.14 F and 5.15 B. Package A sediments here are the thickest within area 2 at ∼350 m (∼0.3 s TWTT). Sediments clearly tilt northward toward the West Channel fault, but stratigraphic thickening is minimal due to the axial channel location which disrupts sediment deposition patterns. Between the West Channel fault and the area more greatly influenced by the East Eliki fault to the south, is a zone of minor faulting (Fig. 5.15 B) which can be traced over a distance of 10 km E–W.

The East Channel fault, which dominated stratigraphy within area 1, dies out westward within area 2 (Fig. 5.7). The data suggest the East Channel fault becomes a complex zone at its western tip (shown in Fig. 5.15 C). Package A sediments in the hanging wall of the central South Eratini fault tilt and thicken to the north (Fig. 5.14 F), but further east (Fig. 5.14 D) the sediments reverse their tilt and dip south suggesting a decrease in activity on the South Eratini fault or an increasing dominance of N–dipping faults to the south. Modern to ca. 0.4 Ma sediments within the Eratini sub–basin tilt and thicken toward the North Eratini fault with local drag folding (Fig. 5.3).

5.5.3 Western study area: Area 3

Basin deformation: ca. 1.5 – ca. 0.4 Ma (Package B)

Package B sediments in the far west (area 3) are significantly thinner than to the east (areas 1 and 2). Sediment thicknesses of up to ∼600 m (∼0.5s TWTT) are estimated within the West Channel fault hanging wall, but elsewhere thicknesses of < 80 m (∼0.07s TWTT) are observed (Fig. 5.14 G, H, I). North of the West Channel fault fault trace, very little sediment is deposited, suggesting minimal subsidence.

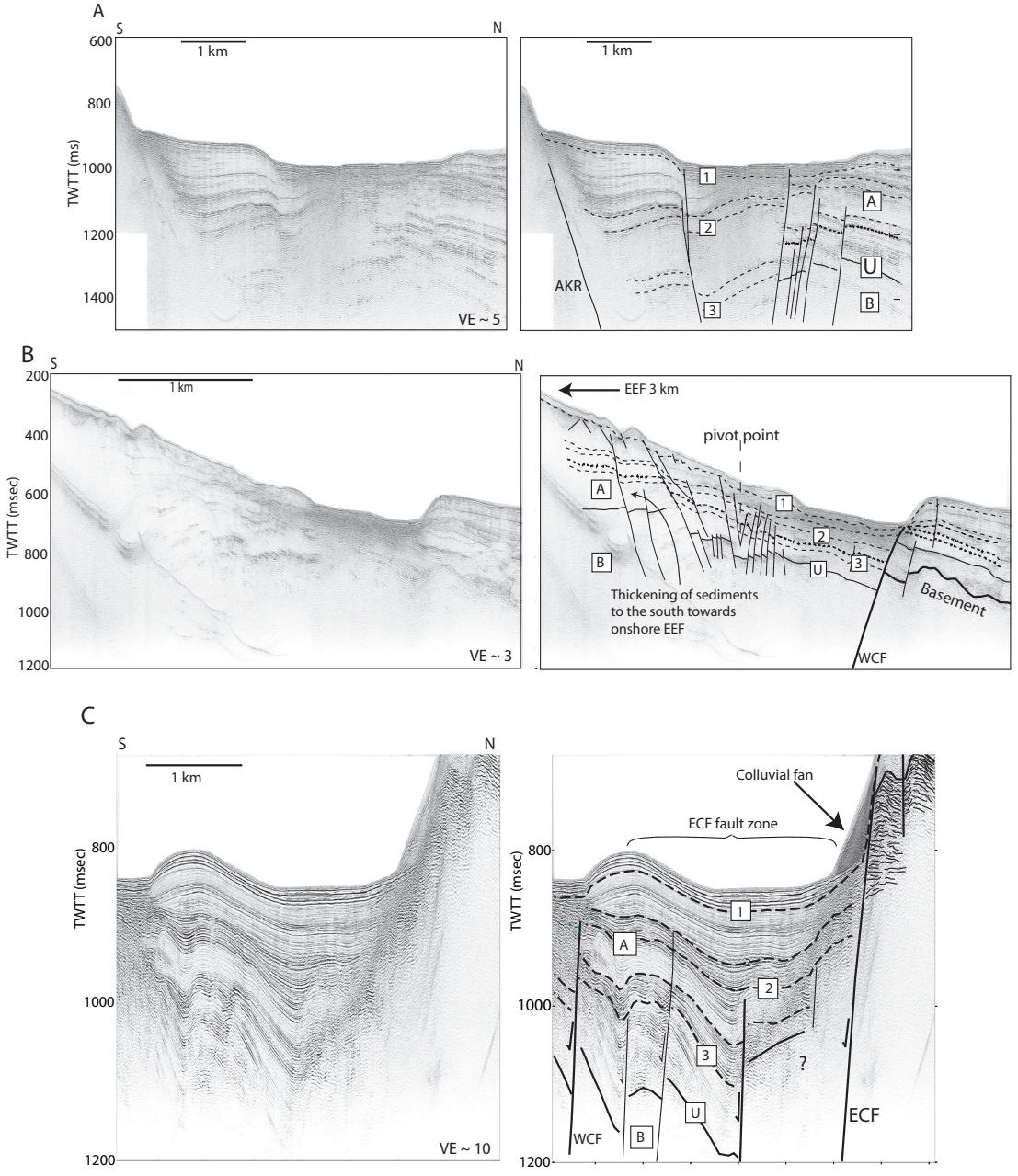

FIGURE 5.15: **A.** Un–interpreted and interpreted MCS data for the boxed region in Figure 5.14 B. Post ca. 0.4 Ma sediments show a southward tilt toward the East Eliki and Akrata faults at the south end of the profile. **B.** Un–interpreted and interpreted MCS data for the boxed region in Figure 5.14 F. Sediments to the south show a preferred southward tilt toward the onshore East Eliki fault, whereas those to the north dip toward the S–dipping West Channel fault. Intense minor faulting exists between sediments dipping with a preferred north and south orientation. **C.** Un–interpreted and interpreted view of the East Channel fault from the central western gulf (Fig. 5.14) **D.** The East Channel fault is a complex fault zone with activity pre ca. 125 ka (horizon 2) being concentrated on a buried fault to the south of the East Channel fault. Note exaggerated vertical scale compared to Figs. 5.15 A and B.

Basin deformation: ca. 0.4 – 0 Ma (Package A)

The thickness of package A is very similar to that further east (areas 1 and 2) reaching ∼350 m (∼0.3 s TWTT) (Figs. 5.14 G, H, I). As well as in the hanging wall of the West Channel fault, deposition occurs within two main symmetrical graben, controlled by the western tips of the North and South Eratini faults (and associated splays), together with a number of shorter basement–offsetting faults (Fig. 5.7). Significant sediment deposition occurs within these graben which were not active prior to ca. 0.4 Ma. A number of significant Holocene debris flow events are seen within package A in area 3.

5.6 Discussion

5.6.1 Offshore western Gulf fault activity

Our analysis has led to a quantitative understanding of the timing and magnitude of activity on offshore western Gulf faults. Based on the stratigraphic age and sedimentation rate interpretations discussed above, the West Channel and East Channel faults began accumulating syn–rift sediments ca. 1.5 Ma, whilst the North and South Eratini faults became active much later at ca. 0.5 Ma. From ca. 1.5 – ca. 0.5 Ma the East and West Channel faults were the dominant offshore faults, having individual slip rates of 0.6 – 1.2 mm/yr averaged over this period, and produced deep subsided depocentres in what is now the center of the western Gulf basin. Their activity during this early stage, and locally greater influence than N–dipping south coast faults, is clear in the northward basement tilt and northward sediment thickening (Fig. 5.8). Slip rates on the West Channel fault decrease toward its western tip, with reduced subsidence in the western area 3.

Since the activation of the North and South Eratini faults at ca. 0.5 Ma, slip rates have decreased on the East and West Channel fault system (∼0.2 mm/yr for the West Channel fault, Fig. 5.13 B). Minimum Late Pleistocene slip rates of ∼1 – 1.5 mm/yr are predicted for the North and South Eratini faults, with slip rates increasing up to ∼5.5 mm/yr in the Holocene. Post ca. 0.4 Ma stratigraphy at the east end of the study area shows that N–dipping faults on the southern margin (East Eliki and Akrata faults) became relatively more dominant at ca. 0.4 Ma, resulting in southward tilting and fanning of sediments. The present overall graben geometry of this eastern area results from the net effect of alternating activity on these faults (similar to interpretations by Sachpazi et al. (2003) in the central Gulf). The central part of the study area is only weakly influenced by south margin faults post ca. 0.4 Ma and the S–dipping South Eratini fault dominates in maintaining a N–thickening half graben, despite the reduction in activity of the West Channel fault. In the west the growth

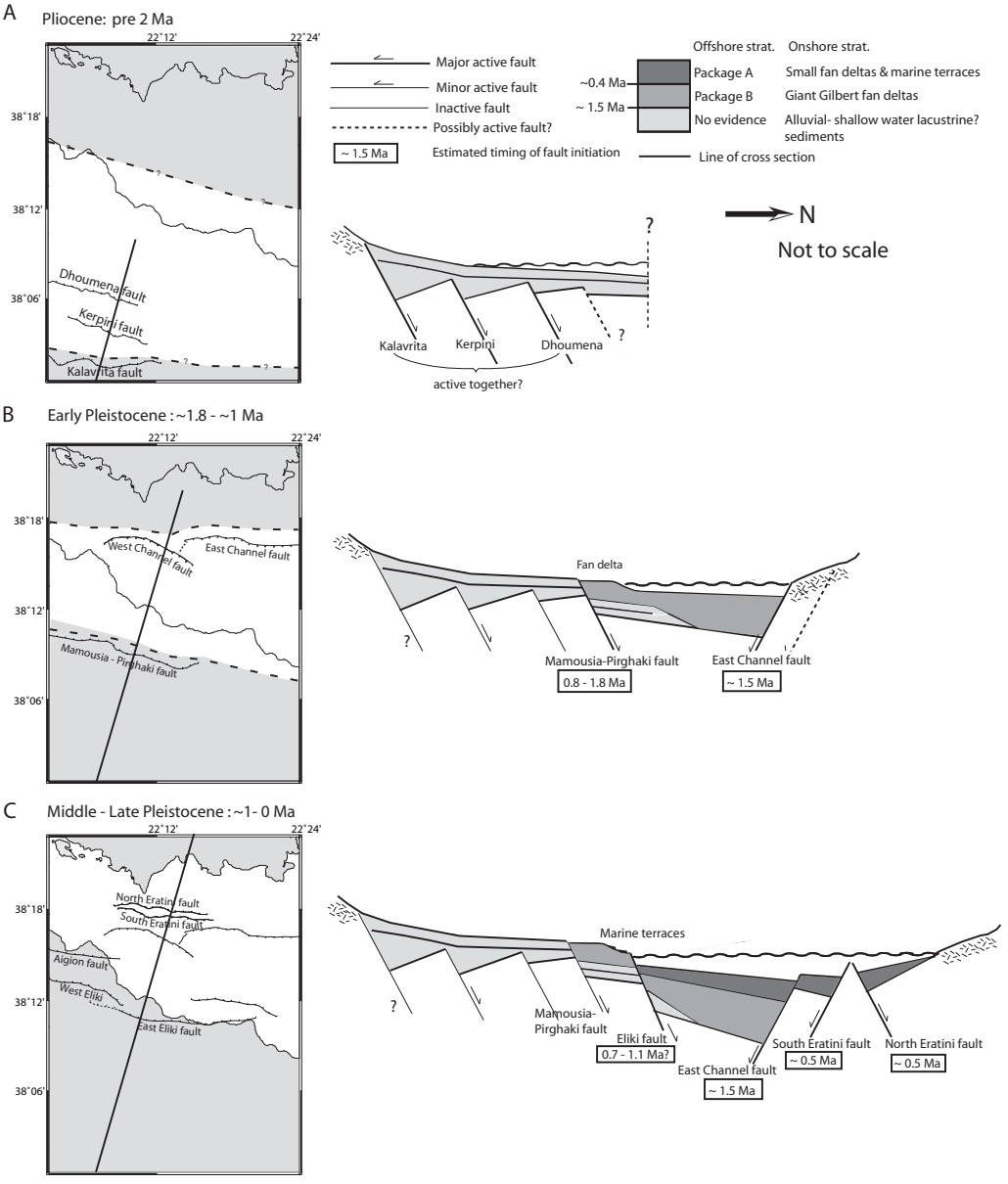

FIGURE 5.16: Maps to show major active faults and possible positions of the coastline during the development of the western Gulf of Corinth, together with schematic cross sections. **A.** Pre ca. 2 Ma a number of faults were active leading to the subsidence of a wide basin with unknown northern extent. **B.** During the Early Pleistocene the rift was controlled primarily by the Mamoussia-Pirgaki fault in the south and the East and West Channel fault system to the north. **C.** Within the last ca. 1 Ma activity has become focused on the Aigion and East Eliki faults along the southern margin and ca. 0.5 Ma activity on the northern margin transferred onto the North and South Eratini faults. South coast rift geometry after Collier & Jones (2003).

of North and South Eratini faults and other basement displacing faults has produced large post ca. 0.4 Ma accumulations of sediment.

5.6.2 Western Gulf of Corinth rift evolution

Various tectonic models have been proposed to explain the evolution of the western Gulf of Corinth based on the south coast geology and stratigraphy (e.g., Ori 1989, Doutsos & Piper 1990, Sorel 2000, Rohais et al. 2007). We attempt to incorporate our findings into the framework of these models and move toward a complete scenario for rift evolution. Figure 5.16 presents schematic cross sections of the dominant faults during different time periods.

The earliest onshore syn–rift sediments from the western Gulf of Corinth have not been dated, but are thought to be similar in age to the oldest sediments found in the Corinth area, ca. 3.6 – 4 Ma (Collier & Dart 1991, Rohais et al. 2007). Geological mapping and onshore stratigraphic analysis suggest that the initial rift was wide, with activity distributed over a number of faults including the Kalavrita, Kerpini and Doumena faults in the Eliki region (Collier & Jones 2003, Rohais et al. 2007). The location of the northern boundary of the rift in the Pliocene (>2 Ma) is unknown, but sediments during this time were deposited under alluvial to shallow water lacustrine conditions (Collier & Jones 2003, Rohais et al. 2007, Fig. 5.16 A).

This period of distributed extension was terminated by the focusing of activity on the Mamoussia–Pirgaki fault and deepening of the rift allowing deposition of giant Gilbert fan deltas (Dart et al. 1994, Collier & Jones 2003, Rohais et al. 2007, Fig. 5.16 B;) in the Early Pleistocene, ca. 0.8 – 1.8 Ma (Symeonidis et al. 1987). We have demonstrated that the offshore East and West Channel faults began accumulating syn–rift sediment in Early Pleistocene time (ca. 1.5 Ma), and so these S–dipping faults may have formed the northern boundary of the Pleistocene rift at this time (Fig. 5.16 B). The focusing of extension resulted in a narrowing of the basin compared to the pre ca. 2 Ma structure.

Extension transferred north onto the Eliki fault systems and other modern south shore faults in the Early–Middle Pleistocene, leaving the Mamoussia-Pirgaki fault relatively inactive (Fig. 5.16 C). The magnitude of Eliki footwall uplift (800 – 1000 m) and Late Pleistocene average uplift rates (McNeill & Collier 2004, 1 – 1.5 mm/yr;) suggest this fault initiated between 0.7 and 1 Ma. Along the northern margin, ca. 0.5 Ma activity transferred from the East and West Channel fault system northwards to the North and South Eratini faults (Fig. 5.16 C); since 0.2 – 0.3 Ma the Aigion fault has initiated, continuing the pattern of northward fault propagation (De Martini et al. 2004, McNeill et al. 2007).

Across a profile 22°15'E there are four major faults, the East Eliki, West Channel, North Eratini and South Eratini faults. Horizontal components of extension for the East Eliki fault are 2 – 4 mm/yr (McNeill et al. 2005a) and have been calculated

in this paper to be 1 – 3.5 mm/yr for the North Eratini fault during the Holocene. Recent rates on the South Eratini and West Channel can not be calculated directly from stratigraphy, but if we assume similar values, the summed horizontal extension component across the western Gulf is 5 – 14.5 mm/yr. This covers the range of recent geodetic measurements of extension of 10 – 15 mm/yr, suggesting geological and geodetic rates of deformation can be reconciled with the major faults identified.

5.6.3 Total Gulf of Corinth structure and evolution

Comparison of our interpretations with those in the central and eastern Gulf of Corinth highlights important structural and evolutionary differences. In the central Gulf the early structure was controlled by S–dipping faults (Stefatos et al. 2002, Sachpazi et al. 2003, also imaged in our Fig. 5.14 B). Later the polarity of the deformation reversed so activity focused on N–dipping faults resulting in sediment thickening to the south. Overall, the net basin geometry caused by these two facing subsiding half grabens with differing border fault polarity, resembles a symmetric graben. Deformation in the eastern Gulf of Corinth and the Alkyonides Gulf has been controlled by N–dipping faults creating a half graben which shows sediment thickening to the south, throughout the basin history (Stefatos et al. 2002, Leeder et al. 2005) (Fig. 5.16 B). On a length scale of ∼20 km the east, central and west parts of the Gulf of Corinth have developed distinctly throughout rift history.

5.6.4 Faulting at depth

We have discussed the evolution of the western Gulf rift as observed from the interpretation of onshore geology and offshore basin fill. We have not directly imaged faults below ∼1.5 km, however our results can contribute to the frequently debated subject of high vs. low angle faulting in young continental rifts (Rosendahl 1987, Taylor et al. 1999). In general, there is limited information on the geometry of Gulf of Corinth faults at depth, and we attempt to combine the various published ideas in the discussion below using Figure 5.17.

Sorel (2000) suggest there is a low angle detachment surface initiating at the Khelmos fault in the Western Gulf; this detachment projects northward into the offshore basin at ∼2 km depth (Fig. 5.17). Collier & Jones (2003) suggest this low angle fault is actually due to rotation of an initially high angle fault. They find detailed mapped fault patterns are inconsistent with propagation along a low angle detachment (Fig. 5.16 A and B and discussion above). Taylor et al. (2003) suggest a 10 – 20° detachment surface offshore at 2.5 – 4 s TWTT in seismic reflection data. This ∼3 km detachment corresponds roughly to the sediment–basement contact in the western Gulf, however a convincing detachment surface at this depth is not clear in this dataset where available. It is unknown if this detachment could link to the unconfirmed Sorel (2000) detachment, however Figure 5.17 suggests they may be at different depths.

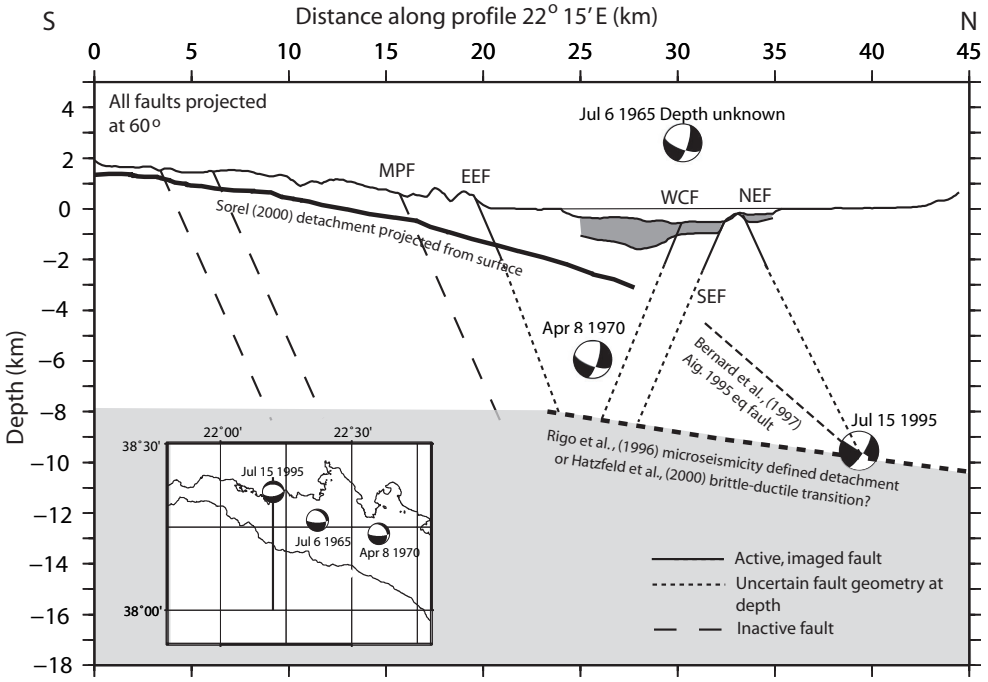

FIGURE 5.17: Summary of evidence concerning the geometry and interaction of western Gulf of Corinth faults at depth. Inset shows the position of the transect and locations of Ms > 5 seismicity in the area from Ambraseys & Jackson (1990) and Bernard et al. (1997). Faults observed on the southern coastline are from Collier & Jones (2003) and offshore faults from this study. Faults have been projected with dips of 60° down to the probable depth of the brittle–ductile transition as dashed lines. The position of the detachment surface proposed by Sorel (2000) and Rigo et al. (1996) have been projected onto this line. Note that these are distinct features at very different depths. The 1965, and 1970 earthquakes may be compatible with slip on either the West Channel or South Eratini faults, given errors in the locations of hypocenters. The best–fit modelled fault plane for the 1995 Aigion earthquake from Bernard et al. (1997) is shown.

Low angle faulting has also been suggested from patterns of microseismicity. Rigo et al. (1996) and Gautier et al. (2006) propose that microseismicity defines a 10 – 20° N–dipping plane at a depth of 8–10 km (Fig. 5.17). This possible low–angle feature must be a different structure from that described by Sorel (2000) and Taylor et al. (2003). Hatzfeld et al. (2000) alternatively suggest that the 8 – 12 km deep seismicity is related to the seismic–aseismic transition.

The few Ms > 5 earthquakes in the area all have focal mechanisms with 30 – 40° N–dipping and ∼60° S–dipping nodal planes (Fig 5.17, Ambraseys & Jackson 1990, Hatzfeld et al. 1996, Bernard et al. 1997). The focal mechanisms of these earthquakes and their approximate depths and locations show they are fundamentally incompatible with slip on a low angle 10 – 20° detachment. If the steep normal faults observed became listric at depth on intersection with the detachment the seismicity could be better explained, however we see no evidence of fault listricity in shallower parts of the basin.

Our study shows that in the area of the Figure 5.17 transect the predominant basement tilt and sediment thickening is toward the north, indicating dominant S-dipping faults. This is incompatible with a low angle N–dipping detachment, be it at ∼3 km or 10 km depth. Unless there was a ramp–flat intersection in the detachment, as described by Gibbs (1984), in the western Gulf creating a roll–over hanging wall syncline we would not expect to see stratigraphy and basement dipping toward an antithetic of a detachment system due to the major space problems involved. Also the modelling of scaled systems by Exadaktylos et al. (2003) shows the greatest shear displacement with such a low angle detachment geometry will always be on the N–dipping synthetic fault (i.e. the East Eliki fault).

We speculate that the shallow geometry is more easily reconciled with a model in which faults are steep to a brittle-ductile transition, at 8 – 12 km (Fig. 5.17, Hatzfeld et al. 2000). In this model the East Eliki and West Channel faults meet the brittle–ductile transition before they would intersect each other (Fig. 5.17). This is further supported by the fact that cumulative extension rates on on- and offshore faults can explain the geodetic extension rates with no need for enhanced low–angle extension. However, this high angle fault model, which fits observed basin geometry of the western Gulf, is more complexly related to Ms $>$ 5 seismicity. The 1965 and 1970 earthquakes could possibly be attributed to the ∼60° S–dipping East Channel fault further to the east of the Figure 5.17 transect. It is, however, equally difficult to match the focal mechanism of the 1995 Aigion earthquake to high angle offshore faults or to a low–angle detachment.

5.6.5 Comparison with other rifts

The Gulf of Corinth shows similarities and differences with other currently active areas of continental extension. Rift zones such as the East African rift, Baikal and Woodlark basin are highly asymmetric with continental break up focused on half graben (e.g., Rosendahl 1987, Taylor et al. 1999, Scholz & Hutchinson 2000). Similarly, the Corinth rift basin seems to be dominated at any one time by a single border fault that produces asymmetric half graben morphology. Gulf of Corinth border faults change polarity along the rift (Stefatos et al. 2002, McNeill et al. 2005a, and this study). Variations in polarity along strike are well documented in the East African rift (Rosendahl 1987), whereas in the Baikal rift dominant activity is consistently with faults on the northwest side of the rift for ∼650 km (Scholz & Hutchinson 2000). Variations in the polarity of faulting with time are observed in the western Gulf of Corinth and changes in the focus of continental break over time have also been reported from the Woodlark basin (Taylor et al. 1999) and East African rift (Rosendahl 1987).

5.7 Conclusions

We have used data from a seismic and bathymetric study of the western Gulf of Corinth to construct a detailed stratigraphic and tectonic framework for the region. Three major S–dipping (South Eratini, East and West Channel faults) and two N–dipping (North Eratini and Akrata faults) offshore faults are responsible for the basin structure. The oldest sediments in the western Gulf basin date from ca. 1.5 Ma and stratigraphy can be divided into two packages separated by a ca. 0.4 Ma unconformity. Analysis of basement and stratigraphic geometry has revealed that the East and West Channel S–dipping faults dominated structure ca. 1.5 to ca. 0.4 Ma. At around ca. 0.5 Ma activity focused more on the S–dipping South Eratini and N–dipping East Eliki, West Eliki (and Derveni) faults, causing a shift in the basin margins of ∼5 km. Estimated Holocene extension rates on the offshore and onshore faults together can account for the current geodetically measured extension rates across the rift. There is therefore no need for enhanced slip on a low angle detachment beneath the western Gulf, and in order to explain the basement and stratigraphic geometry would require the presence of a ramp and flat trajectory in the detachment, for which there is no evidence. Our improved age constraints for western Gulf initiation and evolution will be useful in future Gulf and Aegean models that attempt to explain the mechanisms that drive rifting. The western Gulf of Corinth shows important similarities with other rifts in terms of the significance of asymmetric half graben–style rifting and border fault polarity changes in space and in time.

Chapter 6

Fault architecture, basin structure and evolution of the Corinth rift, central Greece

---

Bell, R.E., McNeill, L.C., Bull, J.M., and Henstock, T.J.

Manuscript (with minor revisions) to be submitted to Basin Research
May 2008

6.1 Introduction

The style of extension and strain distribution during the initiation and early stages of intra–continental rifting is important for understanding the eventual transition to ocean spreading and rifted–margin development. How rifting evolves from initial extension to continental breakup is still poorly understood, partly due to the lack of young active rift zones with histories uncomplicated by tectonic overprinting. The geometry (high versus low angle, Forsyth 1992), number (single versus multiple, Buck 1991), location and strain rate of faults together with patterns of subsidence recorded by syn–rift sediments (e.g., symmetric vs. asymmetric depocentres, Rosendahl 1987, Stewart & Argent 2000, Le Pourhiet et al. 2003; fault propagation vs. segment linkage, Cartwright et al. 1995, Gawthorpe et al. 2003) provide valuable clues to the processes occurring at depth. A full appraisal of early rifting processes can also supply important constraints for numerical continental extension models, assessment of seismic hazard and the early development of oil–bearing basins.

The < 5 Ma (Ori 1989) Corinth rift in central Greece is an ideal natural laboratory in which to analyse the details of early rift history (Fig. 6.1). The rift has high strain rates, has dramatic rift–driven geomorphology, clearly imaged syn–rift infill (both

onshore and offshore), structure uncomplicated by over–printing tectonics, and is a key recent component of larger–scale Aegean deformation. In this contribution we use the stratigraphic infill of the offshore Corinth rift from a compilation of seismic reflection data (published and unpublished) integrated with onshore data, to deduce the structural evolution of the system and investigate strain distribution throughout rift history. We build on the work of Armijo et al. (1996), Stefatos et al. (2002), McNeill et al. (2005a), Sakellariou et al. (2007) and Bell et al. (2008) (Chapter 5), to produce an updated fault framework and we establish a regional stratigraphic correlation to investigate basin subsidence. We compile and establish slip rates on major faults to compare with short term geodetic extension and long term basin subsidence patterns. This high resolution examination of a globally significant rift zone gives an insight into the number of faults, their geometry, strain distribution and rift development at the onset of continental rifting. This work provides constraints for generic fault development and continental deformation models as well as kinematic models of Aegean tectonics.

6.2 Tectonic and geological framework of the Corinth rift

The Corinth rift, which here we define as the Gulf of Corinth, Alkyonides Gulf and onshore areas influenced by extension, is a ∼100 x 30 km high–strain band in central Greece that has been undergoing N–S extension, against the structural grain of the Pindos mountain chain since the Pliocene (McKenzie 1972, Roberts & Jackson 1991, Fig. 6.1). It is younger and more focused than most other areas of contemporary continental extension, such as the East African rift system (Omar & Steckler 1996), the Baikal rift (Mats 1993) and the Basin and Range province (Hamilton 1987, Thatcher et al. 1999). Extensional deformation within central Greece is thought to be related to some combination of: back–arc extension due to subduction of the African plate at the Hellenic Trench (McKenzie 1972, 1978b, Doutsos et al. 1988); westward propagation of the North Anatolian fault (Dewey & Sengor 1979, Armijo et al. 1996); and gravitational collapse of lithosphere thickened in the Hellenide orogeny (Jolivet 2001, Le Pourhiet et al. 2003).

The rift has often been generalized as an E–W striking asymmetric half graben, controlled by a series of en–echelon N–dipping faults on the southern margin (Fig. 6.1, Armijo et al. 1996). A general northward migration of faulting on the southern margin has resulted in ∼2 km of uplift and the progressive uplifting of hanging wall sediments including Gilbert fan deltas that have been modified by marine terraces (Fig. 6.1, Tables 6.1 and 6.2, e.g., Kerauden & Sorel 1987, Ori 1989, Dart et al. 1994, Gawthorpe et al. 1994, Armijo et al. 1996, De Martini et al. 2004, McNeill & Collier 2004, Malartre et al. 2004, Rohais et al. 2007, Ford et al. 2007). Uplifted Holocene wavecut notches along the southern margin (e.g., Pirazzoli et al. 1994, Stewart & Vita-Finzi 1996, Pirazzoli et al. 2004) and seismicity confirm that the south–margin

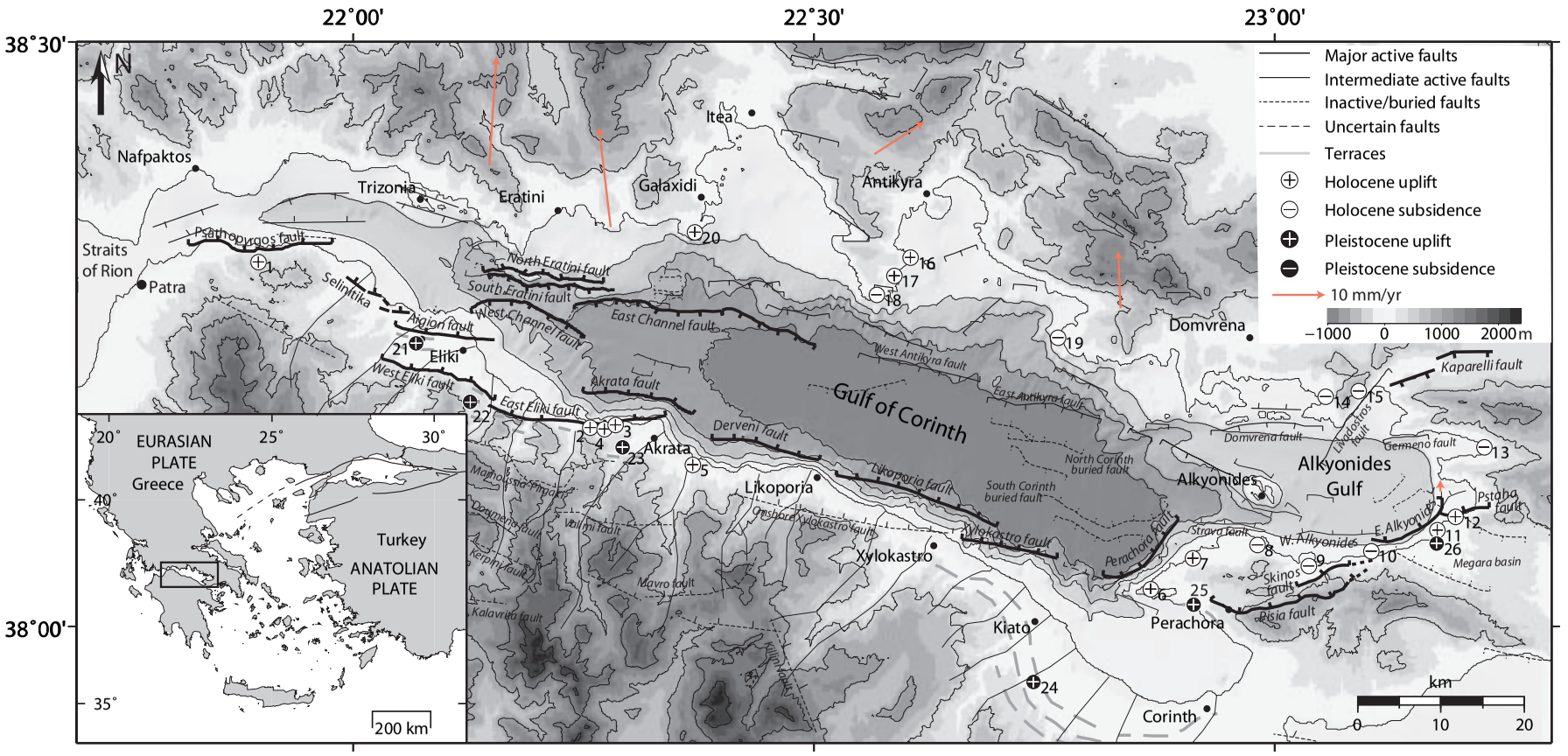

FIGURE 6.1: Tectonic framework of the Corinth rift. The locations of major offshore faults have been interpreted in this study, and we build on the fault maps developed by Armijo et al. (1996), Stefatos et al. (2002), Leeder et al. (2005), McNeill et al. (2005b), Palyvos et al. (2005), Rohais et al. (2007) and Bell et al. (2008). Topography is from the Shuttle Radar Topography Mission (http://srtm.usgs.gov), bathymetry is derived from the swath bathymetry M.V. Vasilios 2003 cruise (McNeill et al. 2005a) and R/V Maurice Ewing 2001 (Zelt et al. 2004). South coast drainage from Zelilidis (2000). Uplift and subsidence measurements at the coastline are explained in Tables 6.1 and 6.2. Arrows are north coast GPS velocity vectors (for a stationary southern coastline), from Clarke et al. (1998) Fig. 16. Inset: Summary of map of the Aegean region.

faults are recently active (Fig. 6.1 and Table 6.1). The northern coastline has a much more sinuous trace, suggesting it is subsiding (Stefatos et al. 2002). Field work we have conducted as part of this study (Chapter 4) shows this is the case along some of the northern coastline (Fig. 6.1; points 13, 14 and 15), but there are areas that show geomorphology characteristic of localised uplift (Fig. 6.1; points 16 and 20).

Estimates of slip rate for the en-echelon south margin faults have been deduced from Holocene and late Quaternary uplifted geomorphic features. Late Quaternary uplift rates of 1 – 1.5 mm/yr for the south margin have led to estimates of slip rate in the range ∼3 – 11mm/yr based on several different methods (Armijo et al. 1996, De Martini et al. 2004, McNeill & Collier 2004, McNeill et al. 2005b). Uplift rates in the Holocene are generally higher along the south Gulf shore around 1.3 – 2.2 mm/yr suggesting higher modern slip rates (Stewart 1996, Stewart & Vita-Finzi 1996, Pirazzoli et al. 2004). Uplift rates in the Alkyonides Gulf are lower, around ∼0.3 mm/yr for the Quaternary (Leeder et al. 1991) and ∼0.5 mm/yr for the Holocene (Pirazzoli et al. 1994, Kershaw & Guo 2001). Short term regional geodetic extension rates increase from <5 mm/yr in the east to >10 – 15 mm/yr in the west (e.g., Davies et al. 1997, Clarke et al. 1998, Briole et al. 2000, Avallone et al. 2004, Nyst & Thatcher 2004).

Major active faults are typically orientated E-W to WNW-ESE (Fig. 6.1). The typical segment length is ∼15 – 25 km (in agreement with Roberts & Jackson 1991, McNeill & Collier 2004), although we do not discount that multiple segments of this length may be connected at depth and could rupture together. Equally the surface expression of these faults may take the form of multiple shorter segments. Ori (1989) propose that rift propagation and fault development occurred from west to east in the rift. A propagation of fault activity from east to west is now more commonly supported from rigid block modelling of the Aegean velocity field (Le Pichon et al. 1995, Clarke et al. 1998, Nyst & Thatcher 2004) and the influence of the North Anatolian fault from the east (Armijo et al. 1996). However, age estimates of stratigraphy from basins along the rift or detailed dating of uplifted syn-rift material onshore is required to confirm dates of individual fault initiation.

Seismic reflection surveys show that major active faults exist in the offshore part of the Corinth rift, dipping both N and S in addition to the south margin coastal faults. The distribution and polarity of these faults produce rift basin structures more complex than a simple asymmetric half graben controlled by N–dipping faults on the south coast (Stefatos et al. 2002, Moretti et al. 2003, Sachpazi et al. 2003, McNeill et al. 2005a, Bell et al. 2008, Chapter 5). In the western rift Bell et al. (2008) and McNeill et al. (2005a) show that the high geodetic extension rates in this area can be explained by combined activity on both offshore and south margin faults. An alternative model involving a dominant deep, low angle N-dipping detachment zone (Rigo et al. 1996, Sorel 2000, Gautier et al. 2006), is not compatible with onshore footwall uplift and topography (Armijo et al. 1996), offshore basin stratigraphy (Bell et al. 2008) or

Site Number and location	Study	Neo-tectonic indicator	Quantitative measurements
East Eliki fault:			
1. Diakofto	Pirazzoli *et al.*, 1994; Stewart, 1996; Stewart & Vita-Finzi, 1996	Uplifted notches	Uplift 0.9 – 1.5 mm/yr
2. Paralia Platanou	Pirazzoli *et al.*, 1994; Stewart, 1996; Stewart & Vita-Finzi, 1996	Uplifted notches	Uplift 0.8 – 2.1 mm/yr
3.Ladopotamos fan	McNeill & Collier, 2004	Uplifted beach and fauna	Uplift 1.4 – 2mm/yr
Derveni fault:			
	Pirazzoli *et al.*, 1994	Uplift of ancient harbour	2m of uplift since 2000b.p.
4. Aegira/ Mavra Litharia	Mouyaris *et al.*, 1992; Stewart & Vita-Finzi, 1996	Uplifted notches	Uplift 1.3 – 2.2 mm/yr
	Pirazzoli *et al.*, 2004	Uplifted fauna.	Uplift 3.2 ± 0.3 mm/yr
Perachora fault:			
5. Heraion	Pirazzoli *et al.*, 1994; Kershaw & Guo, 2001	Uplifted notches and fauna	Uplift ~0.5 – 0.7 mm/yr
6. Mylokopi	Pirazzoli *et al.*, 1994; Kershaw & Guo, 2001	Uplifted notches and fauna	Uplift ~0.5 – 0.7 mm/yr
Skinos fault:			
7. Strava	Jackson *et al.*, 1982; Vita-Finzi & King, 1985	Observed submergence	Subsided after 1981 earthquakes
8. Skinos	Jackson *et al.*, 1982; Vita-Finzi & King, 1985	Observed submergence	Subsided after 1981 earthquakes
9. Mavrolimni	Jackson *et al.*, 1982; Vita-Finzi & King, 1985	Observed submergence	Subsided after 1981 earthquakes
East Alkyonides fault:			
10. Alepochori	Jackson *et al.*, 1982; Vita-Finzi & King, 1985	Observed emergence	Uplifted after 1981 earthquakes
Psatha fault:			
11. Psatha	Jackson *et al.*, 1982; Vita-Finzi & King, 1985	Observed emergence	0.2 m uplift in 4 years after 1981 earthquakes
	Leeder *et al.*, 1991	Uplifted notch	Uplift 0.3 mm/yr
General Alkyonides Gulf locationa:			
12. Porto Germeno	Vita-Finzi & King, 1985 and this study	Submerged 2400b.p. archaeological remains	Subsidence 0.68 mm/yr
13. Aliki	Vita-Finzi & King, 1985 and this study	Submerged 2400bp. archaeology	Subsidence 0.83 mm/yr
14. Livadostros	This study	Possible submerged multiple notches	?
General North Gulf coast:			
15. Pangalos/ Mikalanos peninsula	This study	Possible uplifted wave cut platform	?
16. Pangalos/ Mikalanos peninsula	Moretti *et al.*, 2003	Uplifted beach rock	Beach rock under dating
17. Pangalos/ Mikalanos peninsula	Papatheodorou and Ferentinos 1995	Submerged wave cut platforms	?
18. Velanidia peninsula	Papatheodorou and Ferentinos 1995	Submerged wave cut platforms	?
19. Galaxidi	This study	Possible uplifted wave cut platforms	?

TABLE 6.1: Summary of Holocene coastline vertical movements studies along the Corinth Rift shoreline categorized by the fault probably responsible for the movement.

Site number and location	Study	Neo-tectonic indicator	Quantitative measurements
Psathopyrgos fault:			
20.	Houghton *et al.*, 2003	Uplifted fauna	Uplift 0.7-0.8 mm/yr
Aigion fault:			
21.	De Martini *et al.*, 2004; McNeill *et al.*, 2007	Uplifted terraces Displaced stratigraphy	Uplift 1-1.2 mm/yr
West Eliki fault:			
22.	De Martini *et al.*, 2004	Uplifted terraces	Uplift 1.25 mm/yr
East Eliki Fault:			
23.	McNeill & Collier, 2004; De Martini *et al.*, 2004; McNeill *et al.*, 2005b	Uplifted terraces	Uplift 0.9-1.1 mm/yr
Xylokastro fault:			
24.	Keraudren, 1987; Armijo *et al.*, 1996	Uplifted terraces	Uplift ~1.3 mm/yr
Perachora peninsula:			
25. Perachora peninsula	Leeder *et al.*, 2005	Uplifted terraces	Uplift 0.2-0.3 mm/yr
26. SE Alkyonides fault, Alepochori	Leeder *et al.*, 1991	Uplifted terraces	Uplift 0.2-0.3 mm/yr
27. Pisia fault	McNeill *et al.*, in prep	36Cl exposure ages	Slip rate ~1.5 mm/yr
28. Skinos fault	McNeill *et al.*, in prep	36Cl exposure ages	Slip rate ~1 mm/yr

TABLE 6.2: Summary of late Quaternary vertical movements from studies along the Corinth Rift shoreline categorized by the fault probably responsible for the movement.

focal mechanisms with dips steeper than the detachment plane (Hatzfeld et al. 1996, Bernard et al. 1997).

The basin fill involves primarily hemipelagic settling, turbidite and debris flows, with fan deltas common along the southern margin (Brooks & Ferentinos 1984). The northern margin is now largely sediment starved (Stefatos et al. 2002). The Corinth rift is connected to the Mediterranean at the Straits of Rion by the Rion sill at is western end (Fig. 6.1), which lies 60 – 70 m below sea level and allows the rift to become an isolated lake during marine lowstands (Perissoratis et al. 2000). Due to the general regional uplift of the Corinth Isthmus area, a marine connection at the eastern end of the rift (before the construction of the Corinth canal) is deemed unlikely since at least 450 – 800 ka (Collier & Dart 1991, Leeder et al. 2005). The presence of periodic lowstand lacustrine deposition is also confirmed by offshore sediment cores (Collier et al. 2000, Moretti et al. 2004). This lowstand–highstand variation in depocentre environment has a strong signature in the seismic stratigraphy in the western, central and eastern parts of the Corinth rift (Perissoratis et al. 2000, Sachpazi et al. 2003, Leeder et al. 2005, McNeill et al. 2005a, Lykousis et al. 2007, Sakellariou et al. 2007, Bell et al. 2008).

6.3 Methodology

6.3.1 Datasets

We have compiled swath bathymetry data and seismic reflection profiles from a number of offshore studies, summarised in Table 6.3 and Fig. 6.2. In some cases we have access to primary data and in others we have used published data only.

In the western Corinth rift (between Aigion and Akrata) we have high resolution multichannel seismic reflection profiles from the 2003 M.V. Vasilios survey (Table 6.3 and Fig. 6.2, McNeill et al. 2005a, Bell et al. 2008). The area to the west of Aigion (i.e. the Trizonia basin) is not studied in detail here. In the central rift (between Akrata and Perachora) we have reduced coverage, but profiles are fortunately orientated such that the sub–surface of the whole area has been imaged at a range of resolutions and penetration depths. In this area we have used some profiles from the RRS Shackelton 1982 dataset, described by Brooks & Ferentinos (1984), Higgs (1988) and Stefatos et al. (2002) (Fig. 6.2 and Table 6.3) and the three deep penetrating lines published by Clement (2000), Sachpazi et al. (2003) and Clement et al. (2004) (Fig. 6.2). In the Alkyonides Gulf we have used the sparker and pinger seismic profiles from the 1996 M.V. Vasilios cruise (Collier et al. 2000, Leeder et al. 2002, 2005).

Some profiles from the extensive R/V Maurice Ewing 2001 cruise are available from Goodliffe et al. (2003) and Zelt et al. (2004) and lower resolution images of these data can be viewed at (http://www.ig.utexas.edu/sdc/), giving us additional information on the broad-scale structure (i.e. basement depth) at key locations (Fig. 6.2 and Table 6.3).

6.3.2 Depth conversion

To make quantitative assessments of fault activity we have depth–converted some parts of our seismic data or estimated depths from velocities on published profiles. Depth conversion was conducted based on a velocity profile compiled from typical interval velocities used during stacking of the 2003 MV Vasilios multichannel data (Table 6.3), velocity estimates from cores (Collier et al. 2000, Moretti et al. 2004) and generalized sediment velocity curves from Hamilton (1979, 1980). We estimate that sediments with a two way travel time (TWTT) of between 0 – 0.5 s and 0.5 – 1 s below the seafloor have average velocities of 1.5 – 2.0 km/s and 2.0 – 2.5 km/s, respectively.

6.3.3 Onshore data

Fig. 6.1 and Tables 6.1 and 6.2 show the authors and key results/observations at onshore localities along the Corinth rift shoreline. Vertical movements of the entire

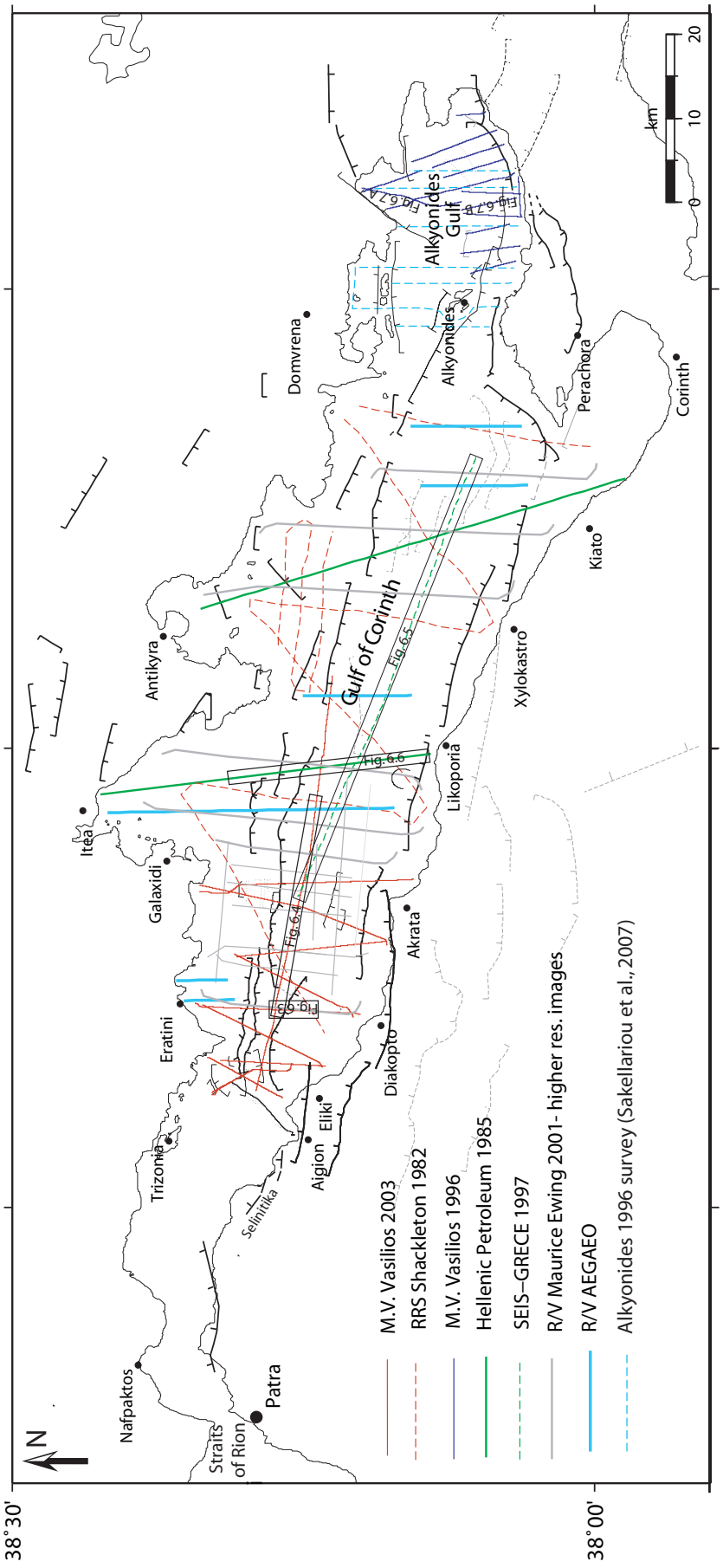

FIGURE 6.2: Map to show the coverage of seismic profiles used in this study. Table 6.3 gives further details for each of the surveys.

Survey	Source	Maximum TWTT from sea-surface (s)	Publications
*RRS Shackleton 1982	Single-channel air-gun	2	Brooks & Ferentinos, 1984 Higgs, 1988 Stefatos *et al.*, 2002
*DEP-Hellenic Petroleum 1985	Maxipulse explosive source Multi-channel	6	Sachpazi *et al.*, 2003 Moretti *et al.*, 2003 Clement, 2000
*M.V. Vasilios 1996	Single-channel sparker	0.85	Leeder *et al.*, 2002 Leeder *et al.*, 2005 Collier *et al.*, 2000
*SEIS-GRECE 1997	Air gun	4	Clement, 2000 Clement *et al.*, 2004 Sachpazi *et al.*, 2003
R/V Maurice Ewing 2001	Multi-channel air-gun	6	Goodliffe *et al.*, 2003 Zelt *et al.*, 2004 UTIG Marine Seismic Data Centre
**M.V. Vasilios 2003	Multi-channel 150 – 2000 Hz Sparker	1.5	McNeill *et al.*, 2005a Bell *et al.*, 2008
R/V AEGAEO	Single channel airgun	1.8	Lykousis *et al.*, 2007
Gulf of Alkyonides 1996	Single channel air gun	0.9	Sakellariou *et al.*, 2007

*Surveys that we have access to some unpublished profiles or higher quality images to supplement published data.
** Data collected by us
No stars : Seismic profiles viewed from publications or data archive websites only

TABLE 6.3: Summary of seismic data compiled for use in this study.

Corinth rift coastline are now documented in some detail, where lithology has allowed preservation of geomorphic features (see also Chapter 4).

6.4 Fault architecture in the Corinth rift

We combine all available data to produce an up–dated interpretation of major faulting in the Corinth rift, building on earlier maps by Brooks & Ferentinos (1984), Higgs (1988), Armijo et al. (1996), Leeder et al. (2002), Stefatos et al. (2002), McNeill et al. (2005a), Sakellariou et al. (2007) and Bell et al. (2008). Fig. 6.1 shows major basement displacing faults in the Corinth rift. These are categorised as; major active faults with throws > 500 m, intermediate active faults with throws < 500 m and inactive major faults. Minor sediment displacing faults which sole out onto the basement surface are not included in Fig. 6.1. Most of the faults shown in Fig. 6.1 have been noted by other authors; however here we use all available data to further constrain their position and connectivity. The western (Aigion to Akrata), central (Akrata to Xylokastro), central-eastern (Xylokastro to Perachora peninsula) and eastern Corinth rift (the Alkyonides Gulf) are bordered by distinct fault segments and are described as distinct tectonic areas below.

6.4.1 Western Corinth rift fault structure

The currently active faults bordering the south coastline of the western Corinth rift are the East and West Eliki and Aigion faults (Fig. 6.1). To the south is a series of now presumed inactive faults (e.g. the Mamoussia–Pirgaki to Kalavrita faults). Pre ca. 2 Ma, extension within the western Corinth rift is thought to have been distributed over a number of these faults defining the older proto-Corinth rift (Sorel 2000, Collier & Jones 2003, Rohais et al. 2007). Extension focused onto specific N–dipping faults (e.g. the Mamoussia-Pirgaki and Valimi faults) in the Early–Pleistocene ca. 0.8 – 1.8 Ma, causing deepening of the rift and allowing the deposition of giant fan deltas (Dart et al. 1994, Rohais et al. 2007, or slightly younger age of 0.7 – 1.1 Ma recently proposed by Ford et al. 2007). These fan deltas have since been uplifted in the footwalls of the south coast faults defining the present day rift since ca. 0.8 Ma. These patterns of faulting indicate a northward shift in major fault location (Ori 1989, Collier & Jones 2003, Rohais et al. 2007). Since ca. 0.2 – 0.3 Ma the south coast Aigion fault has initiated and is potentially part of a continuing pattern of northward propagation (De Martini et al. 2004, McNeill et al. 2007).

We have previously described the fault structure of the western part of the offshore Corinth rift, (McNeill et al. 2005a, Bell et al. 2008) and present a summary here. Bathymetry in the western part of the rift is more variable than elsewhere. The North and South Eratini faults each have a length of ∼15 km and overlap completely, resulting in the uplift of a prominent basement horst (McNeill et al. 2005a, Bell et al. 2008). The North Eratini fault dips 60° N and the South Eratini fault 50 – 60° S. A prominent axial channel draining the western rift is underlain by the ∼45 – 60° S dipping West Channel Fault. At the eastern tip of the West Channel fault the basin floor widens, with the northern margin controlled by the ∼60 – 70° S dipping East Channel fault 2 km farther north. The Akrata fault, just north of the Akrata offshore of the southern margin, dips ∼60° N and may be a splay of the major East Eliki fault, 4 km to the south which controls southern margin topography (e.g., McNeill & Collier 2004).

We have not examined structures to the west of Aigion, but published faults are indicated on Fig. 6.1.

6.4.2 Central Gulf fault structure

Traditionally the fault bordering the southern margin of the Corinth rift, between Akrata and Xylokastro has been shown as a single fault with a length of ∼30 – 40 km, named the Derveni or Corinth fault (Brooks & Ferentinos 1984, Higgs 1988, Stefatos et al. 2002). Others have split the fault into two parts (e.g., Moretti et al. 2003). We support the view that there are two fault segments bordering the central rift and interpret the break between the two segments to lie at the cusp in the coastline

seen at Likoporia, based on limited seismic data and coastal morphology (Fig. 6.1). We name the western segment the Derveni fault (interpreted originally by Brooks & Ferentinos 1984, Higgs 1988) and the eastern segment the Likoporia fault. The northern boundary of the basin floor is bounded by the S–dipping West Antikyra fault and the eastern extension of the East Channel fault (western end described by Bell et al. 2008).

From the few seismic profiles that traverse the region south of the Antikyra bay, a number of small, active surface displacing faults have been interpreted. We also note the possibility of coastline uplift at point 16 on Fig. 6.1, which may indicate fault activity. The inactive onshore Xylokastro fault now lies in the footwall of the offshore Likoporia fault which is currently uplifting the older onshore Xylokastro fault hanging wall (Fig. 6.1, Flotte et al. 2001).

6.4.3 Eastern Gulf of Corinth fault structure

The south margin bathymetry and basement structure of the central–eastern Corinth rift between Xylokastro and the Perachora peninsula is controlled by the 50 – 55° N–dipping Xylokastro fault and NE trending Perachora fault. The connectivity between the offshore western tip of the Xylokastro fault and probably inactive onshore Xylokastro fault (Flotte et al. 2001), as well as the Perachora fault and the eastern tip of the Xylokastro fault is unclear. Some interpretations connect or overlap these faults (e.g., Armijo et al. 1996), whilst others leave a gap (e.g., Moretti et al. 2003, Stefatos et al. 2002). The coherent uplift of terraces on the south coast around Corinth could be evidence for one fault. However, such coherent uplift could also be due to regional uplift (e.g., Collier & Dart 1991, Westaway 2002, Leeder et al. 2003, 2005). The northern margin is defined by shorter less significant fault segments, like the S–dipping East Antikyra fault (Fig. 6.1). A series of buried inactive faults produce localised lows in basement (Fig. 6.1, the North and South Corinth Buried faults).

In the Corinth Isthmus region, to the south of Xylokastro very few large faults have been interpreted compared to the many interpreted inactive faults on the south margin to the west of Akrata (Fig. 6.1). The Kenchreai fault and a number of other interpreted faults bound the Pliocene–Quaternary sediments of the Corinth Isthmus to the south (south of Fig. 6.1, discussed by Collier & Dart 1991, Roberts 1996, Goldsworthy & Jackson 2001, Ghisetti & Vezzani 2004).

6.4.4 Eastern Corinth rift (Alkyonides Gulf) fault structure

Our interpretation in the Alkyonides Gulf closely follows Collier et al. (2000), Stefatos et al. (2002) and Leeder et al. (2005). The most important offshore faults are the N–dipping West and East Alkyonides faults. Although there are limitations in data coverage, it seems that these fault segments are not linked, and the seismic data show

that the East Alkyonides fault likely overlaps the western end of the West Alkyonides fault by 1 km to the south (Fig. 6.1). The eastern end of the East Alkyonides fault splays into two, and the Psatha fault (to its east) propagates offshore to the south of these splays (Leeder et al. 2005, Sakellariou et al. 2007). The East Alkyonides and Psatha faults have cut across the NW trend of the older Megara basin (Fig. 6.1; Leeder et al. 1991, Collier et al. 1992). The onshore Pisia and Skinos faults are also active and control the significant onshore topography (Jackson et al. 1982, Leeder et al. 1991, Collier et al. 1998, Leeder et al. 2005). The S–dipping Domvrena, Livadostros, Germeno and Kaparelli faults are less significant faults along the northern margin. The Kaparelli fault slipped in the 1981 sequence of earthquakes (as did the Skinos, Pisia and an uncertain offshore fault) but paleoseismology studies suggest long recurrence intervals of 2500 – 10000 years (Jackson et al. 1982, Benedetti et al. 2003, Kokkalas et al. 2007). Activity on the other north margin faults (e.g. Domvrena, Livadostros, Germeno, Fig. 6.1) is more questionable.

6.5 Stratigraphy

The syn–rift infill of the Corinth rift can be divided into two major stratigraphic units with different seismic character (e.g., Moretti et al. 2003, Sachpazi et al. 2003, Bell et al. 2008). The older tectonic unit (unit B, Bell et al. 2008) is generally non–reflective, whereas the younger (unit A, Bell et al. 2008) is well stratified with repeating seismic facies (Figs. 6.3 and 6.4). The stratigraphy of unit A has been proposed to correlate with eustatic 100 ka sea level cycles, including fluctuations between high–stand marine and low–stand lacustrine conditions (Perissoratis et al. 2000, Sachpazi et al. 2003, Bell et al. 2008). An unconformity between units A and B is a key horizon in investigating changing tectonic regime in the rift and we attempt to correlate this surface across the rift using seismic profile tie lines and seismic facies recognition. Where possible we have also extended the interpretation of unit A 100 ka cyclicity (Bell et al. 2008) across the rift.

The style of stratigraphy is distinct in the west, central and eastern parts of the rift, and is described in reference to these three geographic localities below.

6.5.1 Stratigraphic architecture of the Western Corinth rift

We summarise here the stratigraphy of the western Corinth rift, which is discussed thoroughly in Bell et al. (2008) and McNeill et al. (2005a). In the western rift, the distinction between unit A and unit B is clear (Fig. 6.3). The 2003 MV Vasilios multichannel seismic data penetrate to a maximum time of 1.5 – 1.8 s TWTT and fails to image the older parts of unit B and basement everywhere (Table 6.3). In deeper areas our interpretations are therefore supplemented by images from the 2001

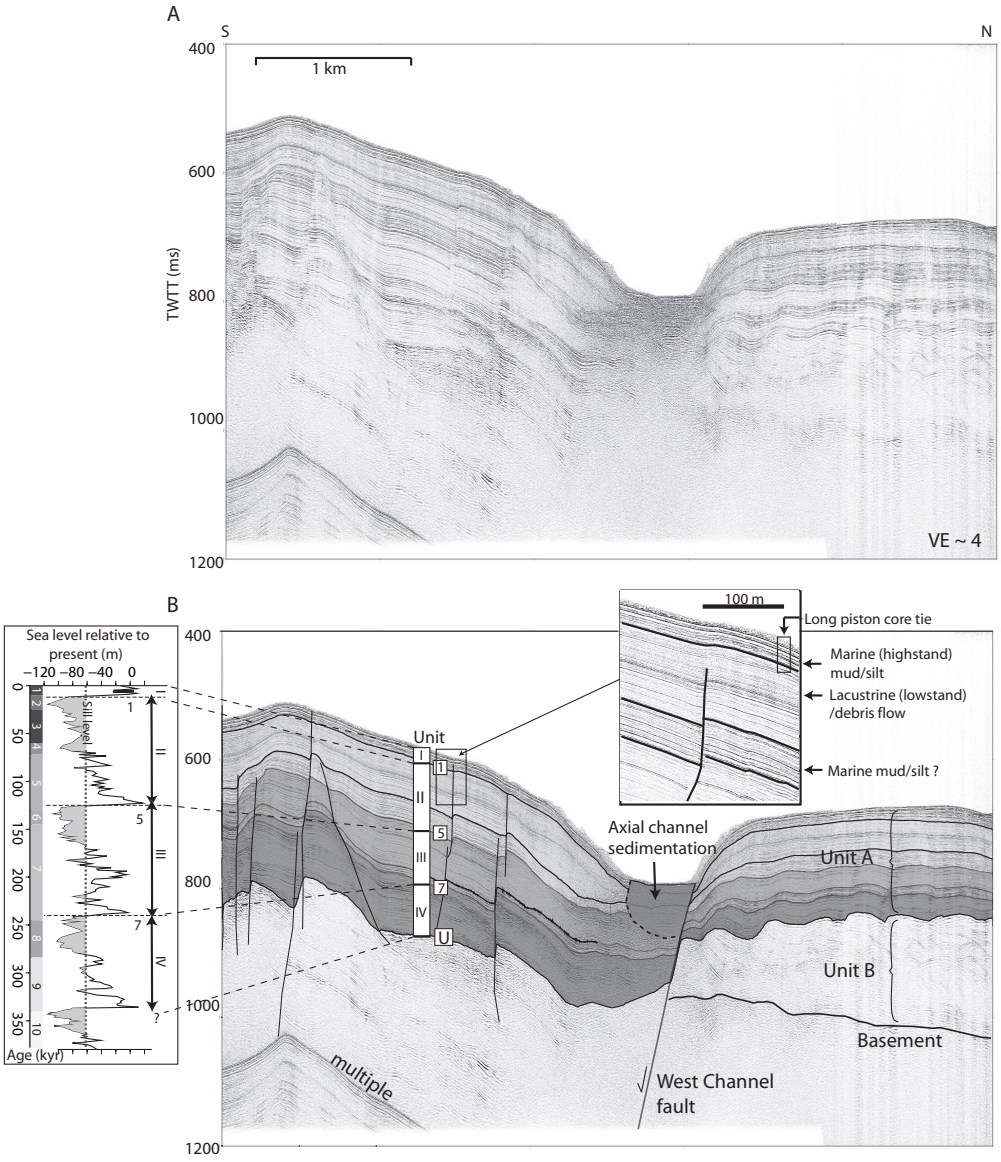

FIGURE 6.3: **A.** Multichannel seismic profile (M.V. Vasilios 2003 survey) from the western Corinth rift. **B.** Interpreted stratigraphy from the western Corinth rift. Stratigraphy has been correlated with the eustatic sea level curve of Siddall et al. (2003), modified for Corinth rift lowstands. Horizon numbers relate to Oxygen Isotope stage correlation. U is the unconformity between well stratified unit A and poorly stratified unit B. Location of profile shown in Fig. 6.2. After Bell et al. (2008).

RV Maurice Ewing survey (Goodliffe et al. 2003, Zelt et al. 2004, Marine Seismic Data Center website (http://www.ig.utexas.edu/sdc/)).

On the northern margin a series of buried clinoforms are capped and onlapped by parallel horizons (Bell et al. 2008). These clinoforms have been interpreted as low-stand delta deposits that form when eustatic sea level falls below the 60 – 70 m level of the Rion sill and the rift becomes an isolated lake (McNeill et al. 2005a, Lykousis

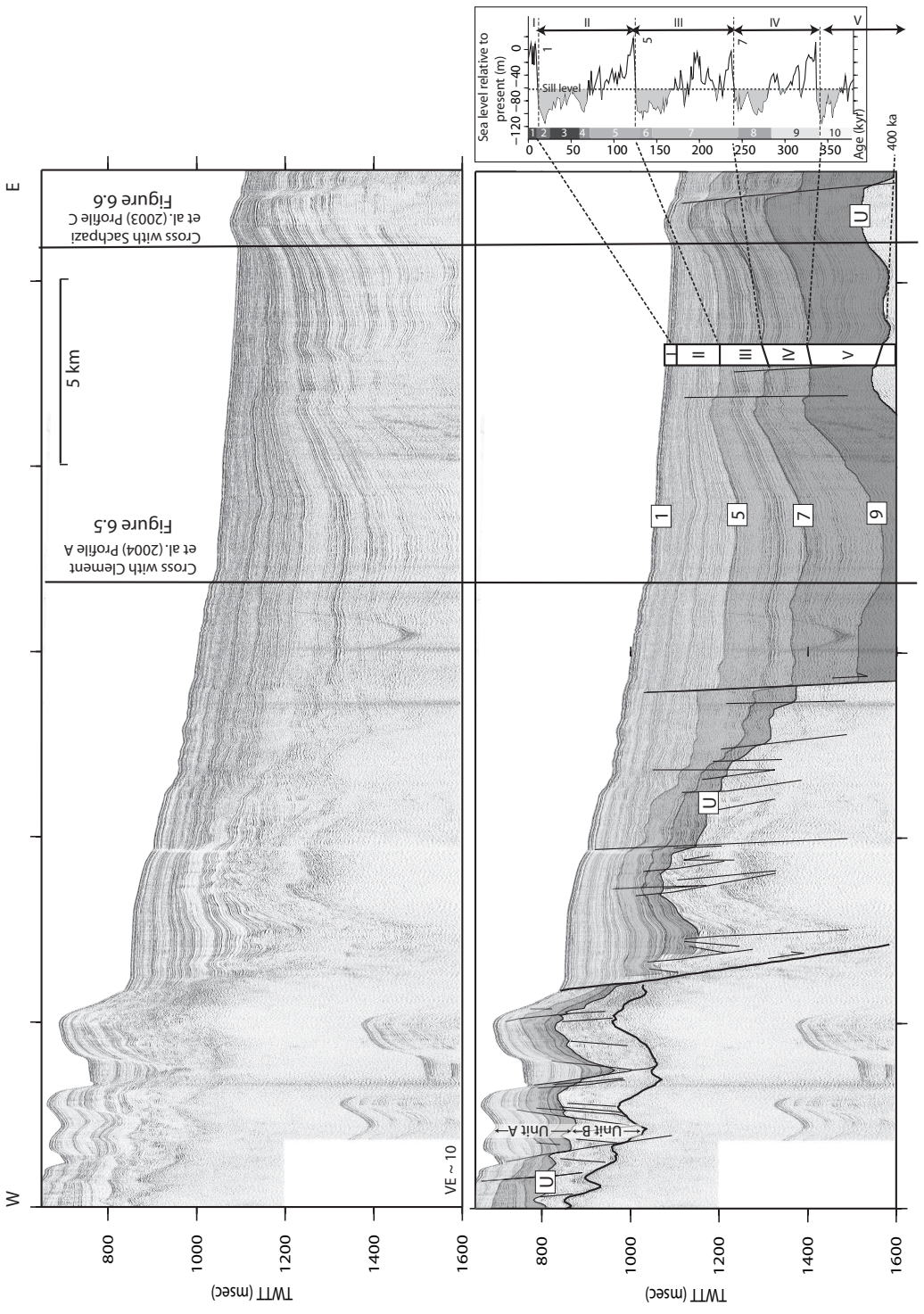

FIGURE 6.4: **A.** E–W Multichannel seismic profile (M.V. Vasilios 2003 survey) across the western to central rift **B.** Interpreted stratigraphy in the western to central Corinth rift, location shown in Fig. 6.2. Stratigraphy has been correlated with the eustatic sea level curve of Siddall et al. (2003) modified for Corinth rift lowstands. Horizon numbers relate to Oxygen Isotope stage correlation. U is the unconformity between well stratified unit A and poorly stratified unit B. Vertical lines indicate intersection with seismic profiles shown in Figs. 6.5 and 6.6. After Bell et al. (2008).

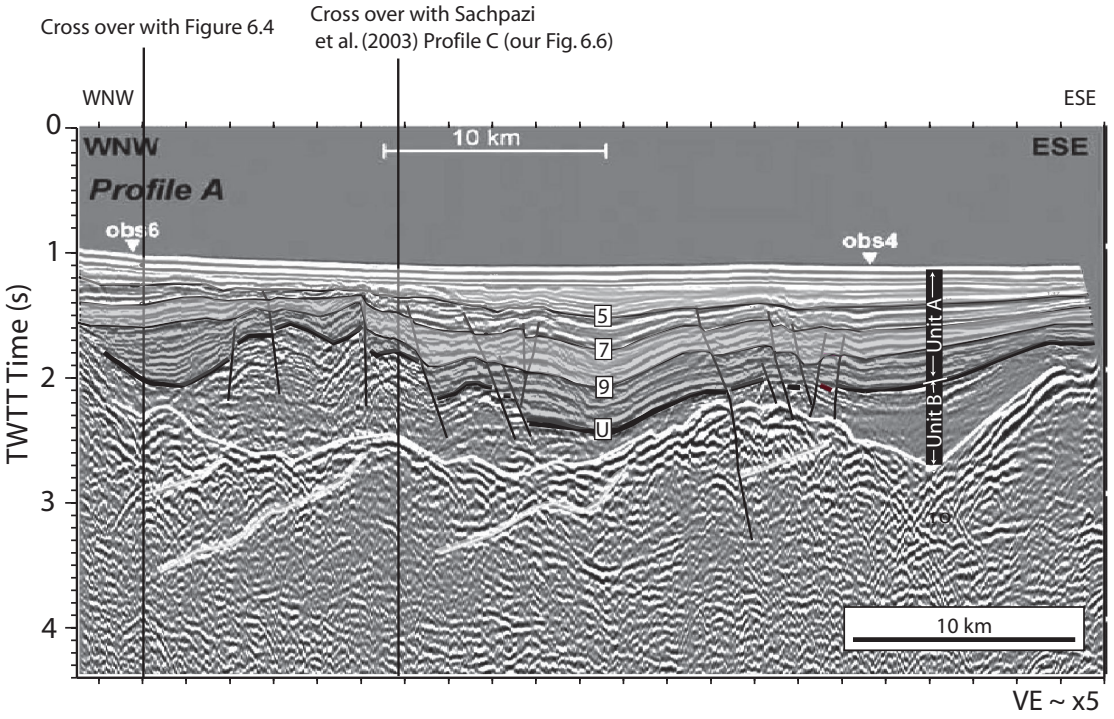

FIGURE 6.5: Our interpretation of stratigraphy along the E–W central rift SEIS–GRECE line following Clement (2000) and Clement et al. (2004). Note y–axis is in time. Location shown in Fig. 6.2. Interpretations are based on correlation with the higher resolution seismic data (e.g. seismic profile Fig. 6.4) and seismic facies recognition. Numbered horizons correspond to Oxygen Isotope stages as in Figs. 6.3 and 6.4.

et al. 2007). We have interpreted end lowstand horizons at ca. 12, 130, 240 and 340 ka (onset of Oxgyen Isotope Stages (OIS) 1, 5, 7 and 9).

An extrapolation of unit A stratigraphy into the main basin is provided by Bell et al. (2008). Unit A shows alternations of thin high amplitude, low frequency bands with thicker layers of low amplitude and higher frequency (Figs. 6.3 and 6.4). The uppermost seismic facies transition (lacustrine–marine) has been cored by Moretti et al. (2004) elsewhere and dated at ca.12 ka (Fig. 6.3). Similar older transitions between high and low amplitude seismic facies have been interpreted to represent previous eustatic sea level fluctuations (Bell et al. 2008). The cyclic stratigraphy can be traced around most of the western rift, becoming harder to distinguish eastward toward the central rift. This interpreted chronostratigraphy gives an estimated age of the unit A/B unconformity of ca. 0.4 Ma (Bell et al. 2008).

6.5.2 Stratigraphic architecture of the Central Corinth rift

In the central Corinth rift the unit A to B unconformity is below the 1.5 s penetration of our high–resolution data (Bell et al. 2008, Figs. 6.3 and 6.4). To continue our stratigraphic interpretations into the central rift we rely on more deeply penetrating

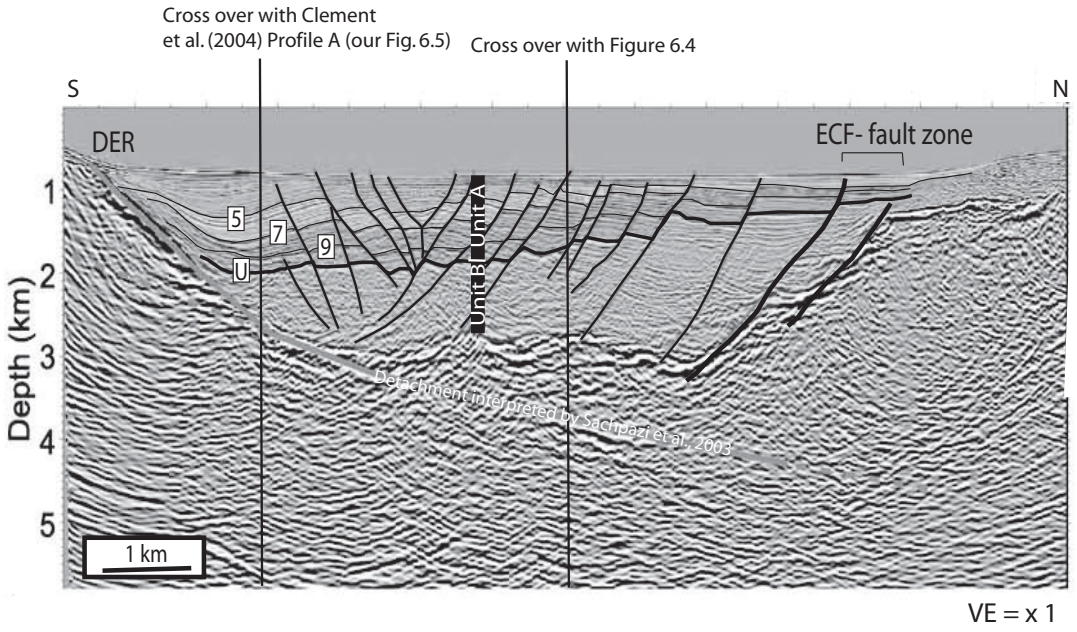

FIGURE 6.6: Our interpretation of stratigraphy along the Hellenic Petroleum line, Profile C after Sachpazi et al. (2003) and Moretti et al. (2003). Note y–axis is in depth. Locations shown in Fig. 6.2. Interpretations are based on correlation with the higher resolution seismic data (e.g. seismic profile Fig. 6.4) and seismic facies recognition. Numbered horizons correspond to Oxygen Isotope stages as in Figs. 6.3 and 6.4. Note, the detachment surface has been interpreted by Sachpazi et al. (2003), and we do not support the interpretation of this surface.

seismic profiles (Clement 2000, Goodliffe et al. 2003, Sachpazi et al. 2003, Clement et al. 2004, Zelt et al. 2004, Fig. 6.2 and Table 6.3).

The E–W line from Clement et al. (2004) supports our distinction between younger well stratified stratigraphy and deeper poorly stratified sediments separated by an unconformity (Clement 2000, Clement et al. 2004, Fig. 6.5). We have tied our interpretation from the shallow high resolution seismic of Figs. 6.3 and 6.4 with Figs. 6.5 and 6.6 and confirm that this unconformity is the same surface.

Cyclicity within unit A may be extrapolated into the central rift on the shallow penetrating 1982 RRS Shackleton data (Brooks & Ferentinos 1984, Higgs 1988, Stefatos et al. 2002) using the same seismic facies interpretation as in the western rift (Bell et al. 2008). However, the distinction between high amplitude vs. low amplitude packages becomes much less clear toward the east. By tracing interpreted end-lowstand horizons along the deep E–W SEIS-GRECE tie line (Fig. 6.5 Clement 2000, Clement et al. 2004) and to other deep profiles (Fig. 6.6, Sachpazi et al. 2003, note this section is depth converted) we have been able to develop a consistent interpretation of 100 ka cycles across the Corinth rift, albeit with less confidence than for the unit A – B unconformity.

6.5.3 Stratigraphic architecture of the Eastern Corinth rift (Alkyonides Gulf)

The stratigraphy of the Alkyonides Gulf has been extensively studied (Leeder et al. 1991, 2002, 2005, Collier et al. 1998, Sakellariou et al. 2007). At least five buried lowstand clinoform packages exist on the subsiding northern margin, with the delta/shoreline position shifting northward with time (Fig. 6.7, in the same way as was observed in the western rift, McNeill et al. 2005a, Lykousis et al. 2007, Bell et al. 2008). The deltaic packages are each capped by a relatively high amplitude reflector, which in most cases shows angular truncation with the clinoforms below (Fig. 6.7). The clinoforms become continuous and more shallowly-dipping basinward. The deepest reflections of each clinoform set are parallel and onlap against the older clinoform set below. Based on correlation of clinoforms with lowstand delta formation, the oldest sediments on the northern margin are at least ca. 550 kyr old (Fig. 6.7 A).

Extrapolation of these lowstand shoreline horizons southward out into the central Alkyonides Gulf supports differentiation of lowstand-highstand stratigraphic units as in the main Corinth rift (Bell et al. 2008) (Fig. 6.7, and detailed stratigraphic description in Table 6.4). As an example, if we follow the ca. 130 ka end lowstand shoreline horizon into the main basin we see it forms the base of a thin band of high amplitude reflections (Fig. 6.7 A and B). The character of this band is analogous to modern day highstand sediments seen above the ca. 12 ka (OIS 1) horizon, and similar to the band seen above the ca. 130 ka horizon in the western rift (Figs. 6.3 and 6.4). Above this high amplitude band we observe lower amplitude reflections, more characteristic of the lowstand lacustrine sedimentation in the western rift (Figs. 6.3 and 6.4).

Our interpretation of lowstand horizons into the deeper Alkyonides basin follows the interpretation of Leeder et al. (2005), rather than that of Sakellariou et al. (2007) who interpret much younger sediment ages. Onlap of horizons with basement on the north margin means the basement-sediment contact age becomes younger in a northward direction (Fig. 6.7 A). Sediments within the Alkyonides Gulf do not show the same contrasting unit A and unit B character, as seen in the Gulf of Corinth: sediments remain well stratified down to the maximum 0.9 s TWTT depth of recording.

6.6 Basin Geometry

6.6.1 Basement structure

We have incorporated basement depth information from the seismic profiles described in Fig. 6.2 and Table 6.3 to produce, for the first time, an approximate basement surface for the entire Corinth rift (Fig. 6.8). This information is vital to establish the total displacement on faults and the net extension across the rift. The two–way

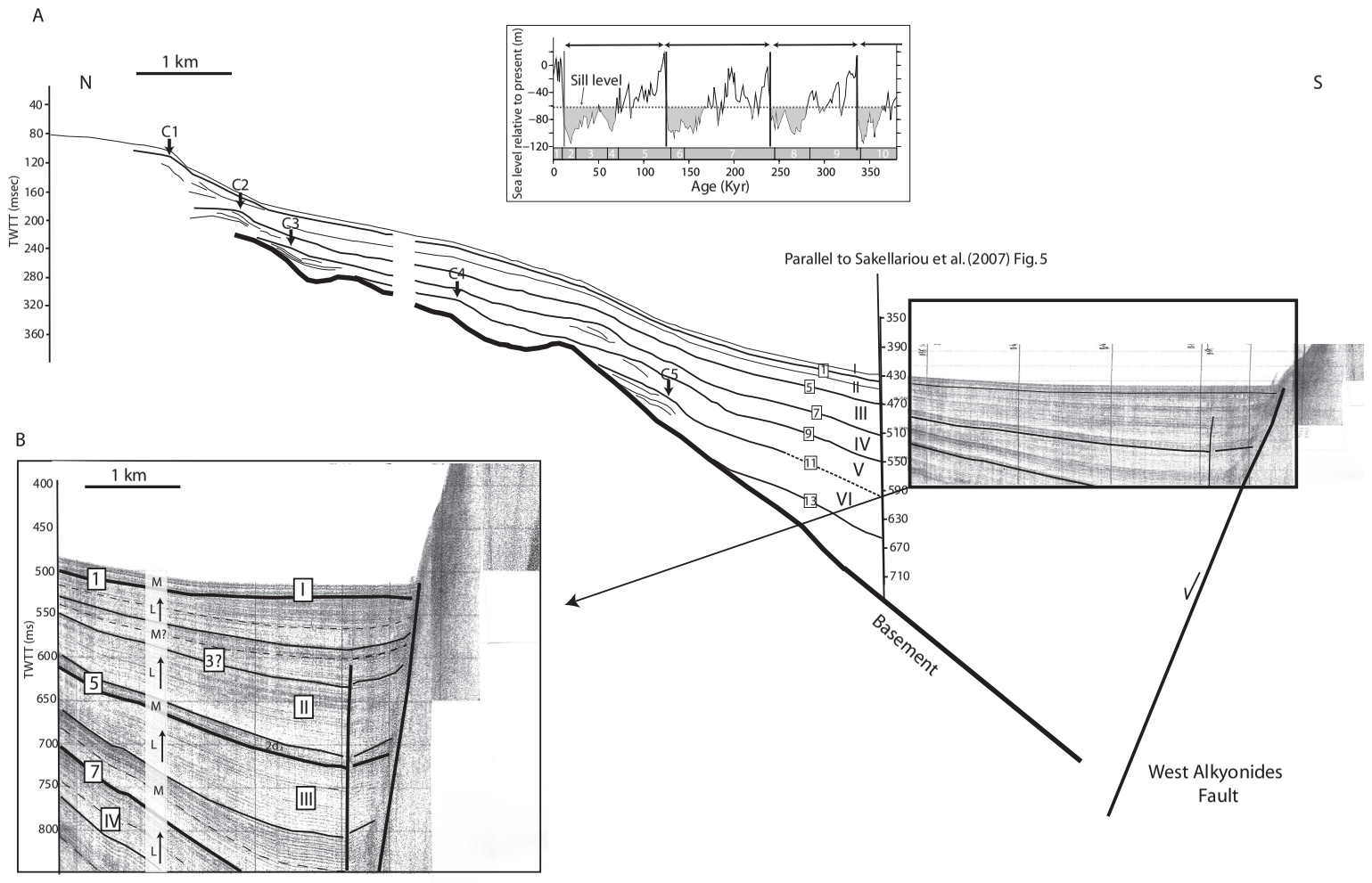

FIGURE 6.7: **A.** Seismic interpretation of profiles from the Alkyonides Gulf from the 1996 M.V. Vasilios cruise, location shown in Fig. 6.2. Stratigraphic interpretation of the northern margin clinoforms follows Leeder et al. (2005), (with slightly different interpretation of horizons corresponding to Oxygen Isotope Stages 11 and 13). The interpretation has been extended south to shallower, higher resolution sparker data. **B.** Vertically exaggerated view of the seismic stratigraphy on the southern coast of the Alkyonides basin adjacent to the West Alkyonides fault. Detailed explanation of stratigraphy can be found in Table 6.4.

Sequence Boundary	Unit	Illustration	Seismic character Description	Average Unit thickness (m)	Geological significance	Horizon age (ka)	Sed. Rate (mm/yr)
Sea bed					0		
	I			13			1.1
1			Few very strong reflections		Highstand/marine	ca. 12	
			Lower amplitude, higher freq. reflections are traced into clinoforms on the north margin		Lowstand/lacustrine		
3?					Short lived marine?	ca. 50 ?	
	II		Narrow band of strong reflections	73	Lowstand/lacustrine		0.6
			Lower amplitude, higher freq. reflections				
5						ca. 130	
			Few very strong reflections		Highstand/marine		
	III		Mostly low amplitude, high freq. reflections that can be traced into clinoforms on the northern margin	40	Lowstand/lacustrine		0.4
			Few strong reflections		Highstand/marine		
7						ca. 240	
			Transparent layer		Lowstand/lacustrine		
	IV			38			0.4

TABLE 6.4: Summary of the interpretation scheme used to interpret Alkyonides basin sedimentation (discussed in text and Fig. 6.7)

travel time (TWTT) depth to basement map (Fig. 6.8) confirms that the central Corinth rift (between Akrata and the Perachora peninsula) is the deepest, with the basement at a depth of 2600 – 3000 ms (∼2700 – 3300 m) in an ESE trending band. The east and west sections of the rift (including the Alkyonides Gulf) are shallower, reaching a maximum of 1600 ms (∼1600 m) with localized intra-basin uplift in the form of fault–controlled horst blocks (Fig. 6.8).

The south margin of the central deep depocentre, between Akrata and the eastern tip of the Perachora peninsula is tectonically controlled by the N-dipping East Eliki–Akrata, Derveni, Likoporia, Xylokastro and Perachora faults (Fig. 6.8). The northern margin of the central-western rift is strongly controlled by the East Channel fault, whereas the north margin of the central–eastern rift is more diffuse and controlled by a number of small S-dipping faults (e.g. East and West Antikyra faults, Fig. 6.8).

Basement depth in the western rift (Aigion to Akrata) is predominantly controlled by the S–dipping West Channel and South Eratini faults and the N–dipping Eliki fault (described in detail by Bell et al. 2008, Fig. 6.8). The transition between the shallower western rift and deeper central rift is coincident with the western tips of the East Channel and Akrata faults, in a line between Eratini and Diakopto (Bell et al. 2008, Fig. 6.8,). These faults have down–thrown basement to a deeper level than is observed in the western rift. A transition between a shallow western and deep central rift has been suggested by Ghisetti & Vezzani (2004) and Papanikolaou & Royden (2007) farther east between Galaxidi and Akrata, due to an inherited structural high and through going N–S detachment respectively. However, we see no evidence of a change in basement depth or major N–S structural features at this location.

In the Alkyonides Gulf, using the basement projection method of Leeder et al. (2005), and basement depth constraints from the 2001 R/V Ewing data (Goodliffe et al. 2003, Zelt et al. 2004), the maximum depth to basement in the hanging wall of the Alkyonides south coast faults is estimated at 1350 ms (∼1500 m) (Fig. 6.8). The divide between the Alkyonides Gulf and the deep central rift involves a rapid deepening of the basement westward, although the exact nature of the boundary is unclear. A tectonic boundary in this area has been suggested previously by McNeill & Collier (2004) based on a marked change in onshore uplift rates.

Major basement subsidence within the entire rift is restricted between the N and S–dipping faults that define the southern and northern margins respectively. We note that the south margin faults (Aigion, Eliki, Derveni, Likoporia, Xylokastro, Perachora, West and East Alkyonides faults) are generally coincident with the modern coastline, whereas the E–W trending major faults defining the northern margin of the main basin (e.g. North and South Eratini, West and East Channel, West and East Antikyra faults) are within the offshore rift. The wide, shallow platforms that exist to the north of these faults are responsible for the sinuous trace of the northern coastline.

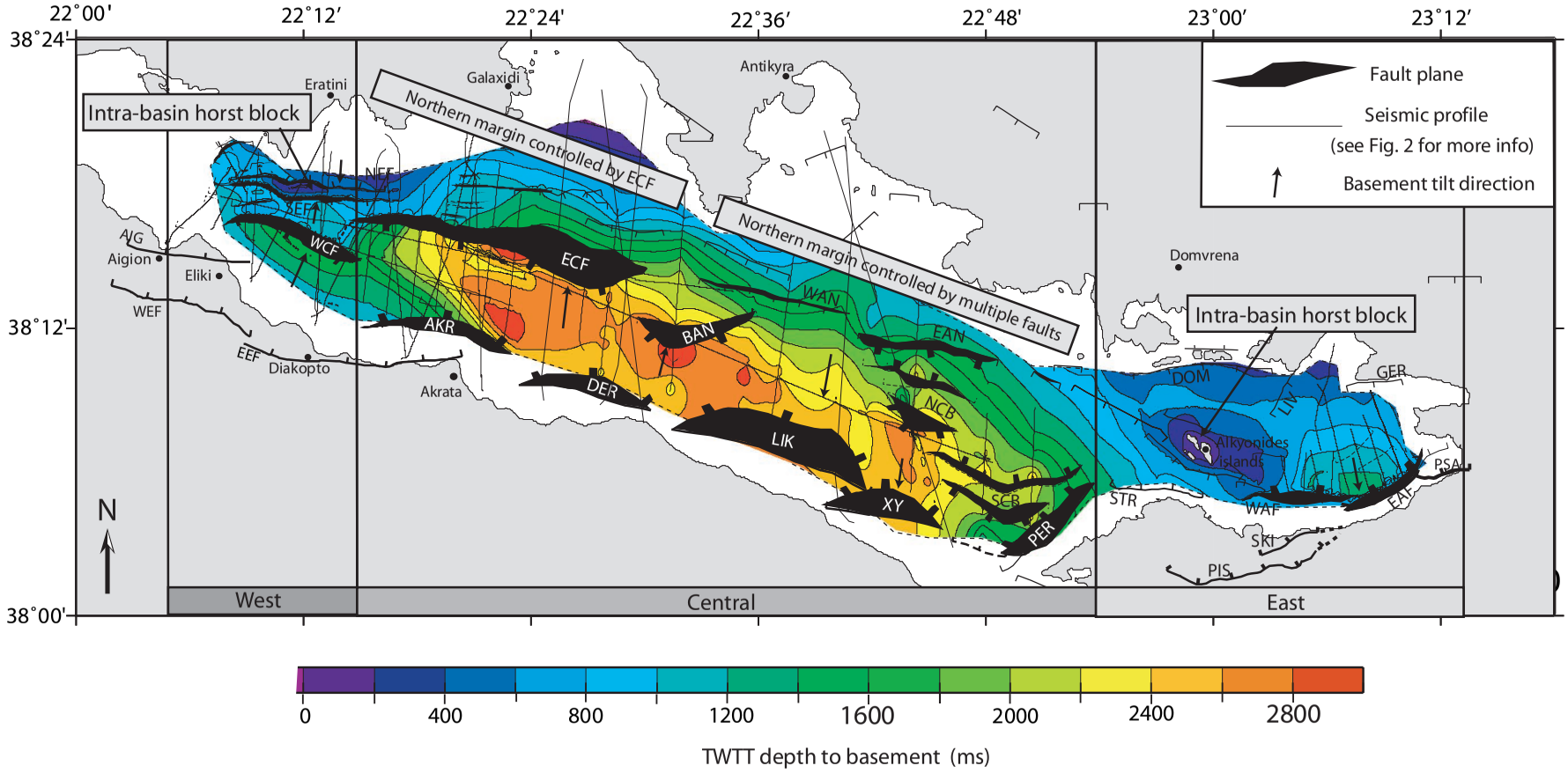

FIGURE 6.8: TWTT depth to the basement–sediment contact. Western rift basement interpretation follows Bell et al. (2008) and uses M.V. Vasilios 2003 multichannel seismic reflection data, supplemented by additional basement interpretations from deep seismic reflection profiles from the R/V Maurice Ewing cruise EW0108/2001 (Goodliffe et al. 2003, Zelt et al. 2004, additional low–resolution seismic images accessed through the Marine Seismic Data Center at http://www.ig.utexas.edu/sdc/). Central interpretation includes seismic profiles from the 1982 RRS Shackleton survey, two Hellenic Petroleum lines (Sachpazi et al. 2003), SEIS–GRECE tie line (Clement 2000, Clement et al. 2004), and some additional control from R/V Maurice Ewing profiles (Goodliffe et al. 2003, Zelt et al. 2004). Alkyonides basement interpretation comes from analysis of 1996 M.V. Vasilios data and projection technique similar to Leeder et al. (2005). See Fig. 6.1 for full fault names. White areas outside of dotted lines are regions of no basement interpretation.

6.6.2 Sediment thickness

Depth to basement (Fig. 6.8) and the interpretation of the ca. 0.4 Ma unit A/B unconformity are used to produce isopach maps for the total, pre and post ca. 0.4 Ma syn-rift sediment thicknesses (Figs. 6.9, 6.10 A and B respectively). Fault plane widths and lengths for the total sediment thickness case (Fig. 6.9) are derived from seismic data (fault width is defined as the horizontal distance between a faults intersection with the sea floor and basement) and bathymetry. The length of faults during the pre 0.4 Ma period has been estimated from the length of sediment depocentres during this time (6.10 A). A knowledge of depocentre distribution during the deposition of unit A and B permits an analysis of fault evolution in a similar way to that performed by Dawers & Underhill (2000), Davies et al. (2000), McLeod et al. (2000) and Dou & Chang (2003), for example.

Total sediment thickness is greatest in the central Corinth rift (coincident with deepest basement; Fig. 6.8) between the western tip of the East Channel fault and Perachora fault (Fig. 6.9). Sediment thickness in this area is relatively constant between the north and south border faults, at 1100 – 1500 ms (1300 – 1900 m), thickening locally in the hanging walls of faults up to 1900 ms (2400 m) (Fig. 6.9). Minimal seafloor topography exists in this central basin (Fig. 6.1), suggesting sediment input along the rift is relatively uniform and sediment transport mechanisms distribute sediments equally within the depocentre. Any differences in total sediment thickness are therefore likely tectonic in origin. Greatest sediment thickness in the western rift occurs in the hanging wall of the West Channel fault (∼1000 m). Sediment thickness in the Alkyonides Gulf increases southward toward the East and West Alkyonides faults to a maximum thickness of ∼900 ms (1000 m), similar to that observed in the western rift (Fig. 6.9).

Typical unit B (pre ca. 0.4 Ma) sediments are imaged in the Gulf of Corinth, but not thought to be present in the Alkyonides Gulf based on seismic character (Fig. 6.10 A). We do however interpret sediments older than ca. 0.4 Ma in the Alkyonides Gulf (Fig. 6.7, Leeder et al., 2005) and the thickness of these sediments are included in Fig. 6.10 A. Unit B in the central Corinth rift forms two main depocentres; one to the north of Akrata (> 1200 ms thick) and the other north of Xylokastro (> 700 ms thick) (Fig. 6.10 A). Between these two depocentres, south of Antikyra, unit B is thin (∼200 ms thick). The eastern rift (Alkyonides Gulf) shows similar thin (∼200 ms thick) pre ca. 0.4 Ma sediment thickness.

There are two possible modes of origin for such a bimodal distribution of sedimentation. Either: 1) the two depocentres are tectonically controlled by enhanced activity on two separated fault systems, creating accommodation space for sediments and uplifted source areas whilst keeping a basement high and area of non-deposition between them; or 2) differences in sediment input form two lobes of positive sediment relief

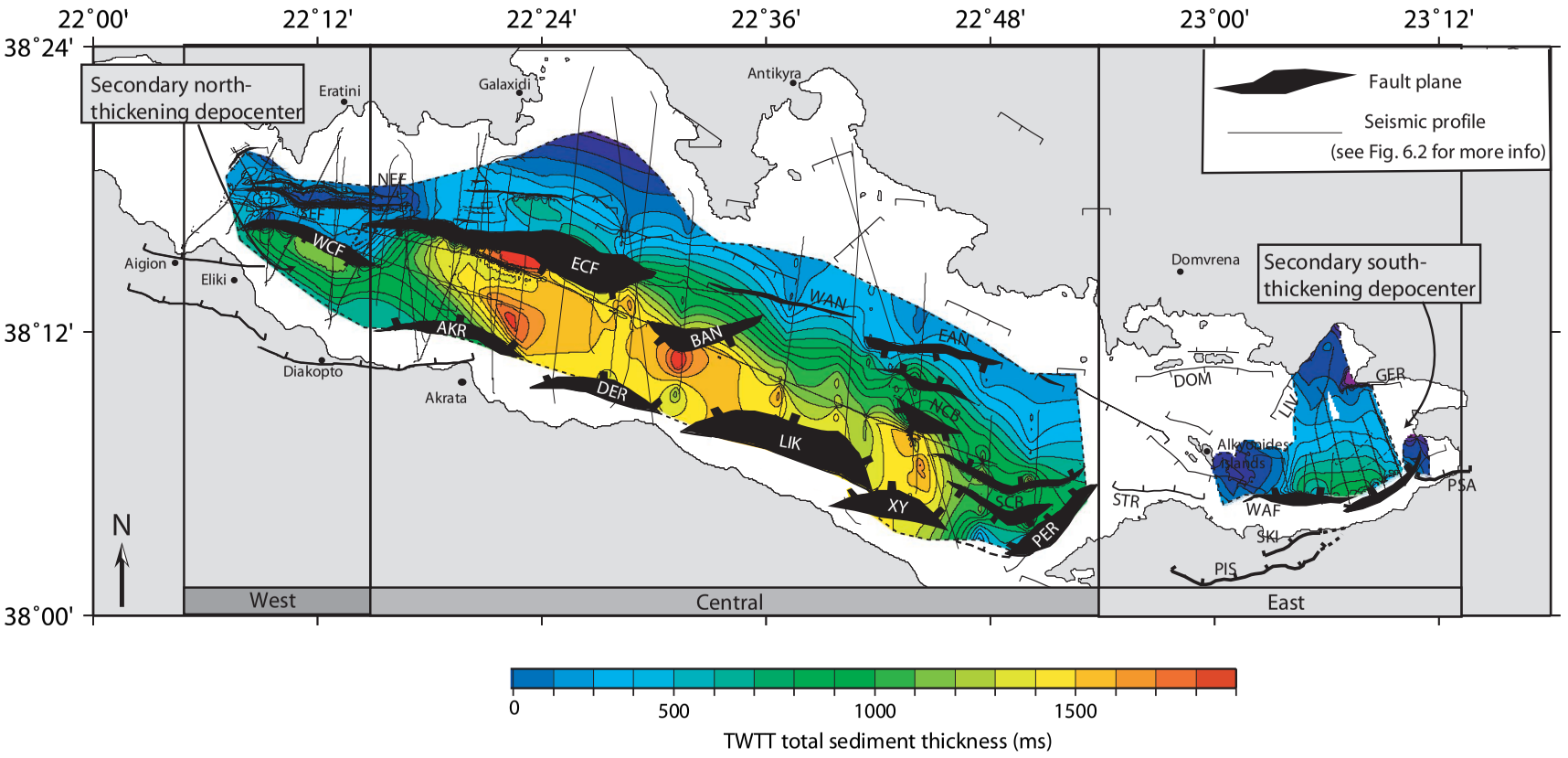

FIGURE 6.9: Total TWTT sediment thickness within the Corinth rift based on the basement interpretation of Fig. 6.8 and the bathymetry presented in Fig. 6.1. Fault plane widths and lengths are derived from seismic data (fault width is defined as the horizontal distance between a faults intersection with the sea floor and basement) and bathymetry. Lines indicate positions where we have access to seismic profiles which penetrate basement. See Fig. 6.1 for full fault names. White areas outside of dotted lines are regions of no sediment thickness interpretation.

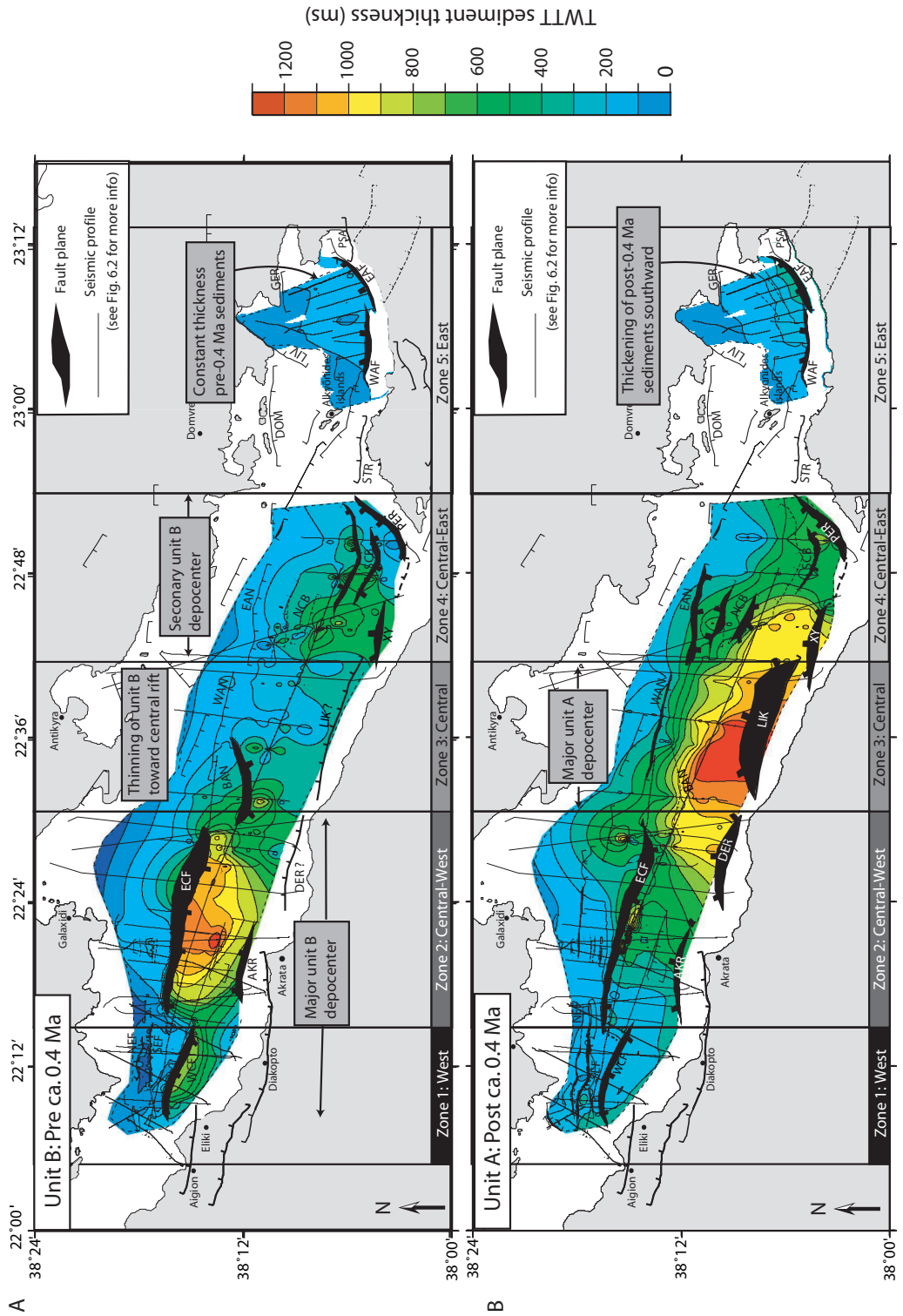

FIGURE 6.10: **A.** Unit B (ca. 1.5 - ca. 0.4 Ma) TWTT sediment thickness within the Corinth rift. Sediments with unit B character are not identified in the Gulf of Alkyonides, however sediments older than ca. 0.34 – 0.4 Ma have been interpreted and their thickness is shown in the isopach. Width of interpreted fault plane corresponds to horizontal extent of fault as seen within unit B. Length of fault during the deposition of unit B is estimated from the extent of major sediment depocentres. **B.** Unit A (ca. 0.4 - 0 Ma) TWTT sediment thickness within the Corinth rift. Width of interpreted fault plane corresponds to horizontal extent of fault as seen within unit A. See Fig. 6.1 for full fault names. White areas outside of dotted lines are regions of no sediment thickness interpretation.

deposited on a consistently subsiding basement. The two unit B sediment depocentres lie within the hanging walls of the West and East Channel and East Eliki–Akrata fault system and the Xylokastro fault, strongly suggesting tectonic control for their origin. The two depocentres are narrower than the modern interpreted fault traces, suggesting fault evolution from originally shorter segments (Fig. 6.10). In further support of a tectonic origin for these features, currently sediment input seems to be consistent along the rift with sediment transport creating a smooth seafloor. The morphology of rivers, geomorphology and lithology of source areas on the south coast does not suggest any reason for such strong bimodal sediment input before ca. 0.4 Ma (Fig. 6.1).

Unit A (post ca. 0.4 Ma) sediments in contrast have a maximum thickness in the central rift south of Antikyra, in the hanging wall of the Derveni–Likoporia faults, with decreasing sediment thickness to the east and west (Fig. 6.10 B). A maximum ∼1300 ms (∼1600 m) thickness of unit A has ponded in the Likoporia hanging wall. Unit A is thin in comparison with unit B in the western rift (hanging wall of the East channel and East Eliki–Akrata faults). In the eastern Alkyonides Gulf post ca. 0.4 Ma deposits are significantly thicker than pre ca. 0.4 Ma (Figs. 6.10 A and B).

The Figure 6.10 B isopach shows that the enhanced input of post ca. 0.4 Ma unit A in the central rift lies directly in the hanging wall of the Derveni, Likoporia and Xylokastro faults, again suggesting that the deposition has been structurally controlled. Increased activity on these faults post ca. 0.4 Ma would have provided accommodation space and an uplifted source area for increased deposition. This is a simpler explanation than calling for large focused changes in the location of major sediment input, of which we have no evidence given river courses (Ziegler 1983). River systems along the south margin are either ancedent (having maintained their direction of flow across topography) or are re–established after a period of tectonically controlled reverse drainage. There is no evidence for changes in the quantity of sediment input by rivers along different parts of the rift axis pre and post ca. 0.4 Ma, and it is hard to explain possible reasons for such a trend without invoking tectonic control (i.e. variations in the location of uplifted source areas).

Although the net pattern of basement subsidence and bathymetry divides the Corinth rift into three structural zones (east and west areas of shallow basement and bathymetry and a central area of deep basement and bathymetry; Figs. 6.1, 6.8 and 6.9), from the distribution of fault controlled sediment depocentres, it has evolved in five distinct tectonic zones with time (Fig. 6.10). Zone 1) The western rift, Zone 2) The central-western rift with thick unit B, Zone 3) the central rift with thick unit A, Zone 4) the central-eastern rift with significant unit A and B and Zone 5) the eastern rift (Alkyonides Gulf) (Fig. 6.10).

6.7 Basin Age

Estimates of the timing of initiation of faults bordering the modern offshore Corinth rift have been derived from geochronology and projections of Quaternary uplift rates onshore and extrapolation of Quaternary chronostratigraphy offshore. These methods all have their own inherent errors and may be biased toward either maximum or minimum values of rift initiation.

The elevation of the uplifted East Eliki footwall is 800 – 1000 m, which has undergone minimal erosion as topsets are preserved (McNeill & Collier 2004). Assuming constant uplift rates McNeill et al. (2005b) have estimated the initiation of activity on the East Eliki fault at ca. 0.7 – 1 Ma. This value could be a maximum as the uplift rate is likely to be over-estimated, due to high Holocene activity. Similarly, Armijo et al. (1996) have derived an age of ∼1 Ma for the Xylokastro fault based on a constant uplift rate assumption and footwall elevation.

An age in this range is further supported by activity of the Mamoussia-Pirgaki fault ca. 0.8 – 1.8 Ma, recorded by hanging wall Gilbert fan deltas, now uplifted in the East Eliki fault footwall (Symeonidis et al. 1987, Rohais et al. 2007), and a slightly younger age of 0.7 – 1.1 Ma has been interpreted by Ford et al. (2007). This hanging wall subsidence pre–dates the initiation of the East Eliki fault (the currently active system) further north. A potentially older maximum age of ca. 0.8 – 2.2 Ma for Alkyonides fault initiation has been proposed by Leeder et al. (submitted), based on the age of the oldest sediments (2.2 Ma) and an uplifted calcrete (0.8 Ma) in the abandoned and uplifted Megara basin.

Offshore stratigraphic horizons in the Gulf of Corinth have been age estimated to a maximum of ca. 0.4 Ma for the unconformity surface (e.g. Figs. 6.3 and 6.4). Offshore sediments, and therefore activity within the modern rift is at least ca. 0.4 – 0.5 Ma. The interpretation of older chronostratigraphy is not possible due to the absence of clear continuous reflections within unit B, although growth patterns within this unit do allow estimations of relative fault activity. In the Alkyonides Gulf we do not see such a change in seismic character ca. 0.4 Ma, and our chronostratigraphy interpretation may be extended to ca. 0.55 Ma. Assuming sedimentation rates have remained constant in the Alkyonides basin, (a fair assumption given the similarity in seismic character of the sediments to basement), we estimate an age of ca. 1 – 1.5 Ma for the basin bounding faults (comparable with the results of Leeder et al. 2005, and contrasting with the much younger ages of 0.5 – 0.7 Ma from Sakellariou et al. 2007). This age is broadly consistent with estimates of initiation of faults derived onshore.

Offshore, in the western rift Bell et al. (2008) interpret the age of oldest sediments as ca. 1.2 – 1.6 Ma, based on extrapolation of constant sedimentation rates derived from the chronostratigraphy of unit A. Although we recognize this method may be an over simplification (the seismic stratigraphy of unit B is clearly different to unit A, and may have deposited with a different rate) the age of the oldest sediments is

comparable with that in the Alkyonides Gulf, where we are more confident of constant sedimentation rates through time.

We have highlighted in the central rift probable enhanced activity of the Derveni and Likoporia faults post ca. 0.4 Ma (Fig. 6.10 B). Here, the application of a constant unit A sedimentation rate assumption applied to unit B sediments would produce ages that are too low, as we expect pre 0.4 Ma sedimentation rates to be lower than those for unit A (due to lower accommodation space production and probable non–deposition). The possibility of variations in fault activity over time also has implications for the use of constant uplift rate assumptions in deriving fault and basin age. However, without further constraint, this gives us a broad approximation of the timing of basin initiation, and the similarity of ages along the rift gives support to this estimation.

6.8 Fault slip rates

6.8.1 Slip rate determination method

Geomorphic features and dated material have been used, with varying degrees of uncertainty, to estimate average slip rates on major onshore and offshore Corinth faults over a range of time periods (e.g., Armijo et al. 1996, McNeill & Collier 2004, McNeill et al. 2005a,b, Bell et al. 2008). We have used four different methods of slip rate determination, based on available vertical displacement information (stratigraphy, basement structure and onshore field measurements) to estimate slip rates on offshore faults (Fig. 6.11 A to D). We then integrate onshore and offshore data and published results to provide an updated summary of Corinth rift fault slip rates (Fig. 6.12).

The most accurate method of determining fault slip is to directly measure hanging wall–footwall stratigraphic offset (Fig. 6.11 A). Unfortunately, we can usually only correlate displaced stratigraphy for moderate–sized faults as many larger faults have footwalls that are eroded basement or outcrop onshore. Alternatively, with knowledge of the uplift and subsidence component of paleoshorelines of equal age either side of a fault, we can estimate total slip rates by correcting far–field uplift and subsidence to that experienced directly at the fault plane using vertical displacement decay curves for normal faults (e.g., Armijo et al. 1996, Fig. 6.11 B).

If only one component of displacement (footwall uplift or hanging wall subsidence) is known slip rates can still be determined, but with higher uncertainty (Armijo et al. 1996, De Martini et al. 2004, McNeill & Collier 2004, Fig. 6.11 C). By applying an appropriate long term uplift to subsidence ratio the missing subsidence or uplift component can be estimated, in order to deduce slip rate. An uplift to subsidence ratio of 1:1.2 – 2.2 is suggested by McNeill et al. (2005b) for the Corinth rift (and other extensional systems). This ratio is further supported by the ratio of onshore Late Quaternary uplift (∼1 – 1.2 mm/yr) to Holocene subsidence (∼1.3 – 2.5 mm/yr)

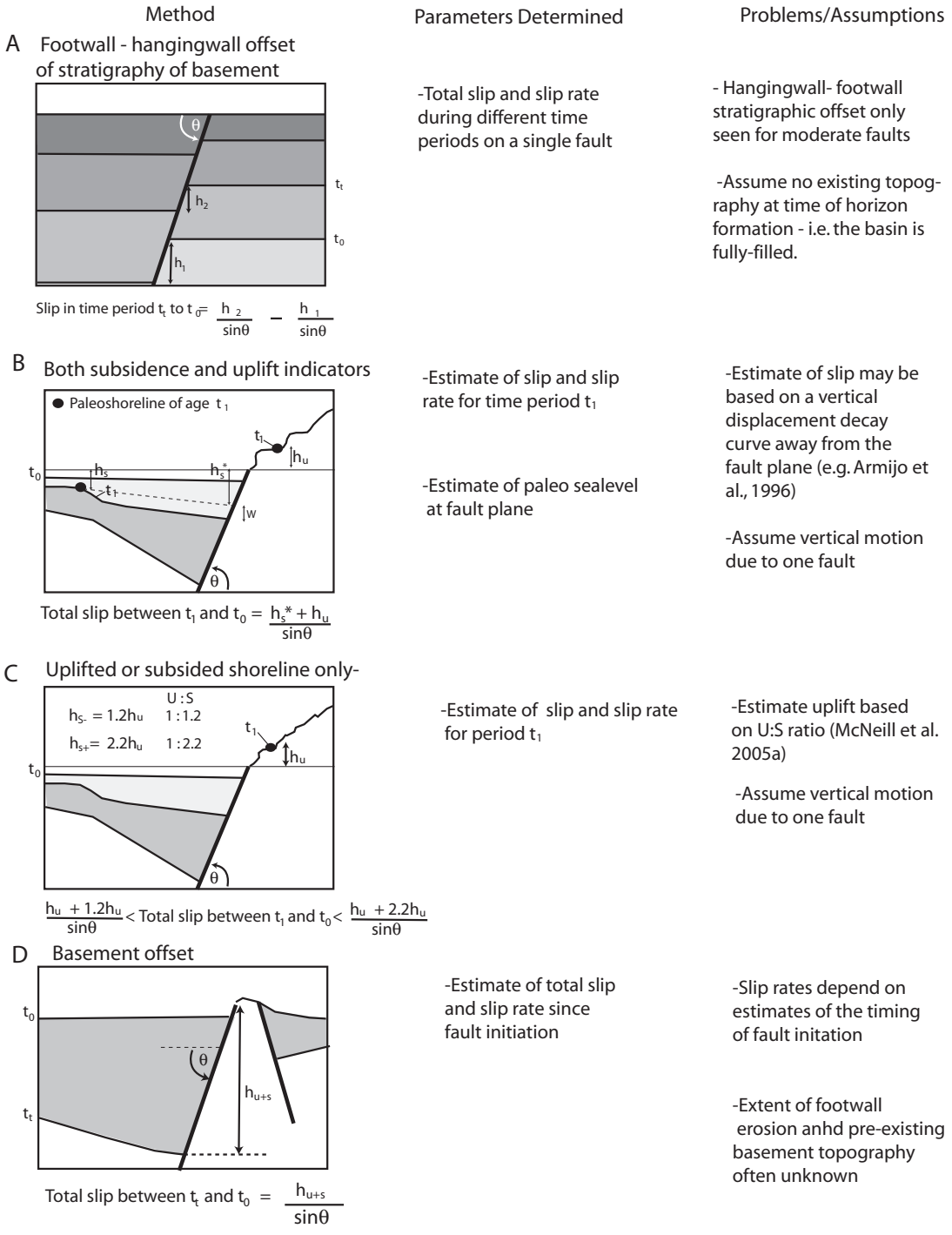

FIGURE 6.11: Schematic to show the four different methods of slip rate determination that have been used in this study and are described in the text. Nomenclature: t_0= time zero, t_t= time t after t_0, h_n=horizon offset, h_s=vertical subsidence, h_u=vertical uplift, h_{s*} =subsidence at fault plane, θ =dip of fault, h_{s+}=maximum subsidence, h_{s-}=minimum subsidence, h_{u+s} = combined subsidence and uplift.

across the Aigon fault (McNeill et al. 2007). Therefore a preferred ratio of 1:1.2 – 2.2 is used in this study.

In some cases total basement offset can be measured to get an estimate of total slip. Slip rates will be based on the estimated age of fault initiation (oldest sediments above basement) and we assume no footwall erosion or pre-existing basement topography (Fig. 6.11 D). Therefore this method is rather less reliable than the others discussed.

6.8.2 Slip rates within the western rift

Slip rates in the offshore western Corinth rift have been discussed by Bell et al. (2008) and McNeill et al. (2005a) and are summarized in Fig. 6.12. Slip rates on the North Eratini fault have been estimated from the subsidence of lowstand delta slope breaks. The North Eratini fault has a Middle–Late Pleistocene to Holocene (0.4 to 0.012 Ma) slip rate of 0.9 – 1.8 mm/yr and 2 – 6.7 mm/yr for the Holocene (0.012 to 0Ma) (Fig. 6.12, McNeill et al. 2005a, Bell et al. 2008). Slip rates across the West Channel fault of ∼0.4 mm/yr are estimated for the last ca. 0.4 Ma and total basement offset predicts a minimum average slip rate of ∼0.45 – 0.9 mm/yr over the faults history (ca. 1.5 Ma to present). The South Eratini fault has a minimum slip rate of $>$ 1.2 mm/yr in the last ca. 0.5 Ma from basement offset (Bell et al. 2008, Fig. 6.12).

Slip rates on the onshore Aigion fault of ∼2.5 – 4.5 mm/yr have been determined by McNeill et al. (2007) by combining middle–late Pleistocene coastal uplift rates and Holocene paleoshoreline subsidence (similar to method Fig.6.11 B). The East Eliki fault has an average late Quaternary uplift rate of ∼1 mm/yr (McNeill & Collier 2004, McNeill et al. 2005b) and McNeill et al. (2005b) suggest a slip rate of ∼3 – 5 mm/yr (Fig. 6.12). Uplift rate averaged over the Pleistocene is lower than during the Holocene (Holocene uplift rates of 1 – 2mm/yr are higher than Quaternary averaged rates; Stewart 1996, McNeill & Collier 2004, Pirazzoli et al. 2004). The West Eliki fault has a Late Quaternary uplift rate of ∼1.25 mm/yr (De Martini et al. 2004). On application of the preferred 1:1.2 – 2.2 uplift to subsidence ratio we derive slip rates of ∼3.5 – 5 mm/yr. The onshore Psathopyrgos fault has a late Quaternary averaged uplift rate of ∼0.7 – 0.8 mm/yr (Houghton et al. 2003), from which we derive a slip rate of ∼2 – 3.5 mm/yr (Fig. 6.12). The onshore Selinilika fault segments described by Palyvos et al. (2005) have a Holocene slip rate of 1.9 – 2.7 mm/yr, determined from paleoseismology.

6.8.3 Slip rates within the central rift

Rohais et al. (2007) report terrace levels in an uplifted Gilbert fan delta with an altitude of ∼200 m in the footwall of the offshore Derveni fault. These terraces confirm activity during the late Quaternary, however detailed correlation or dating of material has not been done to accurately determine their age and uplift rate. Holocene rates

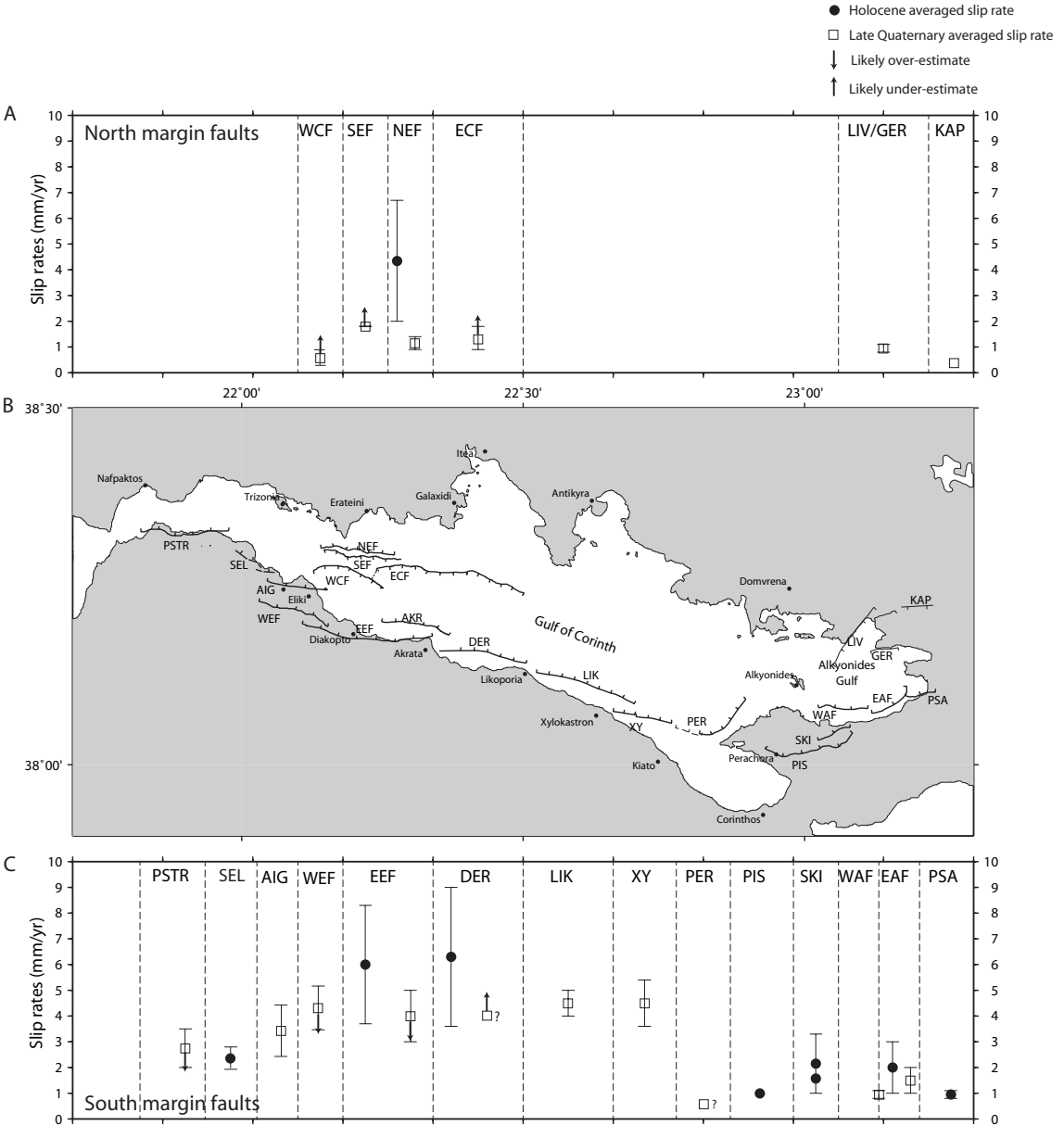

FIGURE 6.12: Summary of Corinth rift slip rates derived in this study and reviewed from the literature. Filled circles are Holocene averaged slip rates and un–filled squares are Quaternary averaged rates. Sources of slip rate measurements are discussed in the text.

in the Derveni area are 1.3 – 2.2 mm/yr, generally similar to Holocene uplift rates in the footwall of the East Eliki fault (0.8 – 2.1 mm/yr, Fig. 6.12 Stewart & Vita-Finzi 1996). Basement depth in the hanging wall of the Derveni fault is generally greater than adjacent to the East Eliki–Akrata fault (Fig. 6.8). This in conjugation with Holocene uplift rates, may indicate slightly higher levels of late Quaternary activity on the Derveni fault compared to the East Eliki fault; however a more detailed study of the terraces in the Derveni footwall is required (Fig. 6.12). We suggest a rate of > 1 mm/yr.

Late Quaternary activity on the offshore Likoporia fault is confirmed by the presence of three uplifted terraces in the footwall close to Kamares (Flotte et al. 2001). The highest ∼200 m strandline has an estimated age of 125 ka, but this age is uncertain. We determine uplift rates of ∼1.6 mm/yr based on this altitude and age of this paleoshoreline. Using our preferred uplift to subsidence ratio we derive a rate of ∼4 – 5 mm/yr. Based on our stratigraphic interpretation and large thickness increase of unit A in the Likoporia hanging wall we would expect that between ca. 0.4 Ma to present slip rates would be higher here than on the Derveni fault. At Xylokastro Armijo et al. (1996) have deduced average fault plane uplift rates of 1.3 mm/yr . Using our preferred uplift to subsidence ratio we derive slip rates of ∼3.6 – 5.4 mm/yr averaged over the last ca. 0.35 Ma.

In order to assess accurately differences in slip rate between the East Eliki–Akrata, Derveni, Likoporia and Xylokastro faults a more detailed analysis of terrace heights in the area between Derveni and Xylokastro is required. From offshore stratigraphy we expect there to be differences in slip rate along strike post 0.4 Ma (Figs. 6.10).

The S–dipping East Channel fault is the only S–dipping fault in the central rift that shows major basement displacement. From the total basement throw observed on this fault slip rates are > 1.8 mm/yr (Bell et al. 2008). This rate is likely to be severely under-estimated due to probable erosion of the basement footwall (Fig. 6.12). This rate is significantly lower than the slip on the Derveni fault on the south coast whereas we would expect it to be similar, given the expected similar basement depths in the hanging walls of these faults (Fig. 6.8). This may be due to footwall erosion reducing the recorded throw on the East Channel fault, or a function of enhanced late Quaternary rates on the Derveni fault compared to the total ca. 1.5 Ma total averaged slip on the East Channel fault.

6.8.4 Slip rates within the Alkyonides Gulf

The series of subsided lowstand delta slope breaks within the offshore Alkyonides Gulf are useful approximate paleosealevel markers and can be used to estimate subsidence. Additionally footwall uplift and slip rate data are available from Collier et al. (1992, 1998), Leeder et al. (2002) and McNeill et al. (in prep).

The ca.12 ka end last glacial maximum lowstand shoreline has subsided to 15 ± 10m below sea level (Table 6.5) and the East Alkyonides fault has been uplifting at 0.3 mm/yr (Leeder et al. 1991), suggesting a Holocene averaged rate of ∼1 – 3 mm/yr incorporating fault dip of 50° (Fig. 6.12). The ca. 340 ka and ca. 240 ka lowstand shorelines have subsided by 135 m and 35 m respectively until ca. 130 ka (Table 6.5). If we assume subsidence is caused by south coast faults ∼10 km away (e.g. the East Alkyonides fault), we estimate slip rates of between ∼1 to 2 mm/yr for the Middle–Late Pleistocene (Fig. 6.12).

Between basin initiation (ca. 1 – 2 Ma) and ca. 0.34 Ma, the Alkyonides Gulf appears to have been an approximately symmetrical basin (Figs. 6.10 A, also suggested by Leeder et al. 2005). Between ca. 0.34 and 0.44 Ma, 70 m of subsidence occurred on paleo–lowstand shorelines (Fig. 6.7 and Table 6.5). Using the assumptions given in Fig. 5.11 B we calculate that if this subsidence is the combined result of both N– and S–dipping faults (i.e. the Livadostros and Kaparelli faults on the north margin, and West, and East Alkyonides, Skinos and Pisia faults on the south margin) on either side of the margin creating symmetrical deposition, both sets of faults must experience combined subsidence rates of 0.44 mm/yr at the fault plane and thereby slip rates in the range 0.8 – 1.1 mm/yr (Fig. 6.12).

From uplift rates on the Psatha fault (Leeder et al. 2002) we derive slip rates of 0.8 – 1.1 mm/yr. Based on displacement rates on the Skinos fault from Collier et al. (1998) we derive slip rates 1 – 3.3 mm/yr, similar to the minimum rates of ∼1.5 mm/yr calculated by McNeill et al. (in prep) from ^{36}Cl exposure dating. McNeill et al. (in prep) also determine minimum slip rates on the Pisia fault of 1 mm/yr. The Perachora peninsula has uniform late Quaternary uplift rates of ∼0.2 – 0.3 mm/yr (Leeder et al. 2005). This is often attributed to regional uplift (due to a lack of tilting of the Perachora peninsula) rather than to fault activity (Leeder et al. 2005). If this uplift was related to activity of the offshore Perachora fault, it would suggest slip rates of 0.25 – 0.5 mm/yr.

More detailed estimates of slip on faults within the Alkyonides Gulf over the last ca. 130 ka are determined by viscoelastic dislocation modelling of long term deformation measurements in Chapter 8.

6.9 3D spatial and temporal rift evolution

The distribution of total unit A and B sediment thickness, imaged in the sediment isopachs (Figs. 6.10 A and B), suggests strong spatial and temporal trends in fault activity within the Corinth rift. Figures 6.13, 6.14 and 6.15 present interpretations from seismic profiles, which in conjunction with sediment isopachs (Fig. 6.10) are used to investigate which faults dominate structure during the deposition of unit A

Paleo-shoreline	Age (ka)	Depth (m)	Vertical subsidence (m)
C1	~12	~85	~15 ±10
C2	~130	~145	~75 ±10
C3	~240	~180	~110 ±10
C4	~340	~280	~210±10
C5	~440	~350	~280 ±10

TABLE 6.5: Vertical subsidence for each of the lowstand shorelines in Fig. 6.7 A, between the age of formation and present day.

and B. For clarity, the stratigraphic architecture is described with reference to each of the five distinct tectonically controlled zones determined above (Fig. 6.10).

6.9.1 Zone 1: Western rift

The thickest accumulations of unit B pre ca. sediments in zone 1 are found in the West Channel fault hanging wall, and the few traceable reflections that occur in this unit tilt and show thickening northward toward this fault (Fig. 6.13 Line A, Bell et al. 2008). Unit B sediments are thin in the West Channel fault footwall, (also the South Eratini fault hanging wall) suggesting the South Eratini fault was relatively inactive during this period (Fig. 6.10 A). Similarly, unit B deposits are thin in the hanging wall of the North Eratini fault, with some southward thickening suggesting minor pre ca. 0.4 Ma activity (Fig. 6.13 Line A).

Unit A sediments also tilt and thicken northward toward the West Channel and South Eratini faults, reaching thicknesses of ∼200 m (Bell et al. 2008). From the small offset of the unconformity surface across the West Channel fault and the large bathymetric scarp produced by the South Eratini fault, Bell et al. (2008) suggest that post ca. 0.4 Ma activity is enhanced on the South Eratini fault, compared to the West Channel fault. Late Quaternary slip rates are also higher on the North Eratini fault than for the West Channel fault (Fig. 6.12 Bell et al. 2008). Slightly thicker sedimentation (∼300 m), however is seen at the southern end of Line A (Fig. 6.13), and the southward tilt of stratigraphy suggest the East Eliki–Akrata faults have increasing structural control here.

Line A (Fig. 6.13) shows that the West Channel fault dominated the structure of the western rift before ca. 0.4 Ma, however activity has since migrated to focus on the North and South Eratini faults further north, and on the East Eliki fault to the south. Currently the N– and S-dipping faults are exerting a similar influence on stratigraphy (causing a pivot point and a change in the polarity of minor faults half way between them, Line A Fig. 6.13). This equivalence however is not reflected in the slip rates. N–dipping faults have rates of ∼3 – 5 mm/yr, compared to the West Channel and South Eratini faults combined >1.8 mm/yr slip rate (Fig. 6.12). If these rates are

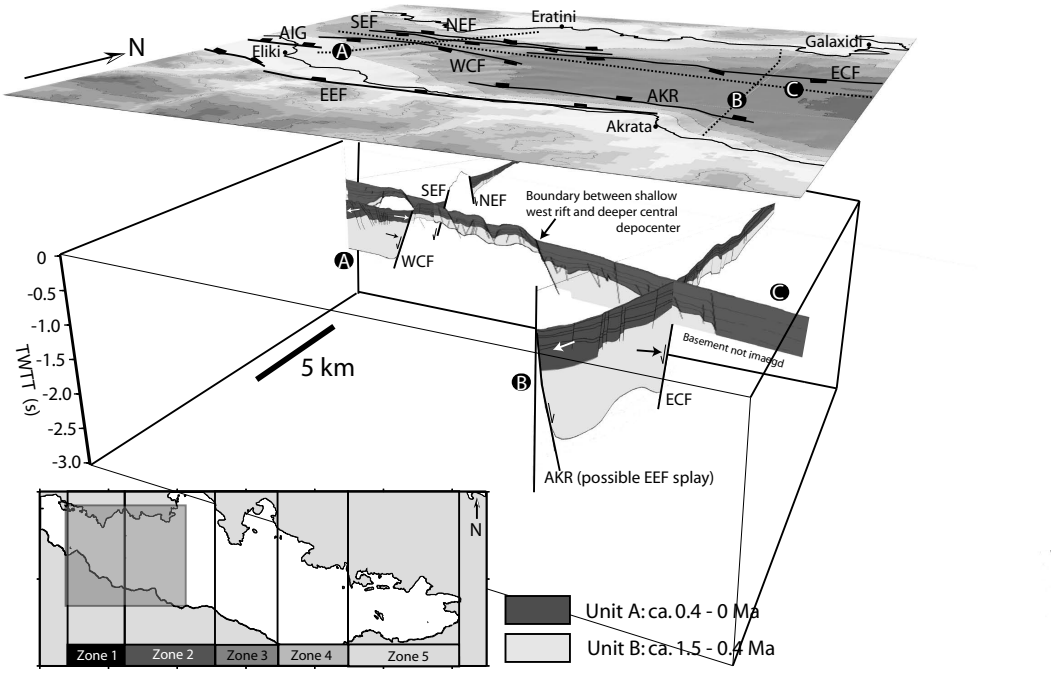

FIGURE 6.13: Interpretation of the 3D subsurface structure of the western (zone 1) and central–western (zone 2) rift showing variations in the thickness of units A and B. Line A is our interpretation of a NS trending profile which crosses the West Channel, South Eratini and North Eratini faults. Line B is from a line further east that crosses the East channel and Akrata faults. Line C is a tie line that connects these two lines and aids confident interpretation (shown in Fig. 6.4). Lines A, B and C have been interpreted from data collected in the M.V. Vasilios cruise, after McNeill et al. (2005a) and Bell et al. (2008).

correct we would expect all stratigraphy to tilt south. Stratigraphy suggests this is not the case and the discrepancy could be due to large amounts of erosion of the South Eratini footwall reducing slip rate estimates.

6.9.2 Zone 2: Central-western rift

The overall geometry of the central rift resembles a symmetric graben (Lines B and E, Fig. 6.14 ; Clement 2000, Sachpazi et al. 2003, Clement et al. 2004). This net geometry is composed of clear changes in rift geometry during the deposition of units A and B (Figs. 6.10 and 6.14).

Figure 6.14 Line E is our interpretation of the Hellenic Petroleum line described by Sachpazi et al. (2003), Moretti et al. (2003) and Clement et al. (2004) (Fig. 6.6 and 6.10). We can confirm that the transition they discuss and tentatively date at ca. 0.5 Ma is the same as our ca. 0.4 Ma unit A to unit B unconformity. Unit B thickens northward toward the East Channel fault zone (Fig. 6.6) and has been severely affected by minor faults that sole out onto the basement surface (Clement

2000, Clement et al. 2004, Fig. 6.6). At the southern end Line B sediments also thicken toward the East Eliki–Akrata fault (Figs. 6.13 and 6.14), but such southward thickening is not seen adjacent to the Derveni fault (Line E, Fig. 6.14). This suggests activity of the S–dipping East Channel and N–dipping East Eliki–Akrata faults were equivalent, whereas activity on the East Channel fault was greater than that on the Derveni fault pre ca. 0.4 Ma.

Clement (2000), Clement et al. (2004) and Sachpazi et al. (2003) interpret unit A in terms of at least five 100 ka sea level cycles, whereas we identify only four distinct units to ca. 0.4 Ma (Fig. 6.6). Unit A has a general southward thickening trend in the central–western rift, suggesting the dominance of N–dipping East Eliki–Akrata and Derveni faults over the East Channel fault post ca. 0.4 Ma (Lines B and E, Fig. 6.14). Line E shows that greatest sedimentation pre 0.24 Ma is in the centre of the current basin, halfway between N– and S–dipping faults (Figs. 6.6 and 6.14). Post ca. 0.24 Ma there is intense southward thickening toward the Derveni fault hanging wall, with extreme thickening post ca. 130 ka.

Slip rates for the East Eliki and Derveni fault, derived from Late Quaternary uplift rates (3–5 mm/yr McNeill et al. 2005b) are much higher than rates on the East Channel fault ($>$ 1.8 mm/yr) as expected from stratigraphic geometry. Slip on the Akrata fault alone is unknown, but its addition will result in slip rates on south coast faults being $>$ 3 – 5 mm/yr.

6.9.3 Zone 3: Central rift

Minimal unit B has deposited in the central rift, and we have argued this is a direct result of tectonics rather than non-tectonically controlled variations in sediment input (Fig. 6.10 A and Line F Fig. 6.14). The small accumulation of unit B is likely to be the result of lower magnitudes of slip on the Derveni and Likoporia faults pre ca. 0.4 Ma compared to faults to the east and west producing thicker unit B accumulations (Fig. 6.10 A), resulting in this area becoming a relative basement high. Unfortunately due to the lack of continuous reflections within unit B, any onlapping relations onto this basement high to prove reduced subsidence on the Derveni and Likoporia faults are impossible to interpret.

Unit A, in contrast, is thicker than is observed to the west and east, and shows strong stratigraphic tilting and thickening to the south in the hanging wall of the Likoporia fault (Fig. 6.10 B and 6.14, Line F). The Derveni, Likoporia and Xylokastro faults are responsible for the large unit A depocentre in the central rift. Isopach Figure 6.10 B suggests that the Likoporia fault has accumulated the greatest throw of the three faults in the last 0.4 Ma, and we may expect higher slip rates for the Likoporia fault than the East Eliki-Akrata and Xylokastro faults. Due to poorly preserved and studied terraces in the Likoporia and Derveni footwalls we can not confirm this

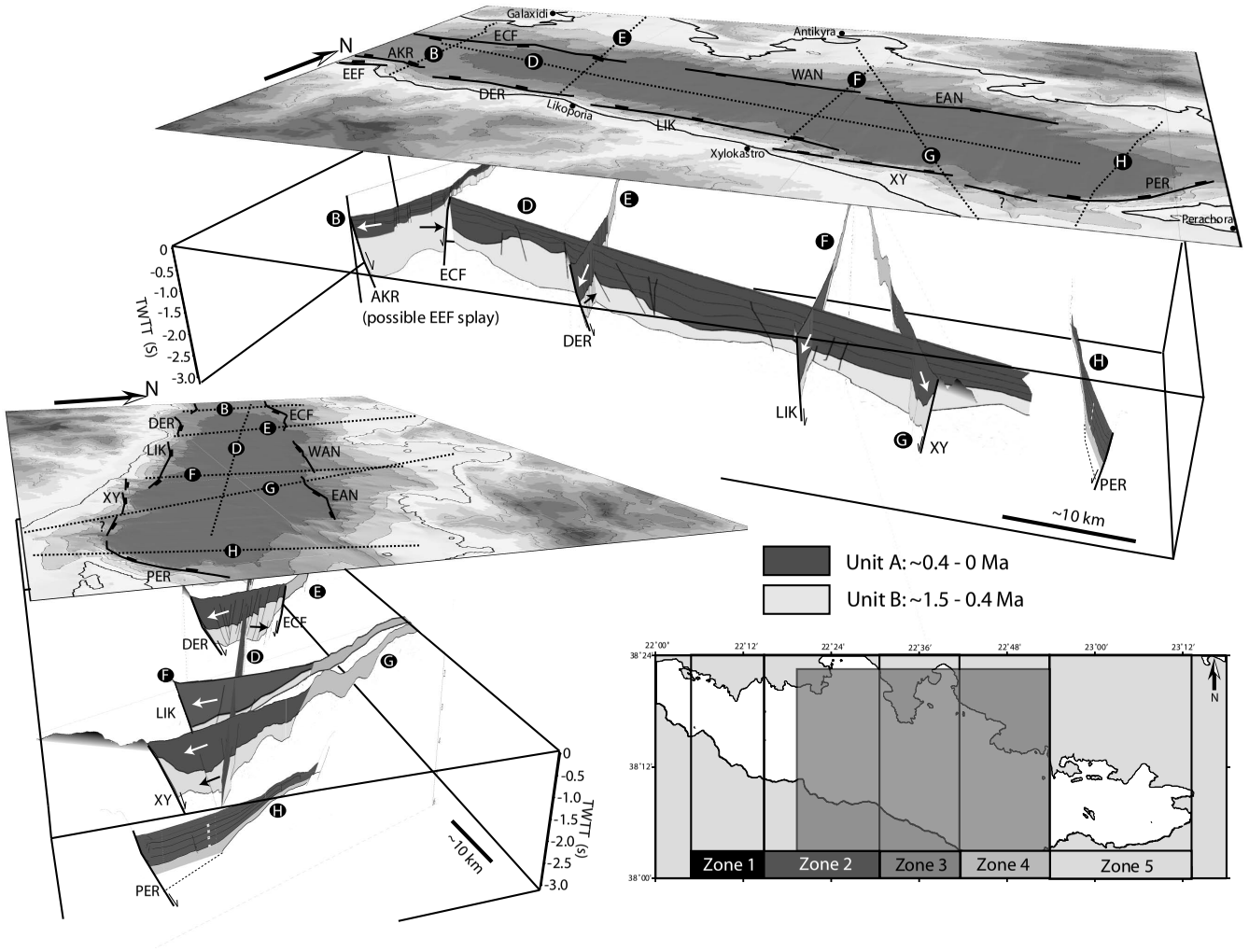

FIGURE 6.14: Interpretation of the 3D subsurface structure of the central–western (zone 2), central (zone 3) and central–eastern (zone 4) rift showing variations in the thickness of units A and B. Line D is our line interpretation of the E–W SEIS–GRECE profile presented by Clement (2000) and Clement et al. (2004); Line E and Line G are our interpretation of the two Hellenic Petroleum lines presented by Clement (2000) and Sachpazi et al. (2003); Line F is an interpretation of line EW0108–35 from the R/V Maurice Ewing dataset (Goodliffe et al. 2003) and Line H is an interpretation of a profile from the shallower 1982 RRS Shackleton survey (Higgs 1988, Stefatos et al. 2002).

hypothesis at present. It is also probable that these three fault segments are in fact connected at depth.

The consistent southward tilt of stratigraphy indicates that, unlike in the central–western rift, an asymmetric S–thickening half graben geometry has dominated throughout rift history, although variations in pre and post 0.4 Ma activity of individual faults are anticipated.

6.9.4 Zone 4: Central–eastern rift

The greatest thickness of unit B in this area is generally in the hanging wall of the offshore coastal Xylokastro fault, however locally it is controlled by now buried inactive faults in the basin centre (North and South Corinth buried faults, Figs. 6.10 A, 6.14, Line G). Unit B sediments are thicker here than observed in the central rift and consistently tilt southward (Fig. 6.10 A and 6.14, Line G).

Unit A also shows a strong southward tilting and thickening toward the Xylokastro fault (Figs. 6.10 B and 6.14, Line G) and is generally thinner than observed in the central part of the rift, although still comprises part of the main central depocentre (Figs. 6.10 B and 6.14, Line F). The central–eastern rift has remained a relatively simple southward thickening asymmetric half graben, controlled by the activity of the Xylokastro fault, throughout rifting history.

6.9.5 Zone 5: Eastern rift- Gulf of Alkyonides

Pre ca. 0.4 – 0.35 Ma sediments within the Alkyonides Gulf are almost constant in thickness (∼150 ms), with only a slight increase to the south-east, in the hanging wall of the East Alkyonides fault (Figs. 6.10 A and 6.15). Active N–dipping faults on the south coast pre 0.4 – 0.35 Ma had a similar activity as the S–dipping faults on the north coast.

A significant change in the overall morphology of stratigraphy occurred ca. 0.35 Ma, after which sediments thicken significantly toward south coast faults (Figs. 6.10 B and 6.15). Sediments between ca.130 – 240 ka show greatest thickening in the hanging wall of the West Alkyonides fault and those between ca.12 – 130 ka are thickest in the East Alkyonides fault hanging wall, suggesting fault activity migrates westward during this time. The East Alkyonides fault is overall the most active offshore structure post ca.0.4 – 0.35 Ma. Onshore, the Pisia and Skinos faults have produced significant footwall topography (> 1 km) and are currently subsiding the footwall of the offshore West Alkyonides fault (Leeder et al. 2005).

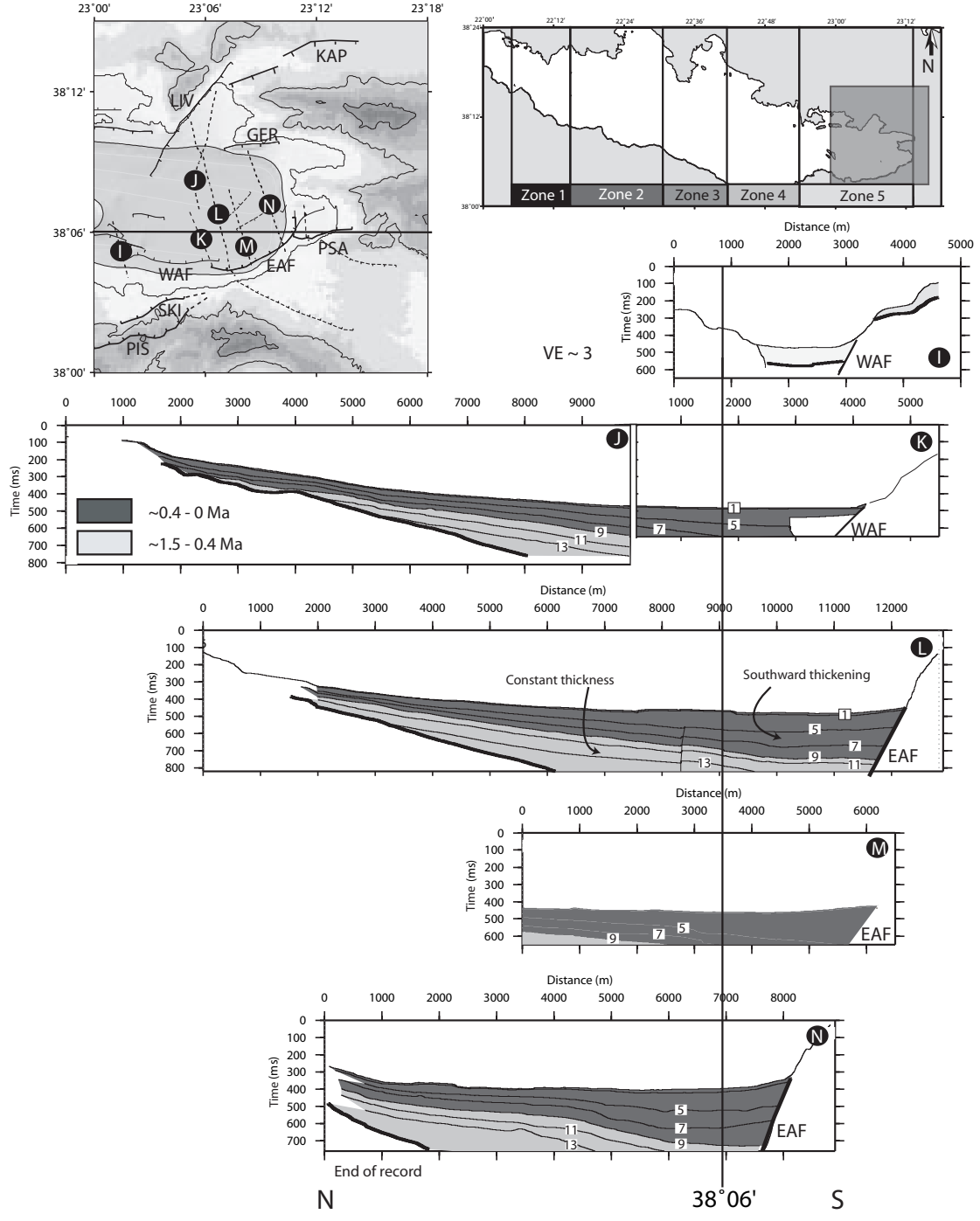

FIGURE 6.15: Line interpretations from the Alkyonides Gulf showing the changing thickness of pre and post ca. 0.34 – 0.4 Ma sediments in the hanging walls of the West and East Alkyonides faults. Interpreted from the 1996 M.V Vasilios data (after Leeder et al. 1991, Collier et al. 2000, Leeder et al. 2005). Numbered horizons correspond to Oxygen Isotope stages correlation (See Fig. 6.7).

6.10 Discussion

6.10.1 Corinth rift evolution summary

The Corinth rift has undergone significant spatial and temporal variations in structure which have been highlighted by the geometry of two distinct basin-wide packages, units A and B, which are separated by a ca. 0.4 Ma unconformity.

Ca. 1- 2 to ca. 0.4 Ma

Between ca. 1 – 2 to 0.4 Ma, the seismically unreflective sediments of unit B were deposited preferentially in two tectonically controlled depocentres in the Gulf of Corinth (Figs. 6.10 A and 6.16 A). The faults responsible for these depocentres were separated by a basement topographic high with little accommodation space available for deposition of unit B (Figs. 6.16 A and C). The length of the major unit B depocentres are shorter than the modern fault traces (Fig. 6.10 A). This suggests that the East and West Channel and Xylokastro faults have evolved to longer lengths since the deposition of unit B (Fig. 6.10). Within the western–most depocentre the S–dipping East and West Channel faults generally had the greatest influence on stratigraphy, although the south coast faults probably were also important (Figs. 6.16 A and B). The oldest unit B deposits were likely influenced by activity on the Mamoussia–Pirgaki fault (ca. 0.8 – 1.8 Ma, Symeonidis et al. 1987, Rohais et al. 2007, or ca. 0.7 – 1.1 Ma Ford et al. 2007) and later by the East Eliki–Akrata and Derveni faults as activity migrated northward ca. 0.7 – 1 Ma (McNeill et al. 2005b).

In the eastern depocentre unit B sedimentation was controlled by the N–dipping Xylokastro fault which is responsible for simple S–thickening half graben geometry (Fig. 6.14). South coast fault slip rates averaged over the pre ca. 0.4 Ma time period cannot be accurately determined due to the lack of dated uplifted material with an age older than ca. 0.5 – 0.4 Ma on the southern coastline. Typical unit B character is not observed in the Alkyonides basin, although sediments older than 0.55 Ma have been interpreted. Pre 0.35 Ma sediments in the Alkyonides Gulf have a constant thickness, suggesting an almost equal influence of N– and S–dipping faults during the development of the early basin with individual slip rates of ∼0.8 – 1.1 mm/yr (Fig. 6.16 D).

Ca. 0.4 Ma to recent

Post ca. 0.4 Ma, the thickness of unit A sediments shows that the geometry of the later rift was very different to that of the earlier rift. The greatest areas of subsidence and sediment accumulation post 0.4 Ma are directly in the area of inhibited unit B deposition, between the two unit B depocentres (Fig. 6.17 A). Post 0.4 Ma sedimentation occurs in a single depocentre centered over the area of low unit B

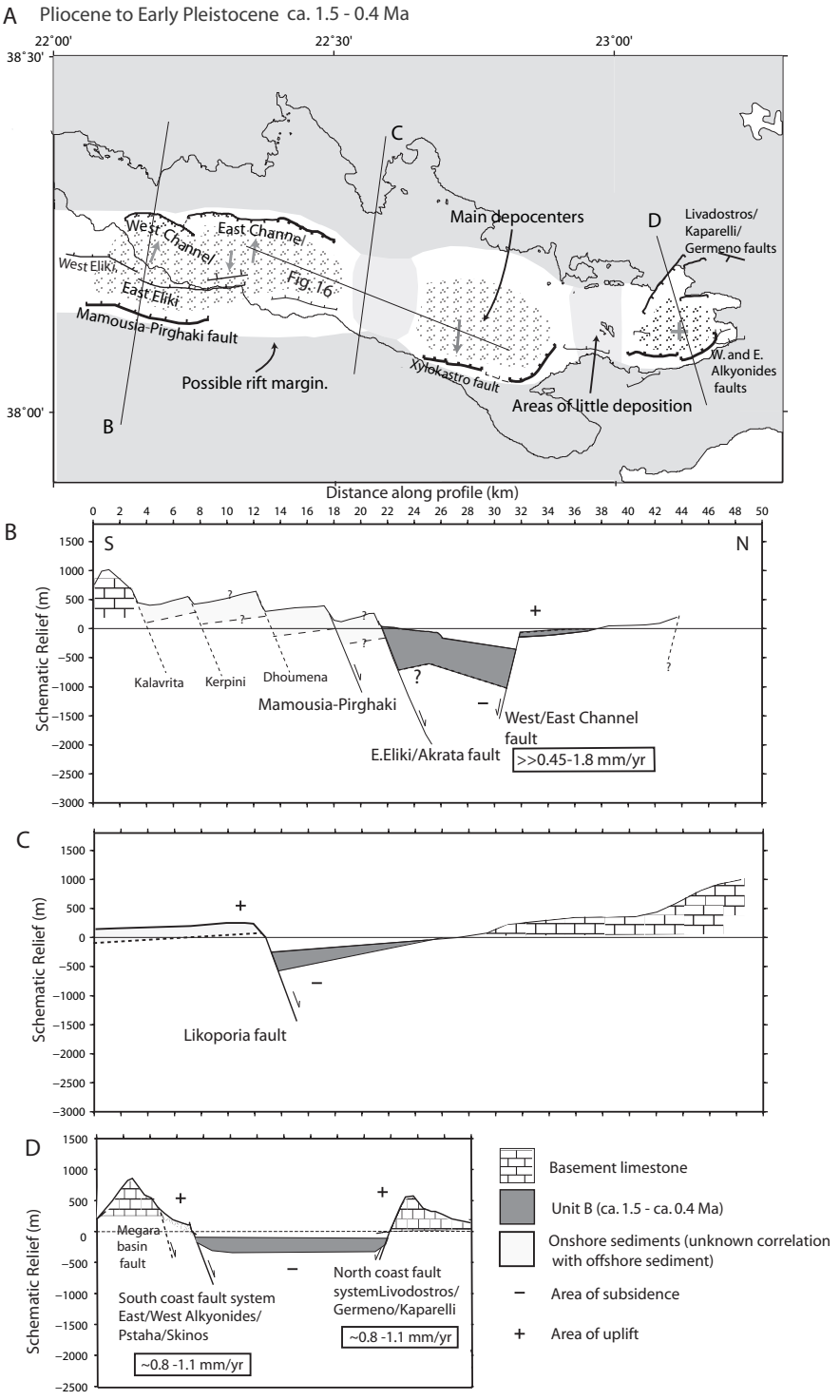

FIGURE 6.16: **A.** Major active faults within the Corinth rift interpreted to be responsible for basement subsidence and sediment distribution in the Pliocene to Early Pleistocene (ca. 1.5 to ca. 0.4 Ma). Possible positions of the coastline and areas of shallow water have been suggested. **B.** Schematic cross section across the western rift highlighting the focusing of extension onto the Eliki and West Channel faults, rather than on a number of south coast faults ca. 1.5 Ma. Basement structure and sediment distribution are strongly affected by the West Channel fault. **C.** Cross section across the central rift schematically showing the structure of the rift here in the Pliocene–Early Pleistocene. Very minor basement subsidence occurs on the south coast Likoporia fault. To the east and west of this area major sediment depocentres are constructed (A). **D.** In the Alkyonides Gulf at this time structure is controlled almost equally by N– and S–dipping faults.

deposition, with much less thickness variation than was observed in unit B. This area, which is controlled by the N–dipping Derveni, Likoporia and Xylokastro faults, must have experienced a significant increase in fault slip compared to that during the pre ca. 0.4 Ma period, allowing the creation of extra accommodation space and uplifted source areas. This would of course suggest enhanced onshore uplift in this region (Fig. 6.17 A, C). Such an increase in late Quaternary slip rates in the central rift has been suggested by Pirazzoli et al. (2004) (a phenomena called the 'Corinth bulge'), however due to the current lack of terrace preservation and study in the Derveni and Likoporia footwalls this change in rate may or may not be preserved onshore. Over the late Quaternary we expect slip rates to be greater in the central rift than the $\sim$3 – 6 mm/yr predicted for the Eliki and Xylokastro faults (Armijo et al. 1996, McNeill et al. 2005b). The increased importance of the Derveni fault post ca. 0.4 Ma relative to the S–dipping East Channel fault (Fig. 6.17 A) means that unit A sediments fill a southward thickening half graben structure, compared to the N–thickening nature of unit B deposition her. The compound effect of these two deformation episodes causes the formation of a net graben basin structure (Line E, Fig. 6.14, Sachpazi et al. 2003).

Although the N–dipping East Eliki–Akrata faults do affect thickening of stratigraphy in the south of the western rift, the S–dipping West Channel and South Eratini faults appear to dominate sediment accumulation in the centre of the basin producing a N–thickening wedge (Figs. 6.17 A and B). Slip rates on north margin faults ($>$ 1.8 mm/yr) are much less than slip rates on south coast faults (3 - 5 mm/yr), probably because of the under–estimation involved in the determination of N-margin fault slip rates (Fig. 6.12). Since at least ca. 0.4 Ma the East Eliki fault has uplifted marine terraces on the south coast, and has been dominant over older inactive onshore faults to the south. Although we also see a migration of faulting to the north offshore (activity has transferred from the West Channel to the North and South Eratini faults) the distance of migration is less than that on the south coast (N. Peloponesse, e.g., Collier & Jones 2003, Rohais et al. 2007, Ford et al. 2007), and in general the western rift is narrowing, rather than migrating northward with a constant width.

In the Alkyonides basin, post ca. 0.4 Ma activity has become focused on N–dipping south margin faults, mainly the offshore East Alkyonides fault and onshore Pisia, Skinos and Psatha faults.

Recent activity from geodesy

Currently the most active area of geodetic extension in the Corinth rift is in the west (Fig. 6.1; Davies et al. 1997, Clarke et al. 1998, Briole et al. 2000, Nyst & Thatcher 2004). This area does not coincide with the area of greatest net subsidence in the central part of the Corinth rift (Fig. 6.8). If these geodetic measurements are correct

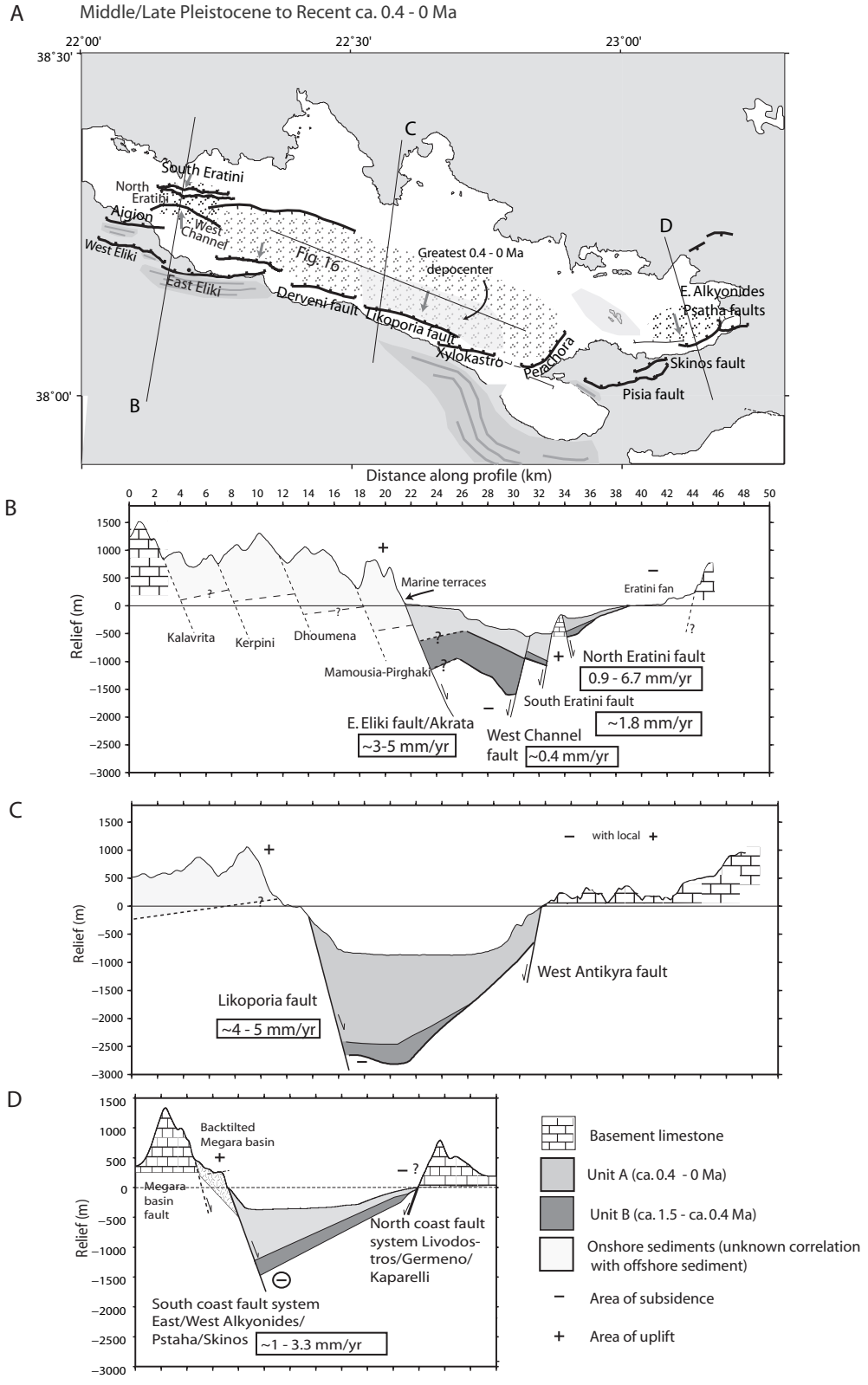

FIGURE 6.17: **A.** Major active faults within the Corinth rift interpreted to be responsible for basement subsidence and sediment distribution from the Middle/Late Pleistocene to recent (ca. 0.4 to 0 Ma). The location of major post ca. 0.4 Ma sediment depocentres is highlighted. **B.** Schematic cross section across the western rift showing the initiation of the South and North Eratini faults during this time and the continuing dominance of S–dipping faults. **C.** Cross section across the central rift shows the extreme sediment thickening post ca. 0.4 Ma due to greatly enhanced activity on the Likoporia fault. **D.** Subsidence is controlled by N–dipping faults on the southern shoreline post ca. 0.4 Ma.

and correlatable with geological rates and time periods, it may suggest that greatest extensional strain has recently changed position.

6.10.2 Rift Geometry

Along axis Segmentation

The offshore Corinth rift basin, as interpreted in this study has been created by short en–echelon ∼15 – 25 km fault segments (although the East Channel fault is up to 30 km long, Fig. 6.1). Basin geometry currently, and in the past, is composed of segmented depocentres with their along axis length dependent on whether they are controlled by one, or more border faults. For example: the Eratini basin is controlled by a single fault and has an along axis length of < 15 km; the Alkyonides basin is controlled by two en echelon faults and has a length of ∼20 km; the largest pre 0.4 Ma unit B depocentre was influenced by the lengths of the West and East Channel faults and had a length of ∼50 km; and the modern central rift depocentre is ∼80 km long controlled by four en–echelon south margin faults.

Segmentation is also observed at other intra–continental rifts (e.g. East African rift, Rosendahl, 1987, Hayward & Ebinger 1996; Gulf of Suez, Gupta et al. 1999,Gawthorpe et al. 2003), spreading centres (e.g. Woodlark basin, Taylor et al. 1999; Red Sea, Steckler & ten Brink, 1986; Gulf of California, Aragon-Arreola et al. 2005a) and is seen in the preserved passive margin record from much older rifted margins (e.g Atlantic margin, Dunbar and Sawyer 1989b; Voring basin, van Wijk & Cloetingh, 2002) and at mid–ocean ridges (Whitehead et al. 1984, Rouzo et al. 1995). Scales of segmentation at mid–ocean ridges are in the range 50 – 100 km, separated by fracture zones. Similar scales of segmented depocentres exist in the East African rift and Gulf of Suez, controlled by a series of border faults (Ebinger 1989, Bosworth et al. 2005, Fig. 2.4). The Corinth rift generally shows smaller scales of segmentation (at the scale of individual faults). However, there is a suggestion in the Corinth rift that earlier smaller basin segments (i.e. the ∼50 km and 20 km segmented unit B depocentres, Fig. 6.10) evolve to become larger scale depocentre segments under the influence of fault interactions as the rift develops (i.e. the central depocentre, between the western rift and Alkyonides Gulf is now ∼80 km long, encompassing the earlier basins). Development of increasing depocentre length with time, controlled by greater numbers of interacting faults may be a feature of evolving rift systems.

Three possible explanations for along axis rift basin segmentation have been proposed: 1) Spatially periodic asthenospheric upwelling, analogous to mid–ocean ridge segmentation; 2) Pre–existing structural heterogeneity; 3) characteristic length scales of segmentation controlled by fault mechanics (Hayward & Ebinger 1996). In the amagmatic Corinth rift the interpreted segmented depocentres now and in the past bear no relation to the NW–SE striking pre–rift structure. This suggests that segmentation is controlled fundamentally by fault mechanics, with fault length and distribution

along–strike related to crustal thickness and rheology. This is similarly thought to be the case in the western branch of the East African Rift (Ebinger 1989).

Fault dip direction and basin geometry

Interpretation of the dominant fault dip direction along rift axis and through time in this study has outlined three interesting trends: 1) Generally there was more variability in dominant fault dip direction along strike in the past; 2) throughout rift history structural control is always with a single dominant dip direction at any one time in a particular area, forming asymmetric half graben rather than symmetric graben structures; and 3) dominant faults having a S dip direction are generally only interpreted in the western side of the rift. Within the Corinth rift pre 0.4 Ma, S–dipping faults were influential in the production of a large N–thickening sediment depocentre (Fig. 6.10 A and 6.14). However, post 0.4 Ma dominant fault dip directions have evolved to become almost exclusively N-dipping (Fig. 6.10 B and 6.14). The emergence of a dominant fault dip direction is predicted in the evolution of fault zones due to fault plane interactions at depth resulting in unfavorable slip vectors and the death of antithetic faults in favour of a single synthetic dip direction (Jackson & McKenzie 1983, Jackson 1999). This process may explain the evolution toward the asymmetry of modern Corinth rift fault activity.

A dominance of half graben structures, rather than graben structures is observed geologically throughout the Aegean (e.g., Gulf of Evvia, Roberts and Jackson, 1991; Gulf of Gediz, Dart et al. 1995) and in many other rift zones (e.g. East African rift, Rosendahl, 1987, Hayward Ebinger 1996; Gulf of Suez, Gawthorpe et al. 2003; and Lake Baikal, Mats 1993) This may be due to a dominant single structural heterogeneity, only sufficient strain for activation of one fault (Rosendahl 1987) or mantle geometry (Le Pourhiet et al. 2003). Analogous to the Corinth rift, other worldwide rift zones show changes in the direction of half graben tilting along axis and show variations in the polarity of the same depocentre with time, due to changing dominant fault dip direction leading to the formation of net symmetrical graben (e.g. East African rift, Rosendahl 1987; Gulf of Suez, Gupta et al. 1999). In the modern Corinth rift significant S–dipping faulting is now largely restricted to the western rift (e.g. South Eratini and West Channel faults), although active S–dipping faults exist in the Alkyonides Gulf (Kaparelli fault). It is unknown why more complex faulting exists in the western rift than in the central rift where N–dipping faults produce simple half graben. The style of faulting and strain distribution in general changes dramatically between the west and central Corinth rift (with the boundary close to Derveni, Fig. 6.1), these variations are discussed in more detail in the following section.

Strain distribution

The width of the active part of the rift, defined by major active faults and the area of deepest basement depth and bathymetry (Figs. 6.1 and 6.8), is fairly consistent along strike at a width of ∼15 km. The number of faults active within this zone, depth of sediment depocentres, and basement geometry, however vary significantly (Figs. 6.1, 6.8 and 6.9). In the western rift, extension within the active zone is distributed on five major faults (the Eliki, Aigion, West Channel, South and North Eratini faults). As such, rift geometry in the west, between Derveni and Aigion, is complex involving a number of sub–basins. Between Derveni and Perachora, extension is focused on single faults bordering the southern coastline (i.e. Derveni, Likoporia, Xylokastro and Perachora fault). Because extension here is focused on a single structure, deeper basement depths have developed in the hanging wall of these faults than to the west where faulting is distributed. In the central–western region (zone 2), activity in the past was concentrated on a S–dipping fault, and extension has since switched to become focused on the N–dipping Derveni fault (Sachpazi et al. 2003). In the central and central–eastern areas (zones 3 and 4) however, rift geometry throughout history has been a simple south thickening half graben (Fig. 6.10 and 6.14). In the Alkyonides Gulf only one or two faults are responsible for current extension in an across rift direction (i.e. the overlapping Pisia and Skinos faults both control the west side and the single East Alkyonides fault controls the east) and rift geometry here is also a simple half graben, not showing the same degree of rift complexity as in the west.

The same pattern of strain distribution is true if the entire rift (including now inactive faults) is considered. Many parallel inactive faults exist on the south west margin (i.e the Kalavrita to Mamoussia-Pirgaki faults) and these faults have been responsible for uplift generating the rugged Peloponesse topography west of Derveni. In contrast, the region to the east of Derveni to Perachora has fairly subdued topography in comparison, and geology is composed of Pliocene-Quaternary sediments with little pre–rift basement outcrop. These sediments likely deposited in the hanging wall of faults further south (e.g., the Kenchreai and other faults systems interpreted by Collier & Dart 1991, Goldsworthy & Jackson 2001, Roberts 1996). The distance between the older Kenchreai and other (probably) older fault systems and the new active Xylokastro, Skinos and Pisia faults is ∼15 km (Goldsworthy & Jackson 2001), compared to the 5 km spacing of faults in the west. This variation in fault properties may be related to differences in crustal thickness and rheology along the rift axis, potentially inherited from the Hellenide orogeny. Although the divide in fault properties lies in the same region as a Pliocene NW detachment structure suggested by Papanikolaou & Royden (2007) we do not see any evidence of such a fault structure offshore and no large variations in basement depth occur at this location.

6.10.3 Rift propagation models

Evidence for/against along axis propagation

The estimated age of the western Corinth Gulf and Alkyonides Gulf from offshore stratigraphy are both similarly ca. 1.5 Ma. By incorporating onshore evidence into this chronology a realistic estimate of fault initiation in both of these regions is in the range 1 – 2 Ma. The similarity in age estimate of both the active western basin bordering faults and Alkyonides Gulf active faults suggest that both initiated at the same time. This would imply that propagation of faulting has not occurred along the rift axis, but faulting initiated at the same time in the western and eastern parts and probably in the centre. This interpretation disagrees with both the Ori (1989) theory of west to east propagation of the Corinth rift and the east to west propagation theory for Corinth rift development based on rigid block modelling of the GPS velocity field (e.g., Clarke et al. 1998, Nyst & Thatcher 2004) and westward propagation of the North Anatolian fault (Armijo et al. 1996). Without a more detailed chronology of the oldest offshore sediments within basins along the Corinth rift axis, any short time–scale propagation below the resolution of our age estimate (i.e. 1 Myr) cannot be constrained.

Evidence for across axis migration

The western part of the Corinth rift to the west of Derveni, has experienced significant across rift migration of fault activity. The sequence of across rift migration of the now inactive Kalavrita, Kerpini, Doumena and Valimi faults is controversial. Ori (1989) suggest that migration continued in a northward direction due to the progressive initiation of high angle faults over a N–dipping low angle detachment surface that lies beneath the western rift. From stratigraphic analysis of uplifted syn-rift sediments Collier & Jones (2003) instead present evidence that all of these faults initiated simultaneously and activity later became focused on the Mamoussia–Pirgaki fault, before transferring north onto the Eliki and Aigion faults.

The Mamoussia–Pirgaki fault, that was active ca. 0.8 – 1.8 Ma (Symeonidis et al. 1987, Rohais et al. 2007) has since become abandoned in favor of the East Eliki fault which initiated 0.7 – 1 Ma (McNeill et al. 2005b), and the initiation of the Aigion fault 0.2 – 0.3 Ma (De Martini et al. 2004, McNeill et al. 2007). It has previously been considered that fault migration occurs into the hanging wall of major western Corinth rift faults exclusively, as in other regions of the Aegean (Goldsworthy & Jackson 2001). However, Bell et al. (2008) show that offshore fault activity shifts from the West Channel fault to the South and North Eratini faults further north in a footwall direction. The general trend seems to be northward fault migration, rather than exclusively in a hanging wall direction. This has implications for the possible controlling mechanism. The migration of south coast faults has occurred over a wider

across rift area than the offshore fault migration, resulting in an overall small amount of rift narrowing in the west (Bell et al. 2008).

To the west of Derveni to the Alkyonides Gulf, across rift migration has not been interpreted to the same extent. Activity has transferred north from the onshore Xylokastro fault to the offshore Likoporia fault; however a relic of other ancestral faults has not been interpreted to the south of the modern day south east coastline to the same extent as in the west. The Kenchreai fault and other N–dipping faults bordering the north–west Saronic Gulf may be considered the ancestors to the now active Skinos and Pisia faults on the Perachora peninsula. In this case northward migration has occurred in a single step 15 km to the north, rather than the more gradual 5 km stepping of faulting in the west (Fig. 6.1). This large step has resulted in the uplift of the wide Corinth Isthmus basin sediments.

Across rift fault migrations are often attributed to the rotation of faults to unfavorable dip angles resulting in the initiation of a secondary fault which often truncates the older first generation faulting (Forsyth 1992, Jackson & McKenzie 1983, Goldsworthy & Jackson 2001). This mechanism could account for the migration of fault activity across the Corinth rift, although does not explain why there are large differences in the rift migration history and pattern along the rift axis. The reason for differences in across rift propagation character are not clear but may be due to rheological or crustal thickness differences to the west and east of Derveni.

6.10.4 Fault interaction and depocentre development

Interpretation of the Corinth rift offshore stratigraphy has identified two pre 0.4 Ma separate sediment depocentres in what is now the main Gulf of Corinth, connected by a basement high covered by thin unit B accumulation. This area of locally reduced pre 0.4 Ma subsidence and high basement topography has since become the area of concentrated post 0.4 Ma subsidence and sediment deposition (Fig. 6.10). The two original basins formed in the hanging walls of the East and West Channel faults (and Derveni fault although comparatively less active at this time) (west basin) and the Xylokastro fault (east basin). The greatest accumulation of post 0.4 Ma sediments occurs in the hanging wall of the Derveni and Likoporia faults, between these earlier two systems (Fig. 6.10 B). Such basin development could be considered to be the result of three different fault interaction scenarios; 1) the eastern Xylokastro and western East and West Channel and Derveni faults initiated first and created the east and west depocentres. Propagation of the Derveni fault to the east and the Xylokastro fault to the west resulted in fault interaction and linkage in the area of the interpreted Likoporia fault. This created one single large through going fault and enhanced subsidence in the centre of the large fault in the Likoporia region; 2) the East and West Channel, Derveni and Xylokastro faults initiated ca. 1.5 Ma, and the Likoproia fault initiated later ca. 0.4 Ma; or 3) the East/West Channel, Derveni,

Likoporia, and Xylokastro faults all initiated together ca. 1.5 Ma. However, prior to ca. 0.4 Ma fault activity was greater on the East and West Channel and Xylokastro faults with the Likoporia and Derveni faults less active. Post 0.4 Ma extension became focused on the Likoporia and Derveni faults.

The first of these scenarios would require that the three south coast faults we interpret as three distinct segments (the Derveni, Likoporia and Xylokastro faults, Fig. 6.1) are in fact connected as a single ∼50 km segment. The coverage of seismic data available mean the exact positions of fault tips cannot be confidently constrained (Fig. 6.1), but given variations in coastline strike and the fact no evidence of propagation is seen in the seismic stratigraphic record this scenario appears unlikely. Secondly, if the Likoporia fault did not exist between the Derveni and Xylokastro faults pre ca. 0.4 Ma, it seems unlikely that the thickness of unit B deposit that has settled in this area could be due solely to flexural downwarping caused by the other two basins, without at least some element of subsidence on the Likoproia fault. The most realistic explanation, in our opinion, is that the faults initiated together, but strain concentrated on the Xyloakstro and East Channel faults initially before transferring to the Likoporia and Derveni faults post ca. 0.4 Ma. This fault development model can only be tested by a more detailed chronology of offshore sediment and study of uplift rates along the south coast in this area.

A similar style of fault controlled depocentre evolution within rift zones has been observed in the East African rift (Ebinger 1989, Hayward & Ebinger 1996), Red Sea (Steckler & ten Brink 1986) and, although a transtensional system and not directly comparable with the Corinth rift, the Gulf of California (Aragon-Arreola et al. 2005a). In the East African rift en–echelon border fault systems produce ∼100 km long basin segments within the rift zone. Chronology of fault initiation has resolved that separated border fault systems can be much older (i.e. 5 – 7 Ma in the case of the Karonga and Rukwa basins separated by ∼100 km) than the border faults between them (2 – 0.5 Ma border faults that form the Songwe basin that join the Karonga and Rukwa basins). Seismic stratigraphy has illustrated a basin development history within the rift that involves the progressive coalescing of ∼100 km smaller basins into single long ∼600 km connected depocentre. This is analogous to the pattern observed in seismic stratigraphy from the Gulf of Corinth, albeit here the single basin segments are controlled by border fault systems ∼20 – 50 km long and final basin length is ∼100 km. Ebinger (1989) suggest that faults may preferentially propagate into the area between two en echelon faults due to stress concentrations in the zone between the crack tips.

In the Red Sea changes in the position of the depocentre experiencing maximum extension have been attributed to lithospheric strength variations controlled by lithospheric thickness, composition, and thermal properties (Steckler & ten Brink 1986). Although lithospheric control may explain variation in tectonic evolution at the entire rift scale it is unlikely to account for individual sediment depocentre development over the

short length and time scale of basin development in the central Gulf of Corinth. In the Gulf of California migration of extension is the result of changes in the locus of strain toward zones of lower yield stress caused by discrete volcanism. This again is not an explanation for the depocentre development in the amagmatic Corinth rift. In summary the East African rift basin development, although at a larger scale, is the best analogy for the pattern of depocentre evolution in the Corinth rift. We suggest that the observed changes in offshore depocentre development are controlled by the evolution of fault systems bordering these basins constrained by fault mechanics.

The evolution of basin depocentres controlled by fault development and interactions has been studied by 3D analogue modelling (e.g., McClay et al. 2002) and numerical modelling (e.g., Cowie et al. 2000). These models suggest that fault systems evolve and grow by the initiation of isolated sub-basins controlled by individual faults that eventually merge into one continuous system (Fig. 8 of Cowie et al. 2000), and such models have been successful in describing basin migration in the Gulf of Suez (Gawthorpe et al. 2003) and the North Sea (Cowie et al. 2000). The change in depocentre geometry with time from isolated basins to a progressively more connected system is predicted by the Cowie et al. (2000) model of fault interaction and is directly applicable to the pattern of basin development in the Corinth rift (Fig. 6.10). There is no evidence of hard–linkage of the Corinth central rift faults at the surface; however they may be linked at depth. Similar total fault throw on the major border faults suggest they are in some way kinematically linked. This has previously been suggested by Stewart (1996) and McNeill & Collier (2004) based on consistent footwall terrace elevations across fault transfer zones and consistent footwall block elevations.

It may be significant that the small Rion graben (between the Straits of Rion and Nafpaktos Fig. 6.1) separating the Gulf of Patras (to the west of the Rion sill, Chronis et al. 1991) from the Corinth rift is the site of major spatial seismicity clustering today (Doutsos & Poulimenos 1992), and high short term extension rates (e.g., Clarke et al. 1998, Briole et al. 2000). The higher elevation of topography between the Patras and Corinth basins is analogous to what we interpret to have occurred ca. 0.4 – 0.5 Ma between the central-western (zone 2, Fig. 6.10 A) and central–eastern Corinth (zone 4, Fig. 6.10 A) grabens. Such an intersection between two grabens is tectonically unstable (Doutsos & Poulimenos 1992). The setting of the western Corinth rift between the deep subsided Gulf of Patras and the central Corinth rift may explain why short–term geodetic extension rates are high here, in a bid to resume equilibrium between the two graben and reduce the intervening topography.

In summary, this study has highlighted the full complexity in the geometry and evolution of individual depocentres within the Corinth rift. We find no evidence of unidirectional rift propagation, either west to east (Ori 1989) or east to west (Armijo et al. 1996, Le Pichon et al. 1995, Clarke et al. 1998, Nyst & Thatcher 2004). Estimates of the age of currently active faults in the east and west are similar, initiating within the last 1 – 2 Myr. A higher resolution determination of fault chronology is necessary

to identify finer scale patterns of rift propagation. Although the active Corinth rift faults likely initiated at a similar time, 1 – 2 Ma, slip rates of these faults have varied resulting in the production of isolated basins which have later coalesced into a single depocentre due to redistribution of extension. The high seismicity and extension rates to the west of Aigion suggest that this area may in the future be the focus of extension, between the more deeply subsided Gulf of Corinth and Gulf of Patras. Important changes in rift geometry exist to the east and west of Derveni, including the number of faults active, spacing of faults, topography, geology and degree of general rift complexity. The reason for these distinct variations in rift character is currently uncertain.

6.11 Conclusions

1. Improved fault interpretations from the offshore Corinth rift confirm that strain is distributed over many more active faults in the western Corinth rift (6 large major faults across strike) than in the central and Alkyonides basins (1 -2 large major faults across strike). Extension is more distributed to the west of Derveni and more localized to the east (Fig. 6.1).

2. Offshore basement depth is greatest in the central rift, where it is consistently ∼2.7 – 3 km below sea level, reaching depths of ∼3.5 km locally. Maximum basement depth in the eastern and western–most parts of the rift is ∼1.5 – 1.6 km.

3. A major unconformity surface with an estimated age of ca. 0.4 Ma divides two tectonostratigraphic packages with different sediment character and geometry. Pre 0.4 Ma, unit B sediments are seismically unreflective and were deposited in two separated depocentres with along axis lengths of 20 – 50 km controlled by N–dipping and S–dipping fault systems. Post 0.4 Ma, well stratified lacustrine and marine unit A sediments are concentrated between the earlier unit B depocentres predominantly controlled by N–dipping faults on the south coast.

4. The dip direction of faults was much more variable pre 0.4 Ma with both N– and S–dipping faults important. Since ca. 0.4 Ma extension has concentrated on N–dipping faults, with active S–dipping faults largely constrained to the western part of the rift (i.e. the West and East Channel and South Eratini faults).

5. Slip rates are generally ∼3 – 6mm/yr on south coast faults in the Gulf of Corinth, although variations in slip rates on south coast faults over the last 0.4 Ma are expected from offshore stratigraphic patterns. Slip rates are significantly lower in the Alkyonides basin (∼1 – 3 mm/yr) and on S-dipping offshore faults (> 1.8 mm/yr).

6. Estimates of basin age in both the western and Alkyonides gulf are 1 – 2 Ma. This suggests that active faults initiated at similar times along the rift, not supporting either a west to east or east to west propagation.

7. The change in rift geometry from isolated depocentres pre ca. 0.4 Ma to the connection of basins into a single large depocentre post ca. 0.4 is similar to basin development in the East African rift and is likely due to the evolution of fault systems controlled by fault mechanics.

8. Currently geodetic extension rate is greatest in the western rift, not coincident with the area of greatest net basin subsidence in the central rift. This may suggest the Corinth rift is undergoing yet another shift in the position of strain focusing, moving the locus of maximum extension from the central rift to the west of the Aigion area (currently a basement high between the Gulf of Corinth and Gulf of Patras).

9. Large differences in strain distribution, topography, geology and rift complexity occur to the west and east of the Derveni region. The explanation for such a large change in basin character here may reflect variations in crustal thickness and rheology inherited from the Hellenide orogeny.

Chapter 7

Total extension and crustal thinning of the Corinth rift

7.1 Introduction

Total extension provides a measure of the change in across rift width since rift initiation. Measurements from rifts worldwide suggest that the total extension along a rift zone can be fairly constant (Taylor et al. 1999), or highly variable (Dunbar & Sawyer 1989a). The total extension across the Corinth rift is relatively poorly known, mainly due to a previous lack of detailed understanding of fault architecture and total fault heave. Roberts & Jackson (1991) estimated extension across the Corinth rift and Gulf of Evvia using a simple domino faulting model (based on the dip angle of faults and tilt of Miocene sediments) to estimate a total extension of 20 – 30 km across the region. This estimation does not incorporate the displacement observed on individual faults in the system, which in reality show variations in dip direction and throw, and are more complex than a simple domino tilting model (Chapter 6). Westaway (1996) summed offset from faults along five profiles across the rift to establish extension. However, from the interpretations presented in Chapter 6 of this study, the offshore vertical displacements used by Westaway (1996) are clearly underestimated and results out–dated.

The presently active Corinth rift is controlled by the coastal and offshore faults discussed in Chapters 5 and 6 (shown in black in Figure 7.1). However, major faults on the southern shore (shown in red on Fig. 7.1) that are now inactive have also contributed toward the total extension over rift history and must be considered. In this chapter, the basement depth and fault architecture presented in Chapters 5 and 6 are used to firstly determine extension across the currently active part of the Corinth rift, where fault throw is reasonably well constrained (section 7.3.1). Secondly, the total

rift extension will be estimated by including the more poorly constrained contribution of extension from now inactive south coast faults in the calculation (section 7.3.2).

7.2 Measuring extension across continental rift zones

In 1978 McKenzie proposed a simple kinematic model to explain the deformational response of tensional forces applied to continental lithosphere. The model, based on Airy isostatically balanced crustal columns, predicts an initial mechanical subsidence caused by the extension and thinning of the lithosphere, followed by a second phase of thermal contraction due to the cooling of the perturbed thermal anomaly. The kinematic model does not define how stretching is accommodated. However, it is generally believed to occur by brittle failure on normal faults in the upper crust and by plastic flow in the lower crust and upper mantle lithosphere (McKenzie 1978a). This simple instantaneous pure shear stretching model can predict the fundamental aspects of extensional rift basin geometry in some cases (e.g. the North Sea; Wood & Barton 1983), although further thermal and mechanical controls are required to explain the details of sedimentary basin architecture. Additional controls include the modifying effects of: flexural strength of the lithosphere (e.g., Watts et al. 1982); finite duration rifting (e.g., Jarvis & McKenzie 1980); depth–dependent stretching (e.g., Royden & Keen 1980); depth of necking (e.g., Braun & Beaumont 1989); and the geometry of faulting (e.g., Wernicke 1985).

Extension (δl) is a measure of the change in length of a line across a rift zone, compared to its original pre–rift length (l_o);

$$\delta l = l - l_o$$

where l is the stretched length. Direct measurement of the heave across normal faults visible on seismic reflection profiles provides an estimate of the extension across a fault zone. Often, due to the difficulty of accurately determining fault dip on seismic sections, it is more accurate to measure the throw on a fault and determine heave for a range of fault dips or an average fault dip (Lamarche et al. 2006). Other assumptions include that: all faults are visible in the seismic section; all extension in the upper crust is taken up by brittle deformation on faults (Hellinger et al. 1988); and the geometry of faults is planar (Sclater & Shorey 1988). It has been suggested that an additional 40% should be added to the calculated fault heave of major faults to account for extension on faults smaller than the seismic resolution (Jackson & White 1989, Walsh & Watterson 1991, Lamarche et al. 2006). The percentage of extra extension that must be added for the omission of sub seismic faults depends on the resolution of data available for fault interpretation. High resolution data will require the addition of a much smaller percentage of missing extension due to sub seismic faulting than will low resolution data. Another consideration is that listric fault

planes could result in reduced fault heave measurements at the fault plane due to internal deformation of the fault block (Sclater & Shorey 1988).

Extension of rift zones is often quantified as the ratio between the stretched length and original length, known as the β stretching factor;

$$\beta = \frac{l}{l_o} = \frac{l}{l - \delta l}$$

Unlike the extension, this quantity is related to strain (strain + 1). β factor can be calculated from the total extension and the measured stretched length (i.e. total distance between all faults considered in the extension measurement). Estimates of β factor can also be determined from the ratio of original crustal thickness to the stretched thickness (i.e. the degree of crustal thinning, e.g., Su et al. 1989, Karner et al. 2000). Whereas β factors derived from the measured extension on faults are a measure of stretching of the upper crust, crustal thinning provides a measure of the stretching factor of the total crust (including both upper and lower crustal stretching). Recent research has highlighted discrepancies between β factors derived from fault extension and crustal thinning methods (e.g., Royden & Keen 1980, Kruse et al. 1991, Roberts et al. 1997, Davis & Kusznir 2004). This variability has implications for the possibility of low angle faulting, earlier extensional events (Wood & Barton 1983), sub–crustal erosion (Ziegler 1983), depth–dependent stretching (Royden & Keen 1980) and lower crustal flow (Bertotti et al. 2000), complicating the rift geometry when compared to a true pure shear model (McKenzie 1978a). Analysis of post–rift sediments from well data can provide an estimate of total lithospheric extension by comparing subsidence history curves with hypothetical stretching models (Su et al. 1989, Roberts et al. 1997). However, the active Corinth rift is immature and has not yet undergone significant thermal subsidence so this technique cannot be used.

In this study two independent methods for quantifying extension are applied:

- Method 1: Extension derived from fault displacement. Providing a measure of total fault induced extension of the brittle upper crust.
- Method 2: Crustal thinning derived stretching factor. Providing an estimate of the degree of total crustal stretching from the level of crustal thinning.

7.3 Method 1: Extension derived from fault displacement

Total extension has been estimated from the total throw on faults along Transects 1 to 4 in Figure 7.1, which are perpendicular to the rift axis. The interpretation of offshore faults and basement depth along these transects follows the offshore fault interpretations and two way travel time basement depth interpretation presented in Chapter 6, Figures 6.1 and 6.8. Onshore interpretations of inactive faulting and geology follow Collier & Dart (1991), Leeder et al. (1991), Roberts (1996), Collier & Jones (2003), Rohais et al. (2007)

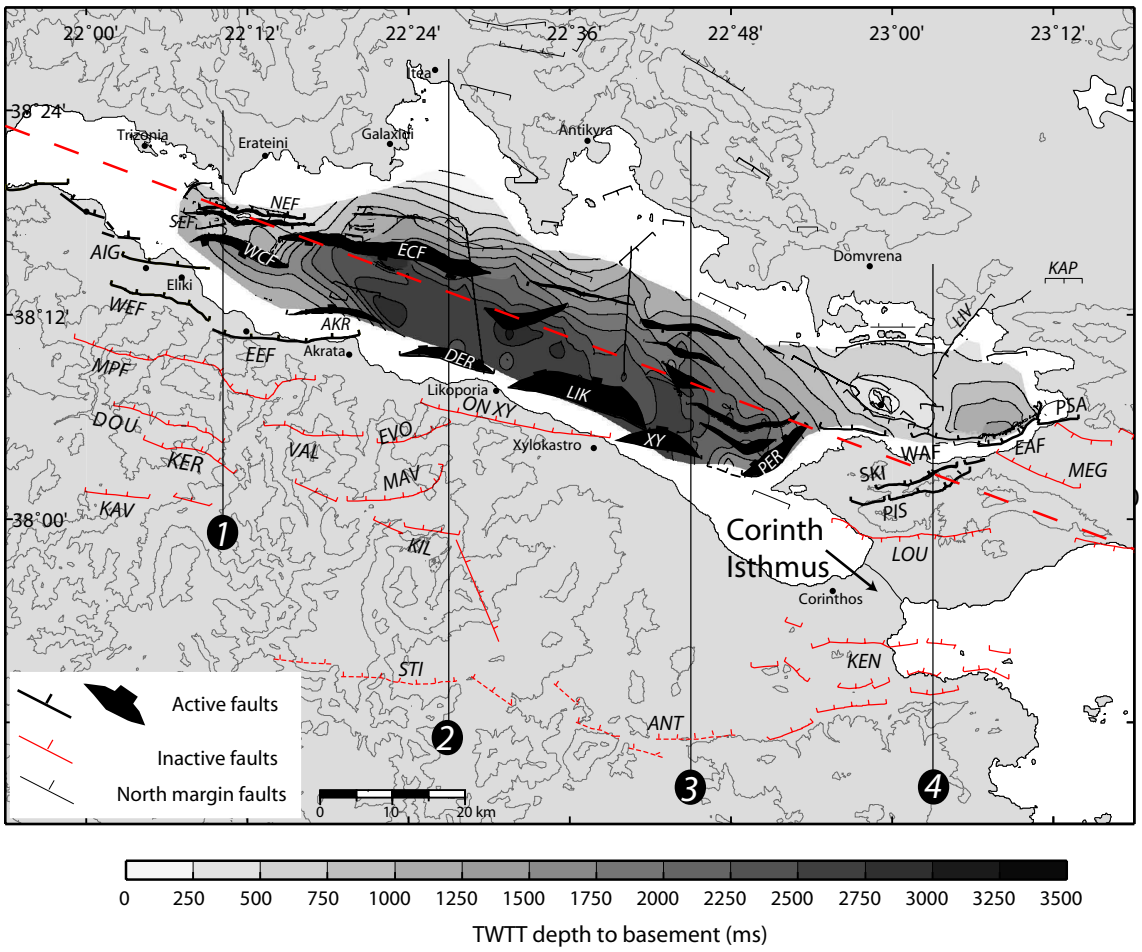

FIGURE 7.1: Interpreted basement subsidence and fault architecture from the offshore Corinth rift (from Chapters 5, 6 and McNeill et al. 2005a). Onshore faults after Collier & Thompson (1991), Roberts (1996), Collier & Jones (2003), McNeill & Collier (2004), Leeder et al. (2005) and Rohais et al. (2007). Transects 1 to 4 are the locations of the profiles shown in Fig. 7.2. Fault names: NEF:North Eratini fault, SEF:South Eratini fault,WCF:West Channel fault, ECF:East Channel fault, LIV:Livadostros fault, AIG:Aigion fault, EEF:East Eliki fault, WEF:West Eliki fault, AKR:Akrata fault, DER:Derveni fault, LIK:Likoporia fault, XY:offshore Xylokastro fault ON XY: onshore Xylokastro fault, PER:Perachora fault, PIS:Pisia fault, SKI:Skinos fault, WAF:West Alkyonides fault, EAF:East Alkyonides fault, MPF:Mamoussia-Pirgaki fault, DOU:Doumena fault, KER:Kerpini fault, KAV:Kalavrita fault, VAL:Valimi fault,EVO:Evrostini fault, MAV: Mavro fault, KIL:Killeni fault, STI:Stimfalia fault segments, ANT:Athikia fault segments, KEN:Kenchreai fault, PSA:Psatha fault, MEG:Megara faults, and LOU:Loutraki fault. Red dotted line represents Clarke et al. (1998) geodetic extension rate profile shown in Fig. 7.3.

and Ford et al. (2007). Fault throw has been measured from seismic profiles in the offshore rift and estimated from geomorphology, geological cross–sections, and projections of uplift rates onshore.

The presently active offshore and coastal faults that border the modern Gulf of Corinth and Alkyonides Gulf have been the focus of this thesis, and robust estimates of slip rate have been collated and derived from offshore stratigraphy and knowledge of uplift rates (Chapter 6, Fig. 6.12). In section 7.3.1, total extension across the presently active part of the Corinth rift is considered, to provide a well constrained estimate of extension over the last 1 – 2 Ma. Although slip rates and throw on the now inactive onshore south coast faults are much more poorly known, their contribution toward total extension must be estimated in order to quantify total Corinth rift extension. This is performed in section 7.3.2, which justifies the choice of fault displacement estimate for the more poorly studied inactive faults.

7.3.1 Active Corinth rift extension over the last 1 – 2 Ma

Total throw measured for each of the active faults is summarised in Table 7.1. For offshore faults that have completely submerged hanging walls and footwalls, total fault throw is given by the measurement of basement offset. This is a minimum due to the unknown and possibly significant effects of footwall erosion.

The total throw of coastal faults must be estimated by either: extrapolating slip rates over the estimated age of the fault; application of an assumed uplift to subsidence ratio on measured footwall topography; or from geological cross-sections reconstructing basement depth. Throw estimates for coastal active faults used in the calculation of active rift extension are explained and justified below.

- **East Eliki fault**: Both the hanging wall basement depth adjacent to the fault plane and footwall basement uplift are unresolved for the East Eliki fault (Fig. 7.2 A). By extrapolating the Late Quaternary slip rate of 3 – 5 mm/yr (McNeill et al. 2005b) over the suspected 0.7 – 1 Ma history of the East Eliki fault (McNeill et al. 2005b) a total throw in the range of 1.6 – 3.8 km is estimated. The upper limit of this estimate predicts basement depth ∼3 km below sea level. From stratigraphic considerations in Chapter 6 it was concluded that the East Eliki and West Channel faults may have had an equivocal effect on rift structure, at least 1.5 to 0.4 Ma. In this case subsidence of the East Eliki hanging wall would not exceed 1.5 km (as for the West Channel fault, Fig. 7.1). Uplifted footwall basement is ∼800 m above sea level (McNeill & Collier 2004), suggesting a realistic range for total vertical throw of 1.6 – 2.3 km (i.e. 1.5 km subsidence plus 0.8 km uplift), however, if the East Eliki fault is more significant than we have estimated from offshore stratigraphy this range may be exceeded.

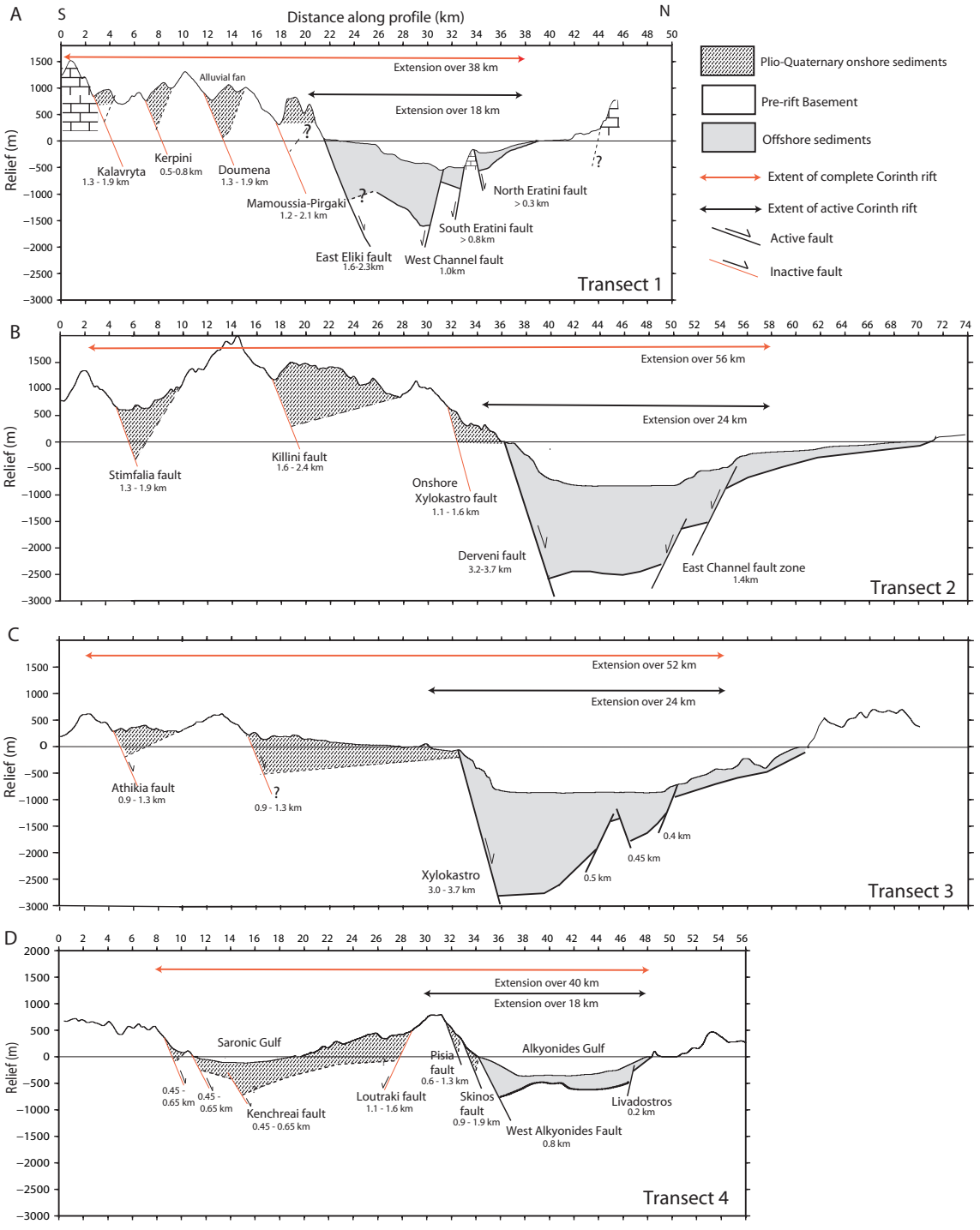

FIGURE 7.2: Interpretation of basement geometry and fault structure for Transects 1 to 4 (Fig. 7.1). Offshore interpretations after Bell et al. (2008), Chapters 5 and 6. Onshore interpretations after Collier & Jones (2003) and Rohais et al. (2007). Fault throw estimates are shown below fault names, and are discussed further in the text.

Fault	Throw (km)	Av. throw (km)	Throw estimation method
Active Faults Transect 1			
East Eliki fault	1.6 – 2.3	2.0	Slip rate extrapolation
West Channel fault	1.0	1.0	Measured from seismic data
South Eratini fault	0.8	0.8	Measured from seismic data
North Eratini fault	0.3	0.3	Measured from seismic data
Active Faults Transect 2			
Derveni fault	3.2 – 3.7	3.5	Basement throw estimate
East Channel fault	1.4	1.4	Measured from seismic data
Active Faults Transect 3			
Xylokastro fault	3.0 – 3.7	3.4	Slip rate extrapolation
Offshore N. margin faults	1.35 total	1.35	Measured from seismic data
Active Faults Transect 4			
Skinos fault	0.9 – 1.9	1.4	Slip rate extrapolation
Pisia fault	0.6 – 1.3	1.0	Slip rate extrapolation
West Alkyonides fault	0.8	0.8	Measured from seismic data
Livadostros fault	0.2	0.2	Measured from seismic data
Inactive Faults Transect 1			
Kalavrita	1.3 – 1.9	1.6	Footwall uplift
Kerpini	0.5 – 0.8	0.65	Footwall uplift
Doumena	1.3 – 1.9	1.6	Footwall uplift
Mamoussia-Pirgaki	1.2 – 2.1	1.7	Footwall uplift
Inactive Faults Transect 2			
Stimfalia fault	1.3 - 1.9	1.6	Footwall uplift
Killini fault	1.5 – 2.2	1.8	Footwall uplift
Onshore Xylokastro fault	1.1 – 1.6	1.4	Footwall uplift
Inactive Faults Transect 3			
Athikia fault	0.9 – 1.3	1.1	Footwall uplift
Corinth isthmus fault	0.9 – 1.3	1.1	Footwall uplift
Inactive Faults Transect 4			
Kenchreai fault	0.45 – 0.65	0.55	Footwall uplift
S. Kenchreai faults	0.9 – 1.3	1.1	Footwall uplift
Loutraki fault	1.1 – 1.6	1.35	Footwall uplift

TABLE 7.1: Summary of throw values for faults along the transects in Figure 7.1

- **Derveni fault:** Basement depth is now ∼2.7 km below sea level adjacent to the Derveni fault (Fig. 7.2 B). From the geological cross–section interpretations of Rohais et al. (2007), basement intersects the Derveni fault plane between 0.5 – 1 km above sea level. This footwall uplift estimate is in the range of that calculated by assuming the Derveni fault has a similar uplift rate and age as the adjacent East Eliki fault. Therefore, the total throw on the Derveni fault is estimated between 3.2 and 3.7 km.

- **Offshore Xylokastro fault:** Hanging wall depth adjacent to the offshore Xylokastro fault plane is ∼2.6 km. From the uplift rates determined by Armijo et al. (1996), and fault dip of 50°, slip rates on this fault of ∼3.5 - 6.0 mm/yr have been estimated in this study (Chapter 6). Assuming an age of 1 Ma, this equates to a total throw of 3.0 – 4.5 km. Given the similarity in basement depth of the Xylokastro and Derveni fault hanging walls, the offshore Xylokastro fault probably has a similar total throw, therefore not likely to exceed ∼3.7 km (Fig. 7.2 C).

- **Pisia and Skinos faults:** The Pisia and Skinos faults are both active and parallel to each other, meaning their vertical displacement fields are superimposed. Slip rates on the Skinos fault are believed to be ∼1.5 mm/yr, and ∼1 mm/yr for the Pisia fault (McNeill et al. in prep). This equates to vertical slip rates of 0.9 – 1.3 mm/yr for the Skinos, and 0.6 – 0.9 mm/yr for the Pisia fault, for fault dips of 40 - 60°. If these faults have been active ca. 1 – 1.5 Ma, as has been suggested, a total throw in the range of 0.6 – 1.3 km for the Pisia fault and 0.9 – 1.9 km for the Skinos is estimated. Topography of up to 1 km exists in the footwall of these two faults, and these estimates appear reasonable. If slip rates for these faults are higher (Collier et al. 1998, suggest up to 2.5 mm/yr) this would lead to significantly greater throw estimates.

- **West Alkyonides fault:** Although the West Alkyonides fault is commonly described as inactive, because of its apparently subsiding footwall caused by activity of the onshore Pisia and Skinos faults, it has contributed significantly toward subsidence of the offshore Alkyonides basin (Leeder et al. 2005). Its total throw of 0.8 km, measured from seismic data is therefore included in the extension calculation for the active part of the rift.

- **Livadostros fault:** The Livadostros fault has produced a seafloor scarp and as will be discussed in Chapter 8 has probably been active over the last 130 ka. Sakellariou et al. (2007) call this fault the Korombilli fault, which together with another S–dipping interpreted fault in the region of Transect 4, have a cumulative throw of ∼200 m. This is similar to the offset in basement depth measured on Transect 4 (Fig. 7.2 D).

Transect	Throw (km)	Heave (km) 50^o	Active rift width (km)	β factor
1	4.1	3.5	18	1.24
2	4.9	4.1	24	1.20
3	4.75	4.0	24	1.20
4	3.4	2.9	18	1.19

TABLE 7.2: Summary of total extension and β factors across the active part of Corinth rift (black faults only on Fig. 7.2). See Table 7.1 for a summary of fault throws included in the calculation.

The total cumulative fault throw, for active faults only along each transect (i.e. the black faults on Figs. 7.1 and 7.2) is shown in Table 7.2, together with calculations of heave assuming an average fault dip of 50^o. Where a range of throw values have been estimated for a fault the average value is included in the total cumulative throw estimate (Table 7.1). For simplicity an estimate of the percentage of missing sub-seismic fault extension has not been applied to the measured fault heaves. This is in light of the fact that this percentage is likely to vary across the rift due to the differing quality of datasets in different areas. The errors this introduces into the interpretations made from these observations are discussed in section 7.5.

Total active fault extension is greatest in the central rift, along Transects 2 and 3 ($\sim$4 km) and reduces to $\sim$3.5 km in the west (Transect 1) and $\sim$3 km in the east (Transect 4). Beta (β) stretching factors have been derived from this total extension length and the measured active rift width. The rift width is measured between the northern most and southern most fault traces included in the calculation, with an additional 2 km added to the ends of each line to include deformation away from the fault plane. The β stretching factor is relatively similar along the rift, although slightly higher in the west (Table 7.2 and Fig. 7.3).

7.3.2 Total Corinth rift (onshore and offshore) extension over > 2 Ma rift history

The extension and β factors derived above do not include extension that has occurred on now inactive faults on the south margin, which have contributed to total rift opening over time. Inactive faults in the south west part of the rift (the area south of Aigion to Derveni) have been well studied and estimates of throw are suggested in the literature, however basement displacement is still difficult to estimate (Collier & Jones 2003, Rohais et al. 2007, Ford et al. 2007). Onshore fault systems to the south of the Corinth Isthmus (e.g. the Kenchreai fault) are also well known (Collier & Dart 1991, Goldsworthy & Jackson 2001). However, in the region south of Derveni to Corinth there are few studies of faulting within the Pliocene–Quaternary sediments. Roberts (1996) suggest from field studies, that

these sediments are bounded to the south by fault segments he names the Stimfalia and Athikia faults (dotted red faults in Fig. 7.1).

The following section outlines throw estimates for inactive faults that are added to the active fault throws shown above (Table 7.2) to obtain a total extension estimate for the entire rift. It is recognised here that the total throw estimated is probably a minimum, because unknown faults are likely to exist within the sediments of the Corinth Isthmus and faulting within the Saronic Gulf crossed by Transect 4 is poorly understood.

- **Mamoussia-Pirgaki fault:** Basement footwall limestone stands 700 m above sediments which infilled the Mamoussia-Pirgaki fault hanging wall. Based on the preferred uplift to subsidence ratio of 1:1.2 – 2.2, discussed in Chapters 5 and 6, a total throw of 1.5 – 2.2 km is estimated. This estimation is similar to total throw estimates determined by Rohais et al. (2007) (2.1 km) and Collier & Jones (2003) (2.5 km) for this fault, based on basement projection on geological cross sections constructed from field studies.

- **Doumena fault:** The Doumena fault is the westward extension of the Valimi fault, which is quoted to have a maximum total throw of 2 km by Rohais et al. (2007). Based on the height of the uplifted footwall above hanging wall sediments, a similar total throw of 1.3 – 1.9 km is estimated here.

- **Kerpini and Kalavrita faults:** The Kerpini and Kalavrita faults have throws of 0.5 – 0.8, and 1.3 – 1.9 km respectively, derived from the topography of their footwalls and the application of uplift to subsidence ratio assumptions. The estimate of throw for the Kerpini fault, however is smaller than predicted by Collier & Jones (2003) and Ford et al. (2007) based on basement projection. These authors, however consider throw at the centre of the fault, whereas Transect 1 crosses the eastern tip.

- **Onshore Xylokastro fault:** Rohais et al. (2007) study the onshore section of the Xylokastro fault in the area of Transect 2 (Fig. 7.2 B), and estimate that it has a maximum throw of 1.5 km, based on projection of basement on geological cross sections. This is within the range of a total throw of 1.1 – 1.6 km, estimated when an uplift to subsidence ratio of 1:1.2 – 2.2 is applied to the total uplift component from topography.

- **Stimfalia fault:** Roberts (1996) interpret that the southern boundary of the Pliocene–Quaternary sediments is fault controlled by the Stimfalia fault (red dotted faults on Fig. 7.1). The 600 m footwall topography created by this fault would equate to a total throw of 1.3 – 1.9 km, based on the uplift to subsidence ratio (1 : 1.2 – 2.2).

- **Killini Fault:** The Killini fault has a topographic footwall uplift of 700 m, equating to a total throw of 1.5 – 2.2 km, assuming a typical uplift to subsidence

ratio. This result is similar to the maximum throw on the Killini fault of 1.8 km from geological cross sections and basement projection by Rohais et al. (2007).

- **Corinth Isthmus faults:** Few faults have been interpreted in the region of the Corinth Isthmus and the area to the south east of Xylokastro (some have been interpreted by Collier & Dart 1991). Geology in this area is mainly composed of Pliocene–Quaternary sediments, however there are a few areas of outcropping basement and higher topography, which may be fault controlled. From the topography and geology along the south part of Transect 3, a fault with suspected total throw of around 0.9 – 1.3 km exists, estimated from the level of uplifted topography and uplift to subsidence ratio assumptions (Fig. 7.2 C).

- **Athikia fault:** Roberts (1996) interpret that the south-east boundary of the Pliocene–Quaternary Corinth Isthmus sediment basin is fault controlled by the Athikia fault. This fault along Transect 3 has a footwall topography of ∼400 m, which equates to a total throw of 0.9 – 1.3 km if an uplift to subsidence ratio of 1 : 1.2 –2.2 is applied (Fig. 7.2 C). Without a knowledge of the depth of sediments in the Corinth Isthmus this estimate cannot be refined further.

- **Kenchreai fault:** The Kenchreai fault and two parallel faults further south extend from the western Saronic Gulf across the Corinth Isthmus, and border the Pliocene–Quaternary sediment basin. These faults produce three steps in the topography, and have also been considered by Goldsworthy & Jackson (2001). Although the depth of sediments adjacent to these faults is unknown, total throw on each fault may be estimated from topography. Each of these faults has an uplift component of ∼ 200 m, determined from Transect 4 and Goldsworthy & Jackson (2001). This equates to a throw of 0.45 – 0.65 km on each fault. Here it is assumed that the offshore part of the Kenchreai fault has a similar throw to its onshore section.

- **Loutraki fault:** The Loutraki fault as viewed along Transect 4, has produced uplifted footwall topography of ∼500 m equating to an estimated total throw of 1.1 – 1.6 km based on the application of the 1 : 1.2 – 2.2 uplift to subsidence ratio.

Errors exist in the determination of south margin inactive fault throws because they are largely based on uplifted footwall topography (likely to have undergone erosion and unknown pre–existing topography), and geological cross-sections drawn from minimal surface basement information. In order to conduct this study the southern margin of the Corinth rift has to be defined. However, these estimates provide the current best approximation for extension across onshore inactive faults. In order to conduct this study of total extension is is necessary to define the limits of the Corinth rift (i.e. the southern most and northern most faults in Fig. 7.1). We recognise that many other faults exist to the south of the defined boundary in Figure 7.1 (i.e. the most southern red faults) and within the Saronic

Transect	Throw (km)	Heave (km) 50^o	Total rift width (km)	β factor
1	9.7	8.1	38	1.27
2	9.7	8.1	56	1.17
3	7.0	5.9	52	1.13
4	6.4	5.4	40	1.16

TABLE 7.3: Summary of total extension and β factors across the entire Corinth rift, including all fault throws presented in Table 7.1.

Gulf, and if these not included faults have contributed toward Corinth system extension they add another degree of error into the estimate.

Figure 7.3 summarises the short–term geodetic extension rate (A), total extension (B) and β stretching factor (C) along the Corinth rift axis. The extension that the currently active rift border faults have accumulated over their history ranges from 3.5 km in the west, to 4 km in the central area and 3 km across the Alkyonides and Saronic Gulfs (Fig. 7.3 B). The similarity in extension estimates from the west and central rift is surprising given the large difference in basement depth between these areas (Fig. 7.1).

Total extension across the rift zone, considering most known faults along the transects, appears to be higher in the western part of the rift zone (Transects 1 and 2, ∼8 km) than to the east (Transects 3 and 4, ∼5 – 6 km; Fig. 7.3 B). The long term extension, therefore follows the same general pattern as the short term geodetic extension rates over the last 10 – 100 years (Fig. 7.3 A; Davies et al. 1997, Clarke et al. 1998, Briole et al. 2000, Avallone et al. 2004). This may suggest that the short term extension rates are reflecting the long term trend, or the eastward decrease in total extension observed here could be an artifact due to the exclusion of faults in the Corinth Isthmus area and Saronic Gulf, which are currently unknown.

The β stretching factors over the currently active Corinth rift are relatively constant (1.2 – 1.25) along strike, due to the similar total extension and fairly consistent active rift width (Fig. 7.3 C and Table 7.2). Total rift (inactive and active faults) stretching factors, considering the full width of the rift zone are higher in the western rift (∼1.27) than in the central and eastern areas (∼1.13 – 1.17, Fig. 7.3 C and Table 7.3). This reflects the fact that although total extension is similar in the west and central areas, in the west this extension has been distributed over a narrower region (Figs. 7.1 and 7.2).

7.4 Method 2: Crustal thinning stretching factor

The β stretching factor has also been calculated from the ratio of original pre–rift crustal thickness and the thickness of the thinnest crust along each profile, providing a measure of the degree of maximum total crustal extension. The Moho depth beneath the Corinth rift

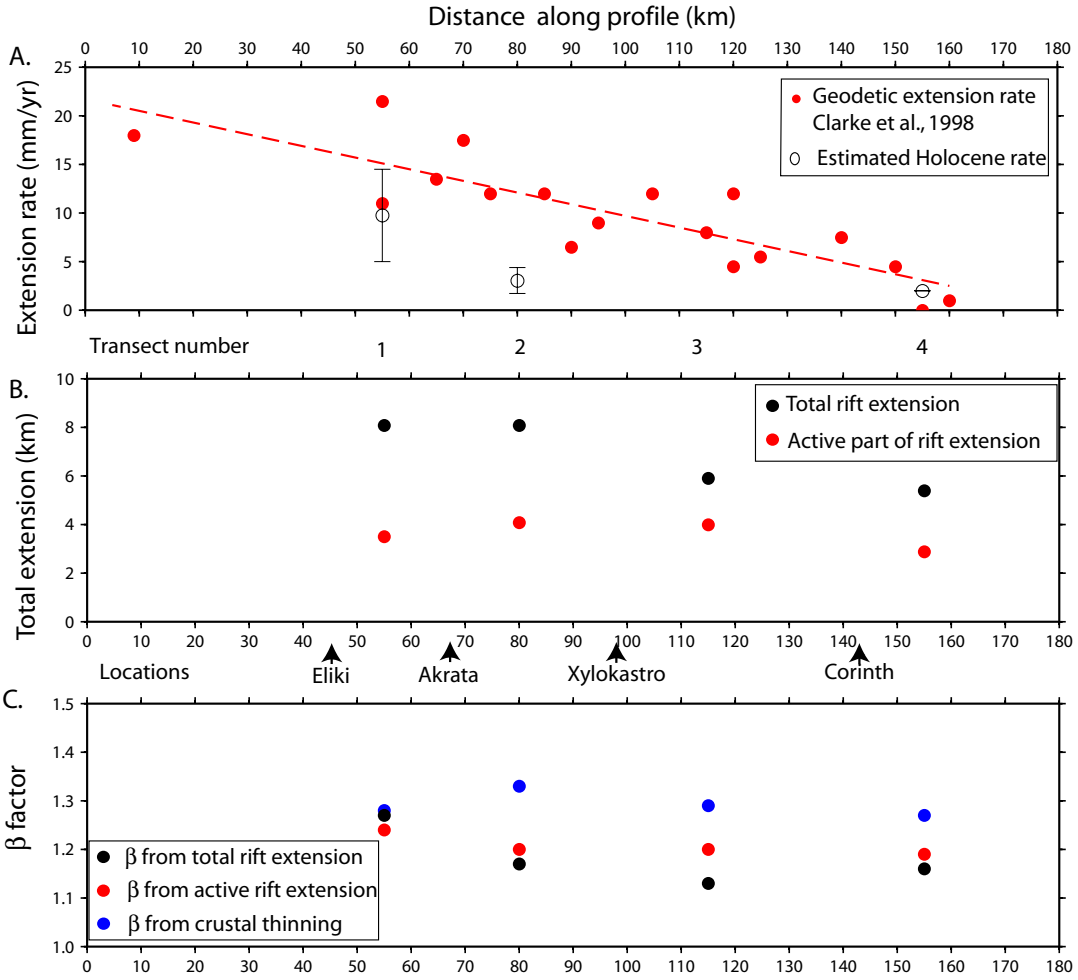

FIGURE 7.3: **A.** Geodetic extension rates from Clarke et al. (1998) along the red dashed profile shown in Figure 7.1. Holocene extension rates from Bell et al. (2008) and derived from uplift rates presented by Stewart & Vita-Finzi (1996) and Armijo et al. (1996). **B.** Comparison of total extension across the currently active part of the Corinth rift (black faults in Fig. 7.1), and total extension of the entire rift including all faults, both active and inactive (red and black faults in Fig. 7.1). **C.** Comparison of β factors derived from method 1 (fault displacement) and method 2 (degree of crustal thinning)

has been estimated by Zelt et al. (2005) and Sachpazi et al. (2007) based on PmP wide-angle Moho reflections (Fig. 7.4). Moho depths > 50 km are seen in the core of the Hellenide mountain belt in the west, and Moho shallows to < 30 km to the east in the Aegean sea. The Gulf of Corinth and Alkyonides Gulf are areas of locally shallow Moho, compared to the deeper Moho observed due north and south. The Moho depth beneath the Gulf of Corinth shallows from 42 km in the west (long. 22°), to < 30 km in the Alkyonides Gulf. Although the active rift does have a shallow moho, the SW onshore area (in the region of Kalavrita to the East Eliki fault, Fig. 7.1) does not (Fig. 7.4). This is unexpected, because this region has experienced significant extension. The seismically active Corinth rift is not the area of thinnest crust in central Greece. Three lobes of Moho depth < 32.5 km are shown on Figure 7.4 (shaded orange and red): one which strikes E–W to the south of the SE Corinth rift underlying Perachora, the Corinth isthmus and the Saronic Gulf; another

	Transect 1	Transect 2	Transect 3	Transect 4
Max. basement depth (km)	0.97	1.93	1.98	0.77
Total extension across the rift (km)	8.1	8.1	5.9	5.4
β factor for total rift from fault disp.	1.27	1.17	1.13	1.16
Initial crustal thickness (km)	42 – 44	39 – 41	38 – 40	35 – 37
Crustal thinning β factor	1.25 – 1.31	1.29 – 1.36	1.25 – 1.32	1.23 – 1.30
Geodetic ext. rate (mm/yr)*	∼13	∼11	∼7	∼3

*Geodetic extension rates from Clarke et al. (1998) Figure 16

TABLE 7.4: Comparison of basement depth, total extension, geodetic extension rates, and β stretching factors across the transects shown in Fig. 7.2

trends NW above the NE rift margin; and one parallels the Gulf of Evvia.

The stretched crustal thickness of the offshore Corinth rift can be calculated from Moho depth (Fig. 7.4, Zelt et al. 2005, Sachpazi et al. 2007) and the basement depth (Fig. 7.1). Crustal thickness beneath the onshore south margin is poorly constrained, due to a lack of knowledge of basement depth. Initial crustal thickness has been estimated by considering the Moho and surface topography far from the Corinth rift, in an area uninfluenced by its extension (Fig. 7.4). The Moho topography at a latitude of 39°, with an additional maximum of 2 km added for surface topography, is taken to be representative of the original crustal thickness before extension. Original crustal thicknesses of 42 – 44, 39 – 41, 38 – 40 and 35 – 37 km are estimated for Transects 1, 2, 3 and 4 respectively.

Crustal extension β factors, derived using method 2, are similar along the rift, ranging from 1.23 to 1.36. Maximum β factor is seen along Transect 2 in the central rift, and is slightly lower to the east and west (Fig. 7.3 C and Table 7.4).

7.5 Discussion: Implications for the extensional history of the Corinth rift

7.5.1 Distribution of extension

The modern active part of the Corinth rift, as defined by major faults on the north and south margins, has a relatively constant width along strike between 18 – 24 km. Although the Gulf of Corinth appears wider in the areas of the Antikyra and Itea bays, these regions are not associated with the main sediment depocentre which is highlighted in yellow in Figure 7.5. Total extension during the last 1 – 2 Ma is greater in the central rift (4 km) than to the west (3.5 km) and east (3 km). This mirrors the variation in depocentre depth along the rift, with maximum extension and basement depth occurring in the central region (Fig. 7.1, Transects 2 and 3). This suggests that normal faulting is the dominant control over basement depth, rather than flexural factors caused by the distribution of extension

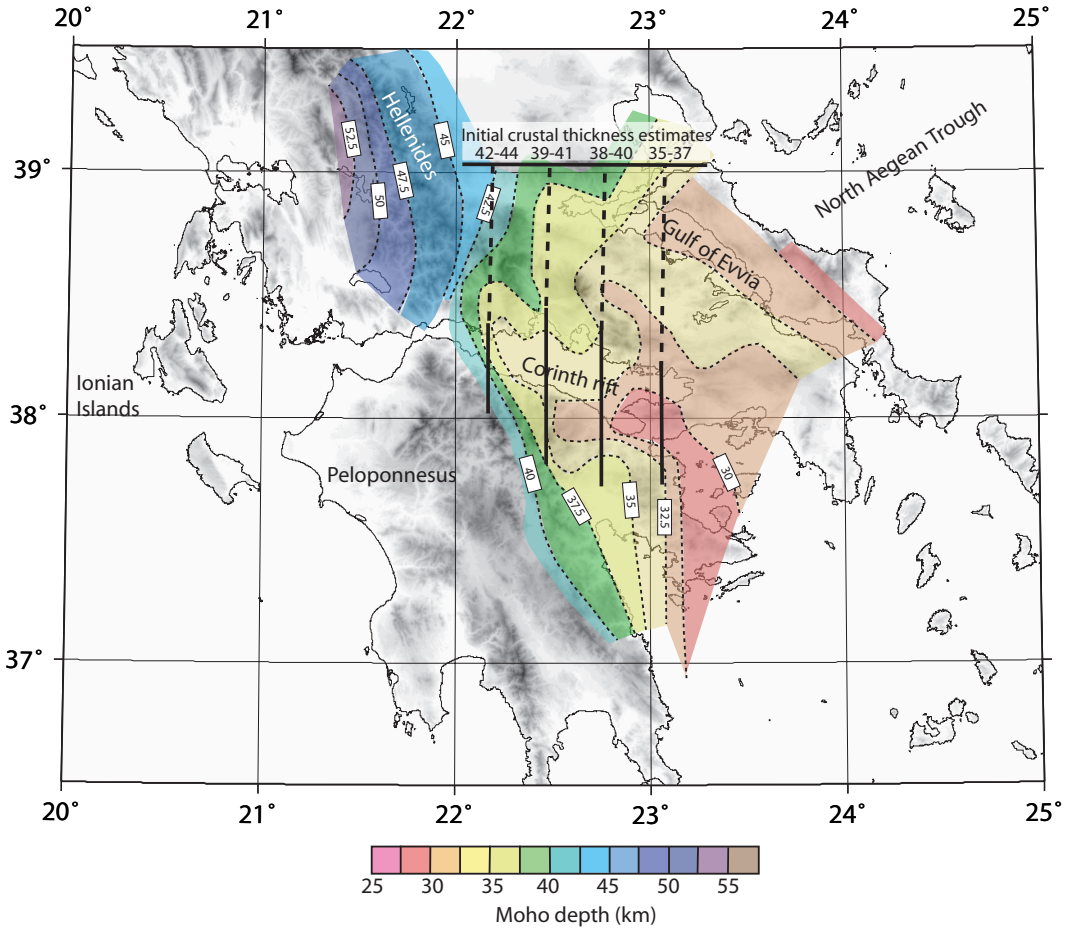

FIGURE 7.4: Depth to Moho beneath Greece from Sachpazi et al. (2007) and Zelt et al. (2005)

and sediment loading. However, although there are major variations in basement depth the extension estimates along the rift axis do not vary by the same degree. This can be explained by considering the number of faults active in each region. In the western rift multiple faults are active (i.e. Eliki, West Channel, South Eratini and North Eratini; Transect 1.), whereas in the central region significant extension occurs on one single large fault (e.g. Xylokastro; Transect 3) or at most two faults (e.g Derveni and East Channel fault; Transect 2). Therefore over the last 1 – 2 Ma, extension has been more distributed in the west forming shallower depocentres, whereas in the central rift extension is concentrated to form a single deep depocentre.

The total rift width (over rift history) can be estimated by the distance between active offshore north margin faults, and the most southern fault that bounds the Pliocene–Quaternary rift–related sediments (Fig. 7.5). The connection between the E–W basin bounded by the Kenchreai fault, and the NE trending Megara basin is uncertain in the Saronic Gulf area (Fig. 7.5). The total rift width is relatively similar along strike, although is narrower in the west (38 km) and east (40 km) than in the centre (56 km). Total extension

is significantly greater in the western and central areas (Transects 1 and 2, 8 km) than to the east (Transects 3 and 4, 5 – 6 km). The greater extension to the west of the Likoporia area is due to the larger number of faults that have been influential over rift history (Fig. 7.5). Numerous south-margin faults including the, Kalavrita, Kerpini and Doumena faults are spaced at ∼5 – 10 km intervals and experience 1 – 2 km of throw. Such multiple large faults have not, as yet, been interpreted in the Corinth Isthmus area between Xylokastro and Corinth. The lack of significant interpreted fault activity here is responsible for the lower estimated extension value. The low extension estimates to the east of Likoporia may be real, if there are no faults in this area, or could be the result of comparatively less study of faulting and the omission of unknown faults. A higher percentage of missing extension due to unaccounted for faulting may be present in the east as offshore datasets are of lower resolution here and less onshore fieldwork has been done.

If the fault interpretation presented in Figure 7.1 includes all major faults, and the extension values presented above are true, this means major differences in extension exist to the west and east of a line through Likoporia. Not only are there apparent variations in extension to the east and west of this line, but differences in other major rift characteristics exist too. For example:

- Variations in the number of across rift and now inactive onshore major faults
- Variations in the number of across rift active offshore and coastal major faults
- Significant changes in across rift fault spacing
- Topographic, geomorphological and geological variations
- Changes in the degree of rift complexity

To the west of Likoporia, extension has accumulated on many onshore and offshore faults forming numerous depocentres separated by footwall basement blocks, creating rugged topography (Fig. 7.5). In the east, however, extension is accommodated on fewer fault systems spaced 15 – 35 km apart. Topography to the east of the Likoporia region is much more subdued, and surface geology is composed of Pliocene–Quaternary sediments over a wide area, disrupted by occasional footwall basement blocks (compare Transects 1 and 2 with Transects 3 and 4, Fig. 7.2). This may suggest that the lack of interpreted faulting in this area is real. The boundary between different styles of onshore faulting in the Likoporia area, is also at the same longitude as the divide between largely distributed extension in the complex offshore western rift (Chapter 5, McNeill et al. 2005a, Bell et al. 2008), and the more simple geometry of the central-eastern rift and Alkyonides basin, where activity is focused on single large faults forming half graben (Chapter 6). In fact, the boundary correlates well with the eastern tips of the East Channel and Derveni faults, which define the eastern limit of the largest unit B pre 0.4 Ma depocentre (Chapter 6, Fig. 6.10 A), suggesting this boundary could be a real, major structural control on rift development.

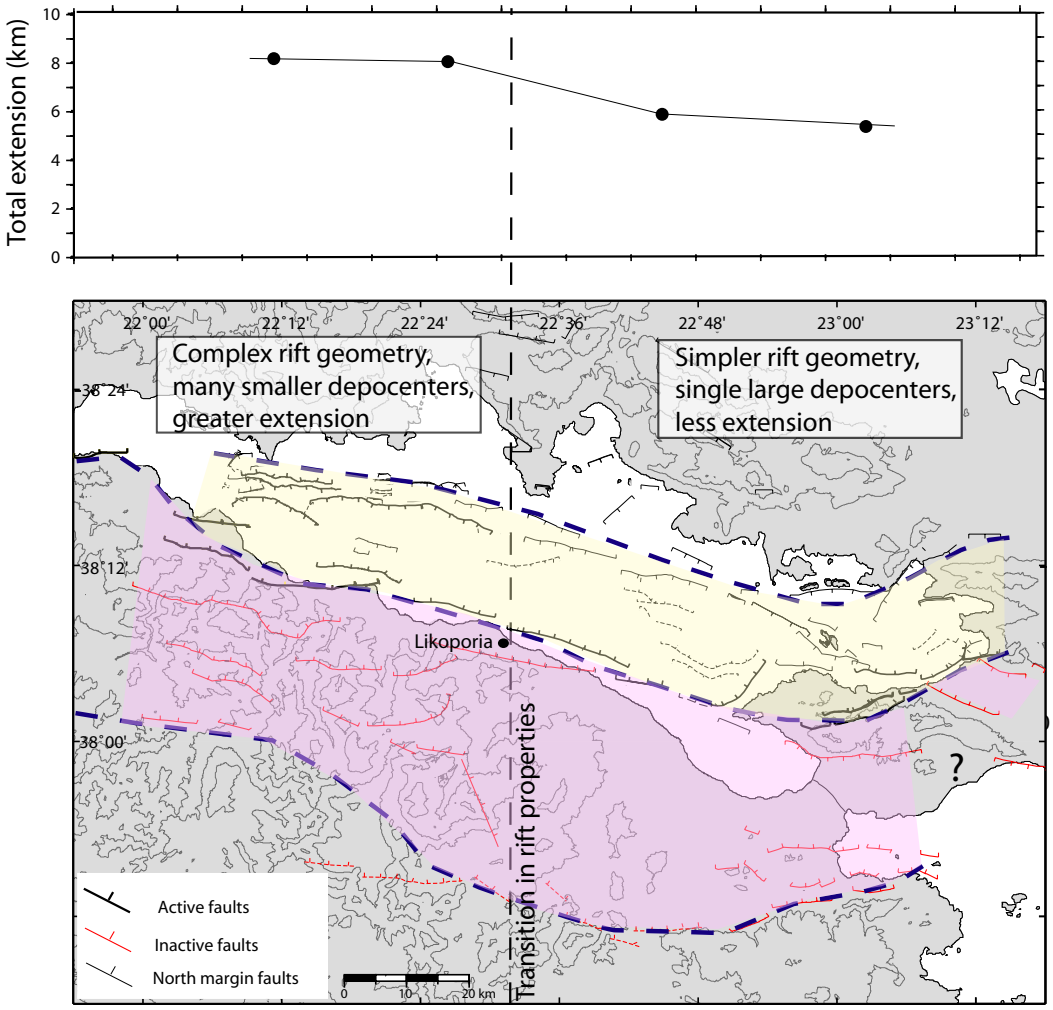

FIGURE 7.5: Schematically outlined boundaries of the modern active Corinth rift (yellow) and the estimated area of the total Corinth rift (yellow and purple areas). The interpretation of the boundaries of the old south margin are unclear in the Saronic Gulf area. Differences in the level of total extension exist to the east and west of the dotted line through Likoporia. Number and character of faults and rift geometry also varies across this boundary.

Total across rift extension has been accumulated by the activity of ∼10 large faults to the west of Likoporia, compared to only 2 – 7 faults in the east. The reason for such a variation in along strike fault character may be due to crustal rheology and pre–existing structural heterogeneity. Papanikolaou & Royden (2007) have also noted the change in south margin topography and onshore sediment depocentre character in the Likoporia area. They suggest from field mapping that the variations can be explained by a NW detachment fault feature, active prior to the development of the E–W faults discussed here. They suggest this older detachment fault formed a NW orientated depocentre, down-throwing the Xylokastro area and allowing sediment deposition, meanwhile uplifting topography to the west. No offshore signature of this detachment has been observed in the seismic data used in this thesis. Papanikolaou & Royden (2007) argue that the older detachment fault is required to explain the ∼3 km of subsidence in the offshore central rift. However, in Chapter 6, slip rates on

major south coast faults were estimated at 3 – 6 mm/yr. If these rates were active over a rift history of 1 – 2 Ma, they are capable of producing basement depths of ∼3 km, therefore this negates the need for any extra subsidence in an older NW basin. Although the interpretations of this work would disagree with the importance of a NW detachment in the formation of the offshore basin, an inherited structural feature is not ruled out as a possible control for the variation in extensional character.

7.5.2 Upper crustal vs. total crustal extension

The β factor derived from faulting (method 1) and crustal thinning (method 2) are within error in the western area (Table 7.4). These results mean that in the western part of the rift, both the upper crust and average total crust are extending by the same degree, as predicted by simple uniform stretching models (McKenzie 1978a). Crustal thinning derived β values in the central and eastern rift (1.23 – 1.36), however, are higher than those derived from faulting (1.13 – 1.17, Fig. 7.3).

In the intra-continental North Sea rift, White (1990) have demonstrated that stretching estimates from the upper crust and whole crust are equivocal, and there is uniform stretching with depth. However, depth dependent stretching is commonly observed at rifted margins, including the: Voring Basin (Roberts et al. 1997); Labrador Sea (Royden & Keen 1980); Galicia Bank (Iberian margin); and South China Sea (Davis & Kusznir 2004). In all of these areas stretching estimates from upper crustal faulting are less than that predicted by stretching of the whole crust (Davis & Kusznir 2004). Possible explanations for the discrepancy include: exclusion of sub–seismic faulting; low angle fault geometry; and aseismic extension (e.g., dyke intrusion, Davis & Kusznir 2004). In the central and eastern areas of the Corinth rift the discrepancy between β factors calculated using methods 1 and 2 may be due to the fact that extension from faults smaller than seismic resolution and unknown onshore faults have not been included in the fault derived extension summation.

7.5.3 Detachment faulting in the western rift?

If listric faults rather than planar faults dominated in the Corinth rift the β values determined above would be underestimates, because listric faulting creates extra extension due to internal deformation of the fault block. In this study it has been shown that upper crustal (fault derived) and total crustal (crustal thinning derived) β factors are compatible in the western Gulf, in the area of the previously proposed detachment (e.g. Rigo et al. 1996, Sorel 2000, Taylor et al. 2003, Gautier et al. 2006). Therefore, no deficit in upper crustal extension is observed when using the planar fault assumption, and there is no clear support for low angle or detachment faults in the west.

7.6 Conclusions

1. Total extension across the active part of the Corinth rift is larger in the centre (4 km) than to the west (3.5 km) and east (3 km). The degree of extension accumulated in the last 1 – 2 Ma mirrors the variation in depocentre depth along the rift, with maximum extension and basement depth occurring in the central region.

2. Total extension throughout the entire rift history is significantly greater in the western and central areas (Transects 1 and 2, 8 km) than to the east (Transects 3 and 4, 5 – 6 km). The greater extension to the west of Likoporia is due to the large number of now inactive faults on the southern margin, and few interpreted faults to the east.

3. Total rift extension has been accumulated by the activity of ∼10 large across rift faults in the western region, compared to 2 – 7 across rift faults in the east, assuming all major faults have been accounted for.

4. Long term extension is greatest in the west and apparently follows the same west to east decreasing trend as the short term geodetic extension rates. Greater extension has been observed in the western rift due to the larger number of major interpreted faults. The difference in the number and spacing of faults to the east and west of Likoporia, both onshore and offshore may be caused by variations in crustal rheology or pre–existing inherited weaknesses. Alternatively, greater estimated extension in the west may be due to the exclusion of unknown faults in the east.

5. Fault derived β factors across the entire Corinth rift, and β factors derived from crustal thinning are similar in the western rift. This suggests stretching is occurring uniformly with depth, as predicted by simple stretching models (McKenzie 1978a). In the eastern and central parts of the rift, however, fault derived β is lower (1.13 –1.17) than that expected from crustal thinning (1.23 – 1.36). This may be due to the omission of unknown faults in the eastern rift due to lower seismic resolution offshore and less detailed field studies onshore.

6. The comparison of fault derived and crustal thinning β values do not call for the presence of low angle faults in the western rift as the β values are within error.

Chapter 8

Long term deformation modelling

8.1 Introduction

In Chapter 6, observations of vertical movement at the coastline and offshore were used to estimate slip rates on faults (Section 6.8, Figs. 6.11 and 6.12). These methods relied on assumptions of the ratio of footwall uplift to hanging wall subsidence and that all deformation was due to the one fault under consideration and not influenced by other faults or a component of regional deformation. Dislocation modelling methods provide a more thorough way to use measured vertical deformation to determine the magnitude of fault slip. This technique considers faults as line dislocations in the Earth's crust that slip and cause stresses and strains in the surrounding rock, which are translated into surface displacements using linear elasticity laws (e.g. Steketee 1958, Okada 1985).

Elastic dislocation modelling has proved to be a powerful tool to model the deformation field associated with earthquakes generated by thrust, strike–slip and normal faulting. Recent advances in the production of 3D surface deformation fields during earthquakes through the use of Interferometric Synthetic Aperture radar (InSAR) make it possible to use dislocation modelling to solve for unknown geometrical parameters of faulting, such as sub–surface slip (e.g. Wicks et al. 2001, Funning et al. 2007). Elastic dislocation modelling can also be used to model sparse data from GPS derived displacement information and field observations (e.g. Smith & Sandwell 2003, Simpson et al. 2006). Long term deformation is the result of many repeating earthquake cycles accumulating vertical displacement. Elastic dislocation modelling cannot be used to model this deformation because viscoelastic relaxation effects accompany deformation at longer timescales. An emerging use of dislocation theory is the inclusion of viscous layers in the model to allow for postseismic relaxation processes.

In this chapter, the magnitude of uplift and subsidence that has taken place in the last ca. 130 ka within the Alkyonides Gulf is modelled using viscoelastic dislocation theory. The aim is to establish how much total slip on individual faults is required to reproduce the observed coastal and offshore deformation, and determine whether slip on a single fault can

realistically produce the observed displacement field. If not, multi–fault scenarios will be tested to derive the magnitude of slip on each fault that can collectively best describe the displacement. The work presented in this chapter should be considered as a preliminary step toward applying such long term deformation models to other parts of the Corinth rift where detailed uplift and subsidence information exists (e.g., the south coast terraces) and in areas where activity on multiple faults is thought to be important (i.e. the western rift). The Alkyonides Gulf has been chosen for this pilot study as rare complimentary uplift and subsidence indicators distributed across the rift for the same time period exist and the region has a relatively simple fault morphology.

8.1.1 Elastic dislocation models

Theory

The surface coseismic deformation associated with earthquakes is now routinely analysed by comparing surface movements derived geodetically or though the use of InSAR with fault dislocation models based on an elastic half–space assumption (Funning et al. 2007). Modelling of this type uses the approximation that a fault can be represented as a dislocation or a plane across which there is a discontinuity in the displacement in an elastic medium. For a normal fault, slip on the dislocation is perpendicular to the dislocation plane and it acts as an edge dislocation. The solution for the displacements and stresses for such an edge dislocation in an elastic half space have been derived analytically by Okada (1985) based on linear elasticity.

A MATLAB program using the Okada (1985) formulation for a uniform half space has been used to explore the effects of variation in fault geometry on the corresponding displacement field (model obtained from P. England, pers comm. 2005). Variables in the elastic dislocation model are: the shear modulus and Poissons ratio of the elastic medium (taken to be 30 GPa and 0.25 respectively, after Deng et al. 1998); the horizontal extent of the fault trace; depth of the upper fault tip below the ground surface; vertical depth extent of the fault; the fault dip; and slip magnitude. The effects of some of these parameters are explored in Figure 8.1. A more thorough investigation of the parameters influencing elastic dislocation modelling is provided by Cattin et al. (1999). The dislocation model used in this study does not include the effects of regional stresses, but only considers internal deformation due to a user–specified dislocation slip.

Dislocation theory explains the asymmetry in uplift and subsidence observed at normal faults due to coseismic footwall unloading which approaches a ratio of 1:8 (uplift:subsidence) for $\sim 50^{\circ}$ dipping faults. Steeper faults show a more equal uplift to subsidence ratio (Fig. 8.1 A). Lower angle normal faults would demonstrate limited uplift at the fault and wide subsidence with far–field flank uplift (although low–angle normal faults are mechanically unfavorable in nature). If the same fault plane is buried, the amplitude of surface uplift and subsidence will be smoothed and reduced in magnitude compared to the surface breaking

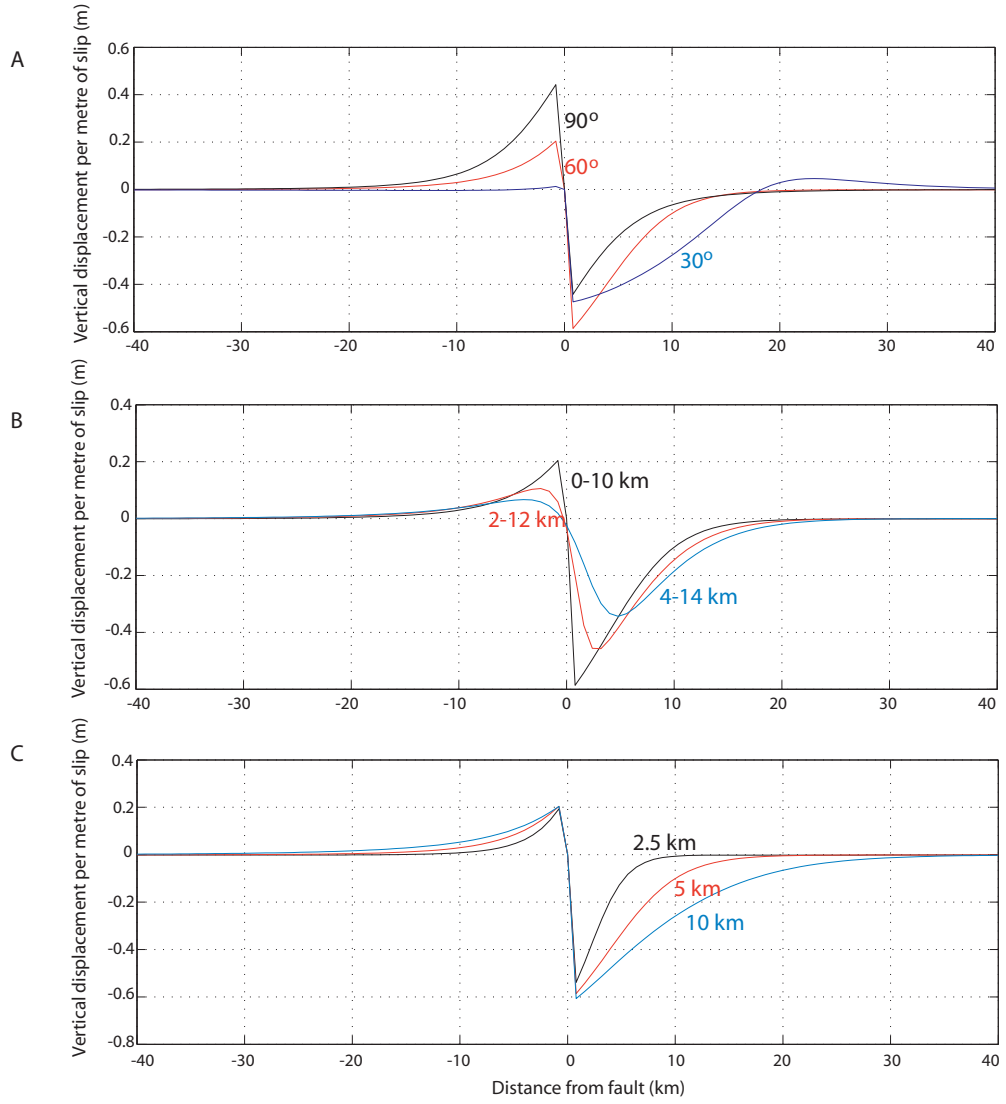

FIGURE 8.1: Effect of changing geometrical fault parameters on the coseismic displacement field created, per metre of slip on a 12 km long normal fault **A.** Variation in deformation field for fault dips of 90, 60 and 30°, for a surface breaking fault with depth of 0 – 10 km. **B.** Variation of depth of fault trace below the surface, from 0 – 10, 2 – 12 and 4 – 14 km for a 60° dipping fault, **C.** Variation in fault width (horizontal distance between upper and lower limits of fault plane) from 2.5, 5, to 10 km for a surface breaking 60^o dipping fault. Created using the formulations of Okada (1985).

case (Fig. 8.1 B). Blind faults therefore create broader but lower amplitude displacement fields. If the width of the fault plane (i.e. the horizontal distance between the upper and lower fault tips) widens, the breadth of the corresponding deformation field also widens, but retains the same maximum values of uplift and subsidence (Fig. 8.1 C). Dislocation studies generally involve either: a priori knowledge of fault geometry and the magnitude of slip is varied to achieve the deformation field; or if the deformation field is very well constrained (i.e. from InSAR), all of the fault parameters may be estimated (Funning et al. 2007, Wright et al. 2006).

Application to the Corinth rift

The deformation field associated with the three 1981 earthquakes in the Alkyonides Gulf has been modelled using elastic dislocation theory by Hubert et al. (1996) and Stiros et al. (2007). Using coastal geomorphology and estimates of seismic uplift and subsidence from the south coast, Hubert et al. (1996) determine that the vertical displacement pattern can best be achieved if slip occurred on two faults, the Alepochori (named the East Alkyonides fault throughout this thesis) and the Pisia fault (Fig. 6.1). The fault geometry that best fits surface deformation is when both faults rupture from the surface to a depth of 12 km and fault dip is 50°. Surface deformation is modelled most effectively when the Pisia fault is 14 km long and undergoes 1.3 - 2 m of slip during the 25th March 1981 event, and the East Alkyonides fault is 13 km long with 0.7 m slip (Hubert et al. 1996).

Stiros et al. (2007) use vertical displacements from triangulation stations and topography change estimated from leveling across the Kaparelli fault, to model the vertical displacement associated with a dislocation on the north margin during the 4th March 1981 event. They conclude that faulting on the 50^o S–dipping Kaparelli fault, with a depth of 12 km (derived from aftershock depths, Hatzfeld et al. 1996), length of 17 km (3 km longer than the surface trace) and 0.45 m slip can best produce the observed displacement. These elastic dislocation studies provide reasonable geometrical constraints for faults in the Alkyonides Gulf which are used in the following viscoelastic long term deformation analysis.

8.1.2 The Earthquake Cycle

Reid (1910) proposed that the deformation and strain associated with coseismic activity, and the intervening interseismic deformation (between earthquakes) was of equal magnitude and opposite sign. This represents 100% elastic deformation and would result in no permanent deformation apart from offset immediately at the fault. However, in reality permanent deformation features do accumulate (e.g. in the form of elevated coastal terraces). A widely accepted model for the behaviour of the Earth's crust and upper mantle consists of an elastic brittle lithosphere overlying a viscous ductile asthenosphere. During an earthquake the upper layer experiences an immediate elastic rebound and the layer maintains its strength (Nur & Mavko 1974, Rundle 1982). The underlying viscous layer, however, relaxes stresses at a rate determined by its viscosity, and as such, surface deformation after an earthquake evolves with time. This explains the observation that immediately after an earthquake on a 45° dipping fault, uplift to subsidence ratios are ∼1:9 (King et al. 1988), whereas some time later they have reduced to ∼1:3 (Armijo et al. 1996). The interseismic deformation is not only composed of this postseismic viscous relaxation, but is also modified by sediment loading and erosion (King et al. 1988).

Sudden slip during an earthquake transfers a shear load to the deeper lithosphere. Response to the redistribution of stresses brought about by an earthquake causes stress relaxation somewhere in the upper part of the lithosphere. There have been a number of suggestions

as to how this stress is relaxed. Some authors argue for after-slip on a lower crustal continuation of the upper crust fault, others opt for flow in the lower crust (Deng et al. 1998, Ryder et al. 2007). Viscoelastic models have been developed to predict this deformation and investigate the time scales involved, in order to either match long term deformation fields (e.g., Sato & Matsu'ura 1992) or use the observations to study the postseismic processes (e.g., Ryder et al. 2007).

8.2 Methodology

8.2.1 Viscoelastic dislocation models

Theory

The Earth's crust can be effectively modelled as an elastic layer overlying a viscous ductile half–space (Fig. 8.2, e.g., Nur & Mavko 1974, Rundle 1982). The elastic lid layer in this model responds elastically to this displacement and obeys Hookes law;

$$\sigma = \mu\epsilon \tag{8.1}$$

Where σ is the applied shear stress, μ is the shear modulus and ϵ is the strain.

Stresses imparted into the lower crust, due to slip during an earthquakes are relaxed by time–dependent viscous deformation in the underlying layer (note strain rate term instead of strain) which is controlled by the viscosity of the fluid;

$$\sigma = \eta\frac{d\epsilon}{dt} \tag{8.2}$$

where η is the viscosity.

The total strain rate from elastic and viscoelastic components combined is thus:

$$\frac{d\epsilon}{dt} = \frac{\sigma}{\eta} + \frac{1}{\mu}\frac{d\sigma}{dt} \tag{8.3}$$

The viscoelastic model responds like a Maxwell solid, which can be considered as a spring and a dash pot (damping component) joined in series. On application of a stress, instantaneous movement occurs on the spring and later, movement occurs on the dashpot. The characteristic time for which viscosity forces have an effect is known as the Maxwell time (τ) and is a function of the shear modulus and viscosity;

$$\tau = \frac{\eta}{\mu} \tag{8.4}$$

Mathematical expressions for this deformation have been provided by Fukahata & Matsu'ura (2005). These equations have been used to develop the fortran code V3FASAT (Fukahata

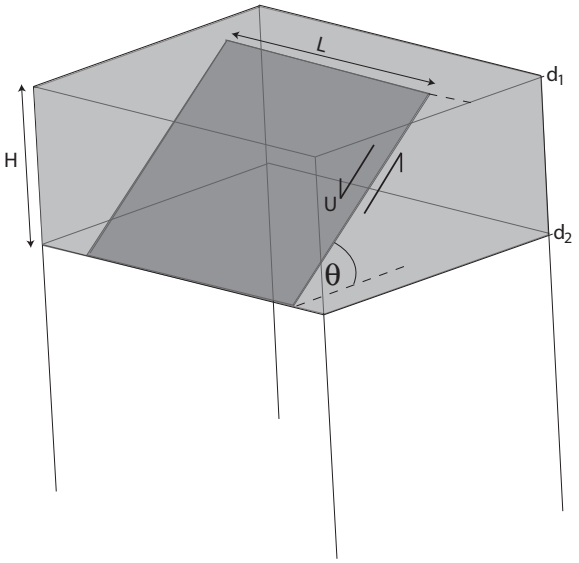

FIGURE 8.2: Schematic diagram of the viscoelastic half–space model. Parameter are explained in text and in Table 8.1

.

& Matsu'ura 2005) for a viscoelastic layered model (model code obtained from Y. Fukahata, pers. comm. 2005), which has previously been used successfully in modelling postseismic deformation (e.g. Ryder et al. 2007). The reader is referred to the publications of Fukahata et al. (2004), Fukahata & Matsu'ura (2005, 2006) for details of the mathematics. The V3FASAT model integrates the solution for point dislocations over a fault surface, and considers only the internal deformation due to a user–defined crustal dislocation. It does not include the effects of horizontal forces or regional uplift or subsidence that may influence the deformation field. In this way the V3FASAT model is fundamentally different to finite element models that investigate fault activity in response to an evolving stress field (e.g. Behn et al. 2002).

Figure 8.3 shows the total surface deformation expected after a time period of 10 to 100000 years after an earthquake (per metre of slip) and has been created using the V3FASAT model (Fukahata & Matsu'ura 2005). The deformation caused by lower crustal postseismic relaxation gradually increases with time, until it reaches a constant level (Fig. 8.3 B). The form of the postseismic deformation component (Fig. 8.3 B) resembles the displacement pattern for faults which are significantly buried (compare with Fig. 8.1 B), showing broader and lower amplitude deformation compared to that produced in the coseismic event with increased footwall uplift. This is expected as postseismic deformation is occurring deeper in the lower crust. When coseismic and postseismic deformation are added together the cumulative effect is a reduction in the uplift to subsidence ratio and a broadening of the deformation field (Fig. 8.3 C). These characteristics have been observed geologically (e.g. Ryder et al. 2007).

If $t < \tau$ elasticity dominates, whereas for $t > \tau$ viscous creep prevails (Fig. 8.3 B). For the Earth, μ is generally around 30 GPa and for the Corinth region η has been suggested to be

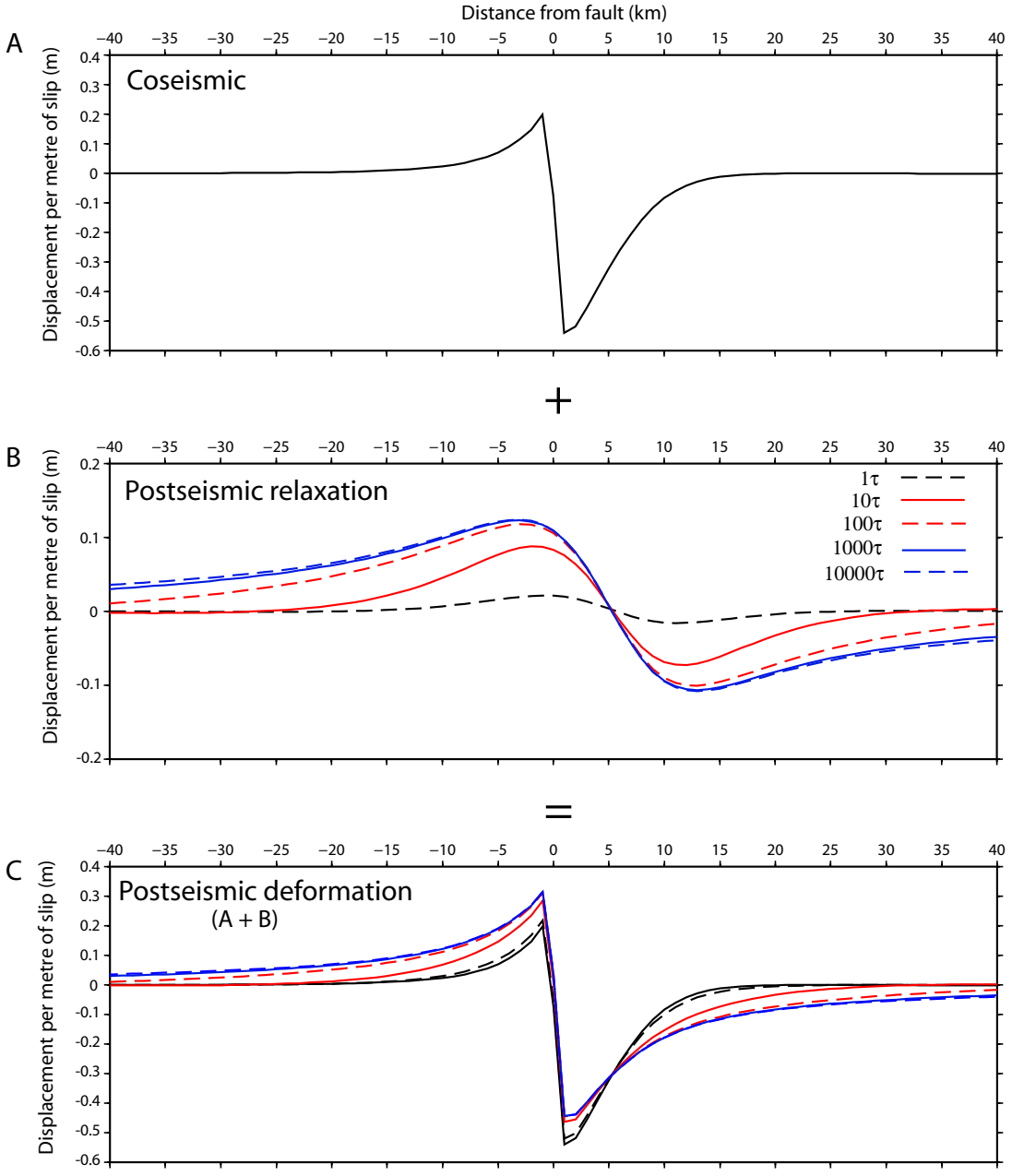

FIGURE 8.3: Temporal variation in postseismic relaxation following an earthquake. Comparison of postseismic relaxation (**B**) and total postseismic deformation (**C**, coseismic plus postseismic relaxation) for a 13 km long, 50° dipping, 10 km deep fault, with viscosity of 10^{19} Pas and shear modulus of 30 GPa. Maxwell time (τ) is 10 years. Created using the fortran code V3FASAT (Fukahata & Matsu'ura 2005).

in the range 10^{19} Pas (Westaway 2002, 2007). This estimate of asthenospheric viscosity is similar to that proposed in viscoelastic deformation studies elsewhere (e.g., ranges of 5 x 10^{18} to 1 x 10^{19} suggested by Nur & Mavko 1974, Pollitz et al. 2001, Ryder et al. 2007). This gives a Maxwell time of ∼10 years, below which very little viscoelastic response is induced and total deformation is not much different from the elastic coseismic case (Fig. 8.3 C). However, for times greater than 100 years, viscoelastic deformation is significant, leading to significant changes in the total displacement field (Fig. 8.3 C). For times greater than 1000–10000 years, the peak in the total viscoelastic response is reached, and the system has completely relaxed (Figs. 8.3 B and C).

The geometrical parameters in the V3FASAT model are: the amount of displacement (i.e. slip) on the dislocation fault (U); the upper and lower bounds of the fault plane (d_1 and d_2); horizontal length of the fault (L); dip angle of the fault (θ); and its rake (Fig. 8.2). Structural parameters are the shear modulus, viscosity of the viscous layer, and the thickness of the elastic layer (H). The V3FASAT model can determine the x, y and z deformation field at user specified times after initiation of slip. At time t=0 (immediately after an earthquake) the deformation is the same as that for the Okada (1985) coseismic model code, as no viscous effects have occurred. For times greater than the Maxwell time (∼10 years) viscous relaxation effects occur. After $\sim 1000\tau$ the maximum postseismic relaxation state has been reached.

Postseismic relaxation is mainly affected by the viscosity of the viscous layer and thickness of the elastic layer (H) (Fig. 8.4). After 100 years (given the structural parameters in Table 8.1), the deformation field associated with a viscosity of 10^{19} Pas has relaxed to a lower uplift to subsidence ratio than for a higher viscosity of 10^{20} Pas. This is expected given the faster creep of lower viscosity fluids. After 100000 years, however, the relaxation has reached a peak that is independent of viscosity (Fig. 8.4 A). Therefore, by considering deformation at a long enough time scale ($t \rightarrow \infty$) the result is independent of the choice of viscosity, reducing the sensitivity of the model by one unknown parameter.

The deformation field is highly sensitive to the thickness of the elastic layer. For an elastic thickness of 10 km and a fault rupturing down to 10 km (i.e. ruptures the entire elastic layer), the postseismic relaxation response is less than for an elastic thickness of 20 km, in which the whole layer is not breached by faulting. If however, given an elastic thickness of 20 km and a fault that ruptures down to 20 km, a very similar result to that observed when a 10 km fault ruptures the elastic layer is seen (compare red and green lines on Fig. 8.4 B). Therefore, this parameter study has determined that the absolute thickness of the elastic layer is not as important as determining if the fault ruptures the entire elastic layer or not.

An example of an application of this technique is the modelling of the long–term steady uplift of marine terraces in south–west Japan, associated with subduction at the Nankai trough (Sato & Matsu'ura 1992).

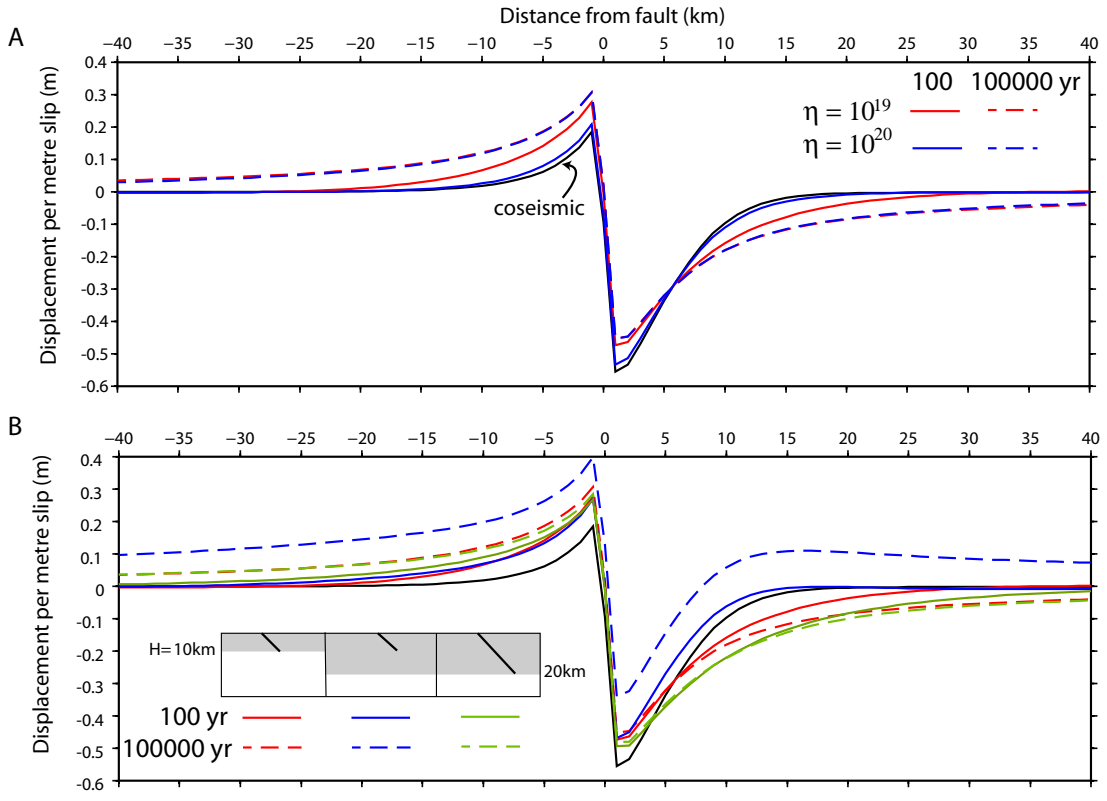

FIGURE 8.4: **A.** Effect of viscosity and **B.** Elastic thickness (H) on the total postseismic deformation field over 100 and 100000 years. Other parameters are the same as those used in Figure 8.3. Created using the fortran code V3FASAT (Fukahata & Matsu'ura 2005).

Relaxation Time

The long term deformation caused by a number of earthquake cycles, if reaching complete relaxation, will show cumulative surface displacements that are linearly additive (Sato & Matsu'ura 1992). For example, the surface deformation associated with five earthquakes, each with 1 m slip will result in exactly the same total relaxed deformation after 10000 years (given structural parameters in Table 8.1) as 1 earthquake with 5 m of slip. This allows modelling of long term deformation features as if they occurred in a single, high slip event. This principle is fundamental to modelling long term deformation in the Alkyonides Gulf and elsewhere in the Corinth rift in future.

This additive method will only work if the deformation associated with each earthquake has been completely relaxed. For low viscosities of 10^{18} Pas and other structural parameters as in Table 8.1, the completely relaxed state is reached after a very short time of only 20 years, and 1000 years for viscosities of 10^{19} Pas. For viscosities $>10^{19}$ the relaxation time is longer, closer to 50000 years for 10^{20} Pas, and greater than 100000 years for 10^{21} Pas.

If the Corinth rift has a viscosity of 10^{19} Pas (Westaway 2002, 2007), similar to other regions (Nur & Mavko 1974, Pollitz et al. 2001, Ryder et al. 2007), only earthquakes that occurred within the last 1000 – 2000 years are still in their relaxation stage. Stresses induced by all

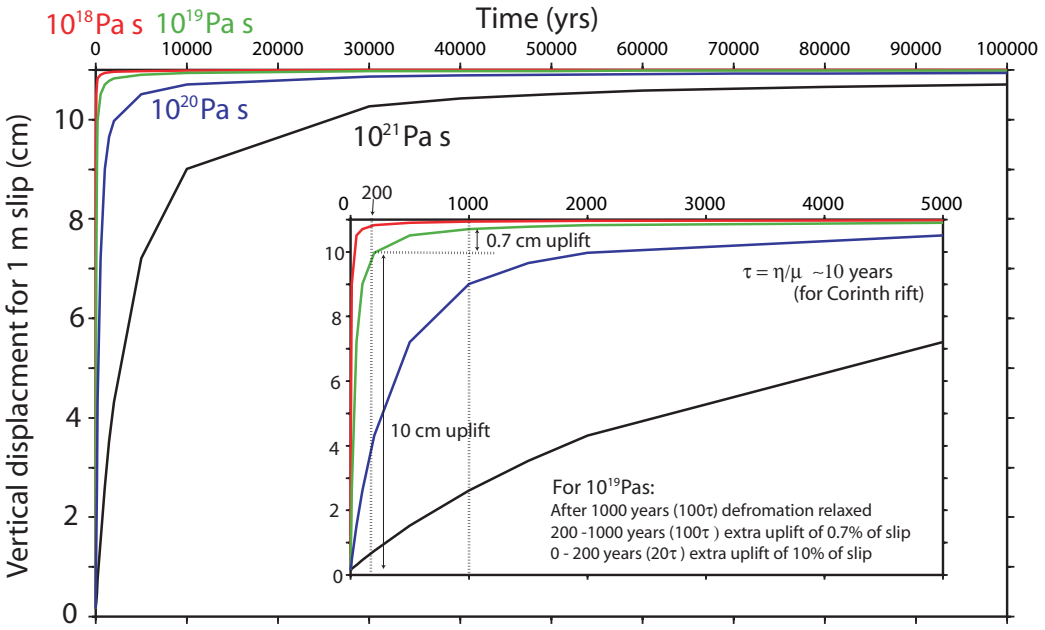

FIGURE 8.5: Analysis of the change in vertical displacement for a single footwall point over time, for viscosities of 10^{18} to 10^{21} Pas. Inset figure shows a close up view of the first 5000 years after earthquake slip. Created using the fortran code V3FASAT (Fukahata & Matsu'ura 2005).

other earthquakes have been completely relaxed. From Figure 8.5 B, in the the first 200 years following an earthquake, the uplift increases by 10% of the total slip, and between 200 and 1000 years increases by only 0.7%. This means, only earthquakes occuring in the last 200 years will significantly affect the result. Recurrence interval estimates from paleoseismology trenching in the Alkyonides Gulf suggest that faults along the more rapidly uplifting southern margin have reccurence intervals of ∼330 years (Collier et al. 1998), and faults on the north margin more like ∼2000 – 10000 years (Benedetti et al. 2003, Kokkalas et al. 2007). From these estimates it is likely that the 1981 earthquake displacement field, and possibly displacement from one previous coseismic event on the southern margin, are still not completely relaxed. The vertical deformation errors due to these earthquakes with incomplete deformation cycles are likely to be in the range < 2 m. Therefore, the use of long term deformation modelling in the Alkyonides Gulf equating displacement to slip in a single large event that has totally relaxed is justified.

8.2.2 Long term deformation modelling in the Corinth rift

Some studies have used the cumulative long term uplifted footwall terrace record in the Corinth rift to forward model deformation to derive realistic slip rates. De Martini et al. (2004) attempt to forward model terrace profiles in the footwalls of the East and West Eliki and Aigion faults. They use an elastic half–space model in order to do this rather than combining viscoelastic terms. Using this type of model to attempt to fit uplift patterns

introduces unrealistic uplift to subsidence ratios for long term deformation (as described above), which will result in over–estimated slip rates. The slip rates De Martini et al. (2004) deduce for these faults are much higher than is predicted by assigning likely and observed long term uplift to subsidence ratios of ∼1:1.2 – 2.2 (as argued by McNeill & Collier 2004, McNeill et al. 2005b). For example, De Martini et al. (2004) suggest that in the footwall of the Eliki fault a 10 ka terrace has an elevation of 10 m. From their model they then suggest a slip rate of 8.5 mm/yr. Their model is generating an uplift to subsidence ratio of around 1:5, appropriate for coseismic deformation but not deformation after 10000 years (Fig. 8.3 C). The viscoelastic V3FASAT model would instead predict an uplift to subsidence ratio of 1:1.5 at this time, and correspondingly slip rates of ∼3 mm/yr, much more appropriate given the total hanging wall basement depth of < 3 km and footwall topography (∼1 km, McNeill et al. 2005b) (Fig. 6.8).

Armijo et al. (1996) model the terraces in the footwall of the Xylokastro fault at Corinth using a thick elastic plate model which accounts for long term behavior by reducing the elastic modulus used. They argue that their model fits terrace uplift patterns best when shear modulus in the upper crust is very low, so the system approximates an elastic half–space. The high slip rates generated by their model (∼11 mm/yr), however, require basement to have subsided to a depth of 6 – 7 km, whereas a depth of only ∼3 km is observed (Chapter 6, Fig. 6.8 and e.g., Sachpazi et al. 2003). In conclusion, this method also produces unrealistically high long term subsidence and slip rates which are not supported by data.

With our improved knowledge of basement depth, this previous long term deformation modelling in the Corinth rift based on elastic models must be revisited with viscoelastic techniques to model the uplift and satisfy basement depth.

8.2.3 Long term deformation in the Alkyonides Gulf

Long term deformation over many earthquake cycles on multiple faults has resulted in subsidence of the ∼1.5 km deep Alkyonides basin and uplift of the older Megara basin along the southern margin. High topography in parts of the northern margin, the active Kaparelli fault scarp, and the surface fault scarp seen along the Livadostros peninsula are also the result of fault activity (Fig. 8.6).

Currently, in the Alkyonides basin there is evidence for activity on the offshore N–dipping East Alkyonides fault (responsible for uplifting the southern coastline), and on the onshore Skinos and Pisia faults, which are actively down–throwing coastline and uplifting the Perachora peninsula (Chapter 6, section 6.4.3). The S–dipping Kaparelli fault (north of the Alkyonides Gulf) slipped during the 4th March 1981 earthquake, and so is active. However, due to its much lower footwall topography compared to south coast faults, lower slip rate, and recurrence interval, Benedetti et al. (2003) and Kokkalas et al. (2007) suggest it is less active than south coast faults (Jackson et al. 1982, Stiros et al. 2007). The presence of submerged wavecut notches cut into the footwall of the Livadostros fault plane, provide evidence for footwall subsidence (Chapter 4, section 4.5.1). But, it has also produced a

modern seafloor scarp and significant footwall topography (up to 0.75 km) has accumulated over its history, suggesting activity. The West Alkyonides Fault on the south coast is not considered here as it is generally believed to be inactive, with its footwall subsiding in the hanging wall of the Skinos fault.

Measurements of the vertical displacement of Quaternary surfaces as marker horizons are rare, due to preservation problems and acquisition of good datable material. Fortunately, there are three independent measurements of relative elevation change over the last ca. 130 kyr, which make modelling long term deformation field possible in the Alkyonides Gulf:

- **Measurement 1:** In Chapter 6 (Fig. 6.7 and Table 6.5) submerged lowstand shorelines are interpreted in the north of the Alkyonides basin, 12 km north of the East Alkyonides fault plane (previously interpreted by Leeder et al. 2005). The surface thought to correspond to the previous end sea level lowstand (ca. 130 ka), is at a current depth of ∼145 m below sea level. This surface was formed close to sea level (M. Leeder, pers. comm. 2005). Therefore, considering that sea level is currently ∼60 m higher than the lowstand level (due to the Rion sill) ∼75 ± 10m of subsidence has occurred in this area since ca. 130 ka (Point 1 on Fig. 8.6 A). The subsided offshore delta lies in the far–field subsidence region of the south coast East Alkyondies, Skinos and Pisia faults, and also lies close to the north margin Kaparelli and Livadostros faults.

- **Measurement 2:** Leeder et al. (1991) have recorded evidence of a shoreline ∼40 m above sea level at Alepochori in the footwall of the East Alkyonides fault. Coral from this level suggests a maximum age of ca. 128 ka, coincident with the Stage 5e highstand. The sea level during the Stage 5 interglacial was not significantly higher than the modern highstand (Siddall et al. 2003), so the shoreline has uplifted by ∼40 m in the last ca. 130 ka (Point 2 on Fig. 8.6 A). The platform lies directly in the footwall of the East Alkyonides and Psatha faults (Fig. 8.6 A, Leeder et al. 1991). In the absence of any other nearby faults it can be constrained that uplift is likely due to these faults alone. For modelling purposes, the East Alkyonides and Psatha faults are considered as a single fault for simplicity and assigned the same geometry as that modelled by Hubert et al. (1996).

- **Measurement 3:** Leeder et al. (2002) find that ∼20 m of subsidence has occurred in the hanging wall of the Skinos fault during the last lowstand (ca. 70 – 12 ka). This is based on the thickness of lowstand delta accumulation offshore in the hanging wall of the Skinos fault. If this subsidence rate prevailed throughout the last ca. 130 ka, a total subsidence in the range of ∼50 m is expected (Point 3 on Fig. 8.6). The lowstand delta lies directly in the hanging wall of the Skinos fault (Fig. 8.6 B). The Skinos and Pisia faults overlap and are parallel in this area and the offshore subsidence is probably due to the combined

activity of the two faults. Again, for the initial simple model a single fault of length 14 km is chosen, having the same geometry as the Pisia fault, modeled by Hubert et al. (1996). It is not possible in this study to distinguish activity on the Skinos and Pisia faults independently and so they are referred to hereafter as the Skinos/Pisia fault.

Although there are only three control points for deformation since ca. 130 ka, compared to the complete 3D coverage used in coseismic InSAR modelling, this is still a good dataset in the field of long term deformation modelling, given the rarity of having knowledge of both uplift and subsidence components for the same time period.

8.3 Results

Five major faults have been identified in the Alkyonides Gulf that likely control vertical displacement at the three sites. The modelling dimensions of the Skinos/Pisia, East Alkyonides and Kaparelli fault follow the work of Hubert et al. (1996) and Stiros et al. (2007) and are summarised in Table 8.1. The Livadostros fault is assumed to have the same depth and dip as these faults. Viscoelastic deformation modelling is first attempted in section 8.3.1 considering independently only the East Alkyonides and Skinos/Pisia south coast faults. The effect of the combined deformation fields of multiple faults over the last 130 kyr is later considered in section 8.3.2.

8.3.1 Single fault model: East Alkyonides fault and the Skinos/Pisia fault

Geometrical parameters used for the East Alkyonides and Skinos/Pisia faults are taken directly from the coseismic dislocation studies of Hubert et al. (1996) (Table 8.1) and values for the shear modulus and viscosity have been justified above. The two key variables in this model are: the magnitude of slip on the fault over the last 130 kyr, and the elastic thickness. The elastic thickness of Corinth rift lithosphere in the Alkyonides Gulf area is constrained to a depth of ∼12 km by the maximum depth of aftershocks following the 1981 earthquakes (King et al. 1985). This estimate of elastic thickness is similar to estimates of *effective elastic thickness* derived from gravity modelling by King (1988a). Throughout the modelling work presented here the the elastic thickness is kept at a constant 12 km, and the magnitude of slip on the fault is varied in an attempt to match the surface displacement.

The first step in the modelling is to recreate the elevation of the uplifted wavecut platform (point 2) and the north margin subsided delta (point 1), each ca. 130 ka years old, along the 2D profile shown in Figure 8.6. A range of possible total displacements on the East Alkyonides fault from 50 – 600 m are modelled in an attempt to recreate the vertical displacements of the two ca. 130 Ma measurements (Fig. 8.7). The deformation field is

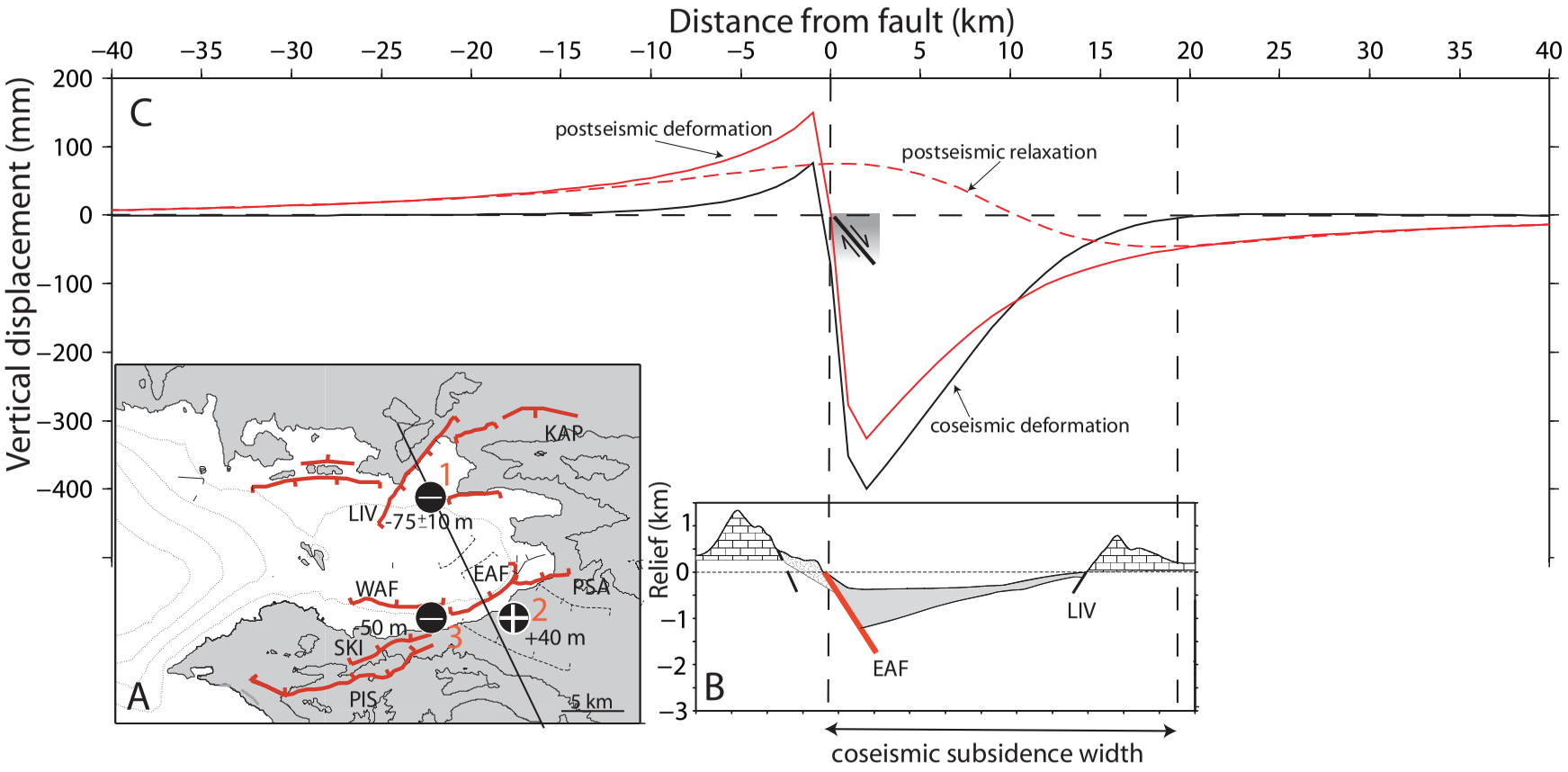

FIGURE 8.6: **A.** Map of the Alkyonides Gulf area annotated with the magnitude of ca. 130 ka displacement (labeled 1 to 3). Onshore uplift of ∼40 m from Leeder et al. (1991) (2), offshore south coast subsidence of ∼50 m, after Leeder et al. (2002) (3) and offshore north coast subsidence derived in Chapter 6 Table 6.5 (1). **B.** Basement relief across the Alkyonides Gulf from Chapter 6 Fig. 6.8. **C.** Comparison of coseismic deformation for one earthquake, post seismic relaxation and total postseismic deformation for 1 m of slip on the East Alkyonides fault. Created using the fortran code V3FASAT (Fukahata & Matsu'ura 2005). EAF: East Alkyonides, WAF: West Alkyonides, SKI: Skinos, PIS: Pisia, PSA: Psatha, KAP: Kaparelli and LIV: Livadostros faults.

Symbol	Parameter	Value
t	Deformation period	10000τ
τ	Maxwell time	10 yr
μ	Shear modulus	30 Gpa
	Poisson ratio	0.25
η	Viscosity	1.0 x 10^{19}Pas
H	Elastic thickness	12 km
d_1	Upper bound of faults	0 km
d_2	Lower bound of faults	12 km
θ	Dip of faults	50^o
	Rake of faults	-90^o
	EAF Horizontal length	13 km
	SKI/PIS Horizontal length	14 km
	KAP Horizontal length	17 km
	LIV Horizontal length	13 km
	Displacement on faults	variable

TABLE 8.1: Parameters used in viscoelastic dislocation modelling. Source of parameters discussed in text.

plotted after a time of 10000τ, so all coseismic deformation has completely relaxed and is independent of chosen viscosity.

From the deformation fields presented in Figure 8.7, it is clear that no single value of slip on the East Alkyonides fault can match the uplift and subsidence pattern of points 1 and 2. Uplift of the Alepochori platform alone (point 2 on Fig 8.7) can be correctly fitted with a slip of ∼300 m, whereas the north margin subsided delta (point 1 on Fig. 8.7) would require ∼500 m slip.

To recreate the vertical displacement of the south margin lowstand delta in the hanging wall of the Skinos/Pisia fault requires a slip of ∼200 m (point 3 on Fig. 8.7). This magnitude of slip on the Skinos/Pisia fault equally also cannot generate the north margin subsidence of point 3.

No single magnitude of slip on either the East Alkyonides or Skinos/Pisia fault over the last 130 kyr can reproduce the vertical uplift of the Alepochori platform (point 2), south margin delta (point 3) and the subsidence of the lowstand north margin delta (point 1). Points 2 and 3 lie immediately in the footwall and hanging wall of the south coast faults and their vertical displacement is used to constrain the slip rate of these faults. There are a number of explanations why offshore north margin subsidence cannot be modelled satisfactorily by slip on south coast faults. Errors in the Rion sill depth create an uncertainty of ±10 m on the north margin subsided delta position. This however, does not change the total slip required on south coast faults significantly. Alternatively, the seemingly incorrect ratio between uplift and subsidence could mean that postseismic relaxation has not been completed on many faults. This is unlikely as only earthquakes occurring in, at most, the last 5000 years

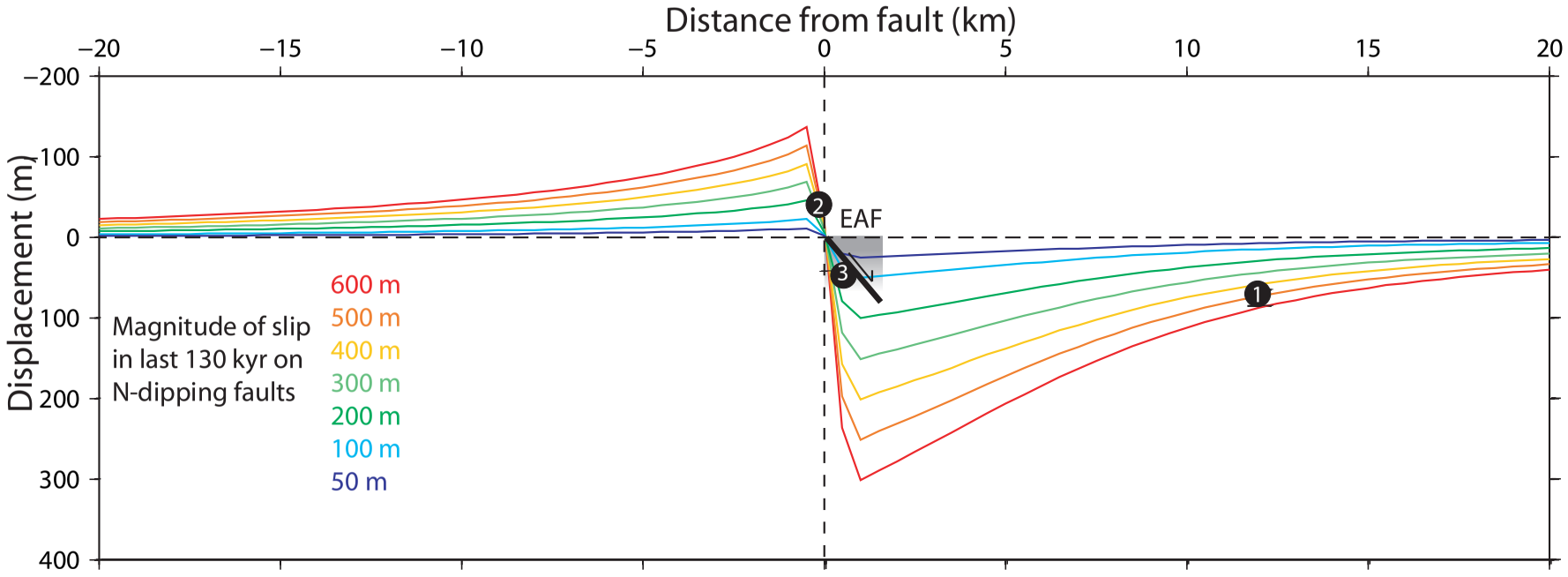

FIGURE 8.7: Attempts to model the uplift of south margin wavecut platform (point 2, Leeder et al. 1991) and subsidence of south margin delta (point 3, Leeder et al. 2002) and north margin delta (point 1, Chapter 6 Fig. 6.7, Leeder et al. 2005) using a viscoelastic model after 10000τ for various magnitudes of net 130,000 year slip on the East Alkyonides fault and Skinos/Pisia faults independently. Numbers indicate positions of displaced features shown in Fig. 8.6 A. Created using the fortran V3FASAT code (Fukahata & Matsu'ura 2005).

would not be completely relaxed. Compared to the deformation field of completely relaxed earthquakes from the previous 125 kyr, errors due to incomplete relaxation would be small (Fig. 8.5). In summary, the most likely explanation for the discrepancy is that other faults contribute to the deformation field of the north margin lowstand delta.

8.3.2 Multiple fault model

Combined deformation field of the East Alkyonides and Skinos/Pisia faults

Above it was estimated from 2D dislocation modelling that slip on the East Alkyonides and Skinos/Pisia faults is ∼300 and ∼200 m respectively over the last 130 kyr, constrained by vertical displacements in their immediate footwall or hanging wall (Figure 8.7). Considering each of these faults independently the subsidence they predict at the location of the north margin lowstand deltas is much too low (point 3, Fig. 8.7). However, the 3D deformation fields generated by slip on these faults are likely to constructively interfere and enhance subsidence in the north margin area, compared to when each of the faults are considered separately. The V3FASAT code has the capability to model the 3D deformation field associated with slip on multiple faults. The combined deformation field for slip of ∼300 m on the East Alkyonides and ∼200 m on the Skinos/Pisia faults is shown in Figure 8.8.

The two south coast fault model with above fault displacements predicts total subsidence over the last ca. 130 ka of only ∼40 m in the area of the north margin lowstand delta: only 50% of that observed. A possible explanation for this discrepancy is that north coast faults (i.e. the Kaparelli and Livadostros faults), which are closer to this area and would exert greater near–field effects, have contributed to the deformation field over the last ca. 130 ka.

Combined deformation field of the East Alkyonides, Skinos/Pisia faults and Kaparelli faults

The north margin Kaparelli fault that slipped during the 4th March 1981 earthquake (Jackson et al. 1982) has been argued from paleoseismology to have been active over at least the last 10000 years with an average slip rate of ∼0.2 mm/yr (Benedetti et al. 2003) to 0.3 mm/yr Kokkalas et al. (2007). Adopting a slip rate of ∼0.3 mm/yr for the Kaparelli fault suggests there has been ∼40 m of slip over the last ca. 130 ka. In order to model the Kaparelli fault the geometrical parameters assigned by Stiros et al. (2007) from coseismic modelling of the 4th March 1981 earthquake are used (Table 8.1). The vertical displacement field produced by Kaparelli fault activity has been added to the expected ca. 130 ka deformation fields for south coast faults in Figure 8.9. But the addition of ∼40 m of slip on the Kaparelli fault does not help generate the extra subsidence necessary at the subsided delta because the fault is located too far to the east to influence the deformation field significantly (Fig. 8.9).

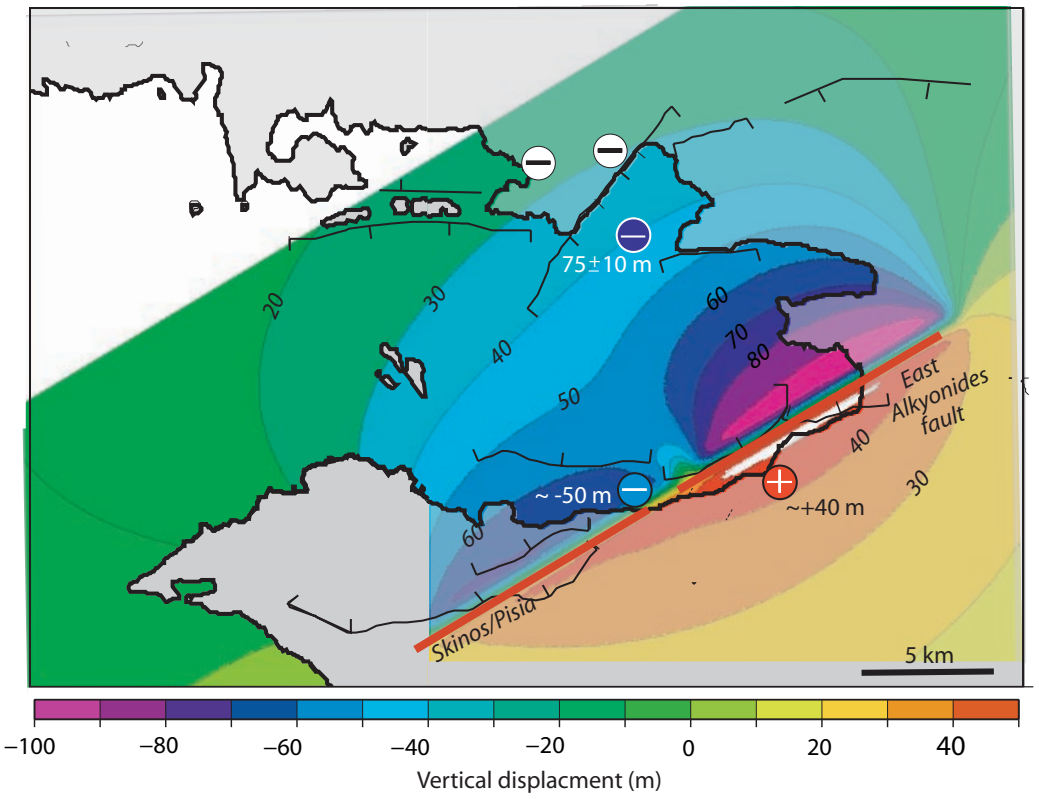

FIGURE 8.8: Deformation field for a total of 300 m slip on the East Alkyonides fault, and 200 m slip on the Skinos/Pisia fault. Modelled fault planes, with the geometry described in Table 8.1 are shown in bold red lines. Uplift and subsidence of ca. 130 ka features are presented in circles color coded by their elevation. Note, the subsided north shore delta is much deeper than that immediately adjacent to the southern margin fault and than subsidence predicted by this model. Created using the fortran V3FASAT code (Fukahata & Matsu'ura 2005).

Combined deformation field of the East Alkyonides, Skinos/Pisia faults, Kaparelli faults and Livadostros faults

The subsided delta is located directly in the hanging wall of the Livadostros fault (Fig. 8.6) and any slip on this fault would create significant subsidence. Field observations suggest the Livadostros footwall is currently subsiding, as it appears to show submerged notched levels (Chapter 4, section 4.5.1). This fault, however has been active in the past because a large topographic scarp (up to 0.75 km) has been produced and seismic profiles across its western tip show evidence of recent activity (Sakellariou et al. 2007).

The next step in the modelling procedure is to investigate how much ca. 130 ka slip on the Livadostros fault is necessary to explain the delta submergence and determine if this slip value is feasible. The results of this work show that at least 50 m of slip on the Livadostros fault is required to achieve the minimum 65 m of subsidence on the north shore delta over the last ca. 130 ka (Fig. 8.10). This slip is greater than estimated slip on the Kaparelli fault in the same time period by ∼10 m.

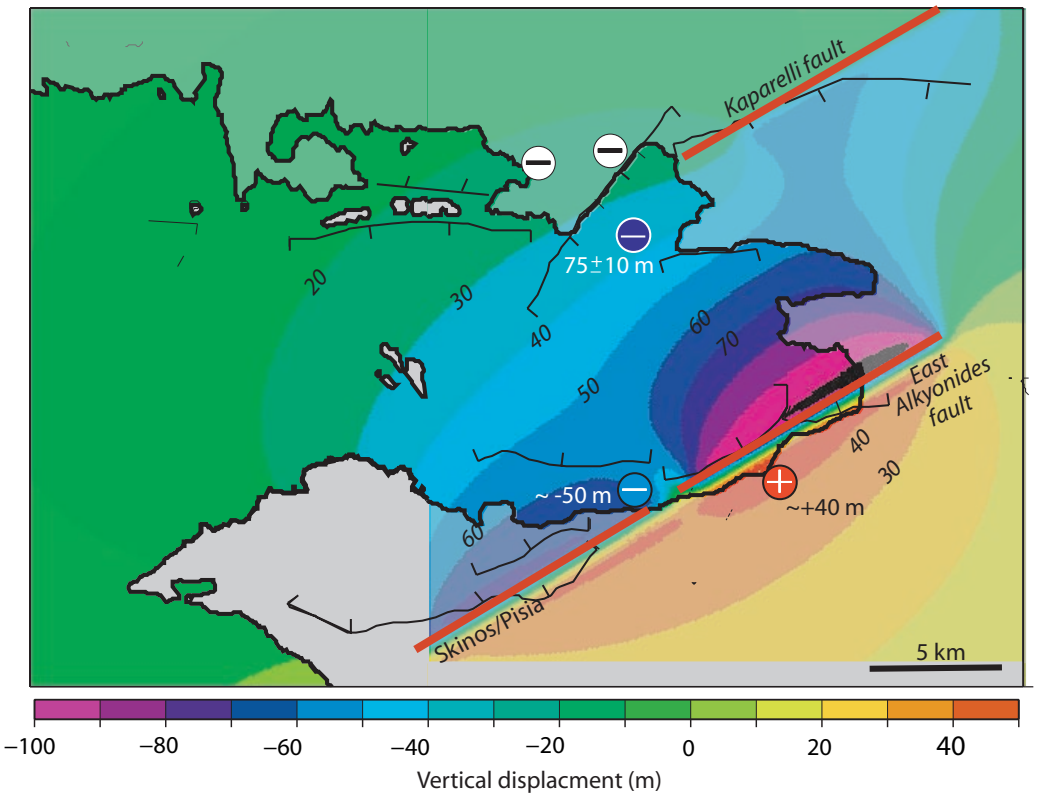

FIGURE 8.9: Displacement field created by ca. 130 ka displacement on the Skinos/Pisia, East Alkyonides and Kaparelli faults. Created using the fortran V3FASAT code (Fukahata & Matsu'ura 2005).

In conclusion, in order to explain all of the observed features, activity comparable to that on the Kaparelli fault is required on the Livadostros fault. Over the last ca. 130 kyr, ∼50 m of slip equates to a slip rate of ∼0.4 mm/yr. Earthquakes on south coast faults are likely to be much more frequent (given higher slip rates and assuming similar slip per event), therefore causing overall subsidence of the Livadostros footwall within the last ca. 130 kyr (Table 8.2).

8.4 Discussion

8.4.1 Implications for the Alkyonides Gulf

In order to explain the three ca. 130 ka vertical displacement measurements in the Alkyonides Gulf, slip is required over this time period on multiple faults in the area. The slip rates determined in this study of ∼2.3 mm/yr and ∼1.5 mm/yr on the East Alkyonides and Skinos/Pisia faults respectively (Table 8.2), are similar to slip rates derived from Holocene notch uplift for the East Alkyonides fault (Leeder et al. 1991) and slip rates derived from exposure dating on the Skinos/Pisia fault (McNeill et al. in prep) and paleoseismology (Collier et al. 1998).

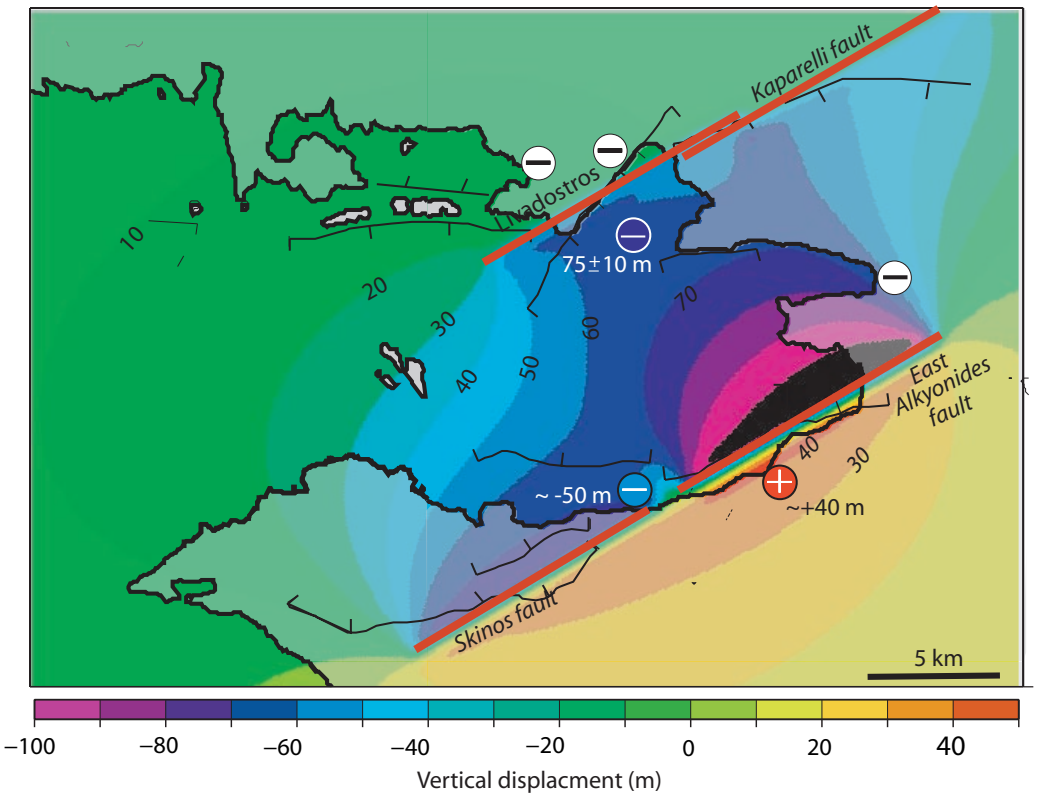

FIGURE 8.10: Superimposed deformation fields for 300 m slip on the East Alkyonides fault, 200 m slip on the Skinos/Pisia, 39 m slip on the Kaparelli and 50 m slip on the Livadostros fault in the last 130 000 years. Created using the fortran V3FASAT code (Fukahata & Matsu'ura 2005).

Fault	Slip (m)	Slip rate(mm/yr)	Constraints
East Alkyonides	300	∼2.3	∼40 m uplifted terrace
Skinos/Pisia	200	∼1.5	∼50 m subsided delta
Kaparelli	40	∼0.3	0.3 mm/yr slip rate
Livadostros	50	∼0.4	modelled slip

TABLE 8.2: Summary of net slip and slip rates for faults in the Alkyonides Gulf that can reproduce the vertical displacement of ca. 130 ka features from viscoelastic dislocation modelling.

Slip rates of ∼0.3 and ∼0.4 mm/yr are required on the north margin Kaparelli and Livadostros faults respectively. This result is important, as it highlights (as during the 1981 earthquakes) that some S–dipping north margin faults are active, but with lower slip rates and probable longer recurrence intervals than south coast faults. This means faults like the Kaparelli fault that have smaller topographic expressions, or like the Livadostros fault that appear old and vegetated, with no record of historic seismicity should not necessarily be considered inactive. These characteristics should not always stop a fault being considered a seismic hazard. The field observations of net subsidence of the Livadostros footwall (Chapter 4, section 4.5.1) are satisfied by the modelled slip values. Due to the probable

higher frequency of earthquakes on south coast faults, overall subsidence at Livadostros is expected, as most of the time it passively subsides in the far–field hanging wall.

Rough estimates of earthquake recurrence interval may be obtained from the estimates of ca. 130 ka slip if the magnitude of slip likely to be experienced during each earthquake is known. Based on the 1981 earthquake series, slip at depth of 0.7 – 2 m occurred on each fault (Hubert et al. 1996, Stiros et al. 2007). If this slip interval is consistent over the last 130 kyr this equates to recurrence intervals on the East Alkyonides and Skinos/Pisia faults of 450 – 650 years using the results of the dislocation modelling. This is similar, albeit slightly higher than that deduced from trenching of the Skinos fault by Collier et al. (1998). Interestingly, recurrence intervals for Alkyonides south coast faults are within range of those predicted for the Eliki fault (270 – 1200 yrs, Koukouvelas et al. 2001, McNeill et al. 2005b) and Aigion fault (∼360 yrs, Pantosti et al. 2004) in the west, where slip rates are higher. Average recurrence intervals for the Kaparelli and Livadostros fault derived from viscoelastic dislocation modelling here are in the range of 2500 – 3300 years, in general agreement with Benedetti et al. (2003) and Kokkalas et al. (2007). However, all of these recurrence intervals must be treated with caution as there is evidence for nonuniform recurrence intervals on Alkyonides Gulf faults (Roberts 1996b, Kokkalas et al. 2007).

The major assumptions that have entered the viscoelastic dislocation model include the choice of viscosity. If viscosities in the Alkyonides Gulf are greater than 10^{18}– 10^{19} Pas, the assumption that all coseismic deformation has relaxed cannot be made. This would result in higher uplift to subsidence ratios for long term deformation. This could potentially explain some of the excess subsidence of north margin deltas without invoking activity on north margin faults. However, lower crustal viscosities greater than 10^{18}– 10^{19} Pas have not been suggested for the Corinth rift. Another potential source of error is the unconsidered activity of the West Alkyonides fault (Figure 8.6 A). This fault is currently inactive and subsiding in the hanging wall of the Skinos fault. However, in the last 130 kyr it may have been influential and any activity would have strongly influenced the accumulation of the south margin lowstand delta (point 3 on Fig. 8.6). The addition of activity of the West Alkyonides fault could potentially significantly alter the magnitude of slip required on north margin faults. An improved knowledge of stratigraphy in the hanging wall of the West Alkyonides fault and in the lowstand delta is required to determine if activity within the last 130 kyr is likely to be significant. Another possible source of error is the state of the regional stress field and components of regional uplift and subsidence, not associated with seismicity. The V3FASAT model used in this study only considers internal deformation due to a dislocation and does not consider regional stress conditions that may be superimposed on the dislocation deformation field.

8.4.2 Future of long term Corinth rift deformation models

The simple viscoelastic modelling presented here has the potential to be used elsewhere within the Corinth rift to attain more accurate estimates of slip on faults and examine

the interaction of multiple faults. Along the south margin a number of terraces exist which provide uplift constraints for time periods up to ca. 400 ka. Previously, dislocation and finite element modelling have been used to determine slip rates from these terraces, as described above (De Martini et al. 2004, Armijo et al. 1996). The results commonly produce slip rates that are very high and over predict hanging wall basement subsidence. This is probably due to the elastic dislocation modelling methods used by these authors, which do not incorporate viscoelastic effects. The terrace uplift profiles in these areas should be re-examined using models like V3FASAT to achieve more realistic estimates of slip rate.

An exciting new use for long term deformation modelling is to investigate the tectonically complex western rift, that was interpreted in Chapter 5, Bell et al. (2008) and McNeill et al. (2005a). In the western rift, four major coastal and offshore faults act to produce the observed basement geometry and stratigraphy. Slip rates for these faults have been estimated based on basement offset, submerged delta depths and uplifted terrace elevation (Bell et al. 2008, Chapters 5 and 6). Although these estimates may be reasonable approximations, another method would be to attempt to model the activity of these faults to reproduce the vertical displacement using long term viscoelastic dislocation techniques. This method would help constrain the slip rates, but also has the potential to investigate two controversies in the western rift (is there a low angle detachment and why do dominant S–dipping faults appear to be subsiding?). The potential future use of viscoelastic methods in the Corinth rift is reviewed in more detail in Chapter 9.

8.5 Conclusions

1. In order to model long term deformation on timescales greater than ∼10 – 100 years, viscous readjustment of vertical displacement profiles following coseismic elastic events must be incorporated. Without this component, slip rates and hanging wall subsidence in particular tend to be over estimated.

2. Long term uplift and subsidence within the last ca. 130 ka within the Alkyonides Gulf cannot be modelled by slip on a single south coast fault. South coast vertical movement constrains total slip of 200 – 300 m on south coast faults, however offshore subsidence can only be modelled by net slip of 500 m on south coast faults. The total Alkyonides Gulf ca. 130 ka deformation field can be much better modelled by also considering slip on the north coast Kaparelli and Livadostros faults of 40 – 50 m over the last 130,000 years.

3. The modelled deformation requires slip rates of ∼2 mm/yr on the East Alkyonides, ∼1.5 mm/yr on the Skinos/Pisia, ∼0.3 mm/yr on Kaparelli (from Kokkalas et al. 2007) and ∼0.4 mm/yr on the Livadostros fault. These are in agreement with published slip rates for the south coast faults.

4. The lower slip rates experienced by north margin faults are likely to produce longer earthquake recurrence intervals than have been measured for south coast

faults and this is confirmed by paleoseismology on these faults (Collier et al. 1998, Benedetti et al. 2003, Kokkalas et al. 2007).

5. The Livadostros fault is currently in the subsidence field of the active south coast faults with higher slip rates. Because the Livadostros fault has a lower slip rate, and probably longer recurrence interval than these south coast faults the footwall appears to have relatively subsided at the coastline, however, offshore an offset in the seafloor has been created confirming the fault is active.

6. In the future, the viscoelastic method may be applied to explain long term deformation of the detailed south coast terrace record, and also to investigate the importance and impact of multiple faults in the tectonically complex western rift.

Chapter 9

Conclusions

In this thesis the tectonic evolution of the entire Corinth rift, including onshore and offshore components, has been assessed. This work offers new contributions to scientific knowledge of the Corinth rift in terms of its rift structure and geometry, spatial and temporal evolution and analysis of individual fault slip rates. In the following final chapter the major conclusions and new contributions that have resulted from this study are outlined. The conclusions are arranged in terms of answering the key thesis objectives proposed in Chapter 1, section 1.4. The thesis ends with a discussion of future work that could be continued in the Corinth rift.

9.1 How has this study improved our understanding of the Corinth rift?

9.1.1 What is the geometry, style and magnitude of subsidence and extension across the rift?

1. **Fault architecture**

   (a) In the Alkyonides Gulf and central Corinth rift (Derveni to Corinth), current activity is focused on N–dipping en–echelon south coast faults. In the western rift, however, fault activity is more distributed occurring on ∼four offshore faults as well as the N–dipping coastal south margin faults.

   (b) Stratigraphic thickening and basement tilt are generally toward the south in the eastern and central rift, indicating that presently N–dipping faults have control on rift geometry. In contrast, as shown in Chapter 5, western rift stratigraphy shows significant thickening and tilting to the north, toward the offshore S–dipping West Channel and South Eratini faults, suggesting they are presently structurally important.

In Chapter 4 it was shown that the northern margin of the Corinth rift is not wholly subsiding, as would be expected if the rift was a simple asymmetric half graben along its length controlled by N–dipping south coast faults. The northern margin of the eastern Alkyonides Gulf is subsiding (submerged archaeology and marine notches) while uplifted wavecut platforms further west on the Milakos and Galaxidi peninsula indicate localised uplift, possibly controlled by offshore S–dipping faults.

The importance of S–dipping north margin faulting has also been highlighted in Chapter 8 by the viscoelastic dislocation modelling of the ca. 130 ka displacement field in the Alkyonides Gulf. Activity on the S–dipping Kaparelli fault and Livadostros fault, are required to explain the displacement field.

(c) All major faults identified from seismic reflection data, are interpreted as high angle, with dips of at least 45° within sediments. Low angle faulting has been previously suggested in the western rift, based on: the low angle of exposed currently inactive onshore faults; geodetic extension rates exceeding slip rates of known faults; low angle of nodal planes of earthquakes and apparent microseismicity defining a low angle N–dipping plane. In this study it has been highlighted that arguments for a detachment presented in the literature do not all correspond to the same detachment level, and so do not support each other (Chapter 5, section 5.6.4). The results of Chapter 5 indicate that geodetic extension rates could be matched by estimated Holocene activity on the newly interpreted offshore western rift faults and coastal faults, negating the need for low angle slip on a detachment. The N–thickening stratigraphic architecture in the western rift presented here is also fundamentally geometrically incompatible with a low angle detachment (Chapter 5, Fig. 5.17).

2. **Structural style**

(a) The fundamental elements of the Corinth rift's geometry are half graben controlled by a single, dominant fault polarity at any one time. Net symmetric graben morphology is observed in the stratigraphy of the central rift, but only as the result of two superimposed opposing half graben (Chapter 6, Fig. 6.14).

(b) The geometry of the major rift bounding faults (N versus S–dipping) changes between different segments of the rift. In the Alkyonides Gulf and central parts of the rift (between Derveni and Corinth) N–dipping faults on the southern shoreline are currently dominating, producing a simple south thickening half graben structure (Chapter 6, e.g., Figs. 6.6 and 6.14). To the west of Derveni, S–dipping offshore faults also influence stratigraphy, producing N–thickening half graben morphology. However,

these half graben are complicated by local southward thickening toward the coastal Eliki–Akrata and Derveni faults on the south margin (Chapter 5, Figs. 5.14 and 5.15).

(c) The suspected pre–rift basement surface reaches consistent depths of ∼2.7 – 3 km in the central rift, with depths of up to ∼3.5 km locally (Chapter 6, section 6.6). Basement depth is much shallower in the western and eastern (Alkyonides Gulf) parts of the rift, where it has a maximum depth of only ∼1.6 km. Basement structure divides the rift into three structural elements from west to east, 1) the shallow western rift controlled by a number of offshore and coastal faults, separated from the deeper basement in the hanging wall of the East Channel fault, 2) the deep central rift, with similar basement depths along the rift axis, controlled by a number of en–echelon faults between Diakopto and Perachora, and 3) the shallow Alkyonides basin separated from deeper basement to the west by the Alkyonides islets basement horst (Chapter 6, Fig. 6.8).

3. **Slip rates**

(a) Slip rates for coastal faults have been collated and derived from uplift rates presented in the literature, stratigraphic offset and subsidence, basement controls, and dislocation modelling (Chapter 5 section 5.4.3, Chapter 6 section 6.8, and Chapter 8). In general, individual fault slip rates are greatest in the central and western rift (between Aigion and Perachora) where they reach ∼3 – 6 mm/yr. Slip rates are lower in the Alkyonides Gulf, where they do not exceed ∼1 – 3 mm/yr. Offshore faults, even in areas where they have a similar influence on stratigraphic architecture as the south coast faults, have a much lower apparent slip rate (>1.8 mm/yr). These rates are likely underestimated because slip rates are determined from basement offset without a knowledge of the extent of footwall erosion.

(b) In general, Holocene slip rates are greater than those averaged over the Late Quaternary as noted previously (e.g., McNeill & Collier 2004). Holocene slip rates for the North Eratini fault are 2 – 6.7 mm/yr, compared to >1.8 mm/yr for the pre–Holocene (Chapter 5, Fig. 5.13). Patterns of offshore syn–rift stratigraphy suggest slip rates on faults have also changed pre and post 0.4 Ma. Slip rates on the Likoporia and Derveni faults appear to have accelerated post 0.4 Ma, since then large sediment depocentres have been constructed in their hanging wall. Unfortunately, due to the lack of dated footwall uplift indicators in this area with ages greater than ca. 0.4 Ma, this cannot be confirmed.

(c) In the Alkyonides Gulf, the presence of three ca. 130 ka vertical displacement markers spaced across the rift has allowed estimations of fault slip on multiple faults using viscoelastic dislocation modelling (Chapter

8). This method has produced estimates of slip on the East Alkyonides, Skinos/Pisia (considering the influence of both faults together), Kaparelli and Livadostros faults over the last ca. 130 kyr of ∼2.3, 1.5, 0.3 and 0.4 mm/yr respectively.

4. **Extension**

   (a) Total extension, derived from the total fault displacement of currently active and inactive faults indicates that the western side of the rift (west of Likoporia) has extended by 8 km (Chapter 7). To the east of Likoporia the rift has only experienced extension of 5 – 6 km. This spatial variation in total extension is directly related to the larger number of across rift faults that have been influential in the western rift (producing rugged topography and complex rift geometry) compared to the eastern rift (where topography is more subdued and rift geometry simpler). This may be a real rift character difference, or be the result of comparatively less study of inactive faulting in the eastern rift.

   (b) Long term extension apparently follows the same west to east decreasing trend as the short term geodetic extension rates. β factors derived from total fault displacement and crustal thinning are similar in the western rift, suggesting uniform depth–independent stretching is occurring. In the central an eastern parts of the rift, however, crustal thinning β factors (1.23 – 1.36) are higher than those derived from fault displacement (1.13 – 1.17, Fig. 7.3). This may be due to the exclusion of extension caused by unknown faults in the east.

9.1.2 How has the rift evolved spatially and temporally?

1. **Tectonics and sediment deposition**

   (a) Offshore syn–rift stratigraphy can be separated into two distinct seismic stratigraphic packages; Units A and B (Chapters 5 and 6). Unit B, is non–reflective whereas unit A contains cyclic bands of high and low frequency reflectors that may be related to alternating marine and lacustrine conditions caused by eustatic sea level fluctuation and moderated by the level of the Rion sill.

   (b) A significant tectonic and stratigraphic change occurs across the entire Corinth rift between ca. 0.5 – 0.35 Ma. The unconformity between units A and B in the Gulf of Corinth has been estimated at ca. 0.4 Ma. This age is also similar, although slightly younger than the initiation of the North and South Eratini faults in the western rift (ca. 0.5 Ma), marking a significant re–adjustment in dominant fault structures (Chapter 5). In the Alkyonides Gulf, seismic character of sediments does not change at this

time, but since ca. 0.35 Ma sediments show extreme southward thickening, indicating enhanced activity on N–dipping faults. Pre and post ca. 0.4 Ma stratigraphy records a significant difference in basin geometry across the entire Corinth rift. It is unknown if this tectonic reshuffling is directly responsible for the change in sediment character.

2. **Change in strain distribution**

   (a) Previous onshore studies indicate that the western rift has experienced a northward migration in fault activity, resulting in the uplift of older syn–rift sediments on the southern margin. In Chapter 5 a similar local northward migration of fault activity is seen in the offshore western rift, from the West Channel fault onto the North and South Eratini faults further north ca. 0.5 Ma. The migration of fault activity on the south margin has occurred over a wider area than offshore migration, resulting in a probable overall decrease in the width of the western rift and a slight north step.

   (b) Between ca. 1.5 – 0.4 Ma rifting was concentrated in two isolated basins at the western and eastern extremities of the modern deep central rift (one controlled by the S–dipping East Channel fault and the other by the N-dipping Xylokastro fault). This resulted in the distribution of unit B sediments into two basins, separated by a probable basement high. Post 0.4 Ma fault activity became focused in the region between the two basins, which lacked significant subsidence pre 0.4 Ma. The result of this change in strain distribution is the formation of a single unit A depocentre with its maximum thickness in the hanging wall of the Derveni and Likoporia faults (Chapter 6, Fig. 6.10).

3. **Rift Chronology**

   (a) This study contributes to a growing knowledge of the timing and evolution of Corinth rifting. From the interpretation of sea level controlled stratigraphy and constant sedimentation rate assumptions prior to ca. 0.5 – 0.4 Ma, an age of ca. 1.5 Ma is estimated for the oldest sediments within the Alkyonides basin (Chapter 6, section 6.7). A very similar age of the oldest offshore syn–rift sediments is estimated in the western rift (1.2 – 1.6 Ma) using the same method. However, in the central rift changes in the thickness of unit A and B are controlled by tectonics and, in detail, variations in sedimentation rates are expected (Chapter 6). Therefore, in this region the constant sedimentation assumption is not appropriate. Deep coring within the Corinth rift is required to further constrain the age of oldest basin sediments along the rift axis.

   (b) Estimates of the age of the oldest offshore stratigraphy (i.e. ca. 1.5 Ma) are within range of age estimates for the initiation of; the presently active

Alkyonides faults uplifting the older Megara basin (ca. 0.8 – 2.2 Ma, Leeder et al. submitted), the inactive Mamoussia–Pirgaki fault (0.7 – 1.8 Ma, Symeonidis et al. 1987, Rohais et al. 2007, Ford et al. 2007) and a little older than the initiation of the active Eliki fault (0.7 – 1 Ma, McNeill et al. 2005b) which post–dates activity on the Mamoussia–Pirgaki fault.

(c) The close similarity in the age of fault initiation in the eastern and western parts of the rift suggests that faulting in these areas may have initiated simultaneously. This indicates that rifting may not have propagated unidirectionally in either a west to east or east to west direction as has been previously suggested (e.g., Ori 1989, Le Pichon et al. 1995, Armijo et al. 1996, Clarke et al. 1998, Nyst & Thatcher 2004). A more refined chronology for offshore sediments is required to investigate higher resolution variations in the age of fault initiation along strike.

4. **Current and future basin geometry**

(a) Current geodetic extensional strain is greatest in the western rift, not coincident with the area of maximum post 0.4 Ma deposition or greatest basement depth in the central rift. This may suggest the Corinth rift is undergoing yet another shift in the position of strain focusing, moving the locus of maximum extension from the central rift further to the west (in an area which is currently a basement high between the Gulf of Corinth and Gulf of Patra).

(b) The current high geodetic rates in this area of high basement topography, may suggest strain has localised in this area in the same way as occurred between the two unit B depocentres ca. 0.4 Ma, attempting to minimise gradients of basement topography. From the past structure of the Corinth rift, it may be a reasonable prediction that strain will remain focused in this area until basement equilibrium between the Gulf of Corinth and Gulf of Patra is reached.

9.2 How has this study improved our understanding of early continental rifting?

9.2.1 How is extension accommodated at the initiation of rifting?

The offshore Corinth rift basin has been created by short ∼15 – 25 km en–echelon fault segments. Basin geometry currently, and in the past is composed of segmented depocentres with their along axis length controlled by one, or more border faults. Segmentation of rift zones along axis is also observed at

other intra–continental rifts, for example the East African rift (Rosendahl 1987, Ebinger 1989, Hayward & Ebinger 1996) and Gulf of Suez (Gupta et al. 1999, Gawthorpe et al. 2003). In the Corinth rift the segmentation is probably related to fault mechanics controlling the positions of fault nucleation and propagation. A similar mechanism is proposed for segmentation of the western branch of the East African rift (Ebinger 1989).

Generally, there was more variability in fault dip direction in the past, with pre 0.4 Ma stratigraphic architecture controlled strongly by both N–dipping (i.e. Xylokastro fault) and S–dipping faults (i.e. East Channel fault). Since ca. 0.4 Ma, dip directions on major basin bounding faults are now almost exclusively N–dipping, except in the western rift. This evolution toward strong rift asymmetry may be the result of oppositely dipping faults crossing at depth and a single orientation emerging as dominant (Jackson & McKenzie 1983, Jackson 1999). Throughout the Corinth rift's history a single fault dip direction has dominated the structure of most areas at any one time forming half graben structural elements, rather than symmetric graben.

The Corinth rift onshore geology provides evidence that faulting initially was distributed over a wider across rift axis area than the presently active rift. Faulting occurred simultaneously on a number of faults, and later focused on single rift bordering faults (Collier & Jones 2003). This is a common feature of the first period of continental extension, and multi–phase evolution is reported from a number of rifts, for example: the Gediz graben of Western Turkey (Dart et al. 1995); and at a larger scale from the West Antarctic rift system (Huerta & Harry 2007). This deformation scheme differs from that experienced at areas like the Basin and Range province where distributed faulting continues (Huerta & Harry 2007).

9.2.2 How do rifts evolve prior to breakup?

The pre 0.4 Ma ∼20 – 50 km scale segmentation of unit B deposits distributed into two depocentres, later evolves into a larger scale ∼80 km long depocentre due to fault interaction and the coalescence of older segments. Extension focuses in the area between the two older unit B depocentres probably due to stress concentration at crack tips. These two depocentres merge creating a single connected depocentre (Chapter 6, Fig. 6.10). Similar segmentation evolution is observed in the East African rift (Ebinger 1989) and this style of depocentre evolution can be reproduced by numerical fault interaction models (Cowie et al. 2000). Although depocentre development has been complex within the rift, there is no evidence that the initiation of faulting propagated along the rift, either in a west to east or east to west direction. The ages of active faults in the

western rift and Alkyonides basin are both in the range ca. 1 – 2 Ma, suggesting a simultaneous initiation with no need to employ propagation.

Geodetic extension rates are highest in the western rift, even though the central rift has experienced greatest unit A deposition and has the deepest basement. This suggests that strain has migrated to the west from the central area, into the area between the more deeply subsided Gulf of Corinth and Gulf of Patra. A shift in strain focusing to this particular area between two subsided basins is analogous to the interpretation of enhanced slip on the Likoporia and Derveni faults ca. 0.4 Ma, between the two subsided unit B depocentres. Such strain migration may be a characteristic feature of rift development.

This study has shown that previous structural models for the Corinth rift that assumed simple consistent half graben geometry along strike controlled by only N–dipping faults, are a gross over–simplification. In reality, the Corinth rift shows similar levels of structural and temporal variation as reported from other young rift zones worldwide.

9.3 Future work

9.3.1 Chronostratigraphic record of offshore sediments

Much of the quantitative work presented in this study, including the calculation of offshore fault slip rates, and the viscoelastic study, relies on the correct correlation of lacustrine–marine alternating stratigraphy with eustatic sea level fluctuations. Although the correlation of lowstand deltas with eustatic sea level is a widely used, and accepted method, at present there is no way to confirm its accuracy in the Corinth rift and there are still some uncertainties in the depth of the Rion sill over time. Proposed 100 kyr sediment packages are traceable throughout the Corinth rift from 2D seismic profiles. Therefore, a reliable and robust chronostratigraphic framework for the Corinth rift could be produced with drilling at a selection of sites throughout the rift, to provide material for dating. The availability of core samples in order to date each of the seismically identified units, and perhaps provide paleobathymetric constraints, would have the following implications for future tectonic studies:

(a) Dating of stratigraphy down–or–close to basement would provide age constraints for the initiation of the offshore rift. In this study constant sedimentation rate assumptions have been employed for stratigraphy predating that characterised by correlatable cycles, to estimate the age of the basement contact at 1 – 2 Ma in the east and the west parts of the rift. Cores taken within each depocentre would allow the determination of any higher

resolution age variation between depocentres along axis, and highlight directions of fault and rift propagation.

(b) A more detailed chronostratigraphic framework would allow the reliable interpretation of the 100 kyr packages within unit A across the whole offshore rift. In this study this has been attempted, however the characteristic seismic facies of these sediments observed clearly in the west (Chapter 5) is difficult to trace everywhere (Chapter 6). With some age constraints on horizons from various locations across the rift the interpretation of 100 kyr horizons would be much more reliable. Interpretation of 100 kyr units within unit A provides the possibility to produce isopach surfaces for each of these packages and investigate changes in rift geometry at a much higher resolution that just comparing the structure during unit A and unit B deposition.

(c) More accurate chronology and paleobathymetry approximations may allow slip rates to be calculated on faults that have their hanging walls offshore, without making uplift to subsidence ratio assumptions.

The need for such a chronostratigraphic record has been recognised, and the Corinth rift has been proposed as a future drilling site to the Integrated Ocean Drilling Program (IODP).

9.3.2 Dislocation modelling of the western rift region and south coast terraces

The viscoelastic dislocation modelling technique was introduced in Chapter 8, and is an important tool in determining slip rates from long term deformation for systems influenced by multiple faults. This technique, in the future, could be used to model the uplift of the south coast terraces and investigate the effect of multiple faults in the tectonically complex western rift.

South coast terrace modelling

Along the south coast, flights of uplifted marine terraces have been well described, and the age of terrace platforms are partly known from coral dating, or have been estimated from sea level correlation. The elevation of terraces has been modelled by Armijo et al. (1996) and De Martini et al. (2004) to determine slip rates on the faults responsible for the uplift. However, as discussed in Chapter 8, both of these studies use techniques that employ elastic assumptions for the distribution of long term displacement. It has been shown in Chapter 8 that over the long term (greater than 10 – 100 years) viscoelastic relaxations should be considered. The elastic assumption has led Armijo et al. (1996) and

De Martini et al. (2004) to calculate slip rates that are too high, and overestimate the depth of basement in the rift. The terrace elevations and ages are well constrained and it is possible to model the total slip magnitude required to achieve the uplift of each terrace, allowing for viscoelastic relaxation. Given the reliable age control of some terraces, robust estimates of slip may be derived for terrace levels using this technique.

Western rift multiple faults

In the western rift there are two major tectonic controversies. Firstly, is there a low angle detachment surface beneath the rift, and secondly, if S–dipping faults influence stratigraphy and basement (as has been argued in Chapter 5) why are their hanging walls and footwalls submerged and appear to be subsiding overall? Viscoelastic dislocation modelling could provide answers to these questions.

In the western rift, in the same way as was observed in the Alkyonides Gulf in Chapter 8, corresponding terrace uplift and lowstand delta subsidence of a similar age are recorded. Both of these features record uplift and subsidence from sea level and are effective markers. In the Western rift, however, four parallel faults directly influence the deformation field of these two control points and the situation is more complex than in the Alkyonides Gulf (Fig. 9.1 C). Because there are so many faults that potentially influence the uplift of the terraces and subsidence of the deltas modelling of the slip required on each fault is extremely ambiguous (Fig. 9.1). In order for this method to provide well–constrained slip rates in the western rift more deformation control points are required. In the future it may be possible from paleobathymetric studies of cored samples to estimate the original deposition depth of sediments, from which to calculate vertical displacement.

Alternatively, the basement surface along the profile provides a marker displacement horizon over the total age of the rift, which could be modelled (assuming the basement surface was originally horizontal). This technique has been used to model uplifted topography in the Nankai trough area by Sato & Matsu'ura (1992). Problems with this method occur because of the unknown extent of basement erosion. Significant erosion is likely in the area of the horst block between the South and North Eratini faults, restricting the height of the horst to the 60 – 70 m lake level (Fig. 9.1).

Viscoelastic dislocation modelling could also be used to investigate if a low angle detachment fault could possibly reproduce the observed basement surface (Fig. 9.1 C). The presence of a low angle fault would result in intersection with the West Channel, North and South Eratini faults and the effects of this on the possible basement geometries would perhaps conclusively dispel, or entertain the possibility of a low angle detachment surface.

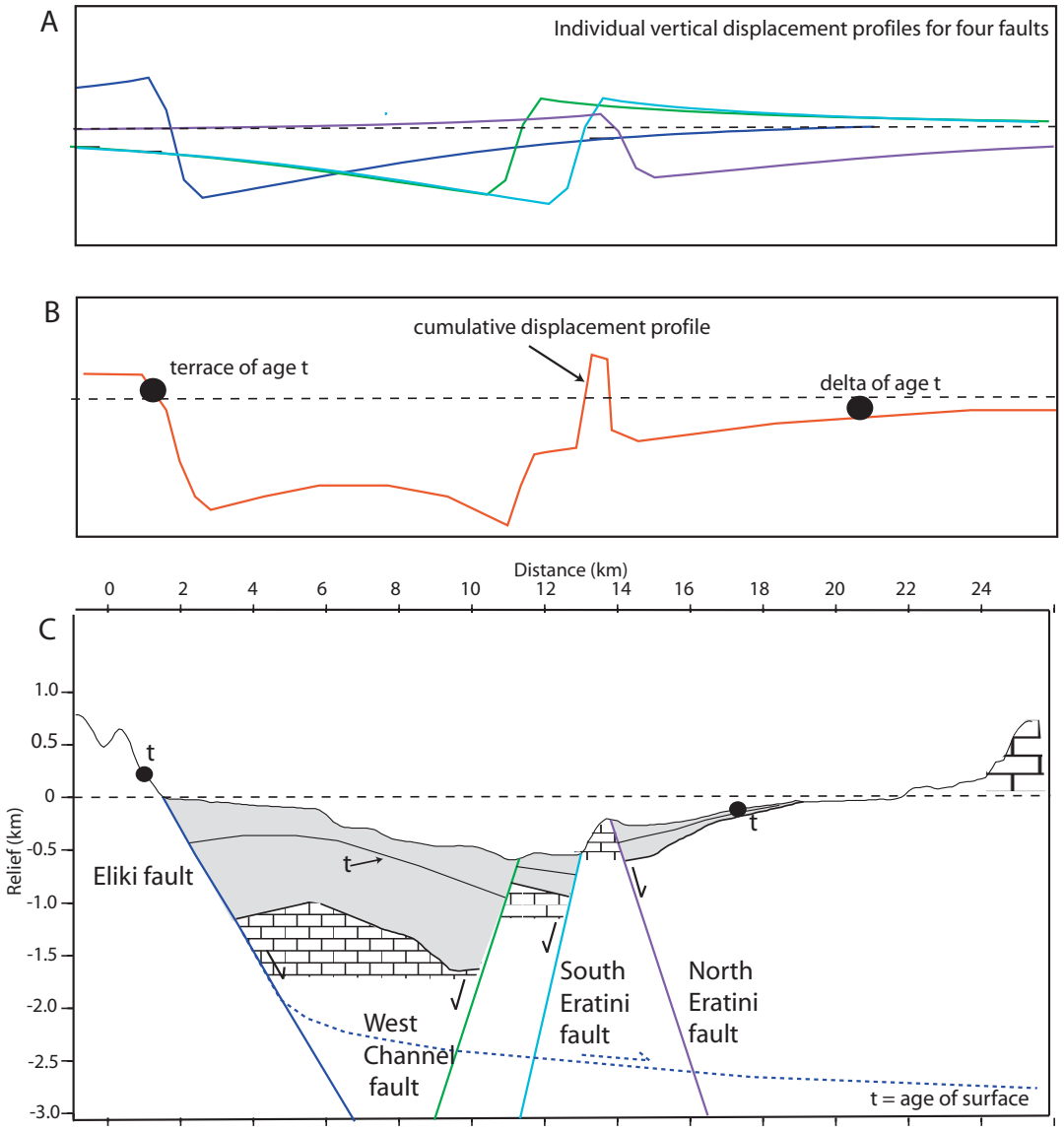

FIGURE 9.1: Cartoon to show the method of investigating multiple fault activity in the western rift. **A.** Vertical displacement profiles are calculated for estimated slip magnitudes for each of the four faults active along the profile. **B.** These fields are superimposed and slip varied to approximate the elevation at the sites of the uplifted terrace and subsided delta **C.** Cross sections of the structure of the area under investigation, showing high angle planar, and low angle detachment fault geometries.

To use this technique to its full effect would require improved chronology and paleobathymetry estimates.

9.3.3 Basin subsidence and strain analysis

The variation in sediment thickness of two distinct seismic packages, units A and B, across the rift has been used in this study to deduce variations in fault activity along the rift axis, pre and post ca. 0.4 Ma. Interpretation of each of the 100 kyr units across the entire rift, would provide at least five other time periods to resolve areas of enhanced, and depleted sediment deposition that may be related to tectonics. With a knowledge of paleobathymetry, as derived from drilling, the basin subsidence history for each of these horizons could potentially be reproduced (if paleobathymetry determination was possible at the scale of a few hundred metres). This technique involves back–stripping away the sediment loading influence, subtracting any paleobathymetry (i.e. the water depth at time of formation) and leaving only the true tectonic subsidence (technique discussed by Bond & Kominz 1984, Stewart & Argent 2000). Each dated horizon is a point on the basin subsidence curve and any slow, or intense periods of subsidence are highlighted by changes in curve gradient. Comparison of basin subsidence curves throughout the Corinth rift will highlight variations in subsidence history, and hence fault activity. This method has been applied to many passive margins (e.g. Bond & Kominz 1984, Leach et al. 1996, Stewart et al. 2000, Cao et al. 2007), however is rarely done for the syn–rift stage of subsidence. This is mainly due to the lack of such high resolution details of the syn–rift stage at older passive margins. If this technique could be carried out reliably at the Corinth rift it would provide a highly detailed, and possibly unique view of syn–rift subsidence patterns during the first ca. 2 Myr of rifting. The lack of sediment chronology to aid confident interpretation, and knowledge of paleobathymetry has prevented the analysis in this study.

The geometry of subsided horizons in the hanging wall of south coast major faults could potentially be used to determine the likely geometry of the faults at depth. The degree of curvature of subsided horizons that were initially horizontal is determined by the level of listricity of the fault plane at depth. Using algorithms, like those developed by White & Yielding (1991) the interpreted sediment stratigraphy could be used to constrain if a low angle detachment is likely beneath the western rift, or (as is suspected in Chapter 5) if it is fundamentally incompatible with the geometry of basin sediments.

9.3.4 Further study into fault activity in the Itea and Antikyra bays

In Chapter 4 evidence for possible localised uplift along the northern margin of the Corinth rift was presented. Potentially uplifted wavecut notches and platforms have been identified along the Milakos and Galaxidi peninsulas that may have been influenced by activity on offshore faults. Only a few sparse seismic reflection lines traverse the Antikyra Bay area, but these have indicated the presence of some actively seafloor displacing faults (Fig. 3.1). A thorough pinger seismic reflection study of this area has been conducted by the University of Patras, however these data were not available in this study. The shallow water Antikyra Bay area would be a potentially interesting area to conduct studies of shallow active faulting. Smaller active faults in this area are likely to show clear footwall and hanging wall stratigraphy, and may be a better place to conduct more classical fault evolution studies than on the large, basin bounding faults to the south of the rift, where only hanging wall stratigraphy is available.

9.3.5 Synthesis and new studies in the western Rion graben

The tectonic interpretation of the Corinth rift as presented in this thesis, did not consider in great detail faulting and basement depth in the area to the west of Aigion due to a lack of available seismic data in this region. This region is known as the Rion graben and is currently the site of intense microseismicity (Doutsos & Poulimenos 1992). This region separates the active Corinth rift from the active Patras rift to the west. The inclusion of tectonic interpretations from this graben, and the Gulf of Patra are the next step in producing a complete rifting evolution scenario for the area. This region is also the site of the large town of Patra and the new Rion Antirrion bridge, and further study is important from a seismic hazard perspective.

Bibliography

Ambraseys, N. & Jackson, J. (1990), 'Seismicity and associated strain of central Greece between 1890 and 1988', *Geophysical Journal International* **101**, 663–708.

Anderson, R., Densmore, A. & Ellis, M. (1999), 'The generation and degradation of marine terraces', *Basin Research* **11**, 7–19.

Andrews, D. J. & Schwerer, E. (2000), 'Probability of rupture of multiple fault segments', *Bulletin of the Seismological Society of America* **90**(6), 1498–1506.

Angelier, J. (1978), 'Tectonic evolution of the Hellenic Arc since the late Miocene', *Tectonophysics* **49**, 23–36.

Aragon-Arreola, M. & Martin-Barajas, A. (2005b), Rift–to–drift transitions in the Northern Gulf of California, *in* 'Salt Lake City Annual Meeting', Salt Lake City.

Aragon-Arreola, M., Morandi, M., Martin-Barajas, A., Delgado-Argote, L. & Gonzalez-Fernandez, A. (2005a), 'Structure of the rift basins in the central Gulf of Califronia: Kinematic implications for oblique rifting', *Tectonophysics* **409**, 19–38.

Armijo, R., Meyer, B., King, G., Rigo, A. & Papanastassiou, D. (1996), 'Quaternary evolution of the Corinth Rift and its implications for the Late Cenozoic evolution of the Aegean', *Geophysical Journal International* **126**, 11–53.

Avallone, A., Briole, P., Agatza-Balodimou, A. M., Billiris, H., Charade, O., Mitsakaki, C., Nercessian, A., Papazissi, K., Paradissis, D. & Veis, G. (2004), 'Analysis of eleven years of deformation measured by GPS in the Corinth Rift laboratory area', *Comptes Rendus Geosciences* **336**(4-5), 301–311.

Bassi, G. (1995), 'Relative importance of strain rate and rheology for the mode of continental extension', *Geophysical Journal International* **122**, 195–210.

Behn, M. & Lin, J. (2000), 'Segmentation in gravity and magnetic anomalies along the U.S. East Coast passive margin: Implications for incipient structure of the oceanic lithosphere', *Journal of Geophysical Research* **105**(B11), 25769–25790.

Behn, M., Lin, J. & Zuber, M. (2002), 'A continuum mechanics model for normal faulting using a strain–rate softening rheology: implications for thermal and rheological controls on continental and oceanic rifting', *Earth and Planetary Science Letters* **202**, 725–740.

Bell, R., McNeill, L., Bull, J. & Henstock, T. (2008), 'Evolution of the offshore western Gulf of Corinth', *Geological Society of America Bulletin* **120**, 156–178.

Benedetti, L., Finkel, R., Armijo, R., Papanastassiou, D., Ryerson, F. & Flerit, F. (2003), 'Motion on the Kaparelli fault (Greece) prior to the 1981 earthquake sequence determined from ^{36}Cl cosmogenic dating', *Terra Nova* **15**, 118–124.

Bernard, P., Briole, P., Meyer, B., Lyon-Caen, H., Gomez, J. M., Tiberi, C., Berge, C., Cattin, R., Hatzfeld, D., Lachet, C., Lebrun, B., Deschamps, A., Courboulex, F., Larroque, C., Rigo, A., Masonnet, D., Papadimitriou, P., Kassaras, I., Diagourtas, D., Makropoulos, K., Veis, G., Papazissi, K., Mitsakaki, C., Karakostas, V., Papadimitriou, E., Papanastassiou, D., Chouliaras, M. & Savrakakis, G. (1997), 'The Ms = 6.2, June 15, 1995 Aigion earthquake (Greece): evidence for low angle normal faulting in the Corinth rift', *Journal of Seismology* **1**, 131–150.

Bertotti, G., Podladchikov, Y. & Daehler, A. (2000), 'Dynamic link between the level of ductile crustal flow and style of normal faulting of brittle crust', *Tectonophysics* **320**, 195–218.

Bond, G. & Kominz, M. (1984), 'Construction of tectonic subsidence curves for the early Paleozoic miogeocline, southern Canadian Rocky Mountains: Implications for subsidence mechanisms, age of breakup and crustal thinning', *Geological Society of America Bulletin* **95**, 155–173.

Bosworth, W., Huchon, P. & McClay, K. (2005), 'The Red Sea and Gulf of Aden Basins', *Journal of African Earth Sciences* **43**(1-3), 334–378.

Bozkurt, E. & Sozbilir, H. (2004), 'Tectonic evolution of the Gediz Graben: field evidence for an episodic, two-stage extension in western Turkey', *Geological Magazine* **141**(1), 63–79.

Brace, W. & Kohlstedt, D. (1980), 'Limits on lithostatic stress imposed by laboratory experiments', *Journal of Geophysical Research* **85**, 6248–6252.

Braun, J. & Beaumont, C. (1989), 'A physical explanation of the relation between flank uplifts and the breakup unconformity at rifted continental margins', *Geology* **17**, 760–764.

Briole, P., Rigo, A., Lyon-Caen, H., Ruegg, J., Papazissi, K., Mitsakaki, C., Balodimou, A., Vieis, G., Hatzfeld, D. & Deschamps, A. (2000), 'Active deformation of the Corinth rift, Greece: results from repeated Global Positioning System surveys between 1990 and 1995', *Journal of Geophysical Research* **105**(B11), 25,605–25,625.

Brooks, M. & Ferentinos, G. (1984), 'Tectonics and sedimentation in the Gulf of Corinth and the Zakynthos and Kefallina channels, western Greece', *Tectonophysics* **101**, 25–54.

Brown, L. & Fisher, W. (1980), 'Seismic stratigraphic interpretation and petroleum potential', *American Association of Petroleum Geologists* **Course Notes Series 16**.

Buck, W. R. (1991), 'Modes of continental lithospheric extension', *Journal of Geophysical Research* **96**, 161–120.

Buck, W. R., Lavier, L. & Poliakov, A. (1999), 'How to make a rift wide', *Philosophical Transactions of the Royal Society of London* **357**, 671–693.

Burbank, D. W. & Anderson, R. S. (2001), *Tectonic Geomorphology*, Blackwell Science, Ltd.

Cao, D., Wang, X., Zhan, W. & Li, W. (2007), 'Subsidence history of the Eastern depression in the North Yellow Sea Basin', *Journal of China University of Mining and Technology* **17**(1), 90–95.

Cartwright, J., Trudgill, B. D. & Mansfield, C. S. (1995), 'Fault growth by segment linkage: and explanation for scatter in maximum displacement and trace length data from Canyonlands grabens of SE Utah', *Journal of Structural Geology* **17**, 1319–1326.

Casten, U. & Snopek, K. (2006), 'Gravity modelling of the Hellenic subduction zone – a regional study', *Tectonophysics* **417**(3-4), 183–200.

Cattin, R., Briole, P., Lyon-Caen, H., Bernard, P. & Pinettes, P. (1999), 'Effects of superficial layers on coseismic displacements for a dip–slip fault and geophysical implications', *Geophysical Journal International* **137**, 147–158.

Causse, C., Moretti, I., Eschard, R., Micarelli, L., Ghaleb, B. & Frank, N. (2004), 'Kinematics of the Corinth Gulf inferred from calcite dating and syntectonic sedimentary characteristics', *Comptus Rendus Geoscience* **336**, 281–290.

Charalampakis, M., Stefatos, A., Hasiotis, T. & Ferentinos, G. (2007), 'Submarine mass movements on an active fault system in the central Gulf of Corinth', *Advances in Natural and Technological Hazards Research* **27**, 67–75.

Chen, W. & Molnar, P. (1983), 'Focal depths of intra-continental and intraplate earthquakes and their implications for the thermal and mechanical properties of the lithosphere', *Journal of Geophysical Research* **88**, 4183–4214.

Chery, J. (2001), 'Core complex mechanics: From the Gulf of Corinth to the Snake Range', *Geology* **29**, 439–442.

Chronis, G., Piper, D. & Anagnostou, C. (1991), 'Late Quaternary evolution of the Gulf of Patras, Greece: Tectonism, deltaic sedimentation and sea level change', *Marine Geology* **97**, 191–209.

Clarke, P., Davies, R., England, P., Parsons, B., Billiris, H., Paradissis, D., Veis, G., Cross, P., Denys, P., Ashkenazi, V., Bingley, R., Kahle, H., Muller, M. & Briole, P. (1998), 'Crustal strain in central Greece from repeated GPS measurements in the interval 1989–1997', *Geophysical Journal International* **135**, 195–214.

Clement, C. (2000), Imagerie simique crustale de la subduction hellennique et du Golfe de Corinthe., These de doctorat, Institut de Physique du Globe.

Clement, C., Sachpazi, M., Charvis, P., Graindorge, D., Laigle, M., Hirn, A. & Zafiropoulos, G. (2004), 'Reflection–refraction seismics in the Gulf of Corinth: hints at deep structure and control of the deep marine basin', *Tectonophysics* **391**, 85–95.

Coleman, M. & Hodges, K. (1995), 'Evidence for Tibetan plateau uplift before 14 Myr ago from a new minimum age for east–west extension', *Nature* **374**(6517), 49–52.

Collier, R. & Dart, C. (1991), 'Neogene to Quaternary rifting, sedimentation and uplift in the Corinth basin, Greece', *Journal of the Geological Society of London* **148**(6), 1049–1065.

Collier, R. & Jones, G. (2003), 'Rift sequences of the Southern Margin of the Gulf of Corinth (Greece) as exploration / production analogues', *AAPG International Conference Barcelona, Search and Discovery Article 90017* .

Collier, R., Leeder, M., Rowe, P. & Atkinson, T. (1992), 'Rates of tectonic uplift in the Corinth and Megara basins, central Greece', *Tectonics* **11**, 1159–1167.

Collier, R., Leeder, M., Trout, M., Ferentinos, G., Lyberis, E. & Papatheodorou, G. (2000), 'High sediment yields and cool, wet winters: test of last glacial paleoclimates in the northern Mediterranean', *Geology* **28**(11), 999–1002.

Collier, R., Pantosti, D., D'Addezio, G., De Martini, P., Masana, E. & Sakellariou, D. (1998), 'Paleoseismicity of the 1981 Corinth earthquake fault: Seismic contribution to extensional strain in central Greece and implications for seismic hazard', *Journal of Geophysical Research* **103**, 30001 – 30019.

Collier, R. & Thompson, J. (1991), 'Transverse and linear dunes in an upper Pleistocene marine sequence, Corinth Basin, Greece', *Sedimentology* **38(6)**, 1021–1040.

Corti, G., Bonini, M., Conticelli, S., Innocenti, F., Manetti, P. & Sokoutis, D. (2003), 'Analogue modelling of continental extension: a review focused on the relations between the patterns of deformation and the presence of magma', *Earth Sciences Reviews* **63**(3), 169–247.

Cotterill, C. (2006), A high resolution Holocene fault activity history of the Aigion shelf, Gulf of Corinth, Greece, Phd thesis, University of Southampton.

Cowie, P., Gupta, S. & Dawers, N. (2000), 'Implications of fault array evolution for synrift depocentre development: insights from a numerical fault growth model', *Basin Research* **12**, 241–261.

Dart, C., Cohen, H., Akyuz, S. & Barka, A. (1995), 'Basinward migration of rift–border faults: implications for facies distributions and preservation potential', *Geology* **23**, 69–72.

Dart, C., Collier, R., Gawthorpe, R., Keller, J. & Nichols, G. (1994), 'Sequence stratigraphy of (?) Pliocene–Quaternary syn–rift, Gilbert–type fan deltas, northern Peloponnesos, Greece', *Marine and Petroleum Geology* **11**, 545.

Davies, R., England, P., Parsons, B., Billiris, H., Paradissis, D. & Veis, G. (1997), 'Geodetic strain of Greece in the interval 1892–1992', *Journal of Geophysical Research* **135**(B11), 24,571–24,588.

Davies, S. J., Dawers, N., McLeod, A. & Underhill, J. (2000), 'The structural and sedimentological evolution of early synrift successions: the Middle Jurassic Tarbet formation, North Sea', *Basin Research* **12**, 343–365.

Davis, M. & Kusznir, N. J. (2004), Depth-dependent lithospheric stretching at rifted continental margins, *in* G. Karner, ed., 'Rheology and deformation of the lithosphere at continental margins', Columbia University Press.

Dawers, N. H. & Underhill, J. R. (2000), 'The role of fault interaction and linkage in controlling synrift stratigraphic sequences: Late Jurassic, Statfjord East area, Northern North Sea', *AAPG Bulletin* **84**(1), 45–64.

De Martini, P., Pantosti, D., Palyvos, N., Lemeille, F., McNeill, L. & Collier, R. (2004), 'Slip rates of the Aigion and Eliki faults from uplifted marine terraces, Corinth Gulf, Greece', *Comptes Rendus Geoscience* **336**, 325–334.

Deng, J., Gurnis, M., Kanamori, H. & Hauksson, E. (1998), 'Viscoelastic flow in the lower crust after the 1992 Landers, California, earthquake', *Science* **282**, 1689–1692.

Dewey, J. (1988), 'Extensional collapse of orogens', *Tectonics* **7**, 1123–1139.

Dewey, J. & Sengor, A. M. C. (1979), 'Aegean and surrounding regions: Complex multiplate and continuum tectonics in a convergent zone', *Geological Society of America Bulletin* **90**, 84–92.

Dia, A., Cohen, H., O'Nions, R. & Jackson, J. (1997), 'Rates of uplift investigated through ^{230}Th dating in the Gulf of Corinth (Greece)', *Chemical Geology* **138**, 171–184.

Dou, L. & Chang, L. (2003), 'Fault linkage patterns and their control on the formation of the petroleum systems of the Erlian Basin, Eastern China', *Marine and Petroleum Geology* **20**, 1213–1224.

Doutsos, T., Kontopoulos, N. & Populimenos, G. (1988), 'The Corinth–Patras rift as the initial stage of the continental fragmentation behind an active island arc (Greece).', *Basin Research* **1**, 177–190.

Doutsos, T. & Piper, D. (1990), 'Listric faulting, sedimentation, and morphological evolution of the Quaternary eastern Corinth rift, Greece; first stages of continental rifting', *Geological Society of America Bulletin* **102 (6)**, 812–829.

Doutsos, T. & Poulimenos, G. (1992), 'Geometry and kinematics of active faults and their seismotectonic significance in the western Corinth–Patras rift (Greece)', *Journal of Structural Geology* **14**(6), 689–699.

Dunbar, J. & Sawyer, D. (1987), 'Implications of continental crust extension for plate reconstruction: An example from the Gulf of Mexico', *Tectonics* **6**(6), 739–755.

Dunbar, J. & Sawyer, D. (1989a), 'How preexisting weaknesses control the style of continental breakup', *Journal of Geophysical Research* **94**(7278-7292).

Dunbar, J. & Sawyer, D. (1989b), 'Patterns of continental margins of the central and north Atlantic oceans and Labrador Sea', *Tectonics* **8**, 1059–1077.

Ebinger, C. (1989), 'Tectonic development of the western branch of the East African rift system', *Geological Society of America Bulletin* **101**, 885–903.

El-Menif, N. T., Jaafar Kefi, F., Ramdani, M., Flower, R. & Boumaiza, M. (2007), 'Habitat and associated fauna of Lithophaga lithophaga in the Bay of Bizerta (Tunisia)', *Journal of Shellfish Research* **26**(2), 569–574.

Eliott, T. (1978), Deltas, *in* H. Reading, ed., 'Sedimentary environments and facies', Blackwell Scientific publications, Oxford, pp. 97–142.

England, P. (1983), 'Constraints on extension of continental lithosphere', *Journal of Geophysical Research* **88**, 1145–1152.

Exadaktylos, G., Vardoulakis, I., Stavropoulou, M. & Tsombos, P. (2003), 'Analogue and numerical modeling of normal fault patterns produced due to slip along a detachment zone', *Tectonophysics* **376**, 117–134.

Ferentinos, G., Papatheodorou.G. & Collins, M. (1988), 'Sediment transport processes on an active submarine fault escarpment: Gulf of Corinth Greece.', *Marine Geology* **83**, 43–61.

Flemming, N. (1978), 'Holocene eustatic changes and coastal tectonics in the north-east Mediterranean: implications for models of crustal consumption', *Philosophical Transactions of the Royal Society of London* **289**, 406–458.

Flotte, N., Plagnes, V., Sorel, D. & Benedicto, A. (2001), 'Attempt to date Pleistocene normal faults of the Corinth–Patras rift (Greece) by U/Th method, and tectonic implications', *Geophysical Research Letters* **28**, 3769–3772.

Ford, M., Williams, E. & Malartre, F. (2007), Stratigraphic architecture, sedimentology and structure of the Vouraikos Gilbert–type delta, Gulf of Corinth, Greece, *in* G. Nichols, E. Williams & C. Paola, eds, 'Special Publication of the International Association of Sedimentologists'.

Forsyth, D. (1992), 'Finite extension and low–angle normal faulting', *Geology* **20**, 27–30.

Fukahata, Y. & Matsu'ura, M. (2005), 'General expressions for internal deformation fields due to a dislocation source in a multi–layered elastic half–space', *Geophysical Journal International* **161**, 507–521.

Fukahata, Y. & Matsu'ura, M. (2006), 'Quasi–static internal deformation due to a dislocation source in a multi–layered elastic/viscoelastic half–space', *Geophysical Journal International* **166**, 418–434.

Fukahata, Y., Nishitani, A. & Mats'ura, M. (2004), 'Geodetic data inversion using ABIC to estimate slip history during one earthquake cycle with viscoelastic slip–response functions', *Geophysical Journal International* **156**, 140–153.

Funning, G., Parsons, B. & Wright, T. (2007), 'Fault slip in the 1997 Manyi, Tibet earthquake from linear elastic modelling of InSAR displacements', *Geophysical Journal International* **169**, 988–1008.

Gautier, S., Latorre, D., Virieux, J., Deschamps, A., Skarpelos, C., Sotiriou, A., Serpetsidaki, A. & Tselentis, A. (2006), 'A new passive tomography of the Aigion area (Gulf of Corinth Greece) from the 2002 data set', *Pure and Applied Geophysics* **163**(2-3), 431–453.

Gawthorpe, R. & Hardy, S. (2002), 'Extensional fault–propagation folding and base–level change as controls on growth–strata geometries', *Sedimentary Geology* **146**(1-2), 47–56.

Gawthorpe, R. L., Fraser, A. J. & Collier, R. E. (1994), 'Sequence stratigraphy in active extensional basins: implications for the interpretations of ancient basin–fills', *Marine and Petroleum Geology* **11**, 642–658.

Gawthorpe, R. L., Jackson, C., Young, M., Sharp, I., Moustafa, A. & Leppard, C. (2003), 'Normal fault growth, displacement localisation and the evolution of normal fault populations: the Hammam Faraun fault block, Suez rift, Egypt', *Journal of Structural Geology* **25**, 883–895.

Ghisetti, F. & Vezzani, L. (2004), 'Plio–Pleistocene sedimentation and fault segmentation in the Gulf of Corinth (Greece) controlled by inherited structural fabric', *Comptes Rendus Geoscience* **336**, 243–249.

Gibbs, A. (1984), 'Structural evolution of extensional basin margins', *Journal of the Geological Society* **141**, 609–620.

Glew, J. R. & Ford, D. C. (1980), 'A simulation study of the development of rillenkaren', *Earth Surface processes* **5**, 25–36.

Goldsworthy, M. & Jackson, J. (2001), 'Migration of activity within normal fault system: examples from the Quaternary of mainland Greece', *Journal of Structural Geology* **23**, 489–506.

Goodliffe, A. M. & Taylor, B. (2007), 'The boundary between continental rifting and seafloor spreading in the Woodlark Basin, Papua New Guinea', *Geological Society, London, Special Publications* **282**(1), 217–238.

Goodliffe, A., Weiss, J., Taylor, B., Sachpazi, M., Hirn, A., Stefatos, A. & Laigle, M. (2003), 'Variations in the distribution and control of syn–rift deformation in the Gulf of Corinth, Greece (poster)', *Geophysical Research Abstracts* **5**, EAE03–A–04697;.

Gupta, S., Cowie, P. A., Dawers, N. H. & Underhill, J. R. (1998), 'A mechanism to explain rift–basin subsidence and stratigraphic patterns through fault–array evolution', *Geology* **26**(7), 595–598.

Gupta, S., Underhill, J., Sharp, I. & Gawthorpe, R. L. (1999), 'Role of fault interactions in controlling synrift sediment dispersal patterns: Miocene, Abu Alaqa group, Suez Rift, Sinai, Egypt', *Basin Research* **11**, 167–189.

Hamilton, E. (1979), 'Sound velocity gradients in marine sediments', *Journal of the Acoustical Society of America* **65**(4), 909–922.

Hamilton, E. (1980), 'Geoacoustic modeling of the sea floor', *Journal of the Acoustical Society of America* **68**(5), 1313–1340.

Hamilton, W. (1987), *Continental Extensional Tectonics*, Vol. 28, Geological Society, London.

Hasiotis, T., Charalambakis, M., Stefatos, A., Papatheoderou, G. & Ferentinos, G. (2006), 'Fan delta development and processes offshore a seasonal river in a seismically active region, NW Gulf of Corinth', *Geo-Marine Letters* **26**, 199–211.

Hatzfeld, D., Karakostas, V., Ziazia, M., Kassaras, I., Papadimitriou, E., Makropoulos, K., Voulgaris, N. & Papaioannou (2000), 'Microseismicity and faulting geometry in the Gulf of Corinth(Greece)', *Geophysical Journal International* **141**(2), 438.

Hatzfeld, D., Kementzetzidou, D., Karakostas, V., Ziazia, M., Nothard, S., Diagourtas, D., Deschamps, A., Karakaisis, G., Papadimitriou, P., Scordilis, M., Smith, R., Voulgaris, N., Kiratzi, S., Makropoulos, K., Bouin, M. P. & Bernard, P. (1996), 'The Galaxidi earthquake of 18 November 1992: A possible asperity within the normal fault system of the Gulf of Corinth (Greece)', *Bulletin of the Seismological Society of America* **86**, 1987–1991.

Hayward, N. & Ebinger, C. (1996), 'Variation in along–axis segmentation of the Afar rift system', *Tectonics* **15**, 244–257.

Heezen, B., Ewing, M. & Leonard Johnson, G. (1966), 'The Gulf of Corinth floor', *Deep Sea Research* **13**, 381–411.

Hellinger, S. J., Sclater, J. G. & Giltner, J. (1988), 'Mid-Jurassic through mid-Cretaceous extension in the Central Graben of the North Sea - part 1: estimates from subsidence', *Basin Research* **1**(4), 191–200.

Higgs, B. (1988), 'Syn–sedimentary structural controls on basin deformation in the Gulf of Corinth, Greece', *Basin Research* **1**, 155–165.

Houghton, S., Roberts, G., Papanikolaou, D. & McArthur, J. (2003), 'New ^{234}U-^{230}Th coral dates from the western Gulf of Corinth: Implications for extensional tectonics', *Geophysical Research Letters* **30**.

Hubert, A., King, G., Armijo, R., Meyer, B. & Papanastasiou, D. (1996), 'Fault re–activation, stress interaction and rupture propagation of the 1981 Corinth earthquake sequence', *Earth and Planetary Science Letters* **142**(3-4), 573–585.

Huerta, A. D. & Harry, D. L. (2007), 'The transition from diffuse to focused extension: Modeled evolution of the West Antarctic Rift system', *Earth and Planetary Science Letters* **255**(1-2), 133–147.

Huismans, R., Podladchikov, Y. & Cloetingh, S. (2001), 'Transition from passive to active rifting: Relative importance of asthenospheric doming and passive extension of the lithosphere', *Journal of Geophysical Research* **106**(B6), 11,271–11,291.

Imbrie, J., Hays, J. D., Martinson, D. G., McIntyre, A., Mix, A. C., Morley, J. J., Pisias, N. G., Prell, W. L. & Shackleton, N. J. (1984), The orbital theory of Pleistocene climate : support from a revised chronology of the marine δ^{18} O record, *in* A. Berger, J. Imbrie, J. Hays, G. Kukla & B. Saltzman, eds, 'Milankovitch and Climate: Understanding the Response to Astronomical Forcing', pp. 269–+.

Jackson, J. (1999), 'Fault death: a perspective from actively deforming regions', *Journal of Structural Geology* **21**, 1003–1010.

Jackson, J. (2002), 'Strength of the continental lithosphere: Time to abandon the jelly sandwich?', *GSA Today* **12**(9), 4–10.

Jackson, J., Gagnepain, J., Houseman, G., King, G., Papadimitriou, P., Soufleris, C. & Virieux, J. (1982), 'Seismicity, normal faulting and the geomorphological development of the Gulf of Corinth (Greece): the Corinth earthquakes of February and March 1981', *Earth and Planetary Science Letters* **57**, 377–397.

Jackson, J. & McKenzie, D. (1983), 'The geometrical evolution of normal fault systems', *Journal of Structural Geology* **5**, 471–482.

Jackson, J. & White, N, J. (1989), 'Normal faulting in the upper continental crust: observations from regions of active extension', *Journal of Structural Geology* **11**, 15–36.

Jarvis, G. & McKenzie, D. (1980), 'Sedimentary basin formation formation with finite extension rates', *Earth and Planetary Science Letters* **48**, 42–52.

Jolivet, L. (2001), 'A comparison of geodetic and finite strain pattern in the Aegean, geodynamic implications', *Earth and Planetary Science Letters* **187**, 95–104.

Karner, G., Byamungu, B. R., Ebinger, C., Kampunzu, A. B., Mukasa, R., Nyakaana, J., Rubondo, E. T. & Upcott, N. M. (2000), 'Distribution of crustal extension and regional basin architecture of the Albertine rift system, East Africa', *Marine and Petroleum Geology* **17**, 1131–1150.

Kerauden, B. & Sorel, D. (1987), 'The terraces of Corinth (Greece)-A detailed record of eustatic sea–level variations during the last 500,000 years.', *Marine Geology* **77**, 99–107.

Kershaw, S. & Guo, L. (2001), 'Marine notches in coastal cliffs: indicators of relative sea–level change, Perachora Peninsula, central Greece.', *Marine Biology* **179**, 213–228.

King, G., Ouyang, Z., Papadimitriou, P., Deschamps, A., Gagnepain, J., Houseman, G., Jackson, J., Soufleris, C. & Virieux, J. (1985), 'The evolution of the Gulf of Corinth (Greece): an aftershock study of the 1981 earthquakes', *Geophysical Journal of the Royal Astronomical Society* **80**, 677–693.

King, G., Stein, R. & Rundle, J. (1988), 'The growth of geological structures by repeated earthquakes', *Journal of Geophysical Research* **93**, 13307–13318.

King, T. A. (1988a), Mechanisms of isostatic compensation in areas of lithospheric extension, Phd thesis, University of Leeds.

Kocyidit, A. L. Y., Yusufodlu, H. & Bozkurt, E. (1999), 'Evidence from the Gediz graben for episodic two–stage extension in western Turkey', *Journal of the Geological Society* **156**(3), 605–616.

Kokkalas, S., Pavlides, S., Koukouvelas, I., Ganas, A. & Stamatopulos, L. (2007), 'Paleoseismicity of the Kaparelli fault (eastern Corinth Gulf): Evidence for earthquake recurrence and fault behaviour', *Bollettino della Societa Geologica Italiana* **126**(2), 387–395.

Kostrov, B. (1974), 'Seismic moment and energy of earthquakes, and seismic flow of rock,', *Izv. Acad. Sci. USSR Phys. Solid Earth* **97**, 23–44.

Koukouvelas, I. K., Stamatopoulos, L., Katsonopoulou, D. & Pavlides, S. (2001), 'A palaeoseismological and geoarchaeological investigation of the Eliki fault, Gulf of Corinth, Greece', *Journal of Structural Geology* **23**(2-3), 531–543.

Kruse, S., McNutt, M., Phipps-Morgan, J. & Royden, L. (1991), 'Lithospheric extension near Lake Mead, Nevada: a model for ductile flow in the lower crust', *Journal of Geophysical Research* **96**(B3), 4435–4456.

Kusznir, N. J., Marsden, G. & Egan, S. S. (1991), 'A flexural–cantilever simple–shear/pure–shear model of continental lithosphere extension: applications to the Jeanne d'Arc Basin, Grand Banks and Viking Graben, North Sea', *Geological Society, London, Special Publications* **56**(1), 41–60.

Kusznir, N. J. & Park, R. (1987), 'The extensional strength of the continental lithosphere: its dependence on geothermal gradient and crustal composition and thickness', *Geological Society Special Publication* **28**, 35–52.

Lamarche, G., Barnes, P. & Bull, J. (2006), 'Faulting and extension rate over the last 20,000 years in the offshore Whakatane Graben, New Zealand continental shelf', *Tectonics* **25**.

Le Pichon, X. & Angelier, J. (1979), 'The Hellenic arc and trench system: a key to the neotectonic evolution of the eastern Mediterranean area', *Tectonophysics* **60**, 1–42.

Le Pichon, X. & Angelier, J. (1981), 'The Aegean sea', *Philosophical Transactions of the Royal Society of London* **300**(1454), 357–372.

Le Pichon, X., Chamot-Rooke, N. & Lallemant, S. (1995), 'Geodetic determination of the kinematics of central Greece with respect to Europe: Implications for eastern Mediterranean tectonics', *Journal of Geophysical Research* **100**(B7), 12675–12690.

Le Pourhiet, L., Burov, E. & Moretti, I. (2003), 'Initial crustal thickness variations control the extension in a back arc domain : the case of the Gulf of Corinth', *Tectonics* **22**(4), 1032–1041.

Leach, P., J.M., D., Lepercq, J.-Y. & Gaulirt, J. M. (1996), 'Two–stage rifting in the North Viking Graben area (North Sea): inferences from a new three–dimensional subsidence analysis', *Marine and Petroleum Geology* **13**(2), 129–148.

Leeder, M., Mack, G., Brasier, A., Parrish, R., McIntosh, W., Andrews, J. & Duermeijer, C. (submitted), 'Late-Pliocene timing of Corinth (Greece) rift-margin fault migration', *Geology* .

Leeder, M., McNeill, L., Collier, R., Portman, C., Rowe, P., Andrews, J. & Gawthorpe, R. L. (2003), 'Corinth rift–margin uplift: new evidence from late Quaternary marine shorelines', *Geophysical Research Letters* **30**(12), 1611.

Leeder, M., Portman, C., Andrews, J., Collier, R., Finch, E., Gawthorpe, R., McNeill, L., Perez-Arlucea, M. & Rowe, P. (2005), 'Normal faulting and crustal deformation, Alkyonides Gulf and Perachora peninsula, eastern Gulf of Corinth rift, Greece', *Journal of the Geological Society* **162**(3), 549–561.

Leeder, M. R., Collier, R., Abdul Aziz, L., Trout, M., Ferentinos, G., Papatheodorou, G. & Lyberis, E. (2002), 'Tectono-sedimentary processes along an active marine/lacustrine half-graben margin: Alkyonides Gulf, E. Gulf of Corinth, Greece.', *Basin Research* **14**, 25–42.

Leeder, M., Seger, M. & Stark, C. (1991), 'Sedimentation and tectonic geomorphology adjacent to major active and inactive normal faults, southern Greece', *Journal of the Geological Society, London* **148**, 331–343.

Little, T. A., Baldwin, S., Fitzgerald, P. & Monteleone, B. (2007), 'Continental rifting and metamorphic core complex formation ahead of the Woodlark spreading ridge, D'Entrecasteaux Islands, Papua New Guinea', *Tectonics* **26**.

Liu, M. & Yang, Y. (2003), 'Extensional collapse of the Tibetan Plateau: Results of three–dimensional finite element modeling', *Journal of Geophysical Research* **108**(B8).

Lizarralde, D., Axen, G. J., Brown, H. E., Fletcher, J. M., Gonzalez-Fernandez, A., Harding, A. J., Holbrook, W. S., Kent, G. M., Paramo, P., Sutherland, F. & Umhoefer, P. J. (2007), 'Variation in styles of rifting in the Gulf of California', *Nature* **448**(7152), 466–469.

Lykousis, V., Sakellariou, D., Moretti, I. & Kaberi, H. (2007), 'Late Quaternary basin evolution of the Gulf of Corinth: Sequence stratigraphy, sedimentation, fault-slip and subsidence rates', *Tectonophysics* **440**, 29–51.

Maggi, A., Jackson, J., McKenzie, D. & Priestly, K. (2000), 'Earthquake focal depths, effective elastic thickness, and the strength of the continental lithosphere', *Geology* **28**, 495–498.

Malartre, F., Ford, M. & Williams, E. (2004), 'Preliminary biostratigraphy and 3D geometry of the Vouraikos Gilbert–type fan delta, Gulf of Corinth, Greece', *Comptes Rendus Geoscience* **336**, 269–280.

Mats, V. D. (1993), 'The structure and development of the Baikal rift depression', *Earth Sciences Reviews* **34**, 81–118.

Mauduit, T., van Wijk, J., Sokoutis, D. & Cloetingh, S. (2007), 'Basin migration: Lithospheric vs. crustal controls', *Geophysical Research Abstracts* **9**, EGU2007–A–07941.

McClay, K., Dooley, T., Whitehouse, P. & Mills, M. (2002), '4-D evolution of rift systems: Insights from scaled physical models', *AAPG Bulletin* **86**, 935–959.

McClusky, S., Balassanian, S., Barka, A., Demir, C., Erginatav, D., Georgiev, I., Gurkan, O., Hamburger, M., Hurst, K., Kahle, H., Kastens, K., Kekelidze, G., King, R., Kotzev, V., Lenk, O., mahmoud, S., Mishin, A., Nadariya, M., Ouzounis, A., Paradissis, D., Peter, Y., Prilepin, M., Reilinger, R., Sanli, I., Seeger, H., Tealeb, A., Toksoz, M. & Veis, G. (2000), 'Global Positioning System constraints on plate kinematics and dynamics in the eastern Mediterranean and Caucasus', *Journal of Geophysical Research* **105**(B3), 5695–5719.

McGlue, M., Scholz, C., Karp, T., Ongodia, B. & Lezzar, K. (2006), 'Facies architecture of flexural margin lowstand delta deposits in Lake Edward, East African rift: Constraints from seismic reflection imaging', *Journal of sedimentary Research* **76**, 942–958.

McKenzie, D. (1972), 'Active tectonics of the Mediterranean region', *Geophysical Journal of the Royal Astronomical Society* **30**, 109–185.

McKenzie, D. (1978a), 'Some remarks on the development of sedimentary basins', *Earth and Planetary Science Letters* **40**, 25–32.

McKenzie, D. (1978b), 'Active tectonics of the Alpine–Himalayan belt: the Aegean Sea and surrounding regions', *Geophysical Journal of the Royal Astronomical Society* **55**, 217–254.

McKenzie, D. & White, R. (1989), 'Magmatism at rift zones: the generation of volcanic continental margins and flood basalts', *Journal of Geophysical Research* **94**, 7685–7729.

McLeod, A., Dawers, N. & Underhill, J. (2000), 'The propagation and linkage of normal faults: insights from the Strathspey-Brent-Stratford fault array, northern North Sea', *Basin Research* **12**, 263–284.

McNeill, L. & Collier, R. (2004), 'Uplift and slip rates of the eastern Eliki fault segment, Gulf of Corinth, Greece, inferred from Holocene and Pleistocene terraces', *Journal of the Geological Society, London* **161**, 81–92.

McNeill, L., Collier, R., De Martini, P., Pantosti, D. & D'Addezio, G. (2005b), 'Recent history of the Eastern Eliki fault, Gulf of Corinth: geomorphology, palaeoseismology and impact on palaeoenvironments', *Geophysical Journal International* **161**, 154–166.

McNeill, L., Collier, R. & Stone, J. (in prep), 'Slip rates of the Eastern Gulf of Corinth (Greece) Skinos and Pisia normal faults from ^{36}Cl cosmogenic surface exposure dating: Implications for fault displacement and rift models', *Geology* .

McNeill, L., Cotterill, C., Bull, J., Henstock, T., Bell, R. & Stefatos, A. (2007), 'Geometry and slip rate of the Aigion fault, a young normal fault system in the western Gulf of Corinth', *Geology* **35**, 355–358.

McNeill, L., Cotterill, C., Henstock, T., Bull, J., Stefatos, A., Collier, R., Papatheoderou, G., Ferentinos, G. & Hicks, S. (2005a), 'Active faulting within the offshore western Gulf of Corinth,Greece: Implications for models of continental rift deformation', *Geology* **33**, 241–244.

Molnar, P. (1988), 'Continental tectonics in the aftermath of plate tectonics', *Nature* **335**, 131–137.

Molnar, P., Fitch, T. & Wu, F. (1973), 'Fault plane solutions of shallow earthquakes and contemporary tectonics in Asia', *Earth and Planetary Science Letters* **19**, 101–112.

Moretti, I., Lykousis, V., Sakellariou, D., Reynaud, J.-Y., Benziane, B. & Prinzhoffer, A. (2004), 'Sedimentation and subsidence rate in the Gulf of Corinth: what we learn from the Marion Dufresne's long piston coring', *Comptes Rendus Geoscience* **336**, 291–299.

Moretti, I., Sakellariou, D., Lykousis, V. & Micarelli, L. (2003), 'The Gulf of Corinth: an active half graben?', *Journal of Geodynamics* **36**, 323–340.

Mourtzas, N. & Marinos, P. (2004), 'Upper Holocene sea level changes: Paleogeographic evolution and its impact on coastal archaeological sites and monuments', *Environmental Geology* **23**, 1–13.

Mouyaris, N., Papastamatiou, D. & Vita-Finzi, C. (1992), 'The Helice fault?', *Terra Nova* **4**(124-129).

Nur, A. & Mavko, G. (1974), 'Postseismic viscoelastic rebound', *Science* **183**, 204–206.

Nyst, M. & Thatcher, W. (2004), 'New constraints on the active tectonic deformation of the Aegean', *Journal of Geophysical Research* **109**, B11406.

Obar, J. (1987), 'Early artillery towers: Messenia, Boiotia, Attica, Megarid', *American Journal of Archaeology* **91**(4), 569–604.

Okada, Y. (1985), 'Surface deformation due to shear and tensile faults in a half–space', *Bulletin of the Seismological Society of America* **75**, 1135–1154.

Omar, G. & Steckler, M. (1996), 'Fission track evidence on the initial rifting of the Red Sea: two pulses, no propagation', *Science* **270**, 1341–1344.

Ori, G. (1989), 'Geologic history of the extensional basin of the Gulf of Corinth (?Miocene–Pleistocene), Greece', *Geology* **17**, 918–921.

Palyvos, N., Lemeille, F., Sorel, D., Pantosti, D. & Pavlopoulos, K. (2007), 'Geomorphological evidence of fast Holocene coastal uplift at the western termination of the Corinth rift (Greece): constraints on minimum holocene uplift rate and potential paleoseismological significance', *Geomorphology* . Earth-prints [http://www.earth-prints.org/dspace-oai/request] (Italy) ER.

Palyvos, N., Pantosti, D., De Martini, P., Lemeille, F., Sorel, D. & Pavlopoulos, K. (2005), 'The Aigion-Neos Erineos coastal normal fault system (western Corinth Gulf Rift, Greece): Geomorphological signature, recent earthquake history, and evolution', *Journal of Geophysical Research* **110**.

Pantosti, D., De Martini, P. M., Koukouvelas, I., Stamatopoulos, L., Palyvos, N., Pucci, S., Lemeille, F. & Pavlides, S. (2004), 'Palaeoseismological investigations of the Aigion fault (Gulf of Corinth, Greece)', *Comptes Rendus Geosciences* **336**(4-5), 335–342.

Papanikolaou, D. & Royden, L. (2007), 'Disruption of the Hellenic arc: Late Miocene extensional detachment faults and steep Pliocene–Quaternary normal faults – Or what happened at Corinth?', *Tectonics* **26**, TC5003.

Papatheoderou, G. & Ferentinos, G. (1995), Marine environmental study of bauxite tailings in the Gulf of Corinth: Bathymetry–morphology–geology, Technical Report No. 24, Laboratory of Marine Geology Physical oceanography, Department of Geology, University of Patras.

Parsons, B. & Sclater, G. (1977), 'An analysis of the variation of ocean floor bathymetry and heat flow with age', *Journal of Geophysical Research* **82**, 803–827.

Parsons, B. & Thompson, G. (1991), 'The role of magma overpressure in supressing earthquakes and topography: worldwide examples', *Science* **253**, 1399–1402.

Pe-piper, G. & Piper, D. (2002), *The igneous rocks of Greece*, Gebr. Borntaeger Verlagsbuchhandlung, Stuttgart.

Peacock, D. & Sanderson, D. (1994), 'Geometry and development of relay ramps in normal fault systems', *AAPG Bulletin* **78**, 147–165.

Peirano, A., Morri, C., Bianchi, C. N., Aguirre, J., Antonioli, F., Calzetta, G., Carobene, L., Mastronuzzi, G. & Orru, P. (2004), 'The Mediterranean coral Cladocora caespitosa: a proxy for past climate fluctuations?', *Global and Planetary Change* **40**(1-2), 195–200.

Perissoratis, C., Piper, D. & Lykousis, V. (2000), 'Alternating marine and lacustrine sedimentation during the late Quaternary in the Gulf of Corinth rift basin, central Greece', *Marine Geology* **167**, 391–411.

Petit, R. & Deverchere, J. (2006), 'Structure and evolution of the Baikal rift: A synthesis', *Geochemistry, Geophysics, Geosystems* **7**(11).

Piper, D. (2006), 'Sedimentology and tectonic setting of the Pindos flysch of the Peloponnese, Greece', *Geological Society of London Special Publication* **260**, 493–505.

Pirazzoli, P. (1986), Marine notches, *in* O. Van de Plassche, ed., 'Sea–level Research: A manual for the Collection and Evaluation of Data.', Vol. Norwich,UK,, pp. 361–400.

Pirazzoli, P., Stiros, S., Arnold, M., Laborel, J., Laborel-Deguen, F. & Papageorgiou, S. (1994), 'Episodic uplift deduced from Holocene shorelines in the Perachora peninsula, Corinth area, Greece', *Tectonophysics* **229**, 201–209.

Pirazzoli, P., Stiros, S., Fontugne, M. & Arnold, M. (2004), 'Holocene and Quaternary uplift in the central part of the southern coast of the Corinth Gulf (Greece)', *Marine Geology* **212**, 35–44.

Pollitz, F., Wicks, C. & Thatcher, W. (2001), 'Mantle flow beneath a continental strike-slip fault: Postseismic deformation after the 1999 Hector Mine earthquake', *Science* **293**, 1814–1818.

Reid, H. F. (1910), 'The mechanics of the earthquake, The California Earthquake of April 18 1906', *Report of the State Earthquake Investigation Commission* **2**(87).

Rigo, A., Lyon-Caen, H., Armijo, R., Deschamps, A., Hatzfeld, D., Makropoulos, K., Papadimitriou, P. & Kassaras, I. (1996), 'A microseismic study in the western part of the Gulf of Corinth (Greece): implications for large–scale normal faulting mechanisms', *Geophysics Journal International* **126**, 663–688.

Roberts, A. M., Lundin, E. R. & Kusznir, N. J. (1997), 'Subsidence of the Voring basin and the influence of the Atlantic continental margin', *Journal of the Geological Society* **154**, 551–557.

Roberts, G. (1996), 'Variation in fault-slip direction along active and segmented normal fault systems', *Journal of Structural Geology* **18**(6), 835–845.

Roberts, G. (1996b), 'Noncharacteristic normal faulting surface ruptures from the Gulf of Corinth, Greece', *Journal of Geophysical Research* **101**(B11), 25255–25268.

Roberts, S. & Jackson, J. (1991), 'Active normal faulting in central Greece: an overview', *Geological Society of London Special Publication* **56**, 125–142.

Robertson, A. & Dixon, J. (1984), Introduction: aspects of the geological evolution of the Eastern Mediterranean, *in* J. Dixon & A. Robertson, eds, 'The Geological Evolution of the Eastern Mediterranean', Vol. Geological Society Special Publication No 17, pp. 1 – 74.

Rohais, S., Eschard, R., Ford, M., Guillocheau, F. & Moretti, I. (2007), 'Stratigraphic architecture of the Plio-Pleistocene infill of the Corinth Rift: Implications for its structural evolution', *Tectonophysics* **440**, 5–28.

Rosendahl, B. R. (1987), 'Architecture of continental rifts with special reference to East Africa', *Annual Reviews of Earth and Planetary Science* **15**, 445–503.

Rouzo, S., Rabinowicz, M. & Briais, A. (1995), 'Segmentation of mid–ocean ridges with an axial valley induced by small–scale mantle convection', *Nature* **374**(6525), 795–798. 10.1038/374795a0 10.1038/374795a0.

Royden, L. & Keen, C. (1980), 'Rifting process and thermal evolution of the continental margin of Eastern Canada determined from subsidence curves', *Earth and Planetary Science Letters* **51**, 343–361.

Rundle, J. (1982), 'Viscoelastic–gravitational deformation by a rectangular thrust fault in a layered Earth', *Journal of Geophysical Research* **87**, 7787–7796.

Ruppel, C. (1995), 'Extensional processes in continental lithosphere', *Journal of Geophysical Research* **100**(B12), 24,187–24,215.

Ryder, I., Parsons, B., Wright, T. & Funning, G. (2007), 'Post–seismic motion following the 1997 Manyi (Tibet) earthquake: InSAR observations and modelling', *Geophysical Journal International* **169**, 1009–1027.

Sachpazi, M., Clement, C., Laigle, M., Hirn, A. & Roussos, N. (2003), 'Rift structure, evolution and earthquakes in the Gulf of Corinth, from reflection seismic images', *Earth and Planetary Science Letters* **216**, 243–257.

Sachpazi, M., Galve, A., Laigle, M., Hirn, A., Sokos, E., Serpetsidaki, A., Marthelot, J. M., Pi Alperin, J. M., Zelt, B. C. & Taylor, B. (2007), 'Moho topography under central Greece and its compensation by Pn time–terms for the accurate location of hypocenters: The example of the Gulf of Corinth 1995 Aigion earthquake', *Tectonophysics* **440**, 53–65.

Sakellariou, D., Lykousis, V., Alexandri, S., Rousakis, G., Nomikou, P., Georgiou, P. & Ballas, D. (2007), 'Faulting, seismic–stratigraphic architecture and later Quaternary evolution of the Gulf of Alkyonides basin', *Basin Research* **19**, 273–295.

Sato, T. & Matsu'ura (1992), 'Cyclic crustal movement, steady uplift of marine terraces, and evolution of the island arc-trench system in southwest Japan', *Geophysical Journal International* **111**, 617–629.

Scholz, C. & Finney, B. (1994), 'Late–Quaternary sequence stratigraphy of Lake Malawi (Nyasa), Africa', *Sedimentology* **4**, 173–179.

Scholz, C. & Hutchinson, D. R. (2000), 'Stratigraphic and structural evolution of the Selenga delta accomodation zone, Lake Baikal Rift, Siberia', *International Journal of Earth Science* **89**, 212–228.

Sclater, J. G. & Shorey, M. D. (1988), 'Mid-Jurassic through mid-Cretaceous extension in the Central Graben of the North Sea - part 2: estimates from faulting observed on a seismic reflection line', *Basin Research* **1**(4), 201–215.

Sengor, A. M. C. & Burke, K. (1978), 'Relative timing of rifting and volcanism on earth and its tectonic implications', *Geophysical Research Letters* **6**, 419–422.

Seyitoglu, G. & Scott, B. C. (1996), 'The cause of N-S extensional tectonics in western Turkey: Tectonic escape vs back–arc spreading vs orogenic collapse', *Journal of Geodynamics* **22**(1-2), 145–153.

Siddall, M., Rohling, E., Almogi-Labin, A., Hemleben, C., Meischner, D., Schmelzer, I. & Smeed, D. (2003), 'Sea–level fluctuations during the last glacial cycle.', *Nature* **423**, 853–858.

Simpson, R., Barall, M., Langbein, J., Murray, J. & Rymer, M. (2006), 'San Andreas fault geometry in the Parkfield, California, region', *Bulletin of the Seismological Society of America* **96**, S28–S37.

Smith, B. & Sandwell, D. (2003), 'Coulomb stress accumulation along the San Andreas fault', *Journal of Geophysical Research* **108**.

Sobolev, P. & Rundquist, D. (1999), 'Seismicity of oceanic and continental rifts – a geodynamic approach', *Physics of the Earth and Planetary Interiors* **111**, 253–266.

Sorel, D. (2000), 'A pleistocene and still-active detachment fault and the origin of the Corinth-Patras rift, Greece', *Geology* **28**(1), 83–86.

Steckler, M. & ten Brink, U. (1986), 'Lithospheric strength variations as a control on new plate boundaries: Examples from the northern Red Sea region', *Earth and Planetary Science Letters* **79**, 120–132.

Stefatos, A., Papatheoodorou, G., Ferentinos, G., Leeder, M. & Collier, R. (2002), 'Seismic reflection imaging of active offshore faults in the Gulf of Corinth: their seismotectonic significance', *Basin Research* **14**, 487–502.

Stein, C. & Stein, S. (1992), 'A model for the global variation in oceanic depth and heat flow with lithospheric age', *Nature* **359**, 123–129.

Stein, R. & Barrientos, S. (1985), 'Planar high–angle faulting in the Basin and Range: Geodetic analysis of the 1983 Borah Peak, Idaho, earthquake', *Journal of Geophysical Research* **90**, 11355–11366.

Steketee, J. A. (1958), 'On Volterra's dislocation in a semi–infinite elastic medium', *Canadian Journal of Physics* **36**, 192–205.

Stewart, I. (1996), 'Holocene uplift and palaeoseismicity on the Eliki fault, western Gulf of Corinth', *Annali di Geofisica* **39**, 575–588.

Stewart, I. & Vita-Finzi, C. (1996), 'Coastal uplift on active normal faults: the Eliki Fault, Greece', *Geophysical Research Letters* **23**, 1853–1856.

Stewart, J, H. (1980), 'Regional tilt patterns of late Cenozoic basin-range fault blocks, Western United States', *Geological Society of America Bulletin* **91**, 460–464.

Stewart, J., Watts, A. & Bagguley, J. (2000), 'Three-dimensional subsidence analysis and gravity modeling of the continental margin offshore Namibia', *Geophysical Journal International* **141**, 724–746.

Stewart, S. A. & Argent, J. (2000), 'Relationship between polarity of extensional fault arrays and presence of detachment', *Journal of Structural Geology* **22**, 693–711.

Stiros, S. C. (2001), 'The AD 365 Crete earthquake and possible seismic clustering during the fourth to sixth centuries AD in the Eastern Mediterranean: a review of historical and archaeological data', *Journal of Structural Geology* **23**(2-3), 545–562.

Stiros, S., Psimoulis, P. & Pitharouli, S. (2007), 'Geodetic constraints to the kinematics of the Kaparelli fault, reactivated during the 1981, Gulf of Corinth earthquakes', *Tectonophysics* **440**, 105–119.

Su, D., White, N. & McKenzie, D. (1989), 'Extension and subsidence of the Pearl River Mouth Basin, northern South China sea', *Basin Research* **2**, 205–222.

Symeonidis, N., Theothorou, G., Schutt, H. & Velitzelos, E. (1987), 'Paleontological and stratigraphic observations in the area of Achaia and Etoloakarnania W–Greece', *Annales Geologiques des Pays Helleniques* **38**, 317–353.

Taylor, B., Goodliffe, A. & Martinez, F. (1999), 'How continents break up: Insights from Papua New Guinea', *Journal of Geophysical Research* **104**, 7497–7512.

Taylor, B., Goodliffe, A., Weiss, J., Sachpazi, M., Hirn, A., Laigle, M. & Stefatos, A. (2003), 'Detachment tectonics in the Gulf of Corinth rift', *EGS – AGU – EUG Joint Assembly, Abstracts from the meeting held in Nice, France, 6 - 11 April 2003* **abstract 7222**.

Taymaz, T., Jackson, J. & McKenzie, D. (1991), 'Active tectonics of the north and central Aegean Sea', *Geophysical Journal International* **106**, 433–490.

Taymaz, T., Jackson, J. & Westaway, R. (1990), 'Earthquake mechanisms in the Hellenic Trench near Crete', *Geophysical Journal International* **102**(3), 695–731.

Thatcher, W., Foulger, G. R., Julian, B. R., Svarc, J., Quilty, E. & Bawden, G. W. (1999), 'Present–day deformation across the Basin and Range Province, Western United States', *Science* **283**(5408), 1714–1718.

Tsimplis, M. N., Proctor, R. & Flather, R. (1995), 'A two–dimensional tidal model for the Mediterranean sea', *Journal of Geophysical Research* **100**, 16223–16239.

Vail, P. R., Mitchum, R. M. & Thompson, S. (1977), 'Seismic stratigraphy and global changes of sea level', *American Association of Petroleum Geologists* **Memoir 26**, 63–81.

van Hinsbergen, D. J. J., Hafkenscheid, E., Spakman, W., Meulenkamp, J. E. & Wortel, R. (2005), 'Nappe stacking resulting from subduction of oceanic and continental lithosphere below Greece', *Geology* **33**(4), 325–328.

van Wijk, J. & Cloetingh, S. (2002), 'Basin migration caused by slow lithopsheric extension', *Earth and Planetary Science Letters* **198**, 275–288.

Vening Meinesz, F. (1950), 'Les graben Africains, resultat de compression ou de tension dans la croute terrestre?', *Inst. R. Colonial Belge, Bull* **21**, 539–552.

Vine, F. & Matthews, D. (1963), 'Magnetic anomalies over oceanic ridges', *Nature* **199**, 947–949.

Vita-Finzi, C. & King, G. (1985), 'The seismicity, geomorphology and tectonic evolution of the Corinth area, Greece', *Philosophical Transactions of the Royal Society of London* **A314**, 379–407.

Walsh, J. & Watterson, J. (1991), 'Geometric and kinematic coherence and scale effects in normal fault systems', *Geological Society Special Publication* **56**, 193–203.

Watts, A. (1989), 'Lithospheric flexure due to prograding sediment loads: Implications for the origin of offlap/onlap patterns in sedimentary basins', *Basin Research* **2**, 133–144.

Watts, A. (2001), *Isostasy and flexure of the lithosphere*, Cambridge University Press, Cambridge.

Watts, A., Karner, G. & Steckler, M. (1982), 'Lithospheric flexure and the evolution of sedimentary basins', *Philosophical Transactions of the Royal Society of London* **305**, 249–281.

Wernicke, B. (1981), 'Low–angle normal faults in the Basin and Range province: nappe tectonics in an extending orogen', *Nature* **291**, 645–647.

Wernicke, B. (1985), 'Uniform sense normal simple shear of the continental lithosphere', *Can.J.Earth Sci.* **22**, 108–125.

Wernicke, B. & Burchfiel, B. C. (1982), 'The opening of the Woodlark Basin, subduction of the Woodlark spreading system and the evolution of northern Melanesia since mid–Pliocene time', *Tectonophysics* **87**, 253–277.

Wessel, P. & Smith, W. (1995), 'New version of the generic mapping tools released', *EOS:Transactions of the American Geophysical Union* **76**, 329.

Westaway, R. (1996), 'Quaternary elevation change of the Gulf of Corinth in central Greece', *Philosophical Transactions of the Royal Society of London* **A354**, 1125–1164.

Westaway, R. (2002), 'The Quaternary evolution of the Gulf of Corinth, central Greece: coupling between surface processes and flow in the lower continental crust', *Tectonophysics* **348**(4), 269–318.

Westaway, R. (2007), 'Improved modelling of the Quaternary evolution of the Gulf of Corinth, incorporating erosion and sedimentation coupled by lower–crustal flow', *Tectonophysics* **440**(1-4), 67–84.

White, N. (1990), Does the uniform stretching model work in the North Sea?, *in* D. Blundell & A. Gibbs, eds, 'Tectonic evolution of the North Sea rifts', Oxford University Press, Oxford.

White, N. & Yielding, G. (1991), 'Calculating normal fault geometries at depth: theory and examples', *Geological Society, London, Special Publications* **56**(1), 251–260.

Whitehead, J., Dick, J. & Schouten, H. (1984), 'A mechanism for magmatic accretion under spreading centres', *Nature* **312**, 146–148.

Wicks, C., Thatcher, W., Monastero, F. & Hasting, M. (2001), 'Steady–state deformation of the Coso Range, East-Central California, inferred from Satellite Radar Interferometry', *Journal of Geophysical Research* **106**, 13769–13780.

Wood, R. & Barton, P. (1983), 'Crustal thinning and subsidence in the North Sea', *Nature* **302**, 134–136.

Wright, T. J., Ebinger, C., Biggs, J., Ayele, A., Yirgu, G., Keir, D. & Stork, A. (2006), 'Magma-maintained rift segmentation at continental rupture in the 2005 Afar dyking episode', *Nature* **442**, 291–294.

Zelilidis, A. (2000), 'Drainage evolution in a rifted basin, Corinth graben, Greece', *Geomorphology* **35**, 69–85.

Zelt, B. C., Taylor, B., Sachpazi, M. & Hirn, A. (2005), 'Custal velocity and moho structure beneath the Gulf of Corinth, Greece', *Geophysics Journal International* **162**, 257–268.

Zelt, B. C., Taylor, B., Weiss, J. R., Goodliffe, A. M., Sachpazi, M. & Hirn, A. (2004), 'Streamer tomography velocity models for the Gulf of Corinth and Gulf of Itea, Greece', *Geophysical Journal International* **159**(1), 333–346.

Ziegler, P. A. (1983), 'Crustal thinning and subsidence in the North Sea', *Nature* **304**(5926), 561–561. 10.1038/304561a0 10.1038/304561a0.

Ziegler, P. A. & Cloetingh, S. (2004), 'Dynamic processes controlling evolution of rifted basins', *Earth-Science Reviews* **64**(1-2), 1–50.